論文 / 著書情報
Article / Book Information

題目(和文)	光閉じ込め効果によるシリコン系薄膜太陽電池の高効率化に関する研究
Title(English)	Study of Light-Trapping Approaches for Silicon-Based Thin Film Solar Cells
著者(和文)	JANTHONG BANCHA
Author(English)	Bancha Janthong
出典(和文)	学位:博士(学術), 学位授与機関:東京工業大学, 報告番号:甲第9571号, 授与年月日:2014年3月26日, 学位の種別:課程博士, 審査員:小長井 誠,岩本 光正,山田 明,中川 茂樹,宮島 晋介,市川 幸美
Citation(English)	Degree:Doctor (Academic), Conferring organization: Tokyo Institute of Technology, Report number:甲第9571号, Conferred date:2014/3/26, Degree Type:Course doctor, Examiner:,,,,,
学位種別(和文)	博士論文
Type(English)	Doctoral Thesis

DOCTORAL THESIS

Study of Light-Trapping Approaches for Silicon-Based Thin Film Solar Cells

A THESIS SUBMITTED IN PARTIAL FULFILMENT OF

THE REQUIREMENT FOR THE DEGREE OF

DOCTOR OF PHILOSOPHY

Presented by

Bancha Janthong

Supervisor: Professor Makoto Konagai

Department of Physical Electronics

Graduate School of Science and Engineering

Tokyo Institute of Technology

March 2014

Abstract

[Study of Light-Trapping Approaches for Silicon-Based Thin Film Solar Cells]

This thesis presents the results of research on light-trapping approaches applied to silicon-based thin film solar cells including a-Si:H/μc-Si:H tandem solar cells. Experimental and theoretical study of the effects of light-trapping approaches, i.e. the introduction of optical layers; intermediate layer (IL) inserted between component cells, n-top layer with function of intermediate layer (nIL), n-bottom layer with function of ZnO back reflective layer (nBRL), front anti-reflection layers inserted between glass/ TCO (FAL) and between TCO/p-layer interface (FALp) as additional refractive-index matching layers, as well as the development of double-textured conductive zinc oxide coated on white glass substrates, on the performance of silicon-based thin film solar cells such as a-Si:H/μc-Si:H multi-junction solar cells was performed. The numerical analysis of nIL, nBRL, FAL and FALp was also systemically conducted using both of simulators called “OPTICAL” and “ASA” (Advanced Semiconductor Analysis). Firstly, optical calculation using OPTICAL simulator was carried out to find the optimal optical properties of optical layers used in this study, corresponding to different function purposes. Also, theoretical analysis using ASA simulator was provided in order to comprehend and confirm the effect of each optical layer on solar cell performance. From optical calculation results, it was found that for IL and nIL, their refractive index and thickness should be 1.7~2.0 and 40~50nm, respectively. At the same time, in case of nBRL, the films with refractive index of ~1.92 is needed and the optimal thickness is 60~80nm. Furthermore, the preferred refractive index and thickness of FAL was investigated to be ~1.74 and 60~80nm, respectively. Secondly, Different silicon oxide (SiO_x) films have been characterized and optimized for applying to several solar cells as

optical layers with those of individual function purposes. N-type hydrogenated silicon oxide (SiO_x:H) film was prepared and optimized by using RF-PECVD technique from a mixture of SiH_4,H_2,CO_2 as a reactant gas and PH_3 as a doping gas. Optical, electrical, and structural properties of the deposited n-SiO_x:H films were investigated by optical band gap (E_{04}), refractive index (n) , in-plan conductivity (σ) and Raman spectrum and XPS measurement. By optimizing deposition condition parameters, especially CO_2, PH_3, H_2 gas ratio and gap distance between electrodes, the SiO_x:H films with considerable optical and electrical properties, i.e. sufficient high conductivity and preferred low refractive index, were obtained and applied into silicon-based thin film solar cells. The optimized µc-SiO_x:H films were then inserted between a-Si:H top and µc-Si:H bottom cell interface as an IL and it was found that this IL was effective to be applied into the tandem solar cells. Also, a-Si:H/ µc-Si:H tandem solar cells with novel structure of p-a-SiC:H/ i-a-Si:H/ n-SiO_x:H/ p-µc-SiO:H/ i-µc-Si:H/ n-SiO_x:H/ Ag/ Al were for the first time proposed as a candidate to lower the optical losses and thus increase the solar cell performance, especially current density (J_{sc}). By using the optimum n-SiO_x:H layer instead of n-µc-Si:H/ZnO back reflector for a µc-Si:H solar cell as a nBRL, the spectral response, particularly, at the long wavelength could be improved and then Jsc was relatively increased up to 4.4%. Similarly, for the novel a-Si:H/µc-Si:H solar cell structure using the proper dual-functional n-SiO_x:H layers as a nIL and a nBRL, the relative improvement in J_{sc} by 9% was obtained and therefore the initial efficiency as high as 11.9% (V_{oc}=1.38 V, J_{sc}=12.24 mA/cm^2, *FF*=0.704) was achieved. These results approved that the first layer of newly developed n-SiO_x:H layers (nIL) can work as an n-top layer and also be functioned as an IL at the same time. Whereas, the second n-SiO_x:H layer (nBRL) can work as both an n-bottom layer and a ZnO back reflective layer. As a result, the reduction in optical losses could be obtained. Furthermore, these novel solar cell structures are beneficial for mass production since they were simplified. Thirdly, a-SiO$_x$ films were characterized and optimized by measuring optical properties such as transmittance, reflectance, and haze value for use as a FAL in µc-Si:H solar cells. The µc-Si:H solar cells with the optimized a-SiO$_x$ FAL were fabricated to compared the ones without FAL. By inserting optimized a-SiO$_x$ FAL with n of ~1.75 into the glass/ZnO interface of the µc-Si:H solar cell, J$_{sc}$ could relatively be increased by about 5%, especially in the 550-950 nm region. Also, this optimized FAL did not deteriorate the properties of the ZnO layer because no significant changes in V$_{oc}$ and FF were observed. As a result, the cell with an efficiency as high as 8.28% (V_{oc} =0.495 V, J_{sc} =25.09 mA/cm^2, FF =0.667) could be realized. Finally, W-textured ZnO:B films, with a very high haze value and greater angular distribution function (ADF), coated on white glass were successfully developed by MOCVD technique. Effects of glass-etching time on the morphology and optical properties of the substrates was investigated to explore the optimal properties for use as a front TCO contact in solar cells. It was found that the surface morphology of ZnO:B films deposited on white glass samples is mountain-chain-like double texture, while the one deposited on soda-lime glass samples shows cauliflower-like double texture. The mountain-chain-like double texture showed higher haze value over the whole wavelength region than the conventional cauliflower-like double texture and a feature size larger than 10 µm were obtained with longer RIE etching times. By applying these white glass substrates to novel a-Si:H/µc-Si:H tandem solar cells, the short-circuit current density J_{sc} could be increased from 12.2 mA/cm^2 to 13.4 mA/cm^2, corresponding to improved spectral response in the long wavelength region (>500 nm). Consequently, the initial efficiency

of the solar cells could be increased up to 13.3 %. Therefore, the ZnO:B films obtained here, by deposition on etched white glass, should be considered as a basis for promising substrates, for use as front transparent contact layers in silicon-based thin film solar cells.

TABLE OF CONTENTS

Chapter 1. Overview and Objectives of This Research

Chapter 2. Fundamental Properties of Silicon Based-Materials and Thin Film Silicon Solar Cells

Chapter 3. Theoretical Analysis of Multi-junction Silicon Thin Film Solar Cells Using Light-trapping Approaches

Chapter 4. Preparation and Characterization of μc-SiO$_x$:H Films Using RF-PECVD Technique

Chapter 5. Fabrication and Characterization of the novel a-Si:H/μc-Si:H double junction solar cells with n-top layer with a function of intermediate layer (nIL) and n-bottom layer with a function of back reflective layer (nBRL)

Chapter 6. Optimization of a Front Anti-Reflection Layer (FAL), inserted between Glass/TCO (FAL) and between TCO/p layer (FALp), and their applications to μc-Si:H single-junction solar cells

Chapter 7. Novel a-Si:H/μc-Si:H double junction solar cells fabricated on the Newly developed double-textured ZnO:B White Glass substrates

Chapter 8. General conclusions and future prospects

Chapter 1

Overview and Objectives of This Study

1.1 Background

This thesis presents the results of research on light-trapping approaches applied to silicon-based thin film solar cells including a-Si:H/μc-Si:H tandem solar cells. We have experimentally and theoretically studied the effects of light-trapping approaches, i.e., employments of n-top layer with function of intermediate layer (nIL), n-bottom layer with function of ZnO back reflective layer (nBRL), front anti-reflection layers inserted between glass/TCO (FAL) and between TCO/p-layer (FALp) as well as double-textured white glass substrate, on silicon-based thin film solar cell performance.

In this chapter, a general background and a purpose of the research are mainly presented. Firstly, motivation of the research, such as needs of renewable energy and the photovoltaic (PV) technology as a promising candidate for future energy sources, is briefly discussed. Then, the thin-film silicon solar cells as a low-cost material for photovoltaic applications are also described. Finally, the objective of this study and the outline of this thesis are then illustrated.

1.1.1 Needs of renewable energy resources

Since the industrial revolution at the end of 19th century, most of industries have been grown by depending on the fossil energy sources. The amount of world energy consumption, especially the energy from the fossil fuels, has rapidly increased for a couple hundred years. As shown in the figure 1.1[1], it shows the world consumption of fossil fuels by each energy source, since 1965. The consumption of fossil fuel energy sources have been increasing more and more yearly up to 4000 million tonnes of oil equivalence. It seems that there is a change in the trends of energy consumption of coal for the developed countries while the developing countries are becoming more and more dependent on energy sources from coal. As a result, there are no changes in the trends of world energy consumption, on the other hand, consumption of energy comes from the fossil fuel sources increased more and more. The world consumption in 2006 increased by more than twice Britain's total annual energy use and is the largest global yearly increase ever recorded. The International Energy Agency (IEA) forecasts that by 2030 demand for energy will be some 60% more than it is now [2]. Unfortunately, the amounts of those kinds of energy sources that can be available are very limited. It was predicted that the oils and coals will be depleted after 43 and 231 years, respectively [3]. Moreover, we also should notice that the consumption of fossil fuels leads to an emission of carbon dioxide (CO_2), one of the greenhouse effect gases. As shown in Figure 1.2 [4], in 2010, the global concentration atmospheric concentration of CO_2 has increased to 35 billion metric tons of carbon dioxide. This value is almost double of that in the 1970s [5]. Most of the CO_2 emissions were produced by the generation of electricity and heat, which come from the transportation and industry sectors. It is well known that CO_2, which one of the greenhouse effect gases, have caused a serious environmental problem so called "global warming issue". The global warming issue has attracted much attention for these several decades. It is also well recognized that the annual temperature in the world has rapidly increased. In fact, the mean annual temperature difference from normal in the world, i.e., the average value between the temperature near the earth and the sea surfaces, increases at the rate of 0.67^{o}C per one hundred years[6].

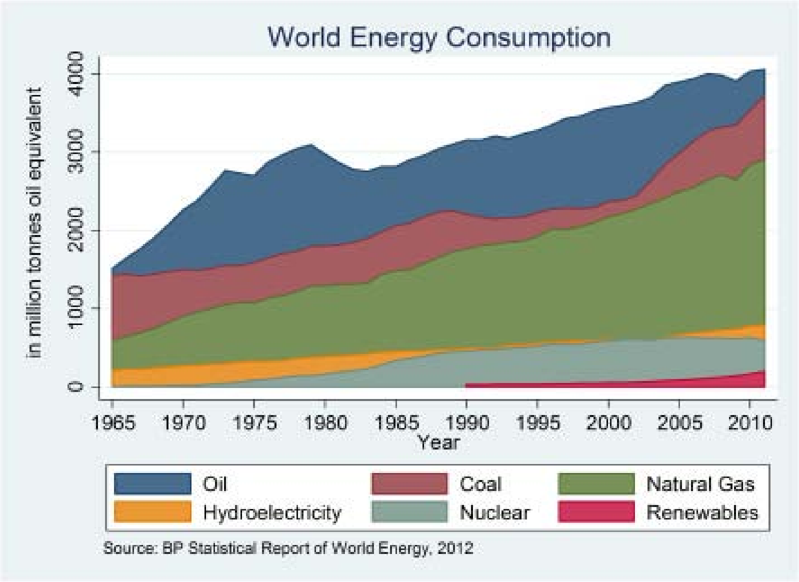

Figure 1.1 World energy consumption divided by energy sources from 1965 to 2010[1]

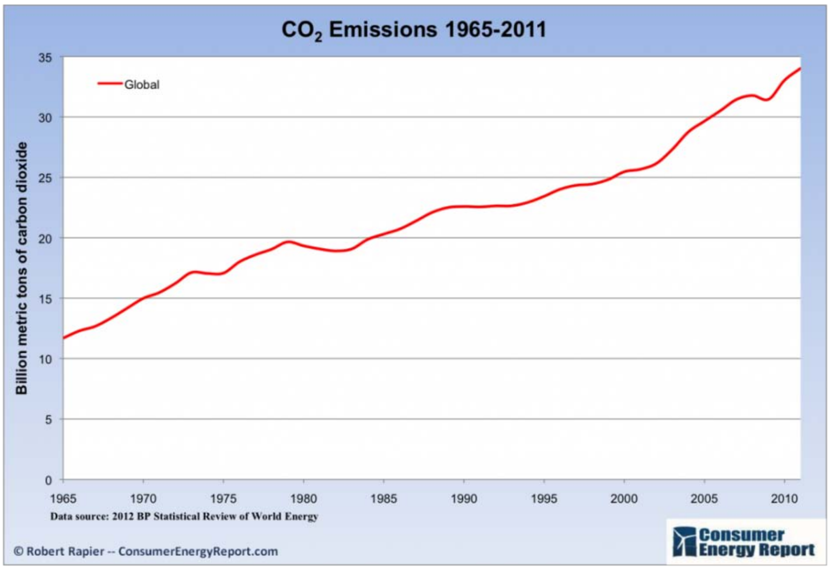

Figure1.2 Global Carbon Dioxide emission in atmosphere from 1965 to 2010[4]

To overcome the energy problems and to reduce the greenhouse effect gas emission explained above, the development of renewable energy with a lower environmental impact is urgently needed. Renewable energy is the energy source generated from non-fossil fuel resources excluding from the nuclear power which is sustainable. These renewable energies have many sources, such as solar light, solar thermal, hydro power, wind power, biomass, and geothermal heat. By their nature, these renewable energy sources are generally carbon-free or carbon neutral. Among these renewable energy sources, the solar power generation using solar light is the most promising candidate as an energy technology for the future energy sources. The solar power is mainly utilized in two ways. One is a conversion into electricity by solar cells; the other is an accumulation of heat in solar collectors. Here, the former called photovoltaics (PV) based on the photovoltaic effect is mainly discussed. Photovoltaics use the solar radiation, which is undoubtedly free and inexhaustible supply, as an energy source. The amount of energy supplied by the sun to the earth is more than five orders of magnitude larger than the world electric power consumption to keep the modern civilization going. Moreover, the solar power generation produces no residue and exhaust gases, and thus is non-polluting. Furthermore, since the photovoltaic power generation employs solar cells that convert the light energy directly into electrical energy, there are no moving parts such as turbines and generators needed in the thermal, atomic, and wind power generation processes. Therefore, the photovoltaic system needs little maintenance and is highly reliable for a long period. Besides, the electricity from the photovoltaics can be generated on wherever it is needed without requiring power transmission lines. Photovoltaics also can be constructed to any size in response to energy needs, from mili-watt size (for items such calculators and wristwatches) to mega-watt size (for solar plants). From the above features, it is clear that the photovoltaic system is the most beneficial sustainable energy. Therefore, significant

R&D efforts of photovoltaics have been made over the past two decades in a wide variety of technical fields, from solar cell materials, device structures, and mass production technologies to the photovoltaic systems themselves.

1.1.2 Current status and future prospects of photovotalics

Photovoltaic have attracted much interest as an alternative for fossil fuels since the oil crises of 1970s. Many research groups from several countries have been studied and developed many kinds of solar cells in order to reduce the costs of solar cells and to improve the performance of solar cells themselves. As a result, about an order of magnitude cost reduction has been achieved in the past 10 years [7].

Photovoltaic conversion is the direct conversion of sunlight into electricity with no intervening heat engine. As indicated above, photovoltaic devices are rugged and simple in design and require very little maintenance. Perhaps the biggest advantage of solar photovoltaic devices is that they can be constructed as stand-alone systems to give outputs from mili-watt to megawatts. That is why they have been used as the power sources for calculators, watches, satellites and space vehicles, and even megawatt-scale power plants. With such a vast array of applications, the demand for photovoltaic is increasing every year. For example here, as shown in Figure 1.3, the cumulative installed PV capacity all over the world is continuously increasing and has reached almost 70 GW peak at the end of 2011, where the unit of watt peak stands for the number of watts output of when the solar modules are illuminated under standard condition of 1 kW/m^2 at 25 °C. It was also indicated that the PV installation will further increase over 300 GW peak in 2016 under the scenarios of continuous moderate policy [8]. At present, the European Union is leading in PV installations with more than 70%

of the total world PV electricity generation capacity. The large expansion of grid-connected PV market in Germany, Spain, and Italy are supported by the Feed-in Tariff (FIT) programs. For countries in Asia region, China dominates the share of the annual installed PV production capacity and Taiwan is the second largest. Also, the introduction or expansion of FIT programs is expected to be an additional big stimulant for solar PV system installations in Asian countries.

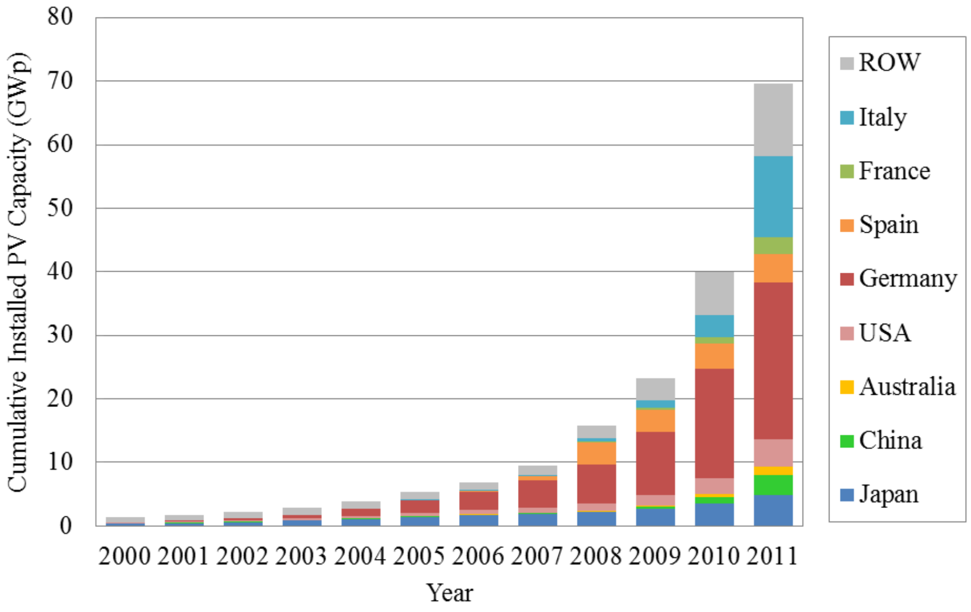

Figure1.3 Cumulative installed photovoltaics capacities by country in the world from 2000 to 2011 [8-10].

The current state of solar cell development is illustrated in Figure 1.4.While single crystalline and polycrystalline silicon solar cells dominate today's solar cell industry, the rapid rise in efficiency of the multi-junction thin-film cells makes a photovoltaic energy source a particularly attractive technology path. Under concentrated sunlight, three multi-junction solar cells have demonstrated to achieve efficiencies 44%

which twice higher than that of single crystalline silicon solar cells, which achieved at efficiency of 25.0%. This means that, in photovoltaic areas, a multi-junction concentrator system can generate electricity almost twice as much as a silicon panel with the same cell area. The concentrator solar cells focus the light onto a small area of cells, reducing the area of the solar cells by a factor of, typically, 500-1000 times. The reduced cell area overcomes the increased cell cost. The cell cost is diminished in importance and is replaced by the cost of optics. If the cost of the optics is comparable to the cost of the glass and support structure needed for silicon flat-plate modules, then the cost per unit area can remain fixed while the electricity production is essentially doubled. Thus, in high direct insolation locations, multi-junction concentrator technology has the potential to reduce the cost of solar electricity by about a factor of two. The efficiency is a moving target; today's triple-junction cell efficiency is over 40%. Thus it may be reasonably extrapolated that multi-junction cells may reach 50% efficiency in the future. As a result, the research and development of multi-junction solar cell is urgently required as a first step in order to achieve higher efficiency multi-junction solar cells concentrators.

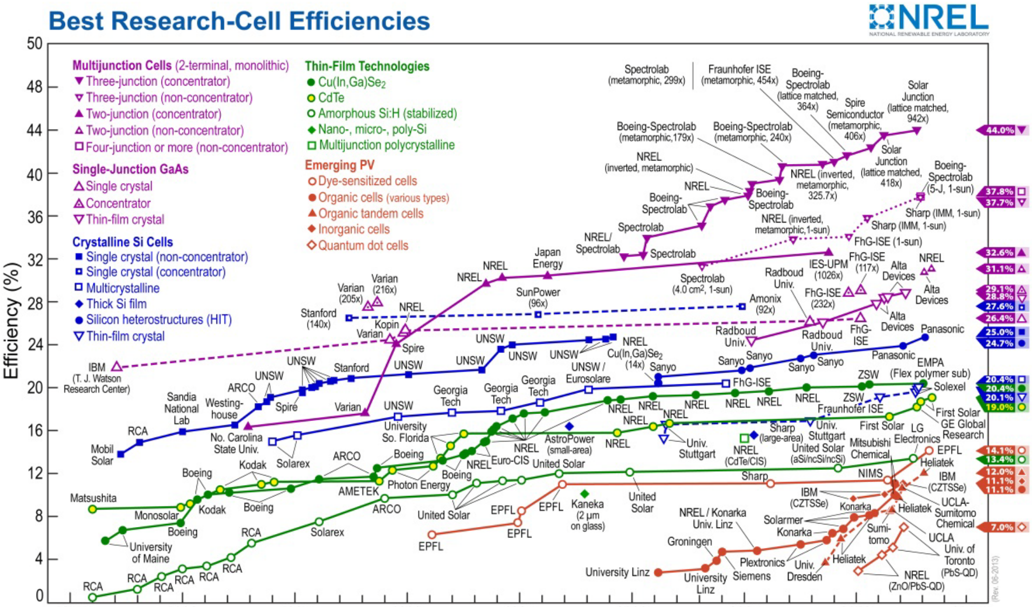

Figure 1.4 World record efficiencies of various PV technologies (Source: NREL)

1.1.3 Role of thin film silicon solar cells

As shown in Figure 1.5, for example, the annual photovoltaic production capacity in Japan is mainly dominated by c-Si and poly-Si solar cells. However, due to production process of c-Si and poly-Si solar cells, higher energy consumption and a large of amount of raw materials are needed compared to thin film solar cells. Crystalline Si is usually produced in the form of an ingot which is subsequently mechanically sawn into slices. The thickness of the Si-wafers used is usually in the range of 150-300 µm, about 100-300 times thicker than thin film silicon solar cells (0.5-3.0 µm). For that reasons, the module price of Si-wafer solar cell is more expensive than that of thin film solar cells. It is believed that the price of c-Si and poly-Si solar cells cannot be reduced even with large production scale due to various limitations, such as a global silicon shortage due to the rapid increase in silicon PV cell production in these years. Therefore, thin film solar cells have been intensively investigated as the alternative materials to crystalline silicon. These types of solar cells need low energy consumption for production as well as low raw material consumptions. They also need simple device processing and manufacturing technology which results in low production cost and better price performance ratio. Thin film solar cells are usually deposited at low temperatures (typically 150-300 ºC). Hence, these types of solar cells also can be deposited on low cost substrates, such as glass and even some plastics. In addition, since the solar cells are very thin, flexible solar cells can be made by depositing the solar cell on a flexible substrate, such as a metal film or plastic foil. Furthermore, thin film solar cells have been produced using various materials such as a-Si:H, CuInGaSe (CIGS), CdTe, and other novel materials. Among these thin film solar cells, a-Si:H based thin film solar cell is considered to be one of the most attractive materials. This type of solar cell does not either use any scarce elements such as selenium and indium in CIGS solar cell, or toxic elements such as cadmium in CdTe solar cell. In fact, present manufacturing of thin film solar cells has been almost occupied by that with a-Si:H based and related materials. However, the conversion efficiency of thin film silicon solar cells is still too poor compared to other types of solar cells. The module efficiency of thin film silicon solar cells is still in the range of 11-13% [12], whereas the module efficiency for c-Si module is about 20% or more [13]. It is well recognized that a remarkable efficiency improvement is needed for a wider practical use.

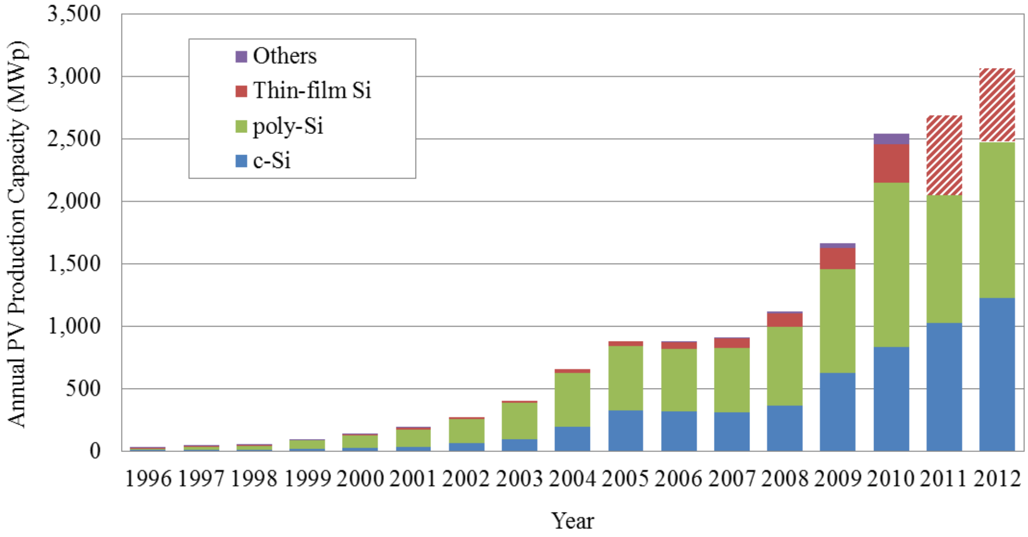

Figure 1.5 Annual photovoltaic productions based on solar cell materials [11]

Therefore, in order to improve solar cell efficiency, a multi-junction structure is considered as a promising candidate for the efficiency improvement in thin film silicon solar cells. This multi-junction structure consists of two or more p-i-n diodes. These solar cells are called tandem or triple solar cells for two or three p-i-n diodes, respectively. For a tandem cell, the p-i-n diode located at the light incident side is usually called as the top cell, and the other diode is called as the bottom cell. Materials with different band gaps are generally used for each sub-cell. The band gap of the top cell is selected to be wider than that of the bottom cell in order to utilize the sunlight more effectively. Although, there are many reports that studied on many type of the tandem solar cells and an efficiency of 14.7% has been obtained [14], the research have still been continuously done in order to achieve higher efficiency target. Here, the study of a-Si:H/μc-Si:H tandem solar cells using light-trapping approaches was performed to achieve the final goal.

1.2 Objectives of this thesis

In order to improve silicon-based solar cell performance, an employment of multi-junction solar cells is indeed required. As be well known, one of main requirements for multi-junction solar cells is a proper current matching between the series-connected cells since the component cell with the lowest current limits the current of complete devices. In a-Si:H/μc-Si:H double-junction solar cells, a thick a-Si:H top cell is generally needed to fulfill the current matching requirement. However, it is well known that thick a-Si:H solar cells tend to degrade more as reported by Staebler-Wronski Effect[15]. In order to improve current-matching between sub-cells and thus increase current density of a complete device without increasing thickness of a-Si:H top cell, which is sensitive to light-induced degradation, light-trapping approaches, e.g., front contact using textured transparent conductive oxide (TCO)[16-18], back reflector with highly reflective textured TCO/metal [19-20] and a transparent and/or reflective intermediate layer (IL) [21-22], have recently been investigated for applications into multi-junction solar cells. Moreover, there are still parasitic absorption loss from out of active layers and reflection loss produced by refractive index mismatch between each layer in silicon solar cells. The study to reduce the losses is extremely required in order to enhance solar cell performance.

As mentioned above, the main objective of this research is to study on light-trapping approaches applied to silicon-based thin film solar cells including a-Si:H/μc-Si:H double-junction solar cells. As shown in the figure 1.6, we have experimentally and theoretically studied the effects of light-trapping approaches, i.e., employments of n-top layer with function of intermediate layer (nIL), n-bottom layer with function of ZnO back reflective layer (nBRL), front anti-reflection layers inserted between glass/TCO (FAL) and between TCO/p-layer (FALp) as well as double-textured white glass substrate, on solar cell performance. The Numerical analysis of nIL, nBRL, FAL and FALp was systemically performed using both of simulators called “OPTICAL” and “ASA” to understand their effect on solar cell performance and to find the preferred properties of them for applications to solar cells. Here, Silicon-oxide-based materials were investigated to use as optical layers, i.e., nIL, nBRL, FAL, and FALp, in solar cells because their refractive index can be adjusted by the oxygen composition. Different silicon oxide (SiO_x) films have been optimized and applied into thin film silicon solar cells as optical layers, corresponding to those of individual application purposes. Also, the silicon-based thin film solar cells, including a-Si:H/μc-Si:H tandem cell with novel structure, using optimized nIL, nBRL,FAL and FALp as optical layers were fabricated and investigated in term of the effect of applied optical layers on their current density.

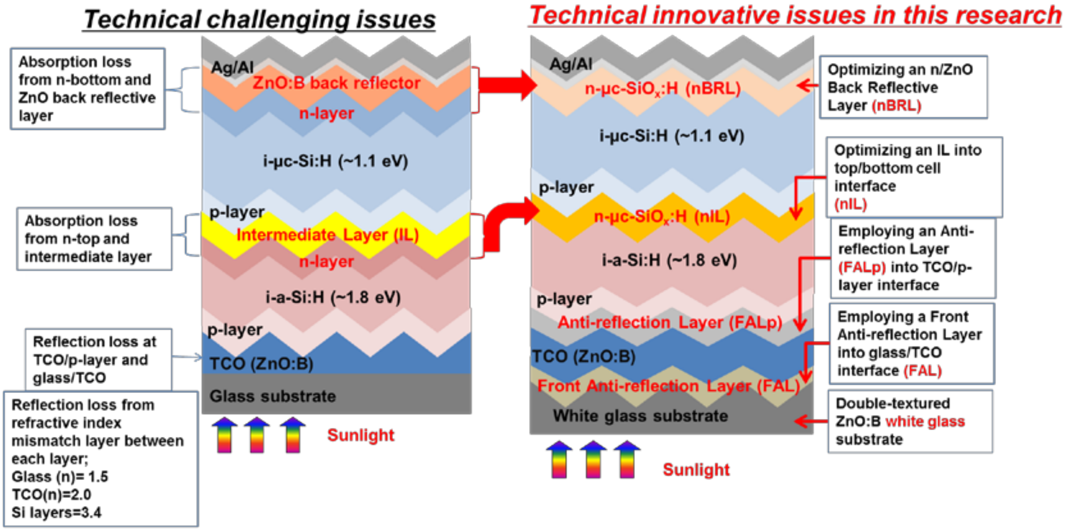

Figure 1.6 the technical innovative issues studied in this research to improve solar cell performance

2.3 Outline of this thesis

The structure of this thesis is summarized as shown in Figure 1.7. From the schematic diagram, the thesis consists of eight chapters. A brief description of each chapter is described as the following.

Chapter 1: The introduction and motivation of this study are described. Then the objective of this thesis is proposed.

Chapter 2: The fundamental properties of silicon-based materials and their related alloying-materials. Also, the introduction of silicon-based solar cells is explained.

Chapter 3: The results of the optical analysis of optical layers, i.e., nIL, nBRL, FAL, performed using simulator called OPTICAL in order to explore the preferred their properties corresponding to application purposes are explained. Additionally, the investigation of effect of these optical layers on the performance of silicon-based thin film solar cells, especially, current density, by simulator called ASA is presented in this chapter.

Chapter 4: The characterization and optimization of SiO_x films by using radio-frequency plasma-enhanced chemical vapor deposition (RF-PECVD) technique for application into silicon-based thin film solar cells are presented. The structural, optical, and electrical properties of the fabricated films were characterized by conductivity (σ), refractive index (n), optical band gap (E_{04}), as well as Raman spectra measurement and their results is demonstrated in this part.

Chapter 5: The fabrication of the novel a-Si:H/μc-Si:H double-junction solar cells applying SiO_x films as a nIL and nBRL is discussed. SiO_x films was firstly optimized and applied into novel μc-Si:H solar cells as a nBRL. Then, the optimized nBRL and nIL were employed in the a-Si:H/μc-Si:H double-junction solar cells with novel structure. The effect of the optimized nBRL and nIL on novel a-Si:H/μc-Si:H double-junction solar cells was reviewed compared with the solar cells with conventional structure. Furthermore, in order to improve the interface between n-μc-SiO_x:H top layer and p-μc-SiO_x:H bottom layer, the CO2 plasma treatment was introduced prior to deposition of p-μc-SiO_x:H of the bottom cells. The effect of CO_2 plasma on novel a-Si:H/μc-Si:H double-junction solar cell performance was also briefly explained compared to the one without CO_2 plasma treatment.

Chapter 6: The optimization of SiO_x films used as front anti-reflection layers inserted between glass/TCO (FAL) and TCO/p-layer (FALp) and their application to silicon-based single-junction solar cells is discussed. Firstly, SiO_x films was optimized by adjusting the oxygen content to apply in μc-Si:H single-junction solar cells as a FAL and its effect on solar cell performance, mainly current density, is reviewed. Next, similar to FAL, optimization of SiO_x films used as FALp was performed and the result of effect of FALp on solar cells, a-Si:H and μc-Si:H single-junction solar cells is presented.

Chapter7: The fabrication of novel a-Si:H/μc-Si:H double-junction solar cells on the newly developed double-textured ZnO:B (W-textured) white glass substrates is examined. The investigation of optical properties and evaluation of surface morphology of ZnO:B films were carried out. The ZnO:B films were optimized and applied into novel a-Si:H/μc-Si:H double-junction solar cells. The effect of W-textured ZnO:B on the a-Si:H/μc-Si:H solar cell performance was discussed compared with the one fabricated on textured glass substrates.

Chapter 8: The results obtained from this thesis are summarized. Even more, suggestions for further improvement are also offered.

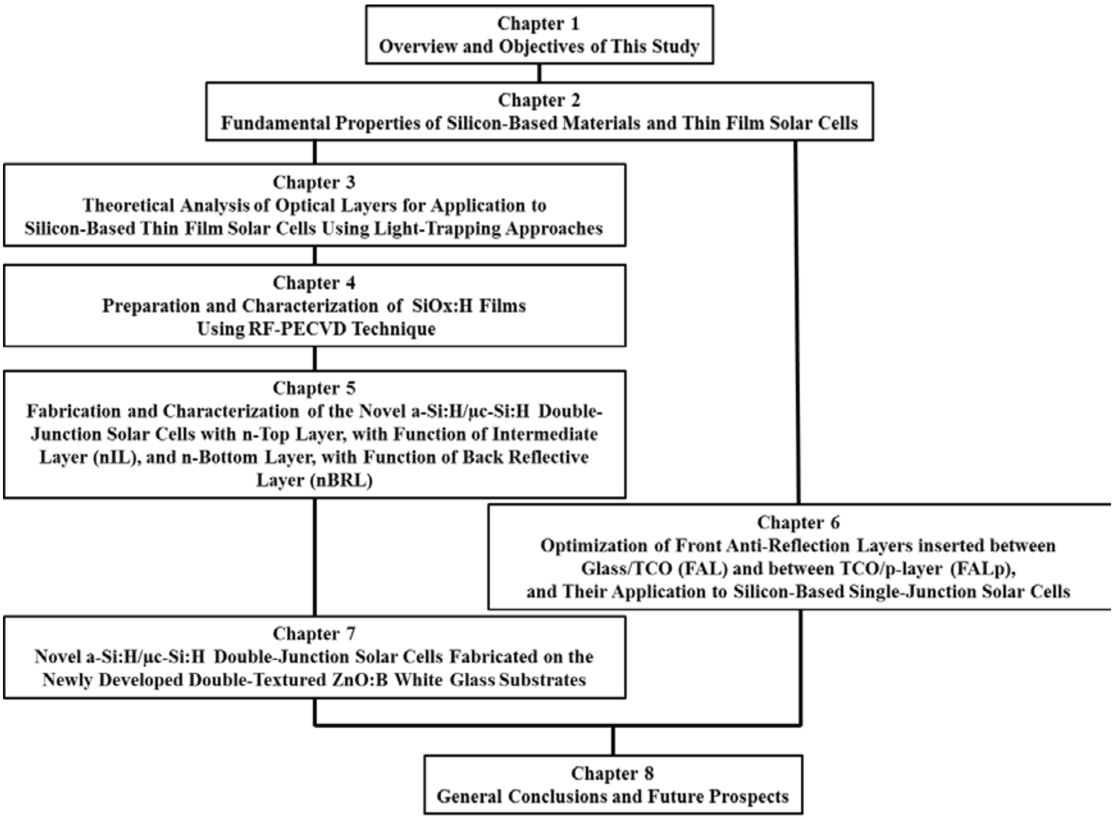

Figure 1-7 the outline of this thesis

References

[1] BP Statistical Review of World Energy report 2013:

[http://www.bp.com/en/global/corporate/about-bp/statistical-review-of-world-energy-2013.html.]

[2] International Energy Agency, Key World Energy Statistics 2013:

[http://www.iea.org/publications/]

[3] Y. Hamakawa: "New Energy Option for 21st Century: Recent Progress in Solar Photovoltaic Energy Conversion",*Oyobutsuri*, **68,** 8 (2000) 993.

[4] PB Statistical Review of World Energy report 2012:

[http://www.energytrendsinsider.com/2012/07/02/global-carbon-dioxide-emission]

[5] International Energy Agency (IEA): *CO_2 Emissions from Fuel Combustion 2012 – Highlights*(2012):[http://www.iea.org/publications/freepublications/publication/CO2emissionfromfuelcombustionHIGHLIGHTS.pdf]

[6] Japan Meteorological Agency, "Climate Change Monitoring Report 2007",

[www.data.kishou.go.jp/climate/cpdinfo/monitor/2007/pdf/CCMR2007_chap1.pdf]

[7] Y. Hamakawa: "*Thin-Film Solar Cells: Next Generation Photovoltaics and Its Application*", Springer, New York (2003) 7.

[8] European Photovoltaic Industry Association (EPIA): *Global Market Outlook for Photovoltaics until 2016* (2012).

[9] Photovoltaic Power System (PVPS) Programme of International Energy Agency (IEA): *Trends in Photovoltaic Applications - Survey report of selected IEA countries between 1992 and 2010* (2011). *IEA PVPS Annual report 2011* (2012).

[10] Joint Research Center of European Commission: *PV Status Report 2012* (2012).

[11] Japan Photovoltaic Energy Association (JPEA):

[http://www.jpea.gr.jp/04doc01.html]

[12] K. Yamamoto, A. Nakajima, M. Yoshimi, T. Sawada, S. Fukuda, T. Suezaki, M. Ichikawa, Y. Koi, M. Goto, T. Meguro, T. Matsuda, M. Kondo, T. Sasaki and Y. Tawada: *Solar Energy* **77** (2004) 939.

[13] J. Hao, A. Wang, E. Abbaspour-Sani, F. Yun, and M.A. Green: *IEEE Electron Device Lett.* **18** (1997) 48.

[14] K. Yamamoto, A. Nakajima, M. Yoshimi, T. Sawada, S. Fukuda, T Suezaki, M. Ichikawa, Y. Koi, M. Goto, H Takata, T. Sasaki, and Y. Tawada: *Proc. of 3rd World Conf. Photovoltaic Energy Conversion* (2003) 2789.

[15] D.L. Staebler and C. R. Wronsky: *Appl. Phys. Lett*. **31**, (1977) 292.

[16] W. W. Wenas, A. Yamada, M. Yoshino, M. Konagai, and K. Takahashi: *J. Appl. Phys.* **70** (1991) 7119.

[17] M. Berginski, J. Hupkes, M. Schulte, G. Schope, H. stiebig, B. Rech, and M. Wuttig: *J. Appl. Phys.* **101** (2007) 074903.

[18] J. C. Lee, V. Dutta, J. Yoo, J. Yi, J. Song, and K. H. Yoon: *Superlattices Microstruct.* **42** (2007) 369.

[19] X. Zhang, Q. Yue, X. zheng, X. Geng, S. xiong, and Ying Zhao: *Proc. 5th World Conf. Photovoltaic Energy Conversion* (2010) 3232.

[20] X. D. Zhang, Y. Zhao, Y. T. Gao, F. Zhu, C. C. Wei, X. L. Chen, J. Sun, G. F. Hou, X. H. Geng, and S. Z. Xiong: *J. non-Cryst. Solids* **352** (2006) 1863.

[21] D. Domine, P. Buehlmann, J. Bailat, A. billet, A. Feltrin, and C. Ballif: *Phys. Status Solidi: Rapid Res. Lett.* **4** (2008) 163.

[22] C. Das, A. Lambertz, J. Huepkes, W. Reetz, and F. Finger: *Appl. Phys. Lett.* **92** (2008) 053509.

Chapter 2

Fundamental Properties of Silicon-Based Materials and Thin Film Solar Cells

2.1 Introduction

As explained in chapter 1, at present, most of solar cells fabricated for commercial production are c-Si based solar cells. However, these types of solar cells are expensive due to the higher energy consumption and more raw materials needed for the production. Thin film silicon solar cells, such as a-Si:H and its alloys, are promising candidates for further cost-reduction of solar cells. In this chapter, the fundamental properties of silicon-based materials and solar cells are presented. First of all, fundamental aspects of silicon based materials, including hydrogenated amorphous silicon (a-Si:H), hydrogenated microcrystalline silicon (μc-Si:H) and hydrogenated-silicon-oxide-based materials are explained. Next, fundamental aspects of a-Si:H based solar cells are explained. Finally, light-trapping techniques employed in this study are also discussed.

2.2 Properties of amorphous silicon based materials

2.2.1 Hydrogenated amorphous silicon (a-Si:H)

Atomic structure of hydrogenated amorphous silicon

In order to comprehend design and operation of a-Si:H based solar cells, which differ from those of crystalline silicon solar cells, the structural and material properties of a-Si:H was discussed compared to single crystalline silicon. Pure silicon thin films can mainly be divided into amorphous, which consists of disordered atomic structure, and microcrystalline, which contains small crystallites with diameters ~1 µm of less: one of crystalline-based silicon materials. They can be deposited by vacuum deposition techniques such as sputtering and evaporation. For amorphous silicon (a-Si) the structural arrangement of the atoms is different from its counterpart of crystalline silicon (c-Si) [1-2]. Figure 2-1 illustrates the difference in atomic structure between hydrogenated amorphous silicon (a-Si:H) and single crystal silicon. Figure 2-1(a) shows the structure of single crystal silicon schematically. Each silicon atom is covalently bonded to four neighboring atoms. All bonds have the same length, and the angles between the bonds are equal. The number of bonds of an atom with its immediate neighbors in the atomic structure is called the coordination number or coordination. Thus, in single crystal silicon, the coordination number for all silicon atoms is four. A unit cell can be defined from which the crystal lattice can be reproduced by duplicating the unit cell and stacking the duplicates next to each other. Such a regular atomic arrangement is described as a structure with a long range order.

Figure 2-2(b) shows the simple structure of a-Si:H materials. It describes that a-Si:H does not exhibit a structural order over a long range. Nevertheless, there is a similarity in atomic configuration on a local atomic scale, where most of the silicon atoms have covalent bonds with four neighbors. Although a-Si:H lacks the long range order, it has the same short range order as single crystalline silicon. The small deviations in bonding angles and bonding lengths between the neighboring atoms in a-Si:H lead to a complete loss of the locally ordered structure on a few atomic distances. However, the variations in bonding lengths and angles are small and therefore the local arrangement of atoms in the periodic structure (lattice) resembles the local arrangement of atoms in the crystalline phase. The lack of long range order will result in a situation where the bonding requirements are not met for all atoms: it is called “dangling bonds”. Due to the dangling bonds assembled in the network, the resulting atomic structure of a-Si:H is considered as a continuous random network.

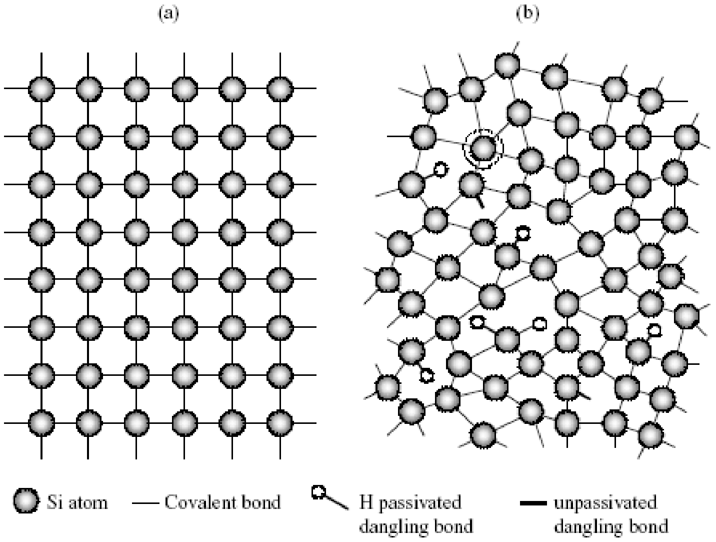

Figure 2-1 the general schematic illustration of the atomic structure of (a) single crystal silicon, (b) hydrogenated amorphous silicon [1]

Due to the short range order, the common semiconductor concept of the energy state bands, represented by the conduction and valence bands, can still be used in a-Si:H. The larger deviations in bonding angles and bonding lengths between the neighboring atoms in a-Si:H result in so-called weak or strained bonds. When enough energy is available, for example in the form of heat, weak bonds can easily be broken. This process leads to the formation of defects in the atomic network. It should be noted that in the continuous random network, the definition of a defect is modified with respect to the crystal structure. In a crystal, any atom that is out of place in a lattice forms a defect. In the continuous random network, an atom cannot be out of place. Because the only specific structural feature of an atom in the continuous random network is the coordination to its neighbors, a defect in a-Si:H is a coordination defect. This phenomena happens when an atom has too many bonds or too few. In a-Si:H, defects are mainly silicon atoms that are covalently bonded to only three silicon atoms (threefold coordinated) and have one unpaired electron, a so-called dangling bond. Since this configuration is the dominant defect in a-Si:H, the defects in a-Si:H are often related to dangling bonds. Some dangling bond defects are depicted in Figure 2-1(b). Another defect configuration is a silicon atom bonded to five silicon atoms (fivefold coordinated). This configuration is referred to as a floating bond. A silicon atom representing this floating bond defect is indicated in Figure 2-1(b) by a dotted circle. In pure a-Si (amorphous silicon that contains no other atoms than silicon), there is a large concentration of about 10^{21} defects per cm^3 in the amorphous atomic structure. Material with such a large defect density cannot be used for building a complete semiconductor device or a functional device. When amorphous silicon is deposited in such a way that hydrogen can be incorporated in the atomic network (as by glow discharge deposition from silane), then hydrogen atoms bond with most of the silicon dangling bonds. Strong silicon–hydrogen bonds are formed, which are illustrated in Figure 5-1(b). Hydrogen passivation of dangling bond defects reduces the defect density from about 10^{21} cm^{-3} in pure a-Si to 10^{15}–10^{16} cm^{-3} in a-Si:H, i.e. less than one dangling bond per one million silicon atoms. It is this material, an alloy of silicon and hydrogen, in which substitutional doping has been demonstrated and which is suitable for electronic applications.

Electrical and optical properties of hydrogenated amorphous silicon

The general discussion of the atomic structure of a-Si:H in the previous section provides a very useful step in understanding the electronic structure of this material. It was shown that the local bonding structure of the material is in a large part responsible for establishing the essential features of amorphous to that of crystalline silicon. Thus the observed similarities in the electronic structure of the two materials exist in a realization that many interesting properties of amorphous silicon are controlled by the bonding chemistry as they are in crystalline silicon. In this section, the correspondence between the atomic structure and the electronic and the optical properties of a-Si:H will be discussed. The disorder represented by fluctuations in atomic configuration causes fluctuations in the potential acting on an electron. As a result, the energies of the electronic states are perturbed and the band broadens as shown in Figure 2-2(b). In this situation, the sharp features prevalent in crystalline density of states become smeared and form band tails which extend into the forbidden gap. Therefore, the sharply defined band edges of the valence and conduction bands are non-existent in amorphous silicon. Calculations based on the tight-binding approach have shown that the energies of bonding states and anti-bonding states are differently affected by material disorder. For example, the energies of the anti-bonding states are less sensitive to the bonding disorder than are the energies of the bonding states. Consequently, the shapes of the band tails in amorphous silicon are not symmetrical, with more states in the valence band tail than in conduction band tail. The asymmetry in the distribution of localized states affects the position of the Fermi level. In an intrinsic (undoped) uniform sample of amorphous silicon, the Fermi level is generally in the center of forbidden band gap. It would be extremely useful if there were some means of determining the forbidden band gap, and it would be valuable as an indication of the characteristics of the semiconductor. When electrons or holes conduct through the solids, their mobility in the conduction band or valence band is large. The conduction between localized states is determined by hopping conduction, resulting in a sharp decrease in mobility. If mobility is expressed as an energy function, a region in which the mobility shows a sharp decrease, as given in Figure 2-2(c), this band gap is called a “mobility gap”, in fact, though the measurement of the mobility gap is impossible. Accordingly, the optical band gap (E_{opt}) obtained from measurement of the absorption coefficient is often employed as one of the standards of the forbidden band gap.

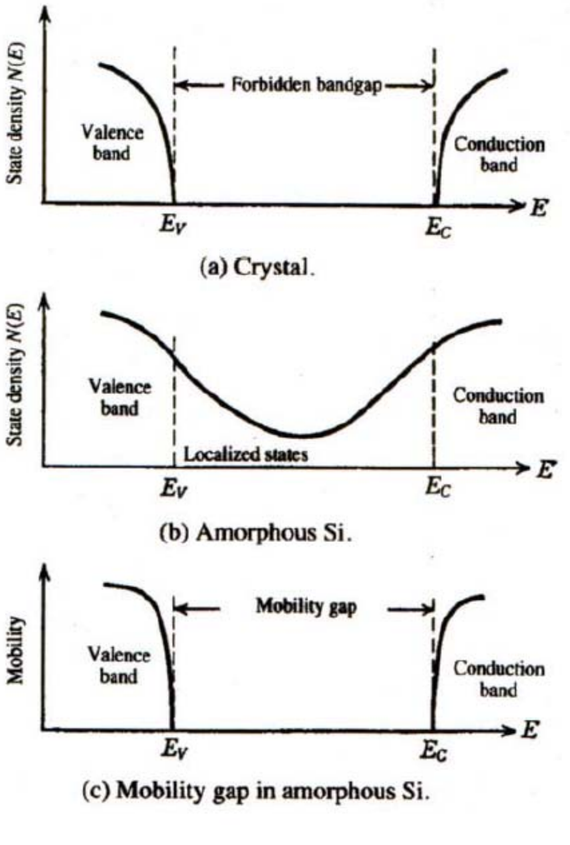

Figure 2-2 Energy band structure in c-Si and a-Si [3]

As mentioned above, the structure of a-Si:H can be described as a continuous random network, but in a real a-Si:H network the short range order may differ from one site to another. The slight distortions in the atomic configuration result in random distribution of charged centers leading to a non-periodic potential. A disordered potential can lead to strong electronic scattering and a short coherence length of the electron wave function. In amorphous silicon the coherence length is approximately of the order of the lattice spacing and the resulting uncertainty in the wave vector is of the same magnitude as the wave vector itself. Under these regimes the momentum is no longer a good quantum number and is not conserved in optical transitions. Thus all optical transitions in amorphous silicon can be considered as direct. The probability of optical transitions in direct band gap material is greater than that of an indirect band gap, for this reason the absorption coefficient of a-Si:H is higher compared to crystalline silicon. The absorption coefficient can be calculated from the optical band gap (Eg). The optical band gap can approximately be determined as a function of photon energy (hν) using Tauc's rule [4].

$$(\alpha h\nu)^{1/2} = A(h\nu - E_{opt}) \qquad 2.1$$

Where α is the absorption coefficient and A is a constant. The $(\alpha h\nu)^{1/2}$behavior is predicted for an amorphous semiconductor if the band edges are parabolic and the matrix elements for optical transitions are independent of energy. However the quadratic energy dependence of the optical band gap is not universally observed. The distribution near the band gap edges can be linear and cubic energy dependence $(\alpha h\nu)^{1/3}$ has been predicted for the optical band gap by Klazes et al [5]. The optical gap does not define the band gap of amorphous silicon, therefore, mobility gap is generally used to define the band gap of amorphous silicon material. The optical gap is slightly smaller than the mobility gap. Since the energy of the mobility edge depends strongly on the extent of material disorder, the band gap of amorphous silicon can be varied according to the degree of disorder.

The optical absorption properties of amorphous silicon are important for understanding the operation of a solar cell and for optimizing its conversion efficiency. The optical band gap can be used to estimate the energy of photons that can be absorbed by a-Si:H. By decreasing the optical gap, one can increase the part of the solar spectrum that is absorbed by a-Si:H. Experimental observations have shown that the absorption edge decreases exponentially with energy. This exponential decrease which “tails” into the band gap is known as the Urbach edge region and is correlated with the width of the band tail. Thus the importance of understanding the absorption processes in a-Si:H stems from their use as a probe for the local structure of a-Si:H network. From absorption measurement, one can deduce information on both the tail and defect states.

2.2.2 Hydrogenated Microcrystalline silicon (μc-Si:H)

It has been known that a necessary condition for growth of microcrystalline silicon is a high density of atomic hydrogen at the growing surface. The density of atomic hydrogen can be enhanced by adding hydrogen to the plasma or by increasing plasma power as observed from plasma optical emission spectra, as well as by increasing plasma excitation frequency. Thus, studies of μc-Si:H layers are often performed on series of layers deposited with varying values of silane concentration (SC = $[SiH_4]$ /$[SiH_4 + H_2]$). Adhesion of micrometer thick layers on glass substrates is another issue, due to the large internal mechanical stress present in μc-Si:H layers .

Microcrystalline silicon is a complex material. Its microstructure consists of the microcrystalline phase itself, made of silicon nanocrystals combined, with some amorphous silicon, into conglomerates. Figure 2-3 shows a plane view of a μc-Si:H conglomerate consisting of silicon nanocrystals possessing a diameter between 10 and 20 nm, embedded into amorphous silicon matrix. The conglomerates are separated by a varying amount of amorphous silicon, grain boundaries and/or cracks. The silicon crystallites in the material are of nanometer scale which also sometimes designated as ‘nanocrystalline silicon’. On the other hand, the term ‘microcrystalline’ comes from the micrometer scale conglomerate dimensions in this material.

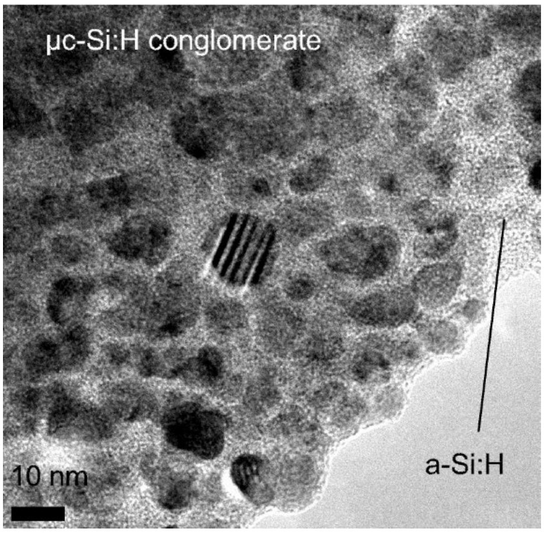

Figure 2-3 transmission electron microscopy micrograph of a plane view taken within a microcrystalline conglomerate [1]

In general, the microstructure of μc-Si:H depends on the fabrication conditions and ultimately on the underlying substrate on which nucleation and growth take place. A sketch of the evolution of microstructure μc-Si:H as a function of SC is given in figure 2-4. At low silane concentration, μc-Si:H consists of elongated nanocrystals separated by cracks that extend through the whole layer. Such layers with a high density of grain boundaries and a columnar structure are prone to post oxidation, a phenomenon that is responsible for a variation in the dark conductivity, activation energy and thus, leads to a change in many of the electronic transport properties. As the value of SC is increased, the material becomes denser and at the same time less crystalline; it is also less affected by post oxidation. Close to the amorphous/microcrystalline transition, μc-Si:H consists of conical conglomerates of microcrystalline silicon separated by amorphous silicon, as shown in figures 2-4 [6]. A vertical section through the microstructure of such layers can be described as follows: first, just above the substrate, is a continuous, fully amorphous layer below the nuclei (so called incubation layer), this is followed by a mixed phase layer (consisting of amorphous and microcrystalline phases), starting at the nucleation points and extending laterally up to the coalescence threshold. Then, the conical conglomerates grow as microcrystalline columns.

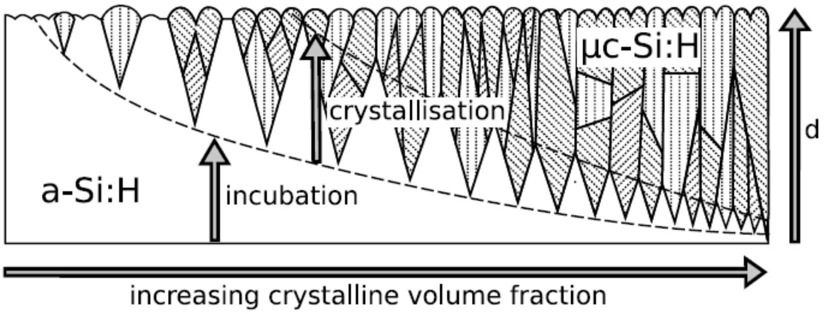

Figure 2-4 schematic diagram of the structural properties of μc-Si:H. From left to right the composition changes from amorphous to highly crystalline (after Collins et al.)

2.2.3 *Silicon oxide based materials*

Hydrogenated amorphous/microcrystalline silicon oxide

In hydrogenated amorphous silicon oxide (a-SiO:H) films, incorporation of oxygen enhances optical gap due to a large number of Si-O-Si bond formation, which lies deep into valence band states. An induction effect of this Si-O on other bonds within the network also takes place. At higher oxygen content micro-void forms and bonded hydrogen accumulates in di and/or polyhydride form. At this stage a phase separation of Si-rich and O-rich region taking place. A peak shift of absorption spectra within 1850 - 2250 cm-1, towards higher wave number is continuous. A gradual increase and broadening of 850 cm-1 absorption band on both sides of peak position indicate higher structural disorder in network formation. It may be considered that the stretching vibration of OH bonded to Si gives rise to 780 cm-1 absorption band. This Si-OH formation is beneficial which prevents deterioration in photosensitivity due to reduction in bonded hydrogen content. Hydrogen content is found reducing as oxygen content increases from zero to ~15 at %. A systematic study is carried out to correlate the optoelectronic property with local atomic arrangement.

On the other hand, hydrogenated microcrystalline silicon oxide (μc-SiO:H) was successfully prepared from a gas mixture of SiH_4, H_2, and CO_2 as a oxygen source gas by P.Sichangrist [7]. For p-type and n-type μc-SiO:H could also be deposited using B_2H_6 and PH_3 as a doping source gas, respectively. Such films have higher optical band gap owing to higher oxygen content, at the same time they also have several order of magnitude higher conductivity as a result of microcrystallinity. As proposed by Watanabe et al. in the two phase model as shown in figure 2-5, the oxygen rich phase is effective in increasing the optical gap and Si rich phase contribute to high conductivity [8]. Therefore, μc-SiO:H become an attractive alternative material for use as a window layer in a-Si based solar cell [9-10]. The optical band gap of a-SiO:H can be widened with increasing oxygen composition, however, after inclusion of certain percentage of oxygen its electrical properties degrade. On the other hand, μc-SiO:H can simultaneously give higher electrical conductivity and optical band gap than that of its amorphous counterpart. It is therefore thought the base candidate among the wide gap materials for use as a window layer in a-Si:H base solar cells

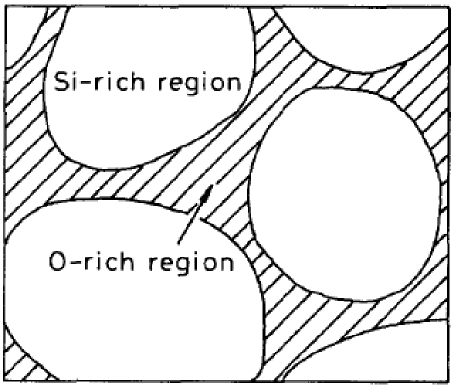

Figure 2-5 Schematic diagram of two phase model of $SiO_{X:}H$ (after Watanabe et al.)

2.3 Properties of amorphous silicon based solar cells

2.3.1 Structure of solar cells

Amorphous silicon material is widely applied for the production of solar cells. With this material, it is possible to produce large-area and low cost thin film solar cells on a variety of substrates. The physics of amorphous silicon based solar cells is quite different from that of the conventional crystalline devices. The existence of localized states greatly impedes the smooth operation of the solar cell. The electron and hole mobilities in the conduction and valence bands are low (10-20 cm^2/Vs for electrons and 1-10 cm^2/Vs for holes). In doped a-Si:H the diffusion lengths are shorter than in the undoped or intrinsic a-Si:H. Thus the charge carriers absorbed in the depletion region are the only ones that can be effectively separated in a-Si:H solar cell. However, an ordinary p-n structure from a-Si:H cannot show photovoltaic phenomenon since the lifetime of photo-excited free charge carriers is too short to make a significant separation of them. For this reason the most efficient a-Si:H solar cells are p-i-n devices. The schematic band diagram of a p-i-n device is shown in Figure 2-6 for zero bias conditions. The p and n layers provide the built-in potential (V_{bi}) of the junction. Shown are the valence band edge (E_V), the conduction band edge E_C as functions of the position of solar cell structure. It should be noted that the thickness of the intrinsic layer can be reduced to improve charge collection. Photo-generated carriers are collected by drift mechanism and not by diffusion as is the case for crystalline solar cells.

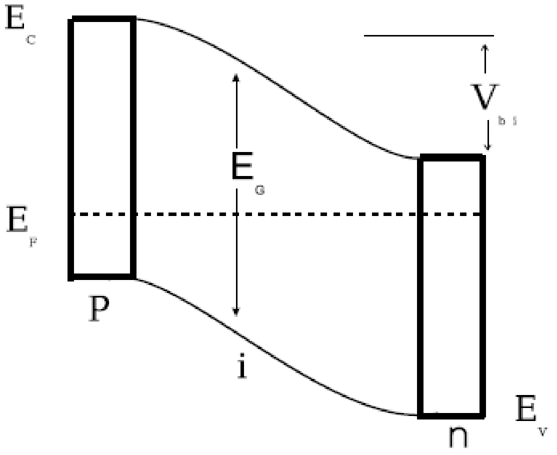

Figure 2-6 Schematic band diagram of a-Si:H p-i-n structure [11]

There are two configurations of amorphous silicon solar cells, superstrate type (p-i-n) and substrate type (n-i-p) devices. The difference of the two structures is determined by the order of the different layers deposited. For p-i-n structures, the p-layer is deposited first on a transparent conductive oxide (TCO)-coated glass substrate and then followed by i- and n-layers. On the other hand, for n-i-p structures, the n-layer is deposited on a metal substrate, i.e. stainless steel or aluminum, followed by i-, p- and TCO layers. The TCO forms the top electrode and the back contact is made of aluminum or silver. As the TCO material, SnO_2:F and ZnO:Al are commonly used. The TCO layer is often textured to scatter the entering light and thus increase the average optical path length through the solar cell. The average optical path length through the solar cell is further increased by using a highly reflective back contact.

2.3.2 Solar cell characteristics

The performance of solar cells under illumination can be described using their current-voltage (I-V) characteristics. In fact, it is sufficient to characterize the current-voltage characteristics only with a few parameters. If considering a typical current-voltage curve of a p-n junction diode in the dark and under illumination, three parameters are defined to give a complete description of the electrical behavior; these are (i) open-circuit voltage (V_{oc}), (ii) short-circuit current (J_{sc}), and (iii) fill factor (FF) [12].

V_{oc} and J_{sc} are the values of voltage and current which are obtained under illumination when $I = 0$ and $V = 0$, respectively, while FF is defined by

$$FF = \frac{V_m I_m}{V_{oc} I_{sc}} \tag{2.1}$$

where V_m and I_m are output voltage and output current at the maximum operating point, respectively. The efficiency η is then defined by

$$\eta = \frac{V_m \times I_m}{P_{in}} = \frac{V_{oc} \times I_{sc} \times FF}{P_{in}} \tag{2.2}$$

where P_{in} is the input energy to the solar cells.

In a dark state (without illumination), the expression of the dark current (I_d) is the same as the current flowing in p-n junction diode

$$I_d = I_0 \left\{ exp\left(\frac{qV}{nkT} \right) - 1 \right\} \tag{2.3}$$

where I_0 is the reverse saturation current, q is the electron charge, V is the applied voltage, n is the diode factor representing deviation from idea diode characteristics, k is Boltzmann’s constant and T is the absolute temperature.

Under light illumination, a photocurrent (I_{ph}) is generated as diode reverse current, hence the current-voltage relationship becomes

$$I = -I_{ph} + I_0 \left\{ \left(\frac{qV}{nkT} \right) - 1 \right\} \tag{2.4}$$

I is the net current which also can be described as $I = I_d - I_{ph}$.

From equations (2.3) and (2.4), the V_{oc} can be expressed as

$$V_{oc} = \frac{nkT}{q} ln\left(\frac{I_{ph}}{I_0} + 1 \right) \tag{2.5}$$

where the reverse saturation current I_0 can be expressed as

$$I_0 = A\left(\frac{qD_e n_i^2}{L_e N_A} + \frac{qD_h n_i^2}{L_h N_D} \right) \tag{2.6}$$

where A is the area, N_A and N_D are the acceptor and donor concentration, respectively, D_e and D_h are the diffusion coefficient for electron and hole, respectively, L_e and L_h are the minority carrier diffusion length for electron and hole, respectively. The intrinsic carrier concentration n_i in equation (2.6) can be expressed as

$$n_i^2 = N_c N_v e^{\left(-\frac{E_g}{kT} \right)} \tag{2.7}$$

where N_c and N_v are the effective density of state in the conduction and valence band, respectively.

From equation (2.5), we can clearly see that high V_{oc} can be obtained when I_0 is as small as possible. Moreover, from equations (2.6) and (2.7) we also can see that that small I_0 can be achieved by using wide band gap materials. This relationship reveals that the use of wide band gap materials will result in high V_{oc} solar cells.

2.4 Key issues to forward high efficiency silicon-based thin film solar cells

2.4.1 Multi-junction structures

As briefly discussed in chapter 1, the multi-junction solar cell is considered as the promising candidate to obtain a higher-efficiency silicon-based thin film solar cell. a tandem solar cell consists of two or three p-i-n junctions (diodes) that optically situated one on top of the other, called a double- or a triple-junction solar cell, respectively. The stack of individual p-i-n junction (the sub-cells) forms a tandem solar cell in series-connected structure.

For example here double-junction solar cells, it contains two sub-cells: the top cell, which is the cell that the light pass through first, and the bottom cell, which the light pass through from the top cell. The incident light is partially absorbed when it pass through the top cell and the remaining part of the light can possibly be absorbed when pass through the bottom cell. For use as an active intrinsic layer in the bottom cell, a narrower-gap material is chosen than while for the top cell the wider-gap material is suitable to be used. Thus the bottom cell effectively absorbs the photons of the longer wavelength range for which the wider-gap top cell is relatively transparent. In order to confirm that the sub-cells with a narrow band gap only absorb light with low photon energies, the sub-cells should be arranged such that, from the top with wider band gap to the each sub-cell, which has a narrower band gap than the previous sub-cell, in sequence. The light enters through the sub-cell with the widest band gap where only the photons with photon energy higher than this band gap are absorbed. The remaining photons are transmitted to the underlying sub-cells with narrower band gaps.

The multi-junction solar cells was developed in order to further absorb solar spectrum using more than two different band gap of absorber layer, which can absorb the different region of solar spectrum, stacked on the top of the other sub-cells in series-connected structure. The one of advantages of multi-junction solar cells is that the thickness of the sub-cells, especially a-Si:H based cells which is sensitive to Staebler-Wronski effect [13], and thus the light-degradation can be reduced and at the same time the thickness of the complete device can be kept thick enough to absorb most of the light. Further advantages are that the open-circuit voltage is increased and the current is reduced, leading to fewer losses due to series resistance. However, as the two component cells are connected in series, the current of the devices is usually limited by one sub-cell. Thus, in order to achieve the highest conversion efficiency the optimization of the thickness of each individual sub-cell, that yield the same photo-current for all sub-cells, is needed to consider. This matching of the thickness of the sub-cell to balance the photo-current between sub-cells is generally referred to as “current-matching”.

In addition to a reduced degradation, the multi-junction concept allows for reducing energy losses from solar cells using a single band gap for the absorber layer. The energy losses from single solar cells are that (i) most photons with energy less than the band gap are lost for power generation because few of these photons are absorbed and (ii) photons with energy much higher than the band gap create electron and hole pairs with excessive energy than the mobility gap and this excessive energy is lost as the photon-generated charge carriers thermalize toward the mobility edges [14].

As a result, a single-junction solar cell with a narrow-gap absorber layer generally generates a high short-circuit current and a low open circuit voltage, while the other single-junction solar cell with a wide-gap absorber layer generally generates a low short circuit current density and a high open circuit voltage. By combining these two single solar cells as a multi-junction structure higher short-current density and improved open circuit voltage of a complete device can be expected.

2.4.2 Light trapping approaches

As previously mentioned in chapter 1, for multi-junction solar cells, light trapping approaches are necessary to enhance the light absorption in the active layer of the solar cells [15-17]. These techniques are preferable to increasing the thickness of the absorber layers as they avoid a reduction of the internal electric field and, consequently, the loss of the light-generated carrier collection efficiency. For a-Si:H based material, the low diffusion length and low drift length of photo-generated carriers limit the device thickness. As the limited thickness, the absorption coefficients of the material at the long wavelength range are not large enough to absorb most of the light. Thus, the light trapping structure is more important for a-Si:H based thin film solar cells to increase the light path inside the solar cells.

In case of silicon-based thin film solar cells with p-i-n configuration, as shown in figure 2-6, textured front transparent conductive oxide (TCO) and textured back reflector are widely used for improving the light trapping structure. Especially, textured front TCO can have much influence on a performance of the resulting solar cells. The main role of textured front TCO is to scatter the incident light at TCO/p interface in order to facilitate incident light with the improved mean optical length in the absorber [18]. Most of the substrate used for silicon based thin film solar cells in this study is glass substrate with conductive zinc oxide layer doped with Boron (ZnO:B) as front TCO. In case of ZnO films, several types of the textures can be easily formed by optimizing a deposition technique or condition. In addition, the surface can be modified easily with a post-treatment [19] of ZnO films or a pre-treatment of glass sheet before deposition of ZnO:B films [20].

Moreover, silicon based thin film solar cells generally employ a back reflector between n-layer and back electrode to improve a light-absorption. A combination of ZnO and Ag has been developed to enhance the reflectance at the back-interface region [21]: the remaining light, passed through the previous absorbing layer and reached back reflector, is sent back again through the absorbing layer [22]. In this study, instead of the conventional back reflector with ZnO:B and Ag, a combination of hydrogenated silicon oxide based material (SiO_x:H) and metal back reflector (Ag/Al) was employed as a back reflector to compare with the conventional ZnO:B/Ag back reflector.

In addition to the textured-TCO and back reflector, the light trapping in a multi-junction solar cell can be enhanced by introducing an intermediate layer at the interfaces of two sub-cells [23-24]. As previously discussed, a proper current matching of the series connected sub-cells is really required in a multi-junction cell because the sub-cell with the lowest current limits the current of complete device. In a-Si:H/μc-Si:H tandem solar cells, for example, a thick a-Si:H top cells is required to fulfill the current matching requirement. By employing an intermediate layer between the a-Si:H top cell and the μc-Si:H bottom cell, an increase of the a-Si:H top cell photocurrent due to the reflection by the intermediate layer can be expected.

Finally, in this study, in order to enhance multi-junction solar cells performance, the reflection losses due to refractive index mismatch of each layer in solar cell and the absorption losses from non-active doping layers have to be taken into account. As mentioned in chapter 1, by using FAL, inserted between glass/TCO, and FALp, inserted between TCO/p-layer, as additional refractive index matching layers, a reduction of the reflection losses due to refractive index mismatch can be expected. Also, the absorption losses resulted from non-active doping layers can be decreased by applying nIL and nBRL.

As explained above, it is pronounced that the development of silicon based multi-junction solar cells with an excellent light trapping structure is indeed required to obtain solar cells with a low cost and a highly stabilized conversion efficiency.

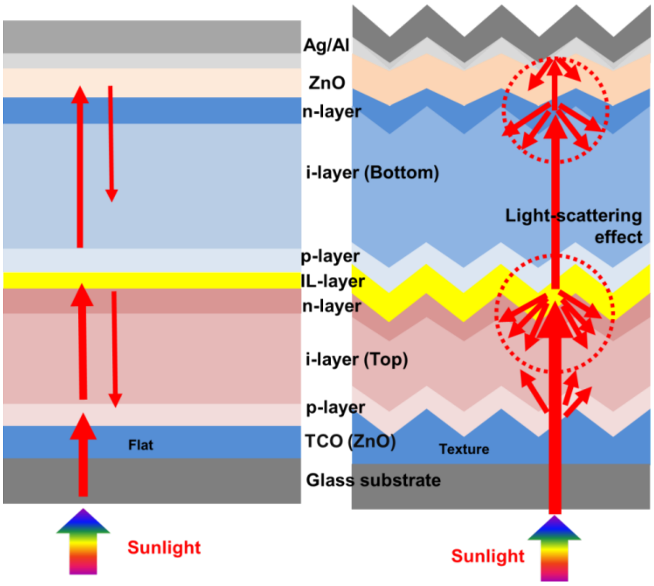

Figure 2-6 Schematic structure of a tandem solar cell with light-scattering effect

References

[1] Jef Poortmans and Vladimir Arkhipov: *“Thin Film Solar Cells Fabrication, Characterization and Applications”*, John Wiley & Sons, Ltd (2007).

[2] B. E. Pieters: “Characterization of Thin-Film Silicon Materials and Solar Cells through Numerical Modeling”, Ph.D Thesis, Delft University of Technology (2008).

[3] K. Takahashi and M. Konagai: “*Amorphous Silicon Solar Cells*”, North Oxford, London (1986).

[4] J.Tauc, A.Abraham, L.pajasova, R. Grigorivici and A. vancu: *Pro. Conf. Physics of Non-Crystal. Solids* (1965) 606.

[5] R.Klazes, M. van den Broek, J.bezemer and S. Radelaar: *Phil. Mag. B***45** (1982) 377.

[6] R.W. Collins, A.S. Ferlauto, G.M.Ferreira, C.Chen, J.Koh, R.J.Koval, Y.Lee, J.M.Pearce, and C.R. Wronski: Sol. Energy Mater. Sol. Cells **78** (2003) 143.

[7] P. Sichanugrist, T. Yashida, Y. Ichikawa ans H. Sakai: *J. Non-Cryst. Sol.* **164-166** (1993) 1081.

[8] H. Watanabe, K. Haga and T. Lohner: *J. Non- Cryst. Solids* **164-166** (1993) 1085.

[9] S. Fujikake, H. Ohta, P. Sichanugrist, M. Ohsawa, Y. Ichikawaand and H. Sakai: *Optoelectronics Devices and Technologies* **9** (1994) 379.

[10] S. Fujikake, H. Ohta, A. Asano, Y. Ichikawa and H. Sakai: *MRS Symp. Proc.* **258** (1992) 875.

[11] G. Munyeme: “Experimental and Computer Modelling Studies of Metastability of Amorphous Silicon Based Solar Cells”, Ph.D Thesis, the University of Utrecht (2003).

[12] M. Konagai, “*Introduction to Photovoltaics*”, Lecture Note, Tokyo Institute of Technology (2006).

[13] D.L. Staebler and C. R. Wronsky: *Appl. Phys. Lett*. **31**, (1977) 292.

[14] Ihsanul Afdi Yunaz: ”Study of Numerical Analysis and Elemental Technology for Amorphous Silicon Based Triple Junction Solar cells”, Ph.D Thesis, Tokyo Institute of Technology (2009).

[15] L. Zeng, Y. Yi, C. Hong, J. Liu, N. Feng, X. Duan, L. C. Kimerling, and B. A. Alamariu*: Appl. Phys. Lett.* **89** (2006) 111111.

[16] C. Eisele, C. E. Nebel, and M. Stutzmann: *J. Appl. Phys.* **89** (2001) 7722.

[17] J. Springer, B. Rech, W. Reetz, J. Muller, and M. Vanecek*: Sol. Energy Mat. Sol. Cells* **85** (2005) 1.

[18] J. Muller, B. Rech, J. Springer, M. Vanecek: *Solar Energy*, **77** (2002) 917.

[19] S. Hiza: “*Study of Hydrogenated Microcrystalline Silicon Thin Films and Solar Cells Prepared with Plasma-Free Processes*”, Doctoral Thesis, Tokyo Institute of Technology (2007).

[20] A. Hongsingthong, T. Krajangsang, I.A. Yunaz, S. Miyajima, and M. Konagai: *Appl. Phys. Express* **3** (2010) 051102.

[21] W. W. Wenas, A. De, A. Yamada, M. Konagai and K. Takahashi: *Sol. Energy Mat. Sol. Cells* **34** (1994) 313.

[22] Arvind Shah: *“Thin Film Solar Cells”*, EPFL Press (2010).

[23] D. Fischer, S. Dubail, J. A. Anna Selvan, N. Pellaton Vaucher, R. Platz, Ch. Hof, U.Kroll, J. Meier, P. Torres, H. Keppner, N. Wyrsch, M. Goetz, A. Shah, and K.-D. Ufert : *Proc. 25th IEEE PVSC* (1996) 1053.

[24] D. Domine, J. Bailat, J. Steinhauser, A. Shah, C. Ballif: *Proc. 4th World Conf. on Photovoltaic Energy Conversion* (2006) 1465.

Chapter 3

Theoretical Analysis of Silicon-Based Thin Film Solar Cells Using Light-trapping Approaches

3.1 Introduction

As mentioned in the previous chapters, multi-junction solar cells based on silicon and its alloying materials are promising candidates to solar cells with greater conversion efficiency and further cost-reduction. The multi-junction thin film solar cell, e.g. an a-Si:H /μc-Si:H solar cell, is widely studied in order to obtain higher efficiency than a traditional single junction solar cell [1-4]. One of main requirements for multi-junction solar cell is a proper current matching of the series-connected cells, since the component cell with the lowest current limits the current of complete devices. In order to solve the problems and thus obtain greater solar cell performance, recently, light-trapping approaches: textured transparent conductive oxide (TCO)-based front contact [5-8], highly reflective textured-TCO/metal back reflector [9-12] and a transparent and reflective intermediate layer (IL) [13-16], have extremely been studied by several research groups. Especially, in multi-junction solar cells, light-approaches, which will be applied into each type of solar cells, should carefully be considered corresponding to current-limited solar cell types: a double-junction solar cell having a top cell with limited-current or having a bottom cell with limited-current. Here, for example, by applying textured-front TCO it can improve the overall light path to further reflect and scatter into active layers in a solar cell and hence enhance current density and conversion efficiency. At the same time, when a reflective intermediate layer or/and a reflective TCO/metal back reflector are employed into tandem solar cells, careful design must be considered in order to balance the current density of each sub-cell. In case of introducing a reflective TCO/metal back reflector, the current density of a bottom cell can be increased and smaller total current density would be observed for a case of a solar cell with top-cell-limit. Also, in case of employing IL to improve light-trapping, the current density of the top cell can be obtained without increasing the thickness of a top cell, which is sensitive to light-induced degradation so called Staebler-Wronski effect [17]. However, introducing intermediate layer generally also causes a drop in current of bottom cells due to high reflection at long wavelength region. Therefore, IL with high reflection at the short wavelength region and low reflection at the long wavelength region is required to avoid this problem. That is to say, numerical study of using of IL and/or TCO/metal back reflector should be performed in order to find the preferred theirs properties for different application purposes.

In this study, optical analysis of optical layers, i.e., intermediate layer (IL), n-layer with function of back reflective layer (nBRL) and front anti- reflection layer inserted glass/TCO substrate (FAL), using device simulator so called OPTICAL will be performed. Firstly, we have systematically investigated the effects of refractive index and thickness combinations of single and triple ILs on the light-reflectance in test structure simulated from tandem solar cells. The reflectance spectrum representing the light-trapping at interface of the top cell and the ILs will be used to evaluate the performance of the ILs to find the optimum intermediate layer with reflectance spectrum close to the ideal one described above. Then, the effect of refractive index and thickness of nBRL on the reflectance of test structured will be investigated to obtain the considerable properties for application to silicon-based thin film solar cell. Next, the transmittance of test structure with glass/FAL/ZnO/p-Si:H will be calculated using several FAL with different refractive index and thickness in order to explore optimal FAL for use in thin film silicon solar cells. Also, the effect of refractive index of each optical layer such as IL, nBRL and FAL on the current density of thin film silicon solar cells will be studied to understand how much the optical layers affect the solar cell performance using ASA simulator.

3.2 Numerical analysis of various "optical layers" applied into silicon-based thin film solar cells using OPTICAL simulator

3.2.1 Overview of OPTICAL simulator

We have calculated the optical spectral, i.e., reflectance and transmittance, of several optical layers by using the simulator called OPTICAL, a computer program that can treat multilayer with any number of coherent and incoherent layers in any position and for any incidence angle using a generalized scattering matrix method. OPTICAL is the software that can compute theoretical Reflectance (R), Transmittance (T) and internal light energy flux of a multilayer; A multilayer is a structure composed of several isotropic layers in intimate contact[18]. By using this simulation program, one can calculate theoretical reflectance (R), transmittance (T), and internal light energy flux of a multilayer. The optical spectral of each optical layer employed in tandem cells (IL, nBRL, FAL) were calculated using wavelength-dependent complex refractive indices obtained from experimental results as show in figure 3.1 in order to explore the preferred layers with excellent properties, corresponding to particular application purposes. The optical properties of all layers were described by wavelength-dependent complex refractive indices N(λ) = n(λ) – ik(λ), where n(λ) is wavelength-dependent real refractive index and k(λ) is wavelength-dependent extinction coefficient. The complex refractive indices of all layers used in this numerical analysis were obtained by measuring the wavelength-dependent refractive index of experimentally deposited silicon oxide (SiO_x) films. The numerical analysis models will be presented in each their calculation parts. Here, it should be noted that the refractive indices mentioned in this article, e.g. tables and figures, were those measured at the wavelength of 600 nm.

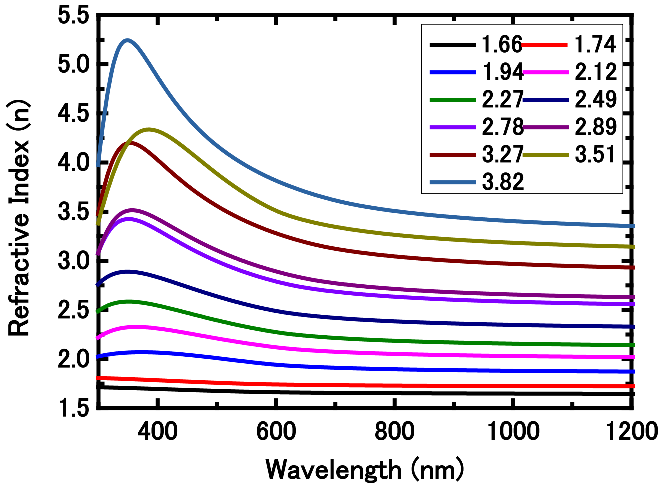

(a)

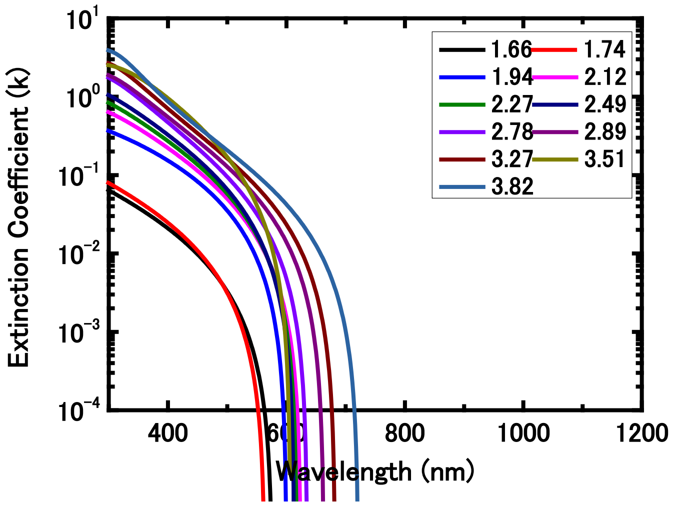

(b)

Figure 3-1 (a) Real refractive index (n) and (b) extinction coefficient (k) of SiO_x film used in the calculations

3.2.2 Optical simulation of intermediate layer (IL)

Firstly, the reflectance spectra of SiO_x single intermediate layers with various refractive indices and thicknesses were computed with the modeling structure as shown in the figure 3-2. Also, Figure 3-3 showed the reflectance spectra of SiO_x single intermediate layer as a function of refractive index at the wavelength of 600 nm. The refractive index at 600 nm was changed from 1.74 to 2.97 when the thickness of IL was fixed at 50nm.

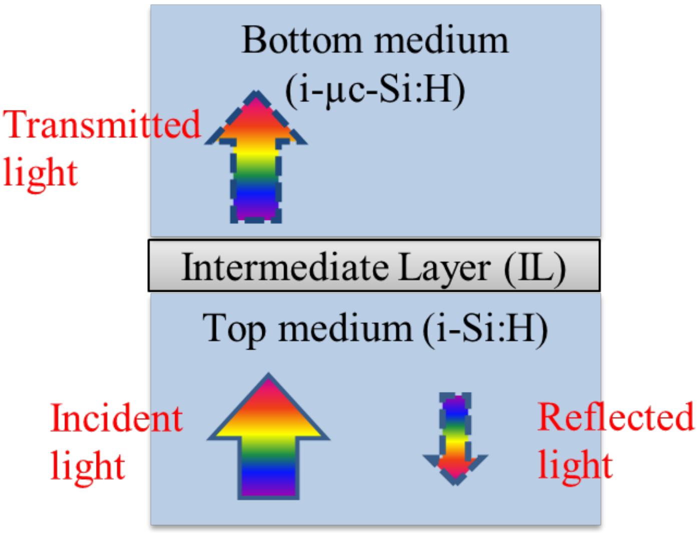

Figure 3-2 Schematic diagram of model structure for IL calculation

From figure 3-3, we can see that the reflectance spectra at the whole wavelength region increase as the refractive index of IL decreased. Furthermore, it should be noted that the maximum reflectance for each reflective index shifted to the short wavelength. For instance, in case of refractive of 2.97, the maximum reflectance was approximately 5% at the wavelength of 650 nm. In contrast, in case of refractive index of 1.74, the maximum reflectance was around 65 % at the wavelength of 300 nm. However, the reflectance at the long wavelength region also increased as the refractive index decreased, for example, at 800 nm increased from 5% to 20 %. Unfortunately, as previously mentioned, such an enlargement of the reflectance spectra at the long wavelength region is not preferable for a multi-junction solar cell. This will lead to a reduction in the current of bottom cells. Thus a further optimal design is required to perform.

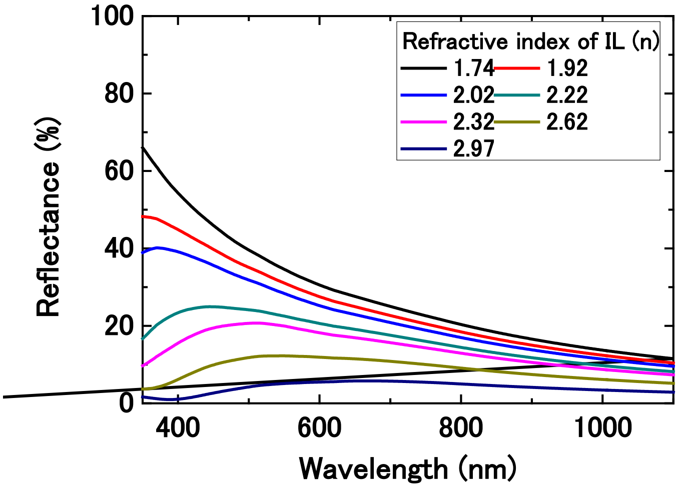

Figure 3-3 Reflectance spectra of SiO_x single intermediate layers (IL) as a function of IL refractive index at the wavelength of 600 nm

Figure 3-4 shows the reflectance spectra of SiO_x single IL as a function of IL thickness. The thickness of SiO_x IL was varied from 30 to 80 nm when the refractive index of IL was fixed at 1.92. As can be seen from Figure 3-4, it was observed that the maximum reflectance for each IL thickness firstly increased with increasing the IL thickness up to 50 nm and then, the maximum reflectance decreased from IL thickness of higher than 60 nm. Here, at the refractive index of 1.92, the optimum IL thickness was clearly found to be 40-50 nm.

The above results indicated that the refractive index and the thickness of SiO_x single intermediate layers significantly affected their optical performance in a-Si:H/μc-Si:H solar cells. It was also confirmed that low refractive index led to higher reflectance spectrum at the whole wavelength region. However, the preferred reflectance spectrum, a high reflectance at the short wavelength region and no reflectance at the long wavelength region, could not be obtained by applying a single intermediate layer, therefore further investigation, e.g. multi-stacked intermediate layers, is still needed.

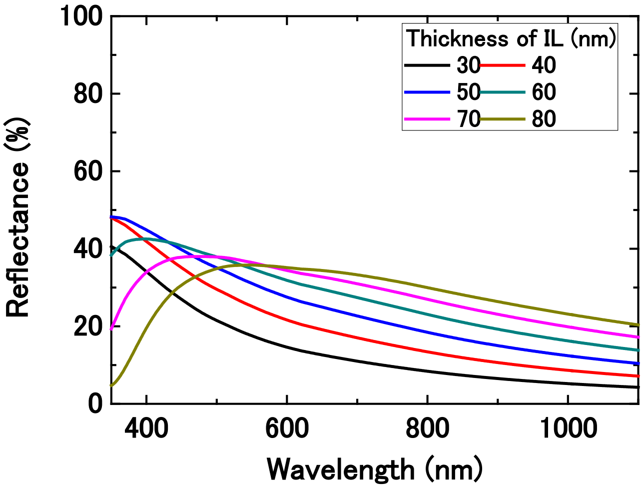

Figure 3-4 Reflectance spectra of SiO_x single intermediate layers (IL) as a function of IL thickness

To further investigate the optical properties of SiO_x multi-stacked intermediate layers, an optical design of SiO_x triple intermediate layer was performed. The simulation structure with a-Si:H/1st layer/2nd layer/3rd layer/μc-Si:H was employed to analyze the reflectance spectra of SiO_x triple intermediate layers with different refractive index and thickness combinations.

First of all, effects of refractive index combinations were investigated. This time, the thicknesses of 1st layer and 3rd layer were both assumed to be 70 nm, while that of 2nd layer was fixed at 17 nm. Figure 3-5 gives the reflectance spectra of SiO_x triple intermediate layer with various refractive index combinations. Four groups of refractive index combination were computed, i.e. these configuration were, (i) 1.9/2.6/3.9 (low refractive index/ medium refractive index/ high refractive index), (ii) 3.9/2.6/1.9 (high/medium/low), (iii) 3.9/1.9/3.9 (high/low/high) and (iv) 1.9/3.9/1.9 (low/high/low). From Figure 3-5 it was found that the combination of 1.9/3.9/1.9 (low/high/low) indicated the best reflectance spectrum compared to other refractive index combinations. The maximum reflectance close to 80% at the 480 nm could be obtained for low/high/low combination. Besides, this refractive index combination could also suppress the reflectance at the long wavelength region.

Since the refractive indices of a-Si:H top and μc-Si:H bottom cells were also close to 3.9, by introducing intermediate layers with this refractive index combination (1.9/3.9/1.9), the refractive index at the interface of a-Si:H top and μc-Si:H bottom cells became high/low/high/low/high, which was close to a photonic crystal (PC) structure[19]. As noted by J. Krc et al., the low reflectance at the long wavelength is not due to light absorption in the layers, but results from the PC-like behavior [20]. In fact, such wavelength-selective reflectance has already been achieved for the realistic structures applied in other fields of applications such as fiber optics for telecommunications [21].

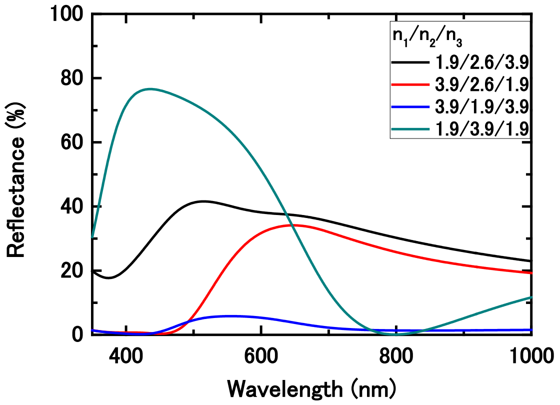

Figure 3-5 Reflectance spectra of SiO_x triple intermediate layers (IL) with various refractive index combination of IL ($n_1/n_2/ n_3$)

Next, effects of thickness combination were studied. In this numerical study, the refractive indices of the 1st layer (n_1) and the 3rd layer (n_3) were both assumed to be 1.9, whereas that of the 2nd layer (n_2) was fixed to be 3.9, which is close to the refractive index of conventional n-a-Si:H or n-μc-Si:H films. From the results in the previous sub-section, it is interesting to note that we should assume the same thickness of each layer whose has the same refractive index in order to easily analyze effects of triple intermediate layers.

Figure 3-6 exhibits the reflectance spectra of SiO_x triple intermediate layers as a function of thickness of 1st layer and 3rd layer. Here, the thickness of 1st layer and 3rd layer was changed from 40 to 100, whereas the thickness of 2nd layer was kept constant at 20 nm. As can be seen from Figure 3-6, the maximum reflectance initially increased as the thicknesses of the 1st layer and the 3rd layer increased to 80 nm. Then, in case of

1st layer and 3rd layer thicknesses higher than 100 nm, the maximum reflectance decreased. We can also see that the maximum reflectance shifted to the long wavelength region as the thicknesses of the 1st layer and 3rd layer increased. In case of the 1st layer and 3rd layer thicknesses of 40 nm, for example, the maximum reflectance was about 65% at the wavelength of 350 nm. On the other hand, in case of the 1st layer and 3rd layer thicknesses of 80 nm, the maximum reflectance was about 75% at the wavelength of about 500 nm. Moreover, by optimizing the thickness of the 1st layer and the 3rd layer, the reflectance at the long wavelength region could be suppressed, which decreased to 0% at wavelength region of 900-1000 nm.

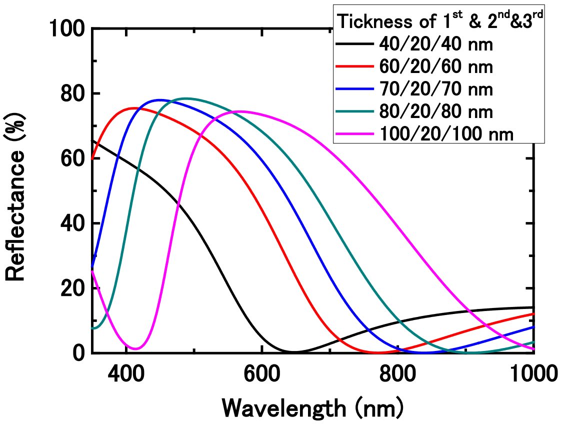

Figure 3-6 Reflectance spectra of SiO_x triple intermediate layers as a function of 2nd layer thickness

3.2.3 Optical simulation of n-layer with function of back reflective layer (nBRL)

We have introduced the silicon oxide (SiO_x) films used as a n-layer with function of back reflective layer (nBRL) to silicon-based thin film solar cells, as mentioned in Chapter 1. Here, we have calculated the reflectance spectrum of back reflective layers nBRL which combined various SiO_x films, having different refractive index and with function of back metal electrodes, in order to compare the conventional one with a structure of n-µc-Si:H/ ZnO/ metal-back-electrode using the simulator called OPTICAL. The model structure used in this calculation was i-µc-Si:H/ n-µc-Si:H/ ZnO/ Ag/ Al as shown in figure 3-7 and the n-µc-Si:H/ ZnO was replaced with n-µc-SiO_x:H with different refractive index to explore the optimal optical properties of n-µc-SiO_x:H films for use as a nBRL . Effects of the wavelength-dependent refractive index and the thickness of each nBRL on the reflectance spectrum at i-µc-Si/nBRL interface were analyzed. The refractive indices of all nBRLs used in this analysis were obtained by measuring the wavelength-dependent refractive index of deposited films as shown in the previous section.

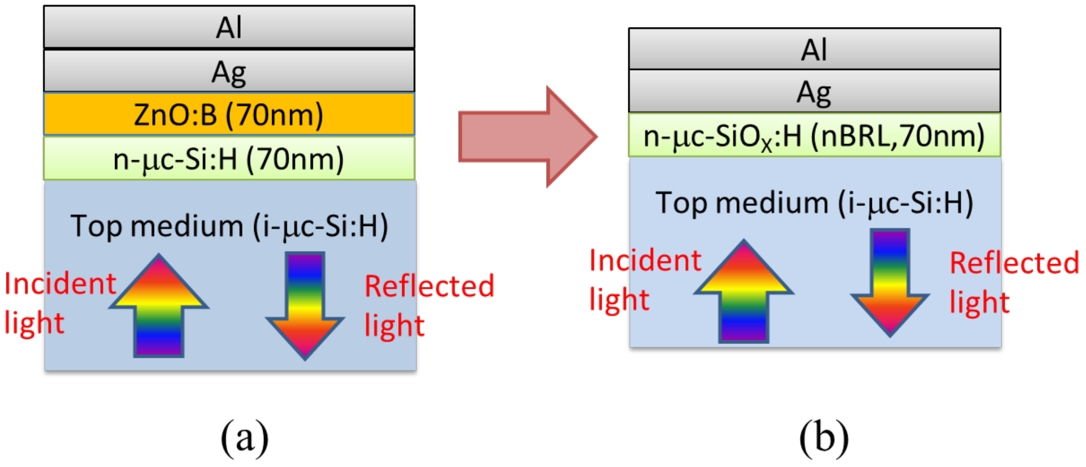

Figure 3-7 Schematic diagram of model structure for nBRL calculation

The reflectance spectra of nBRL with variation of refractive indices and thickness-dependence were firstly calculated. Figure 3-8 shows the reflectance spectra of SiO_x layer used as a nBRL with its refractive index, varied from 1.9 to 3.6, comparing to the one with n-μc-Si/ZnO layer. Here, the thickness of nBRL was assumed to be ~50 nm when its refractive index was varied. From this figure, we can observe that the overall reflectance improved when the refractive index of SiO_x film increased. Also, these results reveal that the SiO_x film with refractive index of ~1.9 could be replaced n-μc-Si/ZnO layer at the back reflector. The SiO_x with refractive index of ~1.9 should be characterized.

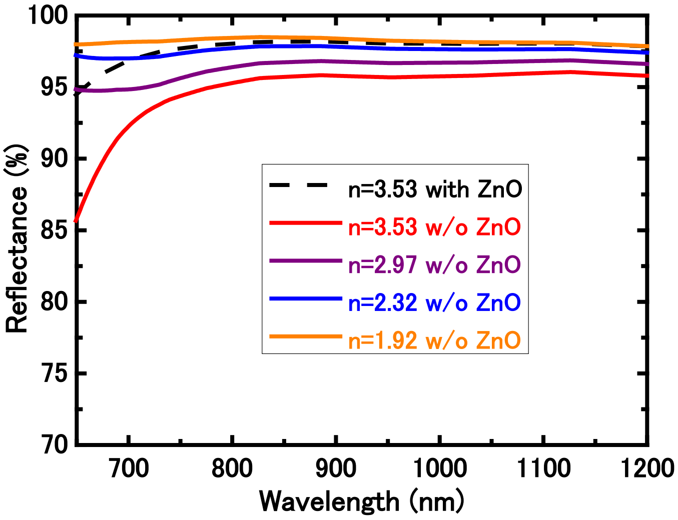

Figure 3-8 comparison of n-SiO_x nBRL with various refractive indices to a n-μc-Si/ZnO layer

Also, the reflectance spectra of nBRL with variation of thickness of n-SiO_x layer were presented in figure 3-9. The thickness of the layer was changed between 40-120 nm when the refractive index was kept constant at 1.9. The reflectance of test structure increased as the thickness increased up to 80 nm. However, when the thickness increased more than 80 nm, the reflectance, in the short wavelength region of less than 850 nm, of test model decreased and only in the long wavelength region slightly increased. From these results, one can conclude that the thickness of nBRL did not affect the optical property when it was increased up to ~80nm. This effect results probably from that the incident light into the device was mostly reflected at the i-μc-Si:H/nBRL interface for thickness of ~80 nm. Therefore, a thicker layer is not effective against improving light trapping for the nBRL with refractive index of ~1.9. As mentioned above, the thickness of nBRL should then be between 60-80 nm to keep excellent optical properties of a device.

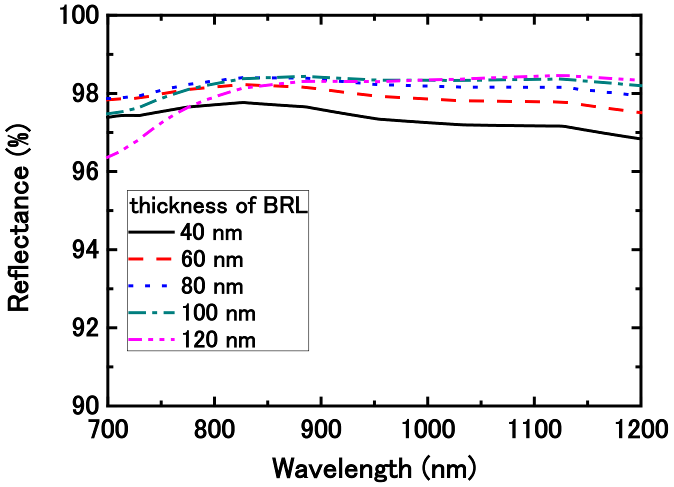

Figure 3-9 Reflectance spectra of nBRLs as a function of thickness

3.2.4 Optical simulation of front anti-reflection layer (FAL) inserted between glass and ZnO:B TCO

Optical calculation of FAL with various refractive indices and thicknesses was performed using the simulator called OPTICAL in order to estimate the optimal thickness and refractive index (n) of FAL. The model structure used in this simulation was glass/FAL/ZnO/p-Si, as shown in Figure 3-10. The effects of the wavelength-dependent refractive index and thickness of each FAL on the transmittance spectrum of the model sample were investigated. Here, the thickness of the ZnO layer was kept at 1.5 μm. The refractive indices of all FALs used in this analysis were obtained from the deposited SiO_x films.

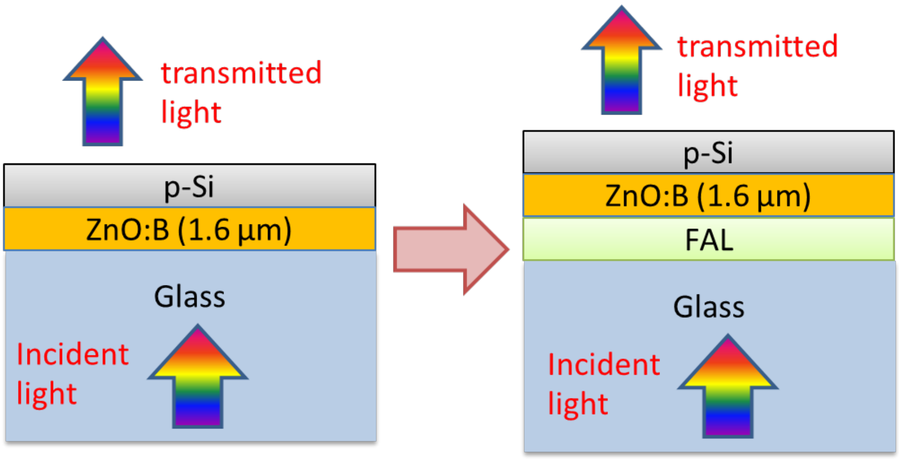

Figure 3-10 Schematic diagram of model structure for FAL calculation

The transmittance spectra of FAL with various refractive indices were computed. Figure 3-11 shows the transmittance spectra of the substrates with FAL, whose refractive index was varied from 1.7 to 2.3 and whose thickness was fixed at 60 nm, compared with those without FAL. From this figure, it was found that the FAL with n of ~1.7 can be expected to suppress optical reflection loss at the glass/ZnO interface. This value is quite close to the value calculated from the equation $n = (n_{glass} \times n_{TCO})^{1/2}$:n of ~1.73.

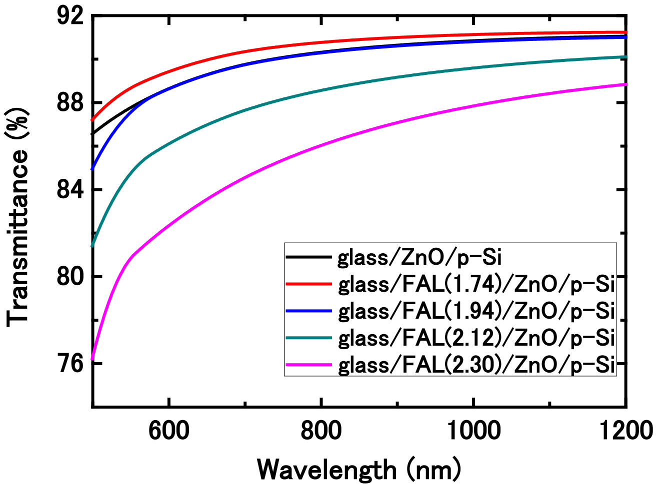

Figure 3-11 comparison of SiO_x FAL with various refractive indices to an n-μc-Si/ZnO layer

Figure 3-12 shows the transmittance spectra of the substrates with FAL of different thicknesses from 40 to 100 nm and a fixed refractive index of ~1.7. As shown in figure 3-12, the transmittance of the substrates slightly increased with increasing FAL thickness. However, the transmittance, particularly at the wavelength of less than 700 nm, decreased when the thickness was increased to more than 80 nm. As a result, the preferred thickness of FAL should probably be approximately 80 nm. It should be noted that the transmittance spectra presented in these optical calculations were the absolute values calculated on the basis of flat glass substrates, which are different from the textured substrates used in the experiments. The improved optical properties of the samples with optimized FAL can be expected from experiments conducted on the basis of textured glass substrate owing to the enhanced light-scattering effect of substrates.

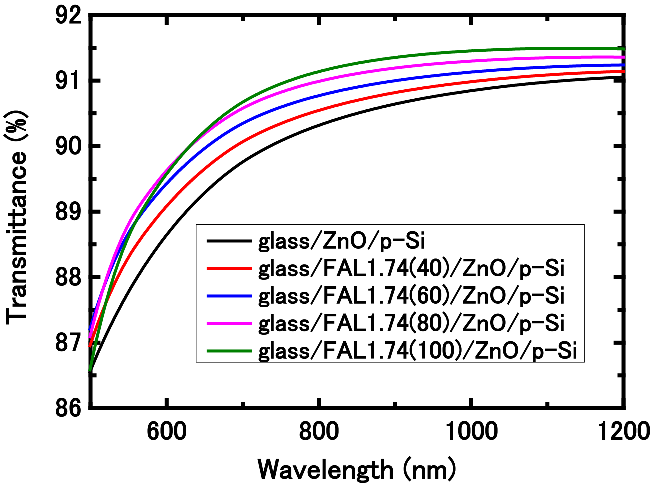

Figure 3-12 Reflectance spectra of FALs as a function of thickness

3.3 Theoretical analysis of silicon-based solar cells using ASA simulator

3.3.1 Overview of ASA device simulator

After we have investigated the effect of optical layers on the optical properties of sample structure calculating reflectance and transmittance by OPTICAL simulator, in this section, the effect of these optical layers on the current density improvement of silicon-based thin film solar cell will then be taken into account using ASA simulator. Advanced Semiconductor Analysis (ASA) is a one dimensional opto-electronic simulator for amorphous-based semiconductor devices [22-23]. As based on calculation of light-trapping effects such as employment of surface-textured substrates for light management research, ASA simulator has been developed the original Genpro model, which the light-scattering model and coherent/incoherent light propagation have to be taken into account, in order to accurately simulate thin-film silicon solar cells. Additionally, most of input parameters can be continuously graded as a function of position in the device or energy level in the band gap [24-27]. This is the important advantage of this simulator to facilitate actually fabrication design of solar cells in order to enhance solar cell performance. To design model of thin film silicon solar cell, carrier recombination process through the single-level states is calculated using Shockley-Read-Hall (SRH) model and through the multi-level states by Sah and Shockley (S-S) model [28]. Also, it contributes to modeling of amphoteric dangling bond states of thin-film silicon materials. Furthermore, the spectral response of each sub-cell of multi-junction solar cells can be calculated by this simulator. ASA is still available for measurement of quantum efficiency of each component cells, which are needed proper optical and voltage biases in order to obtain accurate measurement results. In this work, ASA was therefore chosen to use for calculation of effect of each optical layers involving to light-trapping effects on solar cell performance, especially current density.

3.3.2 Simulation model

The basic set of semiconductor equations represents a mathematical description of semiconductor device operation under non-equilibrium conditions. The basic semiconductor equations include the Poisson equation (3.1), the continuity equations for electrons (3.2) and holes (3.3) and the equations for electron (3.4) and hole (3.5) current densities. Power conversion in solar cells is considered to be steady state operation. The structure and dimensions of thin-film silicon solar cells allow the simulation model to be restricted to one dimension (1-D). In the absence of magnetic field and for a uniform temperature in the device these equations in 1-D have the following forms.

$$\frac{d}{dx}\left(\varepsilon(x)\frac{d\psi}{dx}\right)=-\rho \tag{3.1}$$

$$\frac{1}{q}\left(\frac{dJ_{\mathrm{n}}}{dx}\right) = -G_{\mathrm{opt}}(x) + R(x) \tag{3.2}$$

$$\frac{1}{q}\left(\frac{dJ_{\mathrm{p}}}{dx}\right) = G_{\mathrm{opt}}(x) - R(x) \tag{3.3}$$

$$J_{\mathrm{n}}(x) = q\mu_{\mathrm{n}}n\left(\frac{dE_{\mathrm{Fn}}}{dx}\right) \tag{3.4}$$

$$J_{\mathrm{p}}(x) = -q\mu_{\mathrm{p}}p\left(\frac{dE_{\mathrm{Fp}}}{dx}\right) \tag{3.5}$$

where ε is the permittivity of the semiconductor, ψ is the electrostatic potential with reference to the vacuum level E_{vac}, ρ is the space charge density, J_{n} and J_{p} are the electron and hole current density, G_{opt} is the optical generation rate and R is the recombination rate of electrons and holes, n and p are the free electron and hole concentration, μ_{n} and μ_{p} are the electron and hole mobility, and E_{Fn} and E_{Fp} are the electron and hole quasi-Fermi energy level, respectively.

The space charge density ρ, which appears in the Poisson equation (3.1), is in amorphous semiconductor material given by

$$\rho = q\left(p - n + p_{\mathrm{t}} - n_{\mathrm{t}} + N_{\mathrm{D}} - N_{\mathrm{A}}\right) \tag{3.6}$$

where n_{t} and p_{t} are the trapped electron and hole concentration at localized states, N_{D} and N_{A} are ionized donors and acceptors, respectively. It has to be mentioned, that not all incorporated dopant atoms in thin-film silicon are electronically active at room temperature as it is assumed in the case of crystalline silicon. Therefore N_{D} and N_{A} are not the concentrations of dopant atoms incorporated in thin-film silicon but only the ionized ones. As it is difficult to measure a number of active dopants directly, usually the measurement of the activation energy of the dark conductivity is used to approximate the position of the Fermi level in the doped materials.

Using the Maxwell-Boltzmann approximation for the carrier concentrations as a function of the quasi-Fermi levels and the effective density of states in the valence (*Nv*) and conduction (*Nc*) band we can write:

$$n = N_{\mathrm{C}} \exp\left(\frac{E_{\mathrm{Fn}} - E_{\mathrm{C}}}{kT}\right) = N_{\mathrm{C}} \exp\left\{\frac{E_{\mathrm{Fn}} - (E_{\mathrm{vac}} - q\psi - \chi)}{kT}\right\} \tag{3.7}$$

$$p = N_{\mathrm{V}} \exp\left(\frac{E_{\mathrm{V}} - E_{\mathrm{Fp}}}{kT}\right) = N_{\mathrm{V}} \exp\left\{\frac{(E_{\mathrm{vac}} - q\psi - \chi - E_{\mathrm{mob}}) - E_{\mathrm{Fp}}}{kT}\right\} \tag{3.8}$$

$$n_{\mathrm{i}}^{2} = np = N_{\mathrm{C}} N_{\mathrm{V}} \exp\left(-\frac{E_{\mathrm{mob}}}{kT}\right) \tag{3.9}$$

where χ is the electron affinity, and E_{mob} is the mobility gap.

The primary function of a computer simulation program is to solve this set of coupled partial differential equations. For solving of the semiconductor equations one can choose between different sets of independent variables, for example, ψ, n and p. When solving these equations the proper values of the position dependent parameters of μ, ρ, R, G, and the boundary conditions must be known or evaluated.

There are two boundaries in 1-D device modeling, the front and the back contact of the device. For a-Si:H and μc-Si:H solar cells, Schottky contacts are possibly implied at both of the front TCO/p-layer and back n-layer/TCO contact of the device (x = 0 and L). In the case of a Schottky contact it is assumed that at thermal equilibrium the position of the Fermi level at the contact depends on an effective barrier height (φ_{b}) of the metal semiconductor interface. This barrier is given by the difference between the work function of the metal (φ_{m}) and the electron affinity of the semiconductor (χ_{s}).

$$\varphi_{\mathrm{b}} = \varphi_{\mathrm{m}} - \chi_{\mathrm{s}} = E_{\mathrm{C}} - E_{\mathrm{F}} \tag{3.10}$$

Once the position of the Fermi level at the interface is fixed by φ_{b}, the concentration of electrons and holes at the interface is calculated by

$$n_{\mathrm{eq}} = N_{\mathrm{C}} \exp\left(-\frac{q\varphi_{\mathrm{b}}}{kT} \right) \tag{3.11}$$

$$p_{\mathrm{eq}} = n_{\mathrm{i}}^{2} \big/ n_{\mathrm{eq}} \tag{3.12}$$

The current transport over the Schottky barrier is dominated by the majority carries and is governed by the mechanism of thermionic-emission. According to the thermionic-emission theory the current density is given by

$$J = A^{*} T^{2} \exp\left(-\frac{q\varphi_{\mathrm{b}}}{kT} \right) \left\{ \exp\left(-\frac{qV_{\mathrm{b}}}{kT} \right) - 1 \right\} \tag{3.12}$$

where A^* is the Richardson constant and V_{b} is the external applied voltage.

In thin-film silicon materials, the tail states and dangling bond states act as charge trapping and recombination centers and greatly influence the electrical properties of the material. We will first discuss the description of the density of tail and dangling bond states in a-Si:H followed by a discussion on recombination and charge trapping on these states.

In order to simulate accurately the electrical and optical properties of thin-film silicon solar cells, a DOS distribution as a function of energy is introduced. As explained in Section 2.2, the standard model of the DOS distribution consists of a extended parabolic conduction (CB) and valence bands (VB), an exponentially decaying conduction band and valence band tails, and two Gaussian-distributed dangling bond (DB) states. The density of DB states are described as

$$N_{\mathrm{DB}^{+/0}}(E) = \frac{N_{\mathrm{DB}}^{\mathrm{tot}}}{\sigma_{\mathrm{db}} \sqrt{2\pi}} \exp\left\{ -\frac{\left(E - E_{\mathrm{DB}}^{+/0}\right)^{2}}{2\sigma_{\mathrm{db}}^{2}} \right\} \tag{3.13}$$

$$N_{\mathrm{DB}^{0/-}}(E) = \frac{N_{\mathrm{DB}}^{\mathrm{tot}}}{\sigma_{\mathrm{db}} \sqrt{2\pi}} \exp\left\{ -\frac{\left(E - E_{\mathrm{DB}}^{0/-}\right)^{2}}{2\sigma_{\mathrm{db}}^{2}} \right\} \tag{3.14}$$

$$U = E_{\mathrm{DB}}^{0/-} - E_{\mathrm{DB}}^{+/0} \tag{3.15}$$

where N^{tot} is the total density of states of dangling bond defects and σ_{db} is the standard deviation of the Gaussian distribution and U is the correlation energy which separated transition energy levels from each other.

The CB and VB tail states are described as

$$N_{\mathrm{A}}(E) = N_{\mathrm{A0}} \exp\left(\frac{E_{\mathrm{C}} - E}{E_{\mathrm{A}}}\right) \tag{3.16}$$

$$N_{\mathrm{D}}(E) = N_{\mathrm{D0}} \exp\left(\frac{E - E_{\mathrm{C}}}{E_{\mathrm{D}}}\right) \tag{3.17}$$

where N_{A0} and N_{D0} are the densities of tail states at the CB and VB edges, and E_{A} and E_{D} are the characteristic energy of CB and VB tails, respectively.

The recombination process of electrons and holes occurs through the DB and tail states. Then, the net recombination rate R_{net} is calculated as a sum of the net recombination of DB states (R_{DB}), and CB (R_{CB}) and VB (R_{VB}) tail states.

$$R_{\mathrm{net}} = R_{\mathrm{DB}} + R_{\mathrm{CB}} + R_{\mathrm{VB}} = R_{\mathrm{D}} + R_{\mathrm{I}} \tag{3.18}$$

In this equation, the net recombination rate is also described in other words with a sum of direct (band-to-band) (R_{D}) and indirect (S-R-H) (R_{I}) recombination. The total direct recombination rate can be expressed as

$$R_{\mathrm{D}} = \beta(np - n_0 p_0) = \beta(np - n_{\mathrm{i}}^2) \tag{3.19}$$

Here, β is a proportionality constant which depends on the energy-band structure of the material under analysis, n_0 and p_0 are the carrier concentrations in thermodynamic equilibrium state. The S-R-H net recombination can be expressed by

$$R_\mathrm{I} = \frac{np - n_\mathrm{i}^2}{\tau_\mathrm{p0}\left(n + n_\mathrm{t}\right) + \tau_\mathrm{n0}\left(p + p_\mathrm{t}\right)} \tag{3.20}$$

where τ_n0 and τ_p0 are the reciprocals of the thermal velocity-hole/electron capture cross section and N_t product. The quantities n_t and p_t depend exponentially on the position of the defects in the energy band gap.

For the optical model, the optical generation rate G_opt is determined from the absorption profile of the photons in the solar cell. Simple and straightforward analytical formulas for calculating absorption that are based on the Lambert-Beer absorption formula have been replaced by more sophisticated optical models.

In the Lambert-Beer model, a photon flux density $\Phi(x,\lambda)$ after passing a distance x in a film with absorption coefficient $\alpha(\lambda)$ is defined as

$$\Phi\left(x,\lambda\right) = \Phi_0\left(\lambda\right) e^{-\alpha(\lambda)x} \tag{3.21}$$

where $\Phi_0(\lambda)$ is the incident photon flux density as a function of wavelength λ.

The optical generation rate G_opt is calculated from the spectral generation rate g_sp by integrating over a desired wavelength spectrum

$$G_\mathrm{opt}\left(x\right) = \int_{\lambda_1}^{\lambda_2} g_\mathrm{sp}\left(x,\lambda\right) \mathrm{d}\lambda \tag{3.22}$$

$$g_\mathrm{sp}\left(x,\lambda\right) = \eta_\mathrm{g} \Phi_0\left(\lambda\right) \alpha\left(\lambda\right) e^{-\alpha(\lambda)x} \tag{3.23}$$

where η_g is the generation quantum efficiency. In Addition, given the reflections from the front surface and back contact, eq. (3.23) becomes

$$g_\mathrm{sp}\left(x,\lambda\right) = \eta_\mathrm{g} \Phi_0\left(\lambda\right)\left(1 - R_\mathrm{f}\left(\lambda\right)\right) e^{-\left(\alpha_\mathrm{gl} d_\mathrm{gl} + \alpha_\mathrm{t} d_\mathrm{t}\right)} \alpha\left(\lambda\right)\left(e^{-\alpha(\lambda)x} + R_\mathrm{b} e^{-2\alpha(\lambda)d_\mathrm{i}} e^{\alpha(\lambda)x}\right) \tag{3.24}$$

where R_f and R_b is the reflectance from the front (x = 0) and back side (x = L), respectively. d_i is the thickness of the each layer and L is total thickness in the device. The subscript gl and t means glass and TCO layer, which are non-active layers in a device, respectively.

In this section, we theoretically analyzed the performance of silicon-based thin film solar cells, including a-Si:H, μc-Si:H and a-Si:H/μc-Si:H solar cells, applying "optical layers" (nIL, nBRL and FAL) by using ASA device simulator. The simulated model structure was for a-Si:H solar cells: front electrode (ZnO:B)/ p-a-SiC:H/ i-a-Si:H/ n-a-Si:H/ back electrode (Ag), and for μc-Si:H solar cells: front electrode/ p-μc-Si:H/ i-μc-Si:H/ n-SiO$_x$:H/ back electrode (Ag); the details of each simulated model structure using each "optical layers" were shown in each section. The electrical and parameters were taken from experimental results and some literature which partly used in the doctoral thesis of Dr. Shunsuke Kasashima [29]; most of parameters for each layer are listed in table 3-1 and 3-2. For simulated model in this analysis, continuous density of states (DOS) equation was introduced within the mobility gap as mentioned above. The optical parameters used in this analysis, i.e. complex refractive index which combines refractive index with extinction coefficient, were obtained from measurement results as shown in figure 3-1. This extinction coefficient (k) is related to the absorption coefficient (α) used for other device simulators such as AMPS by the equation: $\alpha = \frac{4\pi k}{\lambda}$. The Tauc gap obtained from spectroscopic ellipsometry (SE) measurement was used as the optical band gap, which was assumed as the mobility band gap used in these calculations. For some calculations, the light trapping effect, i.e. haze parameter and the angular distribution of scattered light which represent the scattering data of the rough interfaces was taken into account. Haze parameters was obtained from experimental result while angular distribution of scattered light was assume to be a standard value given by this ASA simulator. Moreover, it was also assumed that there was no reflection for incident light at the front interface and the back reflection coefficient was set to be

0.9. For numerical analysis of a-Si:H/μc-Si:H solar cells, modelling of the tunnel-recombination junction (TRJ) layer inserted between top and bottom cells proposed by Dr. Ihsanul Afdi Yunaz [30] was considered. The TRJ layer with very thin and highly defective works as an electrical connection between component cells for a two terminal device using the internal carrier exchange effect. This effect can be completed by recombination between electrons from a top cell and holes from a bottom cell through the localized states at the TRJ interface. The parameters of TRJ layer used in this analysis was as follow: thickness 4 nm, mobility gap 1.1 eV and defect density 1×10^{26} cm^{-1}.

Table 3-1 Simulation parameters used for a-Si:H solar cell model.

Parameters and unit	p-a-SiC:H	i-a-Si:H	n-a-Si:H
Thickness (nm)	4	300	35
Mobility gap E_{mob} (eV)	2.0	1.8	1.8
Relative dielectric constant	11.9	11.9	11.9
Electron affinity χ (eV)	3.8	3.9	3.9
Electron mobility μ_e ($m^2V^{-1}s^{-1}$)	15×10^{-4}	100×10^{-4}	50×10^{-4}
Hole mobility μ_h ($m^2V^{-1}s^{-1}$)	0.6×10^{-4}	10×10^{-4}	5×10^{-4}
Donor concentration N_D (m^{-3})	—	—	1×10^{25}
Acceptor concentration N_D (m^{-3})	5×10^{24}	—	—
Effective DOS in conduction band N_C (m^{-3})	1×10^{26}	1×10^{26}	1×10^{26}
Effective DOS in valence band N_V (m^{-3})	1×10^{26}	1×10^{26}	1×10^{26}
Conduction band tail states			
DOS at CB mobility edge ($m^{-3}eV^{-1}$)	5×10^{26}	5×10^{26}	5×10^{26}
Characteristic energy (eV)	0.01	0.01	0.01
Electron capture rate in neutral states (m^3/s)	1×10^{-16}	1×10^{-16}	1×10^{-16}
Hole capture rate in charged state (m^3/s)	1×10^{-14}	1×10^{-14}	1×10^{-14}
Valence band tail states			
DOS at VB mobility edge ($m^{-3}eV^{-1}$)	5×10^{26}	5×10^{26}	5×10^{26}
Characteristic energy (eV)	0.02	0.02	0.02
Hole capture rate in neutral states (m^3/s)	1×10^{-16}	1×10^{-16}	1×10^{-16}
Electron capture rate in charged state (m^3/s)	1×10^{-14}	1×10^{-14}	1×10^{-14}

Dangling bond states parameter			
Density of states (m^{-3})	1×10^{24}	1×10^{21}	1×10^{24}
Peak level above E_v (eV)	1.33	1.2	1.13
Standard deviation σ_{db} (eV)	0.15	0.15	0.15
Correlation energy (eV)	0.3	0.3	0.3
Acceptor-like dangling bond states			
Electron capture rate in neutral states (m^3/s)	1×10^{-14}	1×10^{-14}	1×10^{-14}
Hole capture rate in charged state (m^3/s)	1×10^{-13}	1×10^{-13}	1×10^{-13}
Donor-like dangling bond states			
Hole capture rate in neutral states (m^3/s)	1×10^{-14}	1×10^{-14}	1×10^{-14}
Electron capture rate in charged state (m^3/s)	1×10^{-13}	1×10^{-13}	1×10^{-13}
Operating temperature T (K)	300		
Barrier height at front and back contact φ_{b} (eV)	1.65 / 0.02		

Table 3-2 Simulation parameters used for μc-Si:H solar cell model

Parameters and unit	p-μc-Si:H	i-μc-Si:H	n-μc-Si:H
Thickness (nm)	20	3500300	30
Mobility gap E_{mob} (eV)	1.1	1.1	1.1
Relative dielectric constant	11.9	11.9	11.9
Electron affinity χ (eV)	3.9	3.9	3.9
Electron mobility μ_{e} (m^{2}V^{-1}s^{-1})	50×10^{-4}	50×10^{-4}	50×10^{-4}
Hole mobility μ_{h} (m^{2}V^{-1}s^{-1})	5×10^{-4}	5×10^{-4}	5×10^{-4}
Donor concentration N_{D} (m^{-3})	—	—	1×10^{25}
Acceptor concentration N_{D} (m^{-3})	1×10^{25}	—	—
Effective DOS in conduction band N_{C} (m^{-3})	2×10^{25}	2×10^{25}	2×10^{25}
Effective DOS in valence band N_{V} (m^{-3})	2×10^{25}	2×10^{25}	2×10^{25}
Conduction band tail states			
DOS at CB mobility edge (m^{-3}eV^{-1})	5×10^{25}	5×10^{25}	5×10^{25}
Characteristic energy (eV)	0.01	0.01	0.01
Electron capture rate in neutral states (m^3/s)	1×10^{-16}	1×10^{-16}	1×10^{-16}
Hole capture rate in charged state (m^3/s)	1×10^{-15}	1×10^{-15}	1×10^{-15}
Valence band tail states			
DOS at VB mobility edge (m^{-3}eV^{-1})	5×10^{25}	5×10^{25}	5×10^{25}
Characteristic energy (eV)	0.02	0.02	0.02
Hole capture rate in neutral states (m^3/s)	1×10^{-16}	1×10^{-16}	1×10^{-16}
Electron capture rate in charged state (m^3/s)	1×10^{-15}	1×10^{-15}	1×10^{-15}
Dangling bond states parameters			
Density of states (m^{-3})	2.5×10^{22}	1×10^{21}	2.5×10^{22}

Peak level above E_v (eV)	0.55	0.55	0.55
Standard deviation σ_{db} (eV)	0.15	0.15	0.15
Correlation energy (eV)	0.3	0.3	0.3
Acceptor-like dangling bond states			
Electron capture rate in neutral states (m^3/s)	1×10^{-15}	1×10^{-15}	1×10^{-15}
Hole capture rate in charged state (m^3/s)	1×10^{-14}	1×10^{-14}	1×10^{-14}
Donor-like dangling bond states			
Hole capture rate in neutral states (m^3/s)	1×10^{-15}	1×10^{-15}	1×10^{-15}
Electron capture rate in charged state (m^3/s)	1×10^{-14}	1×10^{-14}	1×10^{-14}
Operating temperature T (K)	300		
Barrier height at front and back contact φ_{b} (eV)	1.65 / 0.02		

3.3.3 Effect of FAL on microcrystalline silicon solar cells (μc-Si:H)

In this part, the effect of front anti-reflection layer (FAL) inserted into glass and TCO interface on the current density (J_{sc}) of μc-Si:H was investigated by using simulation structure as shown in figure 3-13. The solar cell structure used in this simulation was glass/ FAL/ TCO (ZnO) / p-μc-Si:H/ i-μc-Si:H/ n-μc-Si/ metal back electrode. The reflective index (n) of FAL was varied from 1.66 to 2.78 while others parameter was kept the same value. From the figure 3-14 one can see that the J_{sc} of the solar cells was improved as the refractive index of FAL increased. However, the refractive index of less than 1.74, here 1.66, shows the decrease in J_{sc}, which probably results from the refractive index mismatch between glass/FAL/TCO. From the results it means that the refractive index of FAL should be approximately 1.74, which has a good agreement with calculation from previous part, to avoid reflection loss from refractive index mismatch.

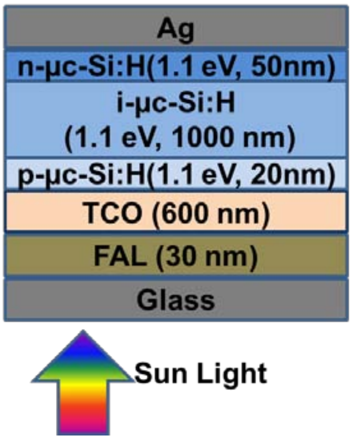

Figure 3-13 Simulation Structure of μc-Si:H solar cells using FAL with different n

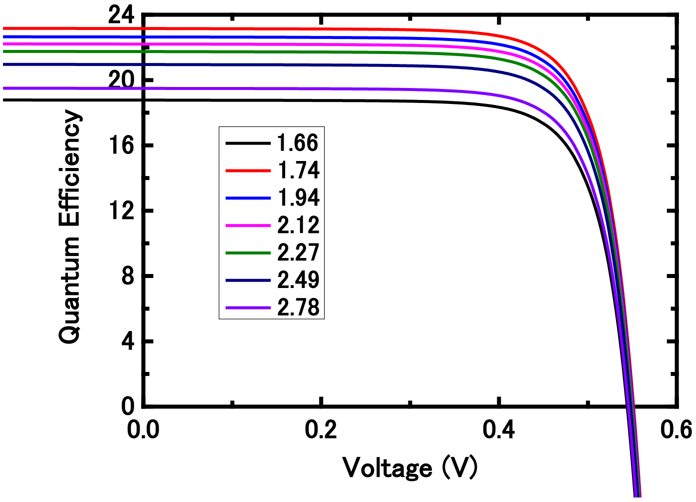

(a)

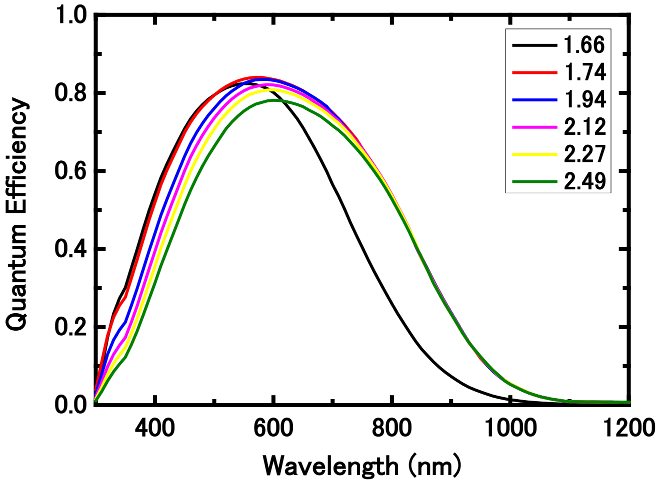

(b)

Figure 3-14 (a) *I-V* characteristic and (b) Quantum efficiency of µc-Si:H solar cell using FAL with different n

3.3.4 Effect of nBRL on µc-Si:H solar cells

Next, the effect of nBRL with different refractive index (n) on the current density (J_{sc}) of µc-Si:H solar cell was examined. The model structure for this simulation was glass/ TCO/ p-µc-Si:H/ i-µc-Si:H/ n-µc-Si/ metal back electrode as shown in figure 3-15. The parameters excluding refractive index of nBRL were kept constant. The refractive index of nBRL was changed from 1.74 to 2.78. As we can see in the figure 3-16, the J_{sc} of the solar cells was increased as the refractive index decreased. By applying nBRL with smaller refractive index, here down to 1.74, the J_{sc} was improved due to greater light-reflection between n-layer/metal electrode; which result in light-trapping in the active layer and thus improved photo-generated current.

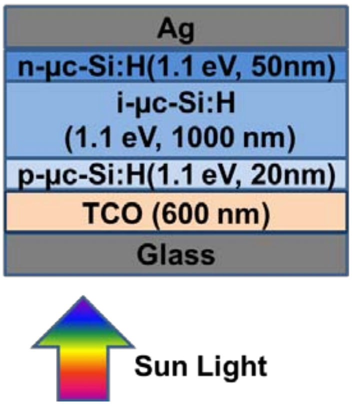

Figure 3-15 Simulation Structure of μc-Si:H solar cells using FAL with different n

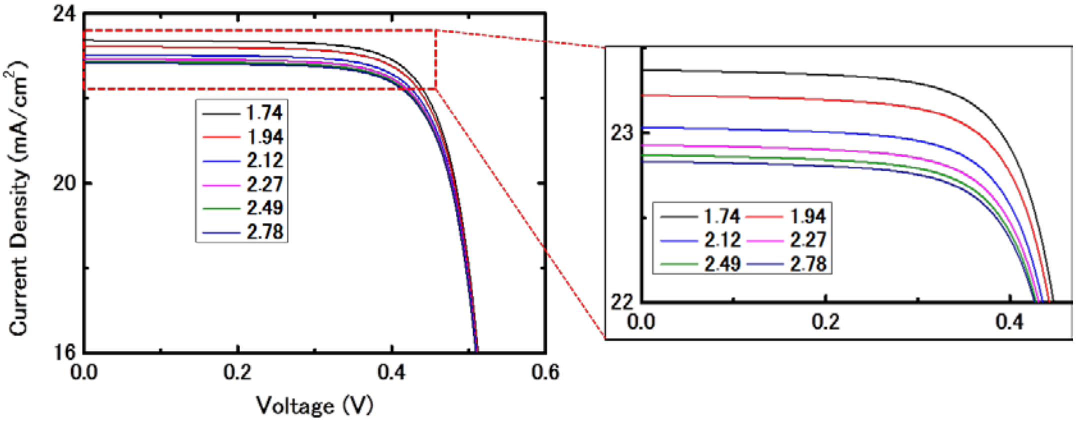

(a)

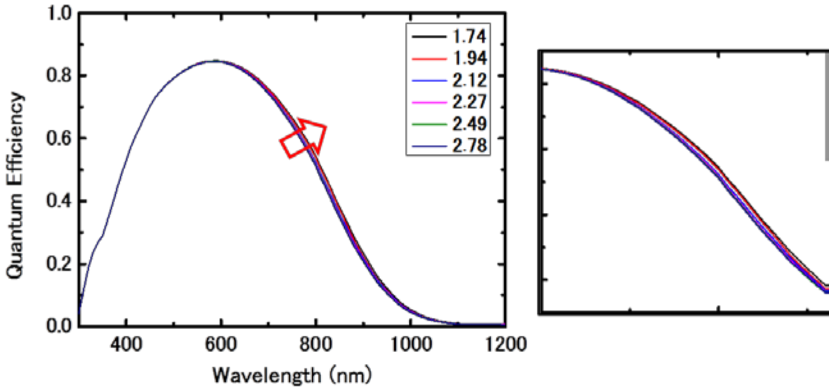

(b)

Figure 3.16 (a) *I*-*V* characteristic and (b) Quantum efficiency of μc-Si:H solar cell using nBRL with different n

3.3.5 Effect of nBRL on the performance of a-Si:H/μc-Si:H solar cells

In this part, the effect of nBRL with several refractive index on performance of a-Si:H/μc-Si:H tandem solar cells, especially current density (J_{sc}), was studied. The model structure for this simulation was glass/ TCO/ p-a-SiC:H/ i-a-Si:H/ n-a-Si/TRJ p-μc-Si:H/ i-μc-Si:H/ n-μc-Si (nBRL)/ metal back electrode as shown in figure 3-17. Here, the tandem used in this simulation was the tandem with good current matching. As can be seen in the figure 13.5, the J_{sc} of the solar cells slightly enhanced when the refractive index of the n-layer of the bottom cell became smaller. One can understand that nBRL with smaller refractive index contributed to the light-reflection back to the active intrinsic layer of the bottom cells and thus, photo-generated current was improved. However, in this simulation, because the solar cell model used was in the good current-matching, the overall J_{sc} of the tandem solar cells was decrease due to only improved J_{sc} of the bottom cells and then their conversion- efficiency was reduced without change in open circuit voltage. From this simulation results, it was found that we can use the nBRL with lower refractive index in order to improve the J_{sc} of the bottom cell in a tandem solar cell with a current-limited bottom.

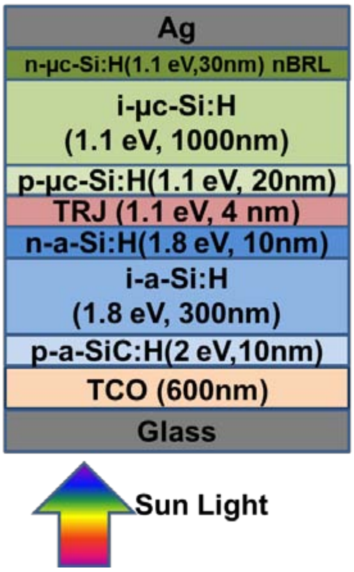

Figure 3-17 Simulation Structure of a-Si:H/μc-Si:H tandem solar cells using nBRLwith different n

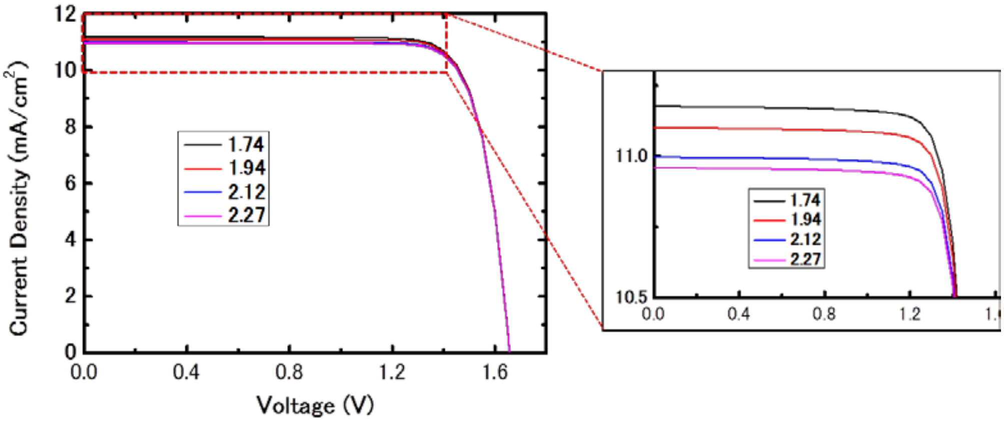

(a)

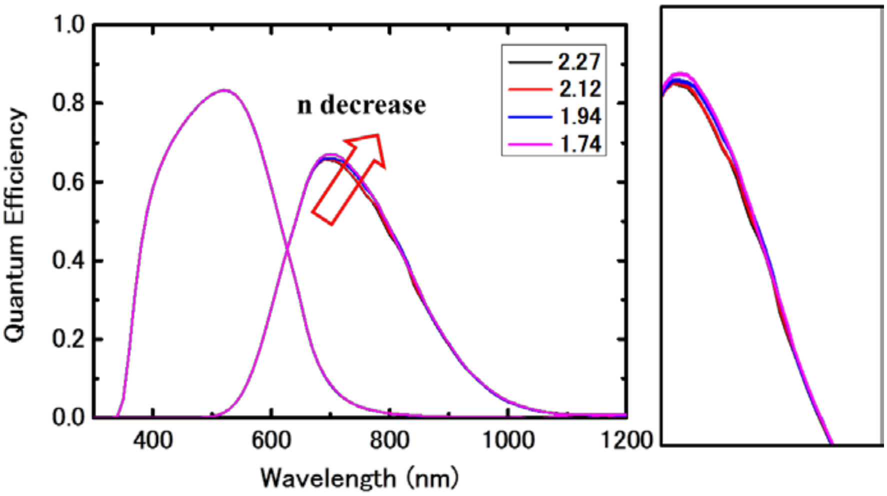

(b)

Figure 13-18 (a) *I-V* characteristic and (b) Quantum efficiency of a-Si:H/µc-Si:H tandem solar cells using nBRL with different n

3.3.6 Theoretical analysis of a-Si:H/µc-Si:H solar cell with novel structure compared to the one with conventional structure

Here, the effect of nIL and nBRL layer on a-Si:H/µc-Si:H solar cell with novel structure was investigated compared to the conventional one by using ASA device simulator. The simulated model structure was for conventional structure: front electrode (ZnO:B)/ p-a-SiC:H/ i-a-Si:H/ n-a-Si:H/ IL/ p-µc-Si:H/ i-µc-Si:H/ n-µc-Si:H/ back electrode (Ag), and for novel structure: front electrode/ p-a-SiC:H/ i-a-Si:H/ n-SiO$_x$:H/ p-µc-Si:H/ i-µc-Si:H/ n-SiO$_x$:H/ back electrode (Ag) as shown in figure 3-17. The electrical and parameters were taken from experimental results and some literature as listed in table 3-1 and 3-2. The optical parameters used in this analysis, here complex refractive index which combines refractive index with extinction coefficient, were obtained from measurement results as shown in figure 3-1. In this calculation, the light trapping effect, i.e. haze parameter and the angular distribution of scattered light which represent the scattering data of the rough interfaces was not taken into account. Only haze parameter which was measured from textured ZnO:B film coated on flat glass sheet was used in this calculation. Moreover, it was also assumed that there was no reflection for incident light at the front interface and the back reflection coefficient was set to be 0.9.

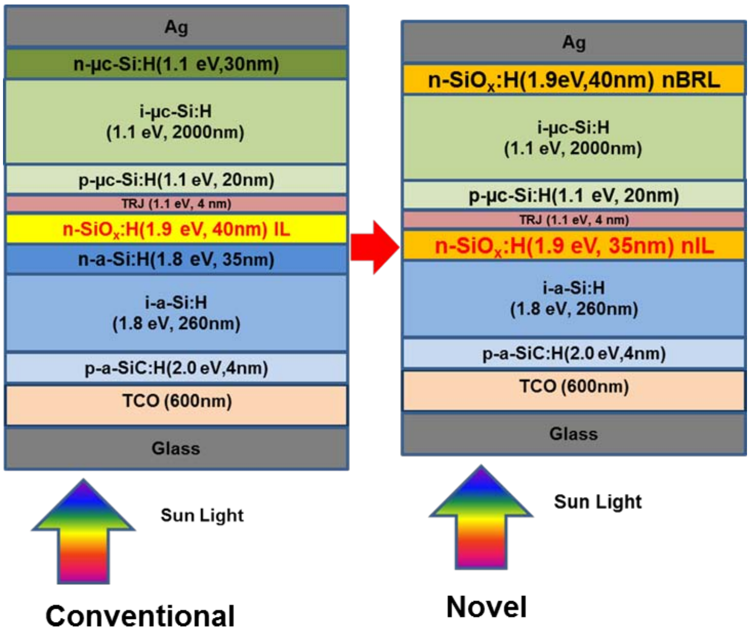

Figure 3-17 Simulated model structure of a-Si:H/μc-Si:H tandem solar cells with novel structure compared to the conventional structure

Figure 3-18 illustrates the simulation results of photovoltaic performance of the a-Si:H/μc-Si:H solar cell with novel structure compared to the conventional one (reference). This simulation model was calculated based on the flat glass substrates without scattering data of the rough interfaces included. From this result, one can see that J_{sc} of the device increased by ~0.8 mA/cm^2 when the novel structure was introduced. Also, from *EQE* results, J_{sc} for the novel structure showed ~ 1.4 mA/cm^2 higher than the conventional structure. This is probably due to reduced absorption losses from non-active layers in solar cells as we can see in figure 3-19. In figure 3-19, it was found that by applying novel structure absorption losses could be reduced especially in n-top and n-bottom layers.

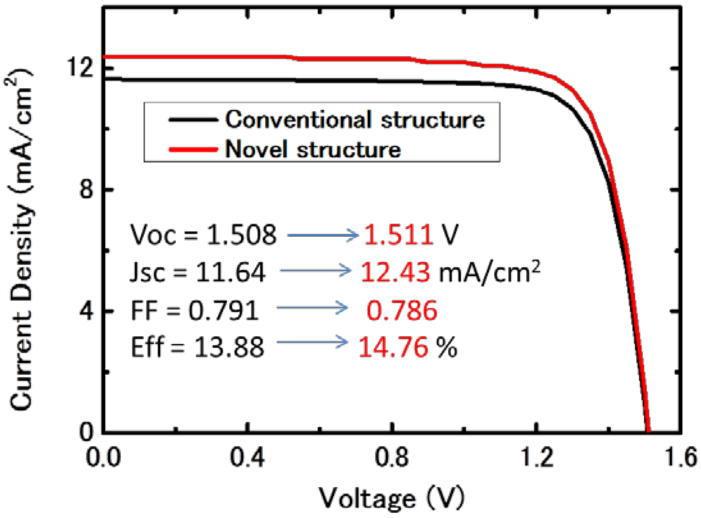

(a)

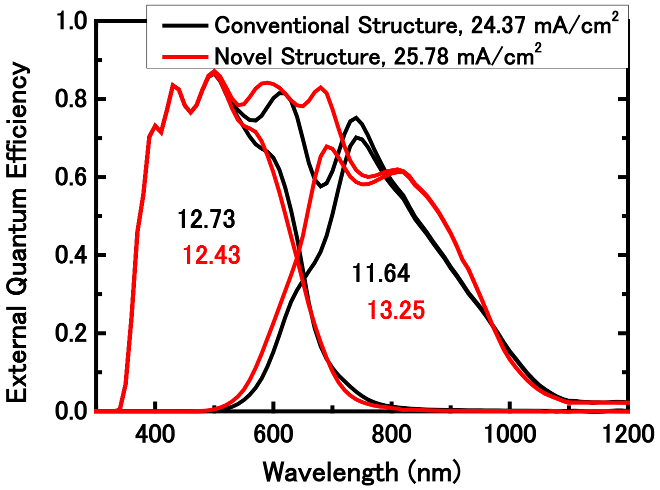

(b)

Figure 3-18 Simulation results of (a) *I-V* characteristics, (b) *EQE* of a-Si:H/μc-Si:H solar cells with novel structure compared to the conventional one

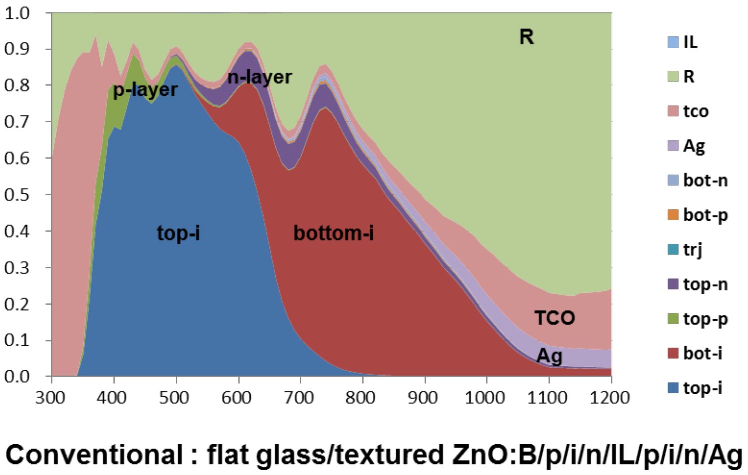

Conventional : flat glass/textured ZnO:B/p/i/n/IL/p/i/n/Ag

(a)

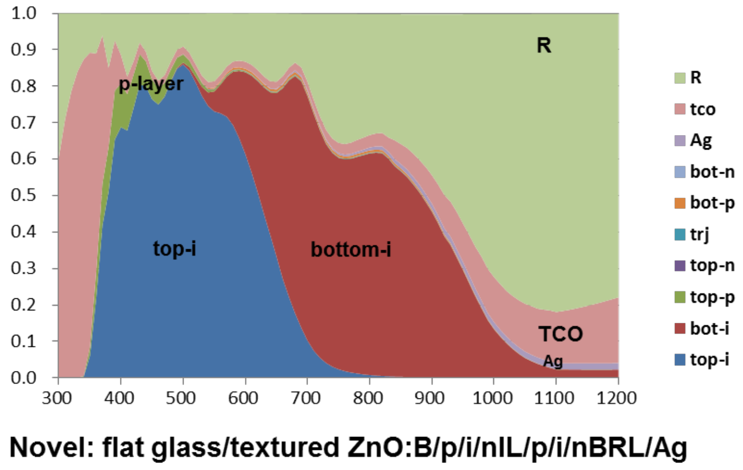

(b)

Figure 3-19 Simulated absorptance in each layer and optical losses for a-Si:H/µc-Si:H solar cells with novel structure compared to conventional one

3.3.7 Comparison of solar cell performance with novel structure using flat and textured glass substrates

In this section, the effect of interface roughness of substrates on solar cell performance was investigated. Here, the haze values measured from the flat glass substrate, which combines flat glass sheet with textured ZnO:B film, and textured glass substrate, which combines etched glass sheet (textured glass) with textured ZnO:B film, as shown in figure 3-20 were used as optical parameters in this calculation. Other electrical and optical parameters were the same values as used for the calculation in the section 3.3.6. The simulated model structures of this analysis were for flat glass substrate: flat glass/ textured ZnO:B/p/i/nIL/p/i/nBRL/Ag and for textured glass substrate: textured glass/ textured ZnO:B/p/i/nIL/p/i/nBRL/Ag. In this calculation, the light trapping effect, i.e. haze parameter and the angular distribution of scattered light which represent the scattering data of the rough interfaces was taken into account. The haze parameter used here was applied into TCO/ p-a-SiC:H, p-a-SiC:H/ i-a-Si:H, and n-SiO$_x$:H/ back electrode interface. Also, all angular distributions used in this calculation were standard COSSQ. Also, no reflection for incident light at the front interface and the back reflection coefficient which was set to be 0.9 were assumed in this simulation.

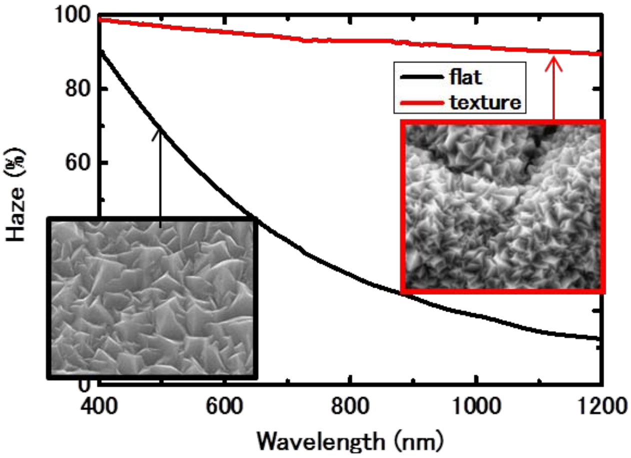

Figure 3-20 Haze value and SEM images of flat and textured glass substrate used for simulation

In figure 3-21, Simulation results of *I-V* characteristics and *EQE* of novel a-Si:H/μc-Si:H solar cells with textured glass substrate (double-textured) was presented compare to the one with flat glass substrate (reference). As we can see from these results, by introducing textured glass substrate which combines etched glass sheet with textured ZnO:B film J_{sc} was improved by ~0.9 mA/cm^2. From the figure 3-21(b), the improved spectral response over whole wavelength region can be observed, especially in the wavelengths of 400-900 nm and thus J_{sc} extracted from *EQE* measurement increased by ~1.2 mA/cm^2. This result reveals that a textured glass substrate can increase haze value and then improve light-scattering effect which results in increase in J_{sc} of a solar cell.

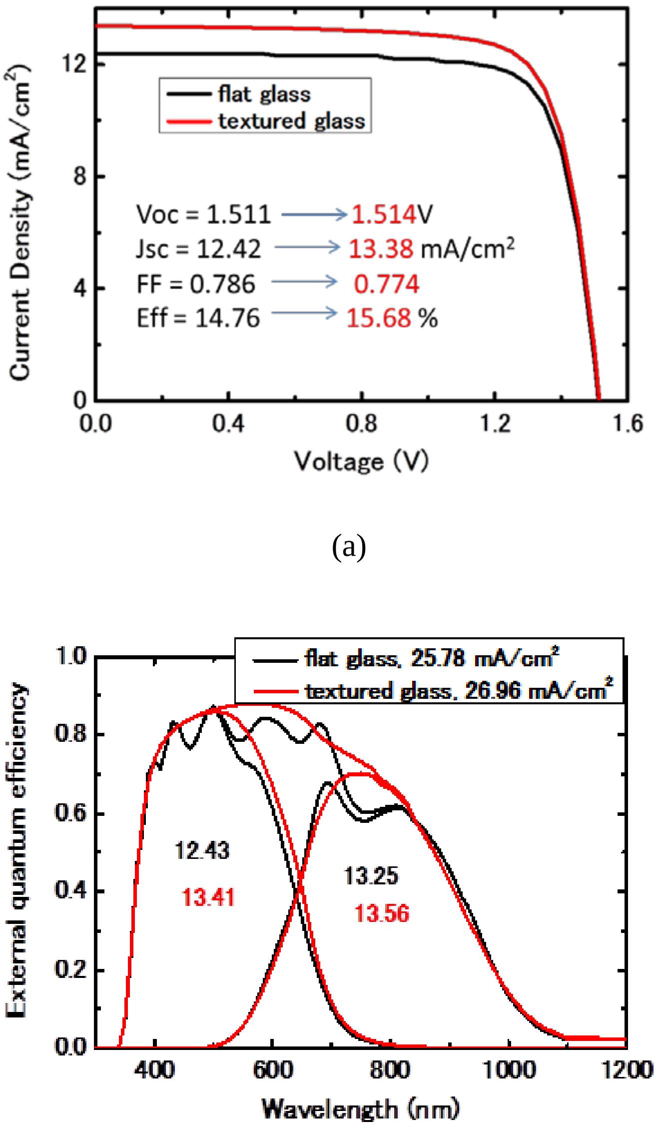

(a)

(b)

Figure 3-21 Simulation results of (a) *I-V* characteristics, (b) *EQE* of a-Si:H/μc-Si:H solar cells using flat and textured glass substrate

3.4 Summary

In this chapter, optical analysis and theoretical simulation was performed using OPTICAL and ASA simulators, respectively. The optical calculation of

IL, nBRL, and FAL using OPTICAL simulator was firstly done to investigate their effect on the optical properties, such as reflectance or transmittance spectra, of the test sample structure simulated from the experimentally fabricated solar cells. We have studied the effect of refractive index and thickness combinations of single and triple intermediate layers on the light-reflectance in the tandem solar cells. From the simulation results, it is clear that the wavelength region of reflection could be freely modified by adjusting the thickness and/or the refractive index of triple intermediate layers. Compared to the single, the reflectance of SiO_x triple intermediate layers at short wavelength region could be increased, whereas at the long wavelength region could be suppressed. Thus, a multi-stacked intermediate layer, especially triple intermediate layer, would be beneficial for use in a-Si:H /μc-Si:H tandem cell. The optical calculation results indicated that, for a single IL, the lower refractive index IL is the higher reflectance over wavelength region the test structure have. For nBRL, the effect of nBRL with variation of refractive index and thickness on the reflectance spectra of test structure was found out. From the result one can understand that the SiO_x film with refractive index of ~1.9 can be expected to replace at the back reflector instead of n-μc-Si/ZnO layer because the same reflectance could be observed. In addition, the thickness of nBRL should be optimized between 60-80 nm. Next, the optical study of FAL with varied refractive index on transmittance of test model was carried out. As can be found from the results, the optimal FAL obtained from this calculation was the one with refractive index of ~1.74 and the thickness should be 60-80 nm. The finding FAL shows the higher transmittance of test structure when it was inserted into glass/ZnO interface and the thickness of FAL of thicker than 80 nm shows the drop in transmittance spectra particularly, in the short wavelength (< 650 nm). Moreover, the effect of these optical layers (nIL, nBRL and FAL) on the current density of silicon-based thin film solar cells including double-junction solar cells was investigated. By inserting FAL with different refractive index into μc-Si:H solar cells, it was seen that the current density of the solar cells improve as the refractive index decreased down to ~1.74 but the refractive index less than that showed the reduction in current density, i.e., lower spectral response in the long wavelength region. In the same way, the current density of μc-Si:H solar cells increased when the refractive index of nBRL was decreased down to ~1.74 ; due to greater light-reflection between n-layer/metal electrode. Additionally, nBRL with varied refractive index was also applied into a-Si:H/μc-Si:H solar cells to observe the effect on solar cell performance. By inserting nBRL into the solar cells, the J_{sc} of the bottom solar cells slightly enhanced when the refractive index of the nBRL of the bottom cell became smaller. From this simulation results, it was found that the nBRL with lower refractive index can be used in order to improve the current density of the bottom cell in a tandem solar cell with a current-limited bottom. Furthermore, the effect of nIL and nBRL on novel a-Si:H/μc-Si:H solar cells performance was analyzed compared to the conventional one without that of nIL and nBRL. From simulation results, it was found that by applying novel structure absorption losses could be reduced especially in n-top and n-bottom layers and thus improved J_{sc} of the complete device. Here, the effect of interface roughness of substrates on solar cell performance was also investigated in order to comprehend the light-scattering effect of a device. As can be seen from this result it reveals that a textured glass substrate can increase haze value and then improve light-scattering effect which results in increase in J_{sc} of a solar cell.

References

[1] D. Fischer, S. Dubail, J. A. Anna Selvan, N. Pellaton Vaucher, R. Platz, Ch. Hof, U. Kroll, J. Meier, P. Torres, H. Keppner, N. Wyrsch, M. Goetz, A. Shah, and K.-D. Ufert: *Proc. 25th IEEE PVSC* (1996) 1053.

[2] D. Domine, J. Bailat, J. Steinhauser, A. Shah, C. Ballif: *Proc. 4th World Conf.on Photovoltaic Energy Conversion* (2006) 1465.

[3] S. Y. Myong, K. Sriprapha, S. Miyajima, and M. Konagai: *Appl. Phys. Lett.* **90** (2007) 263509.

[4] J. Meier, J. Spitznagel, S. Faÿ, C. Bucher, U. Graf, U. Kroll, S. Dubail, and A. Shah: *Proc. 29th IEEE PVSC* (2002) 1118.

[5] W. W. Wenas, A. Yamada, M. Konagai, and K. Takahashi: *Jpn. J. Appl. Phys.* **30** (1991) L441.

[6] A. Yamada, W. W. Wenas, M. Yoshino, M. Konagai, and K. Takahashi: *Jpn. J. Appl. Phys.* **30** (1991) L1152.

[7] M. Berginski, J. Hupkes, M. Schulte, G. Schope, H. stiebig, B. Rech, and M. Wuttig: J. Appl. Phys. **101** (2007) 074903.

[8] J. C. Lee, V. Dutta, J. Yoo, J. Yi, J. Song, and K. H. Yoon: *Superlattices Microstruct.* **42** (2007) 369.

[9] K. Tabuchi, W.W. Wenas, A. Yamada, M. Konagai, and K. Takahashi: *Jpn. J. Appl. Phys.* **32** (1993) L3764.

[10] X. D. Zhang, Y. Zhao, Y. T. Gao, F. Zhu, C. C. Wei, X. L. Chen, J. Sun, G. F. Hou, X. H. Geng, and S. Z. Xiong: *J. non-Cryst. Solids* **352** (2006) 1863.

[11] X. Zhang, Q. Yue, X. zheng, X. Geng, S. xiong, and Ying Zhao: *Proc. 5th World Conf. Photovoltaic Energy Conversion* (2010) 3232.

[12] P. D. Veneri, L.V. Mercaldo, and I. Usatii: *Appl. Phys. Lett.* **97** (2010) 023512.

[13] P. Buehlmann, J. Bailat, D. Domine, A. Billet, F. Meilaud, A. Feltrin, and C. Ballif: *Appl. Phys. Lett.* **91** (2007) 143505.

[14] D. Domine, P. Buehlmann, J. Bailat, A. billet, A. Feltrin, and C. Ballif: *Phys. Status Solidi: Rapid Res. Lett.* **4** (2008) 163.

[15] C. Das, A. Lambertz, J. Huepkes, W. Reetz, and F. Finger: *Appl. Phys. Lett.* **92** (2008) 053509.

[16] T. Grundler, A. Lambertz, and F. Finger: *Phys. Status Solidi* **C7** (2010) 1085.

[17] D.L. Staebler and C. R. Wronsky: *Appl. Phys. Lett*. **31** (1977) 292.

[18] E. Centurioni: *Appl. Optics* **44** (2005) 7532.

[19] H.-Y. Lee and T. Yao: *J. Appl. Phys.* **93** (2003) 819.

[20] J. Krc, M. Zeman, A. Campa, F. Smole, and M. Topic: *Mater. Res. Soc. Symp. Proc.* **910** (2006) A25-01.

[21] F. Du, Y.-Q. Lu, and S.-T. Wu: *Appl. Phys. Lett* . **85** (2004) 2181.

[22] J. A. Willemen, M. Zeman, J. W. Metselaar: *Proc. 1st World Conf. on Photovoltaic Energy Conversion* (1994) 599.

[23] B. E. Pieters, J. Krc, and M. Zeman: *4th World Conf. on Photovoltaic Energy Conversion* (2006) 1513.

[24] R. R. Arya, A. Catalano, and R. S. Oswald: *Appl. Phys. Lett.* **49** (1986) 1089.

[25] S. Guha, J. Yang, A. Pawlikiewicz, T. Glatfelter, R. Ross, and S. R. Ovshinsky: *Appl. Phys. Lett.* **54** (1989) 2330.

[26] J. Zimmer, H. Stiebig, and H. Wagner: *J. Appl. Phys.* **84** (1998) 612.

[27] I. A. Yunaz, K. Hashizume, S. Miyajima, A. Yamada, and M. Konagai: *Proc. 33rd IEEE Photovoltaic Specialists Conf.* (2008) 317.

[28] C. T. Sah and W. Shockley: *Phys. Rev.* **109** (1958) 1103.

[29] Shunsuke Kasashima:”Study of Multi-Junction Thin-Film Silicon Solar Cells for Application to Low-Concentrator Photovolatics”, Ph.D Thesis, Tokyo Institute of Technology (2013).

[30] Ihsanul Afdi Yunaz: ”Study of Numerical Analysis and Elemental Technology for Amorphous Silicon Based Triple Junction Solar cells”, Ph.D Thesis, Tokyo Institute of Technology (2009).

Chapter 4

Preparation and Characterization of SiO_x:H Films Using RF-PECVD Technique

4.1 Introduction

As previously reported in several papers, silicon-based materials including its alloy can be prepared by several deposition techniques [1-6]. The most preferable technique for research and manufacturing of silicon-based thin film solar cells is plasma-enhanced chemical vapor deposition techniques (PECVD). This technique can deposit a variety of thin films at lower temperatures than the conventional ones. Recently, the Radio-Frequency (RF) and Very-High-Frequency (VHF) PECVD techniques have widely been used to reduce production cost and to improve quality of silicon-based thin films like a-Si:H or μc-Si:H films. Although the VHF-PECVD can deposit silicon-based films with a deposition rate over 1 nm/s, reported by Neuchatel group [7-8], in this work, RF-PECVD is preferred to use because of the term of film quality, especially its uniformity as shown in table 4-1 [9].

As mentioned in the chapter 3, the silicon-based films with different properties are needed to apply into silicon-based thin film solar cells in order to improve solar cell efficiency by using light-trapping approaches, i.e., employment of nIL, nBRL, FAL and FALp: here, we call “optical layers”. The refractive index of silicon-based material used in this work should be tunable for use as optical layers with different properties. As reported, the refractive index of silicon-oxide alloys can be adjusted from 1.5 (SiO_2) to 3.8 (Si) by tuning the oxygen concentration [10-11], presently, n-type SiO_x-based material has widely been studied for photovoltaic applications [12-14]. It has successfully been prepared and applied to a p-i-n solar cell instead of ZnO/Ag back contact [12]. Moreover, it has also successfully been used as an intermediate layer (IL) in tandem solar cells [13]. Therefore, in this chapter, the preparation and characterization of hydrogenated silicon oxide (SiO_x:H)-based films, including both hydrogenated amorphous silicon oxide (a-SiO_x:H) and hydrogenated microcrystalline silicon oxide (μc-SiO_x:H) by using RF-PECVD technique, are mainly discussed to understand and find the considerable their properties corresponding to application needs.

Table 4-1 various depositions used for preparation of a-Si-based materials

Processes	**Maximum deposition rate**	**Advantages**	**Disadvantages**
RF-PECVD	3 (Å/s)	High quality, uniform	Slow
VHF-PECVD	15 (Å/s)	Fast	Poor uniformity
DC-PECVD	3 (Å/s)	High quality, uniform	Slow
Microwave-PECVD	50 (Å/s)	Very fast	Film quality not as good
HWCVD	50 (Å/s)	Very fast	Poor uniformity
Photo-CVD	1(Å/s)	High quality, uniform	Slow
Sputtering	3 (Å/s)		Poor uniformity

4.2 Fundamental Aspects of PECVD

PECVD technique, called “glow discharge”, is widely used as a deposition method for amorphous silicon based thin film solar cells , such as a-Si:H or µc-Si:H materials. This technique was used for the first preparations of a-Si:H by Cittick [4] and by Spear and Lecomber in 1969 [5]. Figure 4-1 shows a schematic of a typical PECVD chamber and some important parts (here, RF-PECVD). The PECVD system consists of two electrode plates (cathode and anode) located in parallel, a pumping system, heater, pressure controller and a RF or VHF power supply. The substrate is attached to a ground and is heated by heater. The chamber is evacuated by the pumping system, which usually has a turbo molecular pump backed with a mechanical pump, and the chamber pressure is controlled by a control valve. In the PECVD process, a silicon source such as SiH_4 or a mixture of SiH_4 and H_2 is introduced into the vacuum chamber. A RF (~13.56 MHz) or VHF (30-200 MHz) power line is connected to one electrode plate (cathode) while the other plate connected to the ground (anode). The plasma will occur by passing voltage between the two electrode plates with low chamber pressure. The plasma excites and decomposes the source gas and generates many radicals and ions, and then the radicals diffuse to the substrate and silicon film is grown on the surface. The deposition of PECVD technique can be described as a four- step process [6].

1. The first step is the primary reaction between electrons and SiH_4, which results in mixture of ions and free radicals.
2. The second step is the transport of these species to the surface of the substrate, which is accompanied by a multiplicity of secondary reactions, e.g., ion- molecule, photon-molecule.
3. The third step is the reaction of ions and free radicals with, or their adsorption onto,

the surface of the substrate.

4. The forth step is the process by which these species or their reaction products are incorporated into the growing film or are re-emitted from the surface into the gas-phase.

In the PECVD process, the film quality is influenced by many deposition parameters such as the deposition pressure, plasma power and frequency, substrate temperature and etc. The films with high quality and good uniformity can be fabricated under low deposition pressure while high deposition pressure if preferable for depositing microcrystalline-based materials. The PECVD technique with a radio-frequency (RF) of 13.56 MHz is one of the preferable deposition methods in research and manufacturing of amorphous based solar cell. In general, deposition rate can be increased by using higher RF plasma power for film deposition; however, higher RF power also leads to a silicon polyhydride powder. For general a-Si:H deposition, the typical deposition pressure is set at around 0.5 to 1.0 Torr, while RF plasma power is 10 to 100 mW/cm^2. Also, the substrate temperature is also an important factor for film quality of a-Si:H materials. Normally, the substrate temperature is kept between 150 to 350 ºC. In case of Si films deposited under lower substrate temperature, more hydrogen content incorporated in the films results in an increase in optical band gap. If the substrate temperature is low (<150 ºC), silicon polyhydride will be formed if high hydrogen dilution is not used. In contrast, with a high substrate temperature (>350 ºC), optical band gap is reduced due to less hydrogen content incorporation. The silicon films deposited at high temperature show a high degradation because of the small amount of hydrogen passivation of dangling bonds as well. The electrode gap is usually set at around 1 to 5 cm for a-Si:H deposition. A small gap is needed for a uniform deposition while a wider gap is easier to maintain plasma. However, in order to reduce production cost such as the increase of the deposition rate, improvement of properties of a:Si:H or µc-Si:H films, a very high frequency (VHF) PECVD technique first developed by Neuchtel group in 1987 is an alternative way to obtain a higher deposition rate. In this technique, the plasma excitation frequency is in range of 30 to 200 MHz. It was found that the deposition rate increased linearly with increasing frequency. This technique is suitable for the materials such as µc-Si:H which required high deposition rate. Nonetheless, the disadvantage of VHF-PECVD is poor uniformity of the films.

In this experiment, RF-PECVD technique was chosen to use for n-µc-SiO_x Films as it has a limitation on deposition system and high deposition rate is not much needed for quite thin SiO_x films.

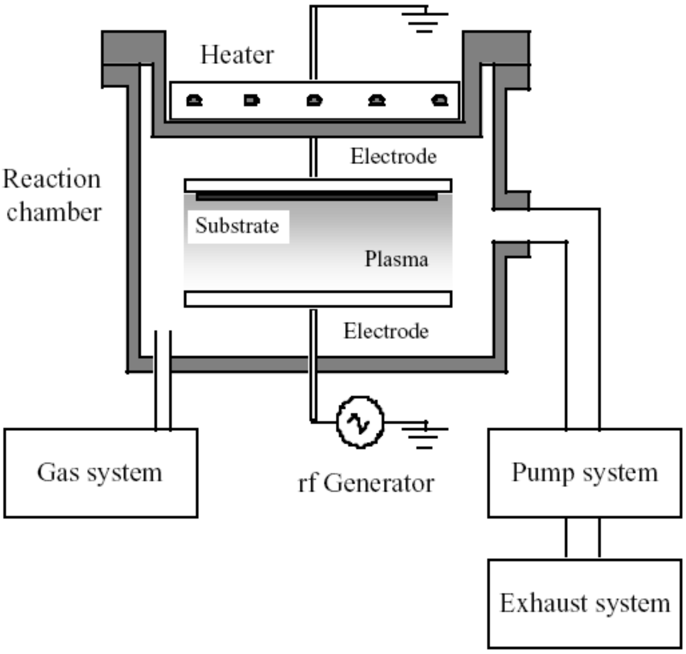

Figure 4-1 Schematic diagram of an RF-PECVD deposition system [19]

4.3 Deposition and Characterization of n-tpye μc-SiO_x:H Films using RF-PECVD Technique

4.3.1 Experimental Details

N-type μc-SiO_x:H films were deposited in 13.56 MHz plasma enhanced chemical vapor deposition chamber on Corning 7059 glass. As shown in Figure 4-2, this system was evacuated by a set of turbo molecular pump (TMP) and rotary pump (RP), and the base pressure measured by an ionization gauge was normally less than 10^{-5} Pa. The process pressure in the chamber could be controlled in the range of 0-1000 Pa by throttle valve. The gas flow rates were also controlled by a mass flow controller (MFC) in order to control the volume of gas accurately. A substrate holder was placed under the heater with gap distance of around 1 cm and heated at set heater temperature. The heater temperature was monitored by thermocouple. However, it should be noted that the substrate temperature value mentioned in this thesis means the setting temperature of the heater. For n-μc-SiO_x:H film deposition, silane (SiH_4), hydrogen (H_2), carbon dioxide (CO_2), and phosphine (PH_3 1% inH_2) were used as source gases. The gas mixture was introduced into the chamber via the gas tube installed on the side of the chamber.

The n-μc-SiOx:H films deposited on Corning 7059 glass were used in order to characterize the electrical, optical, and structural properties of films by spectroscopic ellipsometry (SE), Raman spectroscopy, conductivity and transmittance spectra measurements. The thickness, refractive index and the optical band gap (E_{04}) of deposited films were deduced from fitting results of variable-angle spectroscopic ellipsometry measurement. It should be understood that E_{04}, the photon energy at which the absorption coefficient is equal to 10^{-4}, was used as band gap energy of materials in this study. Moreover, it should also be noted that refractive indices mentioned in this section are the values at the wavelength of 600 nm. For structural characterization the Raman spectroscopy was conducted using an semiconductor laser with a wavelength of 532 nm. Electrical property of n-μc-SiOx:H films was investigated by dark conductivity (σ_d) measurement. Aluminum contacts were evaporated onto the samples deposited on the glass substrate and the in-plane dark conductivity was measured. The transmittance spectra measurement was also performed using UV-VIS-NIR Spectrophotometer.

Prior to film depositions, all substrates were cleaned by using organic solvents sequentially, i.e., ethanol-acetone-ethanol for 10, 10 and 10 minutes, respectively, in an ultrasonic bath and then dried by nitrogen blow, finally, placed on a substrate holder before putting into the load lock chamber. The robotic arm was used to transfer substrate holder from one chamber to another chamber. Before preparation of SiO_x, n-μc-Si:H films were firstly deposited in order to investigate optimal n-μc-Si:H, and optimization of n-μc-SiO_x:H films was also then carried out

For the deposition of n-μc-SiO_x:H films by 13.56 MHz RF-PECVD, the thickness of films were generally fixed at about 40-60 nm which is the thickness of an intermediate layer obtained from the theoretical analysis results for application to silicon based tandem solar cells. Besides, it should be noted that all of the gas flow rate reported in this study are the values displayed on mass flow controller not actual gas flow rate calculated by calibration with conversion factor. As summarized in Table, most of all deposition parameter were varied to optimize the performance of n-μc-SiO_x:H film. However, only effect of CO_2, H_2, PH_3 flow rates and substrate temperature are discussed in this section. It should be noted that the mass flow controllers (MFC) of H_2, PH_3, and SiH_4 are factory calibrated for hydrogen (H_2), on the other hand, MFC of CO_2 are factory calibrated for nitrogen (N_2).

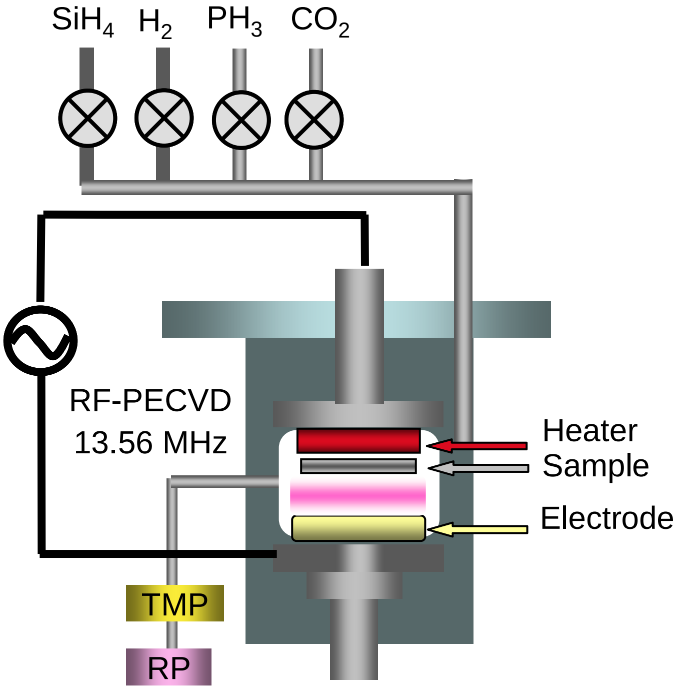

Figure 4-2 Schematic diagram of 13.56 MHz RF-PECVD system for n-μc-SiO_x:H film deposition

4.3.2 Effect of CO_2 Flow Rate

First, it is well recognized that oxygen content mainly affects properties of silicon oxide-based alloys films. Therefore, in this study, effect of CO_2 flow rate on the properties of SiO_x films was investigated. Here, CO_2 flow rate was changed from 8.0 to 12 sccm for the plasma power of 10 and 20 W while SiH_4, H_2, and PH_3 flow rates were set to be 3.30, 300, and 10 sccm, respectively. The substrate temperature, the deposition pressure, and the electrode gap were 200 ºC, 200 Pa, and 1.5 cm, respectively. Table 4-1 displays deposition conditions of SiO_x films. It is important to note that the mass flow controller (MFC) used for CO_2 gas was N_2-calibrated.

Table 4-1 The deposition condition of SiO_x:H films with different CO_2 flow rate

Substrate Temperature (°C)	200
Deposition Pressure (Pa)	200
Plasma Power Density (W/cm^2)	0.065 (10 W),0.13(20W)
Electrode gap (cm)	1.5
SiH_4 flow rate (sccm)	3.30
CO_2 flow rate (sccm)	**2-8**
PH_3 flow rate (sccm) (1 % in H_2)	10
H_2 flow rate (sccm)	300

Figure 4-3 shows the dark conductivity of SiO_x films with different CO_2 flow rate. From figure 4-3, it was observed that the conductivity declined when CO_2 flow rate increased for both plasma densities. In case of plasma density of 10 W, for example, the conductivity decreased from 1.2 S/cm at CO_2 flow rate of 2 sccm to $2x10^{-11}$ S/cm at CO_2 flow rate of 8 sccm. The conductivity markedly dropped to less than 10^{-8} S/cm at the CO_2 flow rate of higher than 6 sccm. The conductivity for the plasma power of 20 W also had the same tendency. The drop of conductivity with increasing CO_2 flow rate given in the figure is mainly due to an increase of Si-O bonding in the oxygen rich phase (a-SiO:H) incorporated in the film [15-16]. Figure 4-4 depicts the Raman spectra of SiO_x films deposited at the plasma power of 10 and 20 W. From the figure 4-4(a), it can be observed that the crystalline peak at 520 cm^{-1} disappeared as CO_2 flow rate increased higher than 6 sccm. These results correspond to the dark conductivity previously shown in Figure 4-3. Thus, it is clear that SiO_x films that have a crystalline phase are needed to obtain a reasonably high conductivity. It should also be noted that for higher power we could not observe the crystalline peaks at 520 cm^{-1}, therefore deposition at high power is not suitable for SiO_x films.

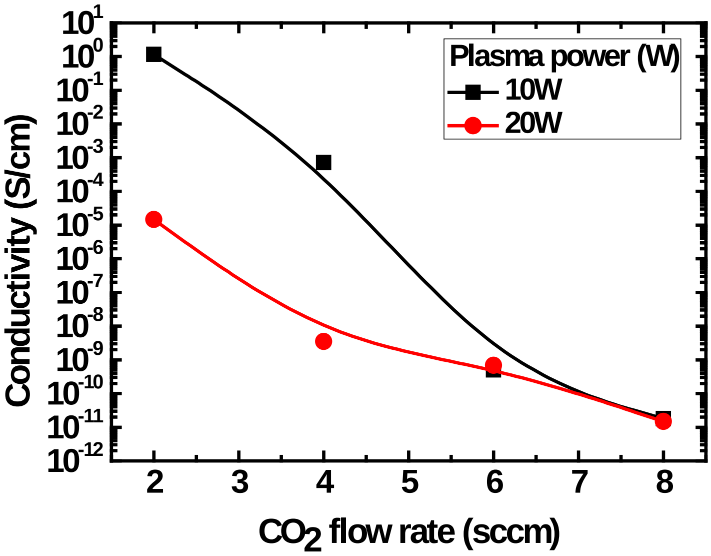

Figure 4-3 Dark conductivity of SiO_x:H films as a function of CO_2 flow rate for plasma power of 10 and 20 W

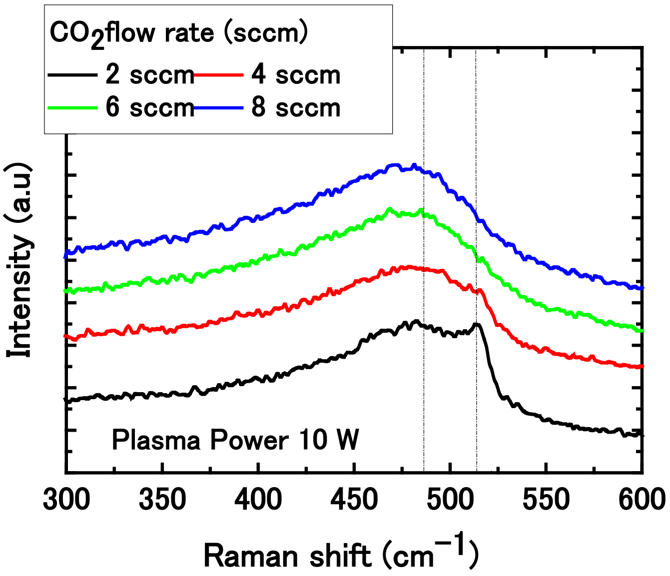

(a)

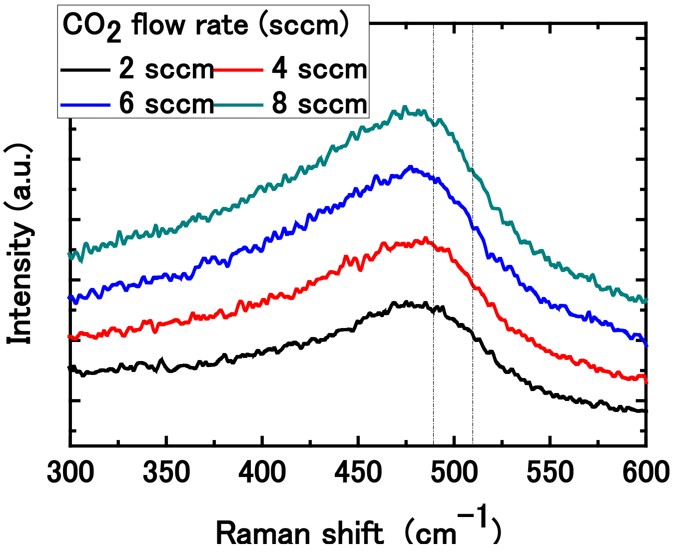

(b)

Figure 4-4 Raman spectra as a function of CO_2 flow rate for plasma power of (a) 10 W and (b) 20W

Figure 4-5 illustrates the refractive index at wavelength 600 nm of SiO_x films as a function of CO_2 flow rate prepared at the plasma power of 10 and 20 W. From figure 4-5, one can see that the refractive indices for both plasma powers decreased lower than 2.0 with increasing the CO_2 flow rate to 8 sccm. These results suggested that the refractive index could be controlled by varying the CO_2 flow rate. The drop of refractive index is probably due to increase of oxygen concentration in the oxygen-rich phase in the films [17]. The oxygen-rich phase is effective in increasing the optical band gap [18]. These results are in good agreement with the optical band gap illustrated in figure 4-6. Here, it was also found that the plasma power of 10 W is more beneficial for deposition of SiO_x films under this regime.

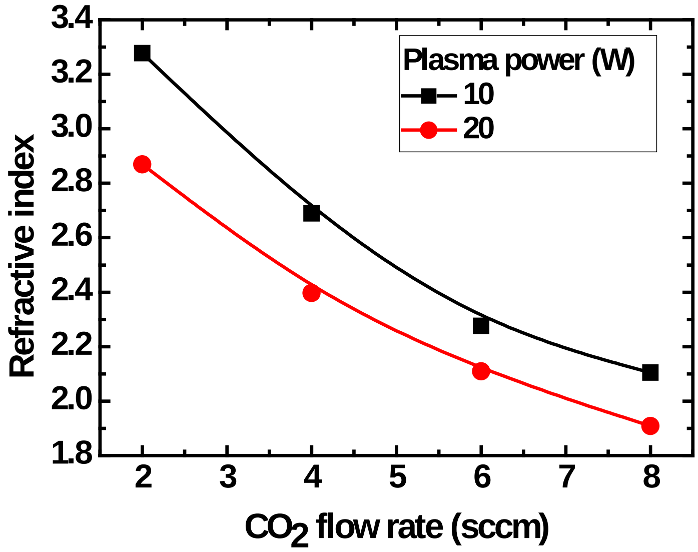

Figure 4-5 Refractive index of SiO_x films at the wavelength of 600 nm as a function CO_2 flow rate for plasma power of 10 and 20W

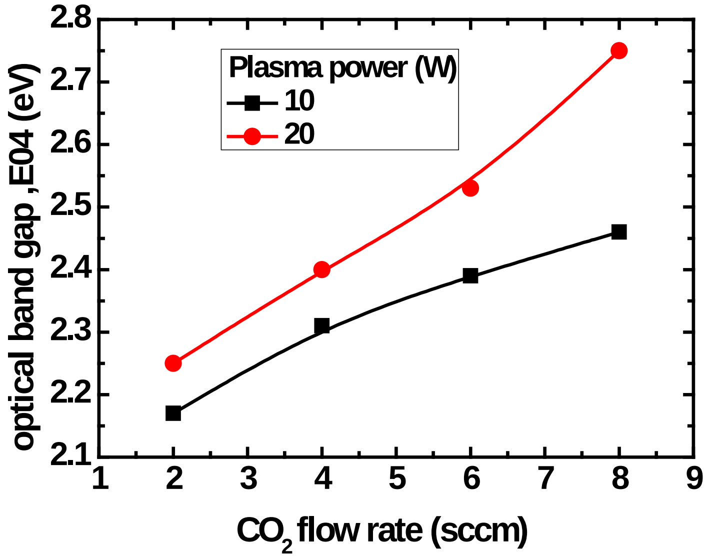

Figure 4-6 Optical band gap as a function of CO_2 flow rate for plasma power of 10 and 20 W

4.3.2 Effect of H_2 Flow Rate

It is well known that the formation of crystalline phase in SiOx material can probably be improved by an optimal hydrogen dilution. Therefore, the effect of H_2 flow rate on the properties of SiO_x:H films was then investigated. The H_2 flow rate was varied from 200 sccm to 400 sccm whereas SiH_4, CO_2, and PH_3 flow rate were kept constant at 3.30, 9.5, and 10 sccm respectively. The substrate temperature, the deposition pressure, the plasma power, and the electrode gap were set to be 200 ºC, 200 Pa, 10 W, and 1.5 cm, respectively. The details of deposition condition are shown in the table 4-2.

Table 4-2 The deposition condition of SiO_x:H films with different H_2 dilution

Substrate Temperature (ºC)	200
Deposition Pressure (Pa)	200
Plasma Power Density (W/cm^2)	0.065 (10 W)
Electrode gap (cm)	1.5
SiH_4 flow rate (sccm)	3.30
CO_2 flow rate (sccm)	9.5
PH_3 flow rate (sccm) (1 % in H_2)	10
H_2 flow rate (sccm)	**200 - 500**

Figure 4-7 gives the dark conductivity (σ_d) of SiO_x:H films with different H_2 dilution. From figure 4-7, we can see that the films with somewhat high conductivity of around 10^{-5} S/cm could be gained when H_2 flow rate was in range of 200-350 sccm. Nevertheless, the conductivity of the films then declined with increasing H_2 flow rate of more than 350 sccm. The main factor for the improvement in conductivity is probably due to the increment in crystalline volume fraction measured by Raman spectra which are shown in Figure 4-8. However, a too much H_2 dilution (H_2 flow rate of more than

350) may cause damage on the surface of films due to an increase in hydrogen atom which caused a hydrogen etching and result in the deterioration in the properties of deposited films.

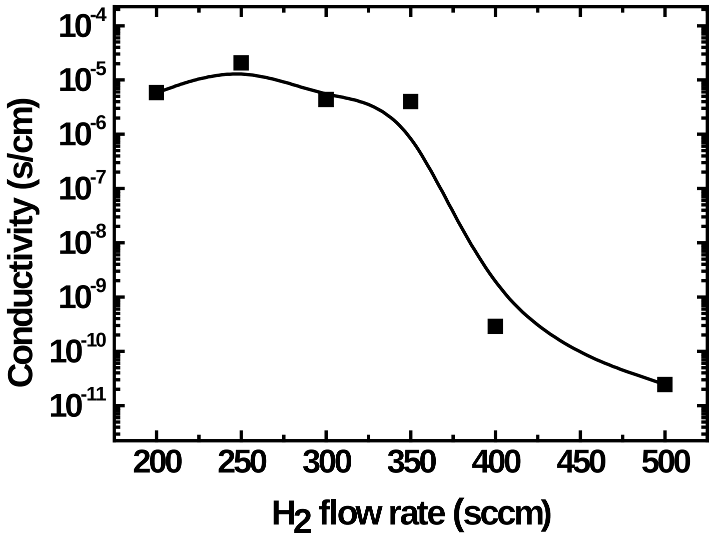

Figure 4-7 Dark conductivity of SiOx:H films as a function of H_2 flow rate

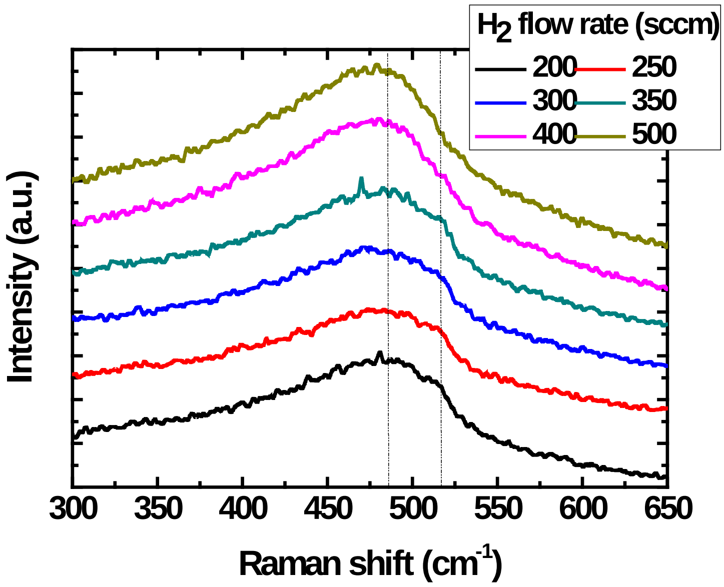

Figure 4-8 Raman spectra as a function of H_2 flow rate

Figure 4-9 shows the refractive index of SiOx films as a function of H_2 flow rate. The refractive indices mentioned here are also the values at the wavelength of 600 nm. From figure 4-9, one can see that the refractive index decreased from ~2.3 at the H_2 flow rate of 200 sccm to ~1.7 at H_2 flow rate of 500 sccm corresponding to the increase in the optical band gap of the films as shown in figure 4-10. These occurrences, i.e. the drop of refractive index and the increase in optical band gap, were due to a change in the structure of the SiOx films. The SiOx films should be correlated with H_2 dilution and probably became more porous as the H_2 dilution increased.

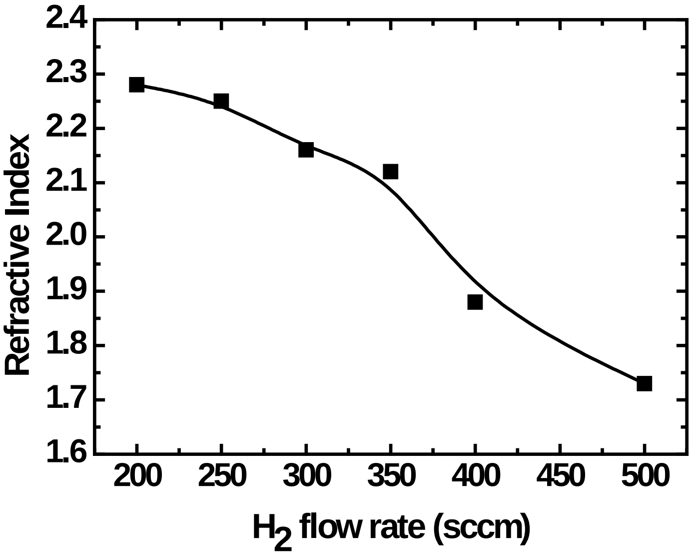

Figure 4-9 Refractive index of SiOx films at the wavelength of 600 nm as a function H_2 flow rate

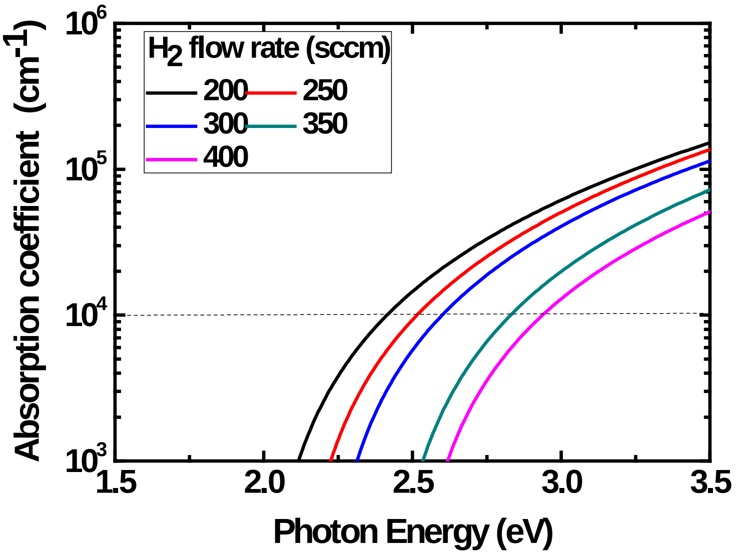

(a)

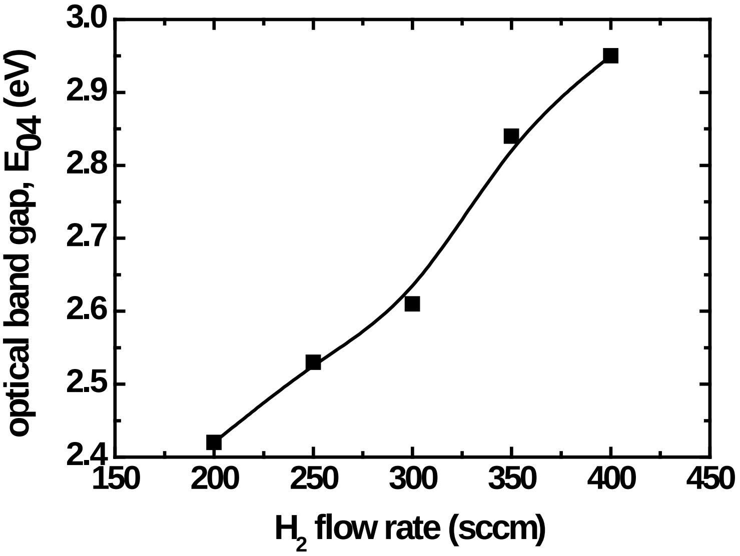

(b)

Figure 4-10 (a) Absorption coefficient (b) Optical band gap as a function of H_2 flow rate

4.3.3 Effect of PH_3 Flow rate

In order to obtain the excellent quality of films, the electrical properties of SiOx films should be improved by doping properly. Here, the effect of PH_3 flow rate on the properties of SiOx films was investigated. In these experimental series, PH_3 flow rate was varies from 4 to 10 sccm for the RF plasma power of 10 W, whereas SiH_4, H_2, and CO_2 flow rates were fixed at 3.30, 300, and 9.5 sccm, respectively. The deposition pressure, the substrate temperature and the electrode gap were 200 Pa, 200 ºC and 1.5 cm, respectively. Table 4-3 shows the condition of this experiment in details.

Table 4-3 The deposition condition of SiO_x:H films with different PH_3 (1% in H_2) flow rate

Substrate Temperature (ºC)	200
Deposition Pressure (Pa)	200
Plasma Power Density (W/cm^2)	0.065 (10 W)
Electrode gap (cm)	1.5
SiH_4 flow rate (sccm)	3.30
H_2 flow rate (sccm)	300
CO_2 flow rate (sccm)	9.5
PH_3 flow rate (sccm) (1 % in H_2)	**4- 10**

Figure 4-11 shows the dark conductivity of deposited SiO_x films as a function of PH_3 flow rate ratio. As can be seen in figure 4-11, the dark conductivity increased more than four orders of magnitude from 10^{-8} to 10^{-4} S/cm when the PH_3 flow rate increased from 4 to 10 sccm. The results show that PH_3 is effective for doping the SiOx films in order to improve electrical property of the films. Moreover, these results had a good agreement with the Raman spectra given in figure 4-12. From figure 4-12, it was observed that the crystalline peak at 520 cm^{-1} decrease with increasing the PH_3 flow rate.

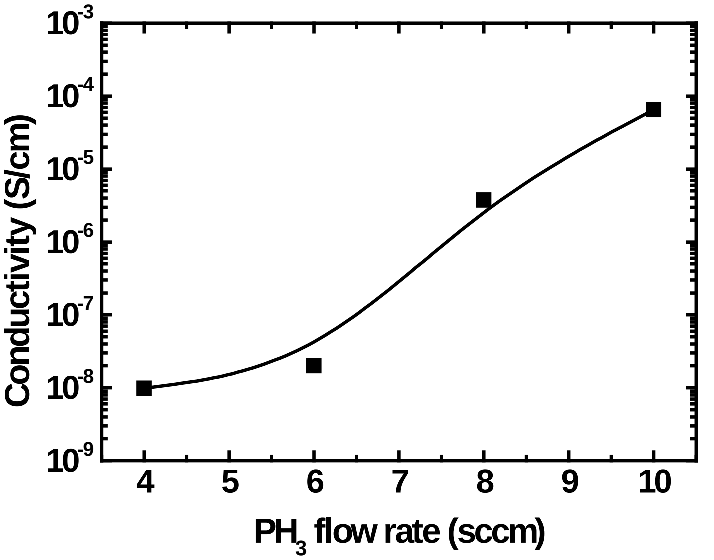

Figure 4-11 Dark conductivity of SiOx films as a function of PH_3 (1% in H_2) flow rate

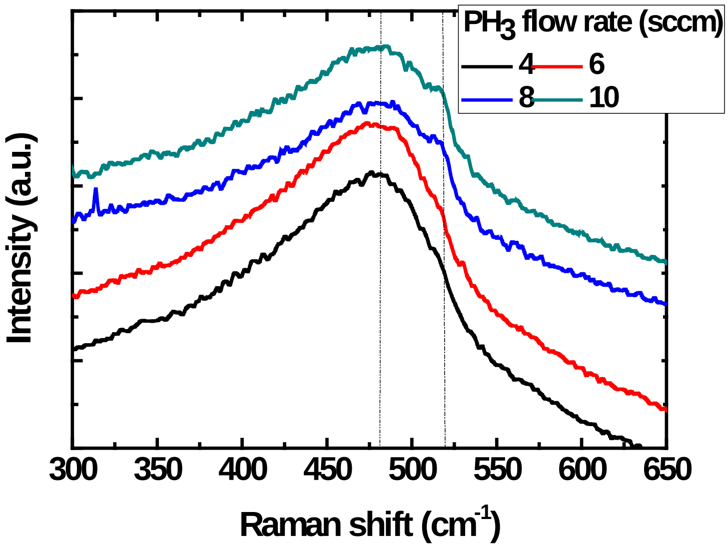

Figure 4-12 Raman spectra as a function of PH_3 (1% in H_2) flow rate

The refractive index of SiOx films deposited with various PH_3 flow rate is displayed in figure 4-13. From figure 4-13 one can see that the refractive index initially increased up to 2.2 at PH_3 flow rate of 8 sccm and tended to keep constant when PH_3 flow rate was higher than 8 sccm. Besides, the absorption spectrum and the optical band gap of SiOx films were shown in figure 4-14. As can be seen in figure 4-14, increase in optical band gap of the films with decreasing PH_3 flow rate corresponds to decreased refractive index. These results implied that further optimization of PH_3 flow rate ratio is considerable to obtain the better properties of SiO_x films.

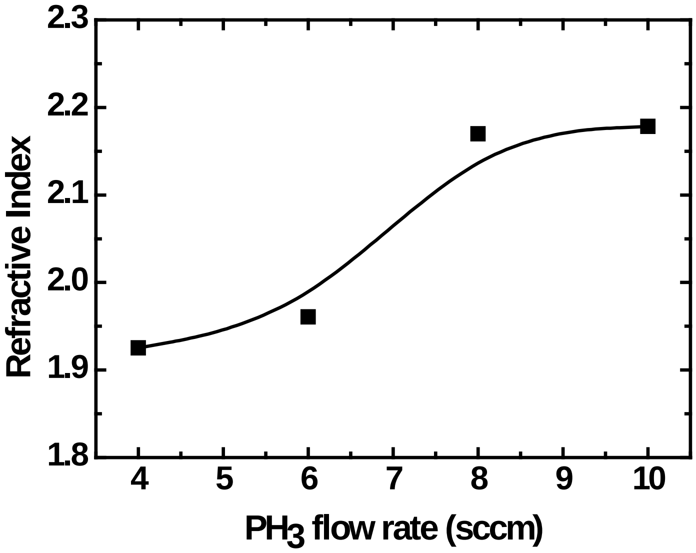

Figure 4-13 Refractive index of SiOx films at wavelength 600 nm as a function of PH_3 (1% in H_2) flow rate

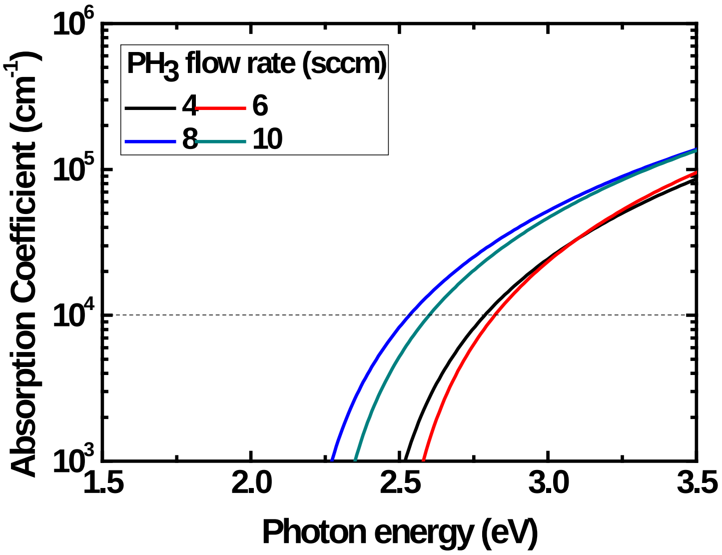

(a)

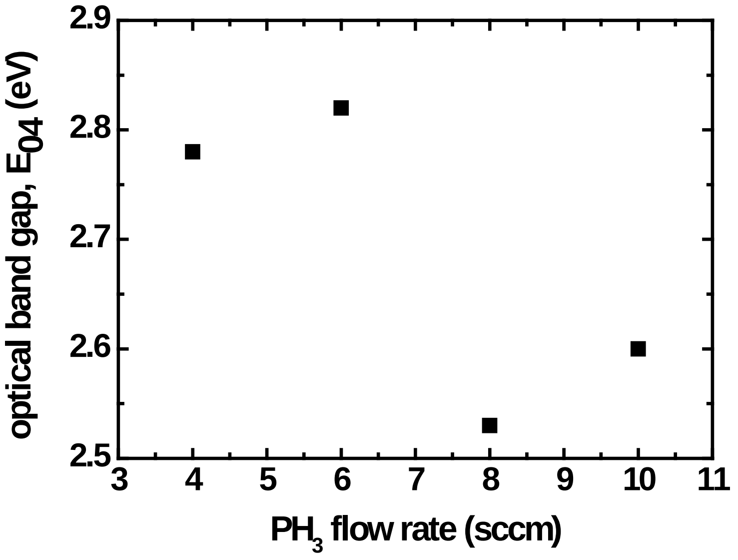

(b)

Figure 4-14 (a) Absorption coefficient (b) Optical band gap as a function of PH_3 (1% in H_2) flow rate

4.3.4 Dependence of substrate temperature

Next, substrate temperature which affects the structure and properties of films is a key factor to film-growth on the substrate. Thus, to recognize further structural and electrical properties of films, the effect of substrate temperature was explored in this section. The substrate temperature was changed from 100 ºC to 300 ºC while the SiH_4, H_2, CO_2 and PH_3 were fixed at 3.30, 300, 11, and 10 sccm respectively. In this case, the deposition pressure, the plasma power and electrode gap were set to be 200 Pa, 10 W and 2.0 cm, respectively. The deposition condition is concluded in Table 4-4.

Table 4-4 The deposition condition of SiOx:H films with vavious substrate temperature

Substrate Temperature (ºC)	**100-300**
Deposition Pressure (Pa)	200
Plasma Power Density (W/cm^2)	0.065 (10 W)
Electrode gap (cm)	2.0
SiH_4 flow rate (sccm)	3.30
H_2 flow rate (sccm)	300
CO_2 flow rate (sccm)	11
PH_3 flow rate (sccm)	10

Figure 4-15 displays the dark conductivity of SiOx films deposited at different substrate temperature. From figure 4-15, it was found that the conductivity increased from 10^{-11} to 10^{-4} S/cm as the substrate temperature increased. It is interesting to note that increase in conductivity of the films with increasing is probably due to change in the film structure and chemical bonding configuration of prepared samples, e.g. , for example, more Si-H bond contained in the samples and thus more crystalline phase, corresponding to the result of Raman spectra given in figure 4-16. From figure 4-16, we can see that crystalline peak at 520 cm^{-1} appeared when the substrate temperature was higher than 200 ℃.

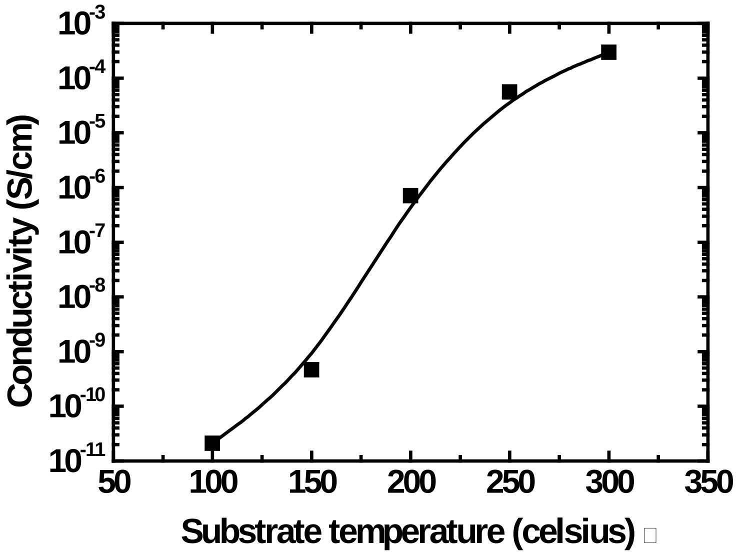

Figure 4-15 Dark conductivity of SiOx films as a function of substrate temperature

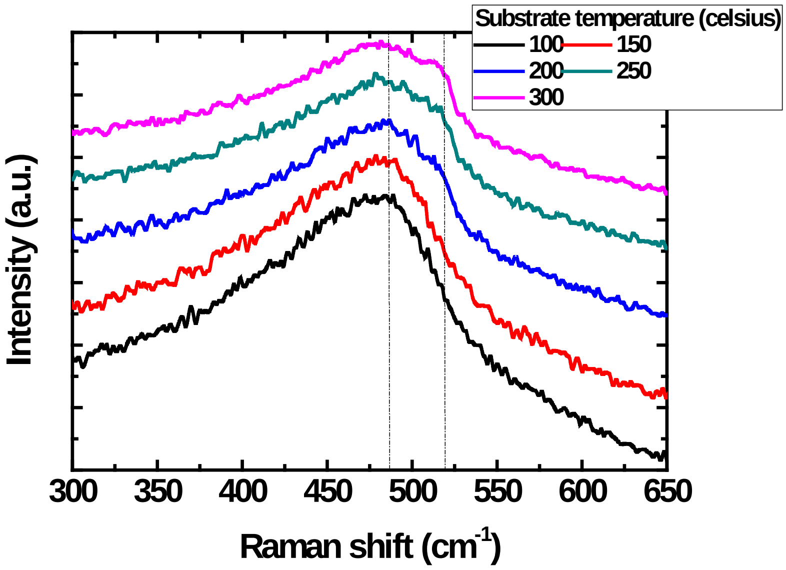

Figure 4-16 Raman spectra as a function of substrate temperature variation

Figure 4-17 depicts the refractive index at wavelength 600 nm of prepared SiOx films with various substrate temperatures. From figure 4-17, one can see that the refractive indices increased as the substrate temperature increased. This result had a good agreement with a drop in optical band gap of the films as shown in Figure 4-18. It is possible that dissociation of oxygen atom at high temperature is worse than that of atoms of other gases incorporated in the films and thus lower amorphous SiO phase could be observed. As a result, narrower optical band gap and higher refractive index of the films appeared.

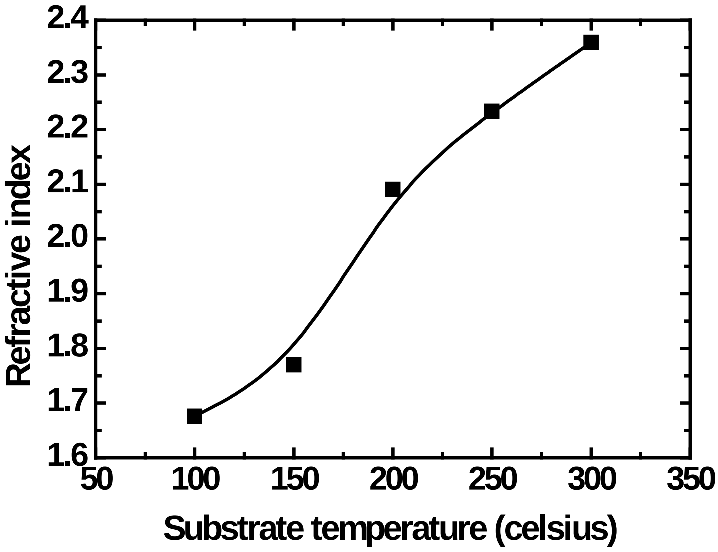

Figure 4-17 Refractive index of SiOx films at wavelength 600 nm as a function of substrate temperature

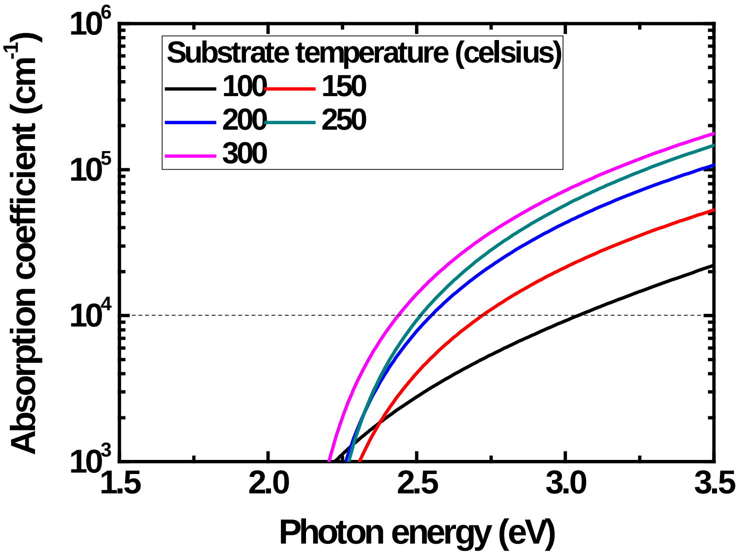

(a)

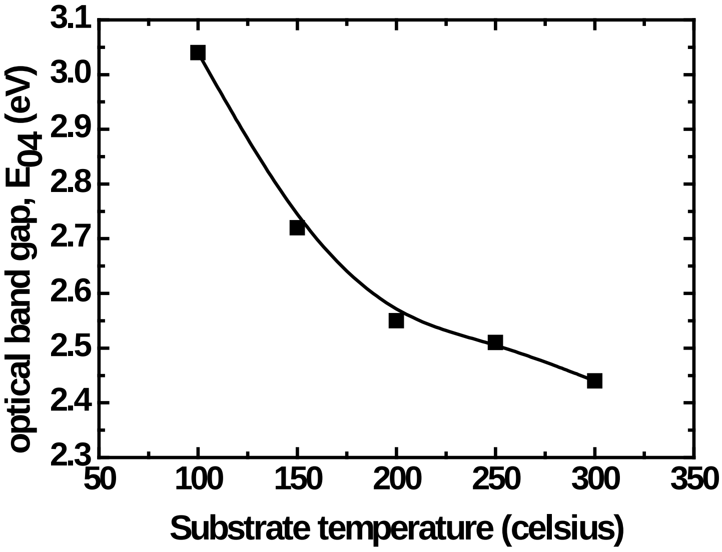

(b)

Figure 4-18 (a) Absorption coefficient (b) Optical band gap as a function of substrate temperature variation

From the above explanation, in this experimental study, it was found that the properties of SiOx films can be adjusted by varying the deposition parameters, for example, the plasma power, substrate temperature, electrode gap, and source gas flow rate. To improve properties of the films, in case of a low CO_2 regime, not high H_2 dilution and PH_3 flow rate were needed, while in case of a high CO_2 regime, higher H_2 dilution and much higher PH_3 flow rate were required. Moreover, in order to enhance the optical properties of the fabricated films, i.e. refractive index or optical band gap, reasonably high CO_2 flow rate is a main factor. In contrast, to improve electrical property of the films, higher H_2 dilution and sufficiently high PH_3 flow rate is mainly needed. The main work in development of SiOx intermediate reflector is to maintain a sufficiency high electrical conductivity while decreasing as much as possible the refractive index. Figure 4-19 shows relationship between refractive index and in-plan dark conductivity of deposited SiOx films. From figure 4-19, we can see that, generally, the conductivity declined with reducing the refractive index. The films with refractive index lower than 2 have so far been obtained. However, most of these films still have the poor in-plane conductivity, a few has sufficiency high conductivity of around 10^{-6}. A further optimization is still required to obtain better film properties.

Nevertheless, it should be noted that a recent report presented that SiO_x-based intermediate layer with a low in-plane conductivity of 10^{-9} S/cm as measured on glass could be employed as an intermediate layer in a-Si:H/µc-Si:H double-junction solar cells. They observed a difference between the in-plane conductivity measured on glass and the perpendicular conductivity of the layer applied in the solar cells. They mentioned that this difference is probably because of the growth of microcrystalline Si grains penetrating through the SiO-based layer. In the cell, their growth is enhanced from the beginning of the film by underlying µc-Si:H doped layer, which allows the creation if high-conductivity passages across the intermediate layers. Thus, they supposed the existence of a low conductivity amorphous SiO_x matrix, with a high transversal conductivity created by the crystalline Si phase. The low in-plane conductivity of SiO_x intermediate layer compared to that of ZnO intermediate layer is actually a desired property because it eliminates the need for an additional insulating laser scribe after the deposition of the intermediate layer. This is very important to facilitate the serial connection for making modules.

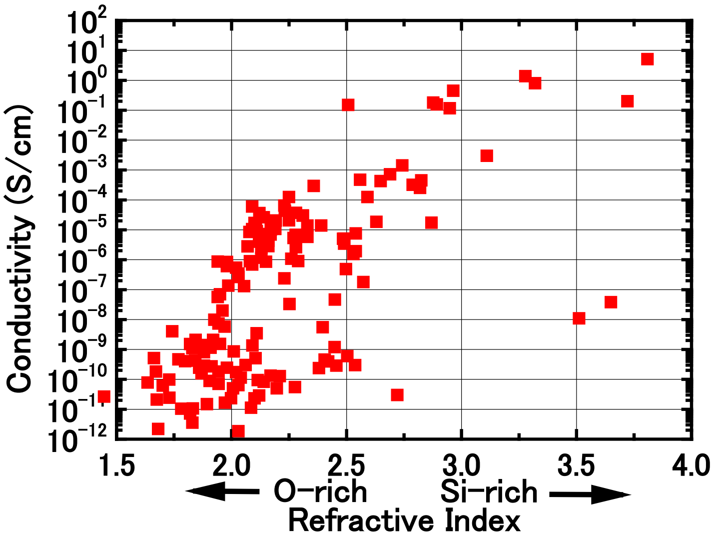

Figure 4-19 Relationship between refractive index and in-plan dark conductivity of deposited SiO_x films

4.4 Summary

In this chapter, the preparation and characterization of n-type SiO_x films were performed. It was found that it is possible to fabricate the n-type SiO_x films using 13.56 MHz RF-PECVD technique from a mixture SiH_4, H_2, PH_3 and CO_2 as a source gas. The optical, electrical, and structural properties of the fabricated n-SiOx films were investigated. The optical band gap (E_{04}) and the refractive index of the films could mainly be controlled by variation of CO_2 and H_2 flow rates. The conductivity of the films increased with increasing the PH_3 flow rate, in contrast, it declined with an increase in CO_2 flow rate. Besides, it can also be seen that the films deposited on the high temperature substrate had better conductivity, however, those of refractive index also increased. By optimizing the source gas flow rates and other deposition condition parameters, a few n-SiO_x films with refractive index lower than 2.0 and reasonably good in-plane conductivity (~10^{-6} S/cm) have been obtained and are expected to be used in silicon-based thin film solar cells as “optical layers”, i.e. intermediate layer (IL), intermediate layer with function of n-top layer (nIL), n-bottom layer with function of back reflective layer (nBRL), as well as anti-reflection layers inserted glass/TCO interface (FAL) and TCO/P-Si layer (FALp) as additional refractive-index matching layers. Afterwards, each of these optimum films will be applied to thin film silicon solar cells including a-Si:H/μc-Si:H double-junction solar cells as reflective optical layers and additional refractive-index matching layers corresponding to function needs.

References

[1] F. W. Smith and Z. Yin: *J. Non-Cryst. Solids*.**137** (1991) 871.

[2] J. L. Guizot, K. Nomoto and A. Matsuda: *Surf. Sci.* **244 (**1991) 22.

[3] R.E.I. Schropp and M. Zeman: *Amorphous and Microcrystalline Silicon Solar Cells Modeling, Material and Device Technology: Kluwer Academic.*, Dordrecht (1998).

[4] R. Chittik, J. Alexander, and H. Sterling: *J. Electrochem. Soc.* **116** (1969) 77.

[5] W. E. Spear and P. G. LeComber: *J. Non-Cryst. Sol.*, **8-10** (1972) 727.

[6] W. Luft and Y.S. Tsuo: *Hydrogenated Amorphous Silicon Alloy Deposition Processes*, Marcel Dekker Inc., Newyork, 1993) (a) 102, (b) 224.

[7] H. Curtins, N. Wyrsch, and A.V. Shah: *Electronics Lett.* 23 (1987) 228.

[8] A.Shah, J. Dutta. N. Wyrsch, K. Prasad, H. Curtins, F, Finger, A. Howling, and C. Hollenstein: *Materials Research Society Symp. Proc.* Vol. 258 (1992) 15.

[9] X.Deng and E.A. Schiff: *Amorphous Silicon Based Solar Cells (a chapter of Handbook of Photovoltaic Engineering,* ed. A. Luque & S. Hegedus, (2002) (john Wiley & Sons, Ltd., England, 2002)

[10] A. Sarker, C. Banerjee and A K Barua: *J. Phys. D: Appl. Phys.* **35** (2002) 1205.

[11] R. E. Carius, *Phil. Mag. B.* **80** (2000) 741

[12] P. Delli Veneri, L. V. Mercaldo and I. Usatii: *Appl. Phys. Lett*. **97** (2010) 23512.

[13] A. Lambertz, T. Grundler and F. Finger: *24th EUPVSEC* (2009) 2402.

[14] X. Zhang, Q. Yue, X. Zheng, X. Geng, S. Xiong and Y. Zhao: *25th EUPVSEC & 5th WIP* (2010) 3232.

[15] A. Janotta, R. Janssen, M. Schmidt, T. Graf, and M. Stutzmann: *Phys. Rev. B* **69**, (2004) 115206.

[16] C. Banerjee, J. Sritharathikhun, A. Yamada, and Makoto Konagai: *J. Phys. D: Appl.*

Phys. **41** (2008) 185107.

[17] H. Watanabe, K. Haga, and T. Lohner: *J. Non–Cryst. Solids* **164-166** (1993) 1085.

[18] P. Buehlmann, J. Bailat, D. Domine, A. Billet, F. Meillaud, A. Feltrin, and C. Ballif: *Appl. Phys. Lett.* **91** (2007) 143505.

[19] Jef Poortmans and Vladimir Arkhipov: *"Thin Film Solar Cells Fabrication, Characterization and Applications"*, John Wiley & Sons, Ltd (2007).

Chapter 5

Fabrication and Characterization of novel a-Si:H/μc-Si:H Double Junction Solar Cells using n-top Layer with a function of intermediate layer (nIL) and n-bottom layer with a function of back reflective layer (nBRL)

5.1 Introduction

The first development of an hydrogenated amorphous silicon (a-Si:H)/ hydrogenated microcrystalline silicon (μc-Si:H) double-junction solar cell, also called "micromorph" tandem cell, was proposed in 1994 by IMT, University of Neuchatel group[1]. This double-junction solar cell, with combination of two different band gap materials corresponding to solar spectrum, is a promising candidate for the new generation of thin film Si solar cells due to higher efficiency and higher stability than conventional amorphous silicon based single-junction solar cells [2-4]. The stability of the micromorph solar cell is mainly influenced by light-induced degradation of a-Si:H top cells which exhibit light-induced degradation after light illumination[5]. To improve the stability of the micromorph solar cell, thickness of the intrinsic layer of the top cell should be reduced. However, it is well know that the reduction in thickness of the intrinsic layer of the top cell leads to lower short circuit current and thus relatively low cell efficiency. This problem can be overcome by employing an intermediate layer between the a-Si:H top cell and the μc-Si:H bottom cell. The intermediate layer can increase short circuit current of the top cell without increasing the thickness of the top cell due to enhanced internal reflection inside solar cells and also improved light-induced degradation because of thinner i-top layer. As reported, transparent conductive oxide materials, e.g. a zinc oxide (ZnO) or a silicon oxide (SiO_x), are commonly used as an intermediate layer for an a-Si:H/µc-Si:H double-junction solar cell [6-9].

Also, recently, multi-junction solar cells have attracted attention for relatively high efficiency solar cells. Light-trapping approaches, e.g., front contact using textured transparent conductive oxide (TCO), back reflector with highly reflective textured TCO/metal and a transparent intermediate layer (IL), are necessary for achieving efficient incident light absorption in intrinsic absorber layer of component cells. In multi-junction structures like a-Si:H/µc-Si:H double junction solar cells, the current of top cells with thinner thickness can be increased by employing an IL between component cells resulting in reduced light-induced degradation. On the other hand, the current of bottom cells can be enhanced by optimizing back reflector (TCO/metal) to increase reflectance especially at the long wavelength region. Recently, n-type SiO_x based material has widely been studied for photovoltaic applications [10-12]. It has successfully been prepared and applied to a p-i-n solar cell instead of ZnO/Ag back contact. Moreover, it has successfully been used as an IL in tandem solar cells as well.

In this chapter, characterization of phosphorous-doped SiO_x:H (n-SiO_x) layers and their applications to silicon-based thin-film solar cells have experimentally been studied. Firstly, n-SiO_x films was optimized for use as an IL inserted between top and bottom cell and the effect of n-SiO_x IL on solar cell performance was then investigated. Sequentially, the µc-Si:H single-junction solar cells with novel structure p-µc-SiO_x:H/ i-µc-Si:H/ n-SiO_x:H/ Ag/ Al were fabricated on textured ZnO:B-coated glasses by employing an n-SiO_x:H film which works both as an n-layer and a back reflective ZnO layer. Secondly, an a-Si:H/μc-Si:H tandem solar cell with novel structure of p-a-SiC:H/i-a-Si:H/n-SiO_x:H/p-μc-SiO_x:H/i-μc-Si:H/n-SiO_x:H/ Ag/ Al was proposed as a candidate to lower the optical losses and increase the tandem cell performance. In this novel structure, 1st n-SiO_x:H layer will work as an n-layer of the top cell and at the same time it can also be functioned as an IL inserted between component cells. On the other hand, 2nd n-SiO_x:H layer will work as both an n-layer of the bottom cell and a back reflective ZnO:B layer. As a result, higher current can be obtained due to no absorption loss from both n-layers and no free-carrier absorption loss from back reflective ZnO:B layer. Higher cell performance can thus be expected by these kinds of solar cell structure.

5.2 Optimization of n-μc-SiO_x:H films used as a nIL (n-layer with function of intermediate layer) and a nBRL (n-layer with function of back reflective layer)

5.2.1 Experimental details

Phosphorous-doped SiO_x:H films were deposited on Corning 7059 glass at 200 ºC substrate temperature from a gas mixture of SiH_4, H_2, PH_3 and CO_2 by using 13.56 MHz radio frequency plasma-enhanced chemical vapor deposition (RF-PECVD) technique. In this study, the flow rate gas ratio of CO_2/SiH_4 (R) was varied in the range of 0 - 5 while the SiH_4/ H_2 flow rate gas ratio, the $PH_3/(SiH_4+ PH_3)$ flow rate gas ratio and the H_2 flow rate were kept constant at 0.7%, 3.8% and 300 sccm, respectively. The deposition pressure and plasma power were set to be 200 Pa and 65 mW/cm^2, respectively. Here, the thickness of all deposited films was kept around 50-60 nm. For film characterizations, the optical, structural and electrical properties of deposited films were analyzed by spectroscopic ellipsometry (SE), Raman spectroscopy and conductivity measurement. The structural property of deposited films was also investigated by Raman scattering spectroscopy. The in-plan dark conductivity was measured by coplanar electrodes. The thickness, refractive index and optical band gap (E_{04}) were deducted from SE measurement. It should be noted that refractive indices mentioned in this paper are the values measured at the wavelength of 600 nm. It is also important to remember that, the effect of CO_2 with high-doping was studied in this chapter; it is different from the effect of CO_2 with low-doping which was investigated in the previous chapter.

5.2.2 Optimization of n-μc-SiO_x:H films by varying CO_2 flow rate with high-doping

Firstly, effect of flow rate gas ratio of CO_2/SiH_4 on the properties of n-SiO_x:H films was studied in order to explore the optimal films used for a nIL and a nBRL. Figure 5-1 expresses the in-plan dark conductivity of n-SiO_x:H films with various CO_2/SiH_4 gas ratio (R). From figure 5-1, it was observed that the conductivity declined from 20 S/cm to nearly 10^{-8} S/cm when R increased up to 4.5. As reported in several papers, the drop of conductivity with increasing R is mainly due to an increase of Si-O bonding in the film which only presents in the amorphous phase [13]. In silicon-oxide-based materials, it was reported that the oxygen-rich phase (a-SiO:H) is effective in increasing the optical band gap or/and refractive index, whereas, silicon-rich phase (μc-Si:H) contributes to a high conductivity. Therefore, if the oxygen content increased, the crystalline volume fraction decreased and conversely the increase of amorphous peak appeared [14]. This explanation is compatible with the Raman spectra result which the crystalline peak at 520cm^{-1} disappeared as R increased more than 3.9 as shown in figure 5-2.

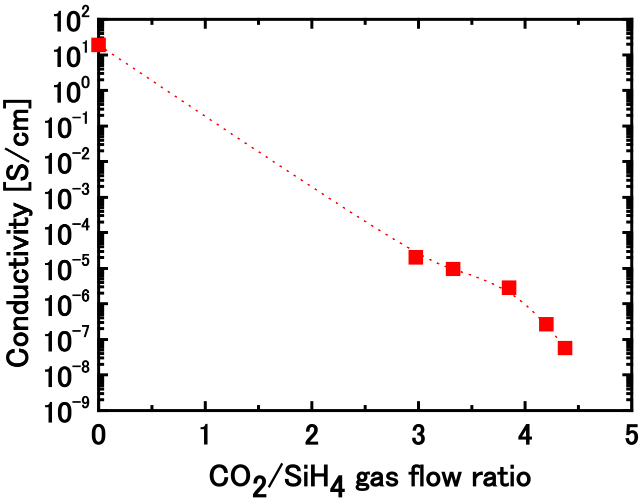

Figure 5-1 In-plan conductivity of n-SiO$_x$:H films as a function of CO$_2$/SiH$_4$ gas ratio

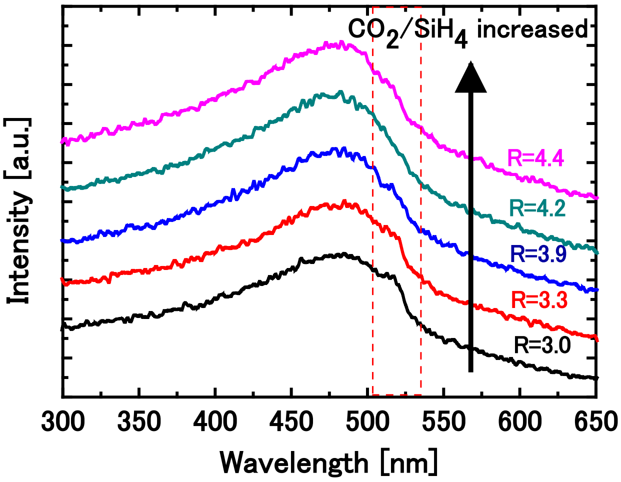

Figure 5-2 Raman spectra of deposited n-SiO$_x$:H films

In Figure 5-3(a), the refractive index of n-SiO$_x$:H films as a function of R is given. It was shown that the refractive indices decreased to less than 2.0 with increasing R of more than 4.2. As previously mentioned, the reduction of refractive index is probably due to an increase of oxygen concentration in the films, which also leads to lower optical band gap. It was proved by the results in Figure 5-3(b) which the optical band gap of n-SiO$_x$:H films was illustrated. From Figure 5-3(b) we can see that the optical band gap (E_{04}) decreased as R increased. From this result, it can be expected that the less optical absorption losses in an n- layer could be obtained.

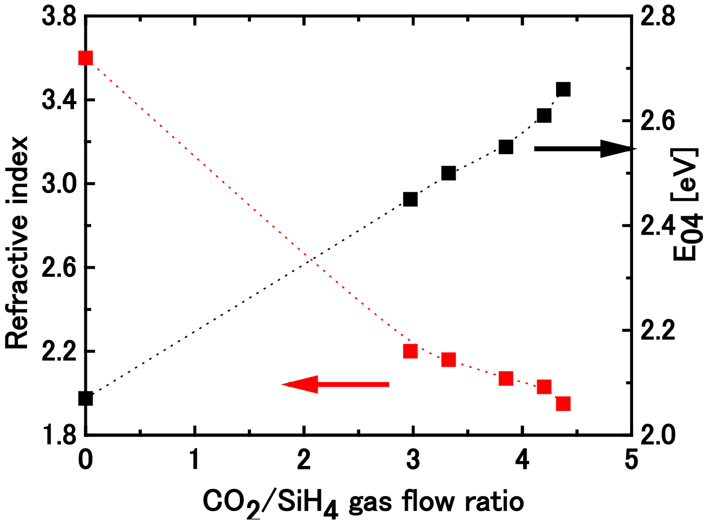

Figure 5-3 (a) Refractive index and (b) optical band gap (E_{04}) of n-SiO$_x$:H films as a function of CO_2/SiH_4 gas ratio

5.3 Fabrication of a-Si:H/µc-Si:H double junction solar cells with the n-µc-SiO$_x$:H films used as an intermediate layer (IL) inserted between a-Si:H top/µc-Si:H bottom solar cells

5.3.1 Fabricated details

Here, the a-Si:H/µc-Si:H double-junction solar cells with intermediate layer (IL) were fabricated on textured Boron-doped zinc oxide (ZnO:B) by using RF and VHF-PECVD techniques. For top cells, the boron-doped and phosphorus-doped layers were deposited using RF-PECVD technique. The p-a-SiC:H layers were deposited from a mixture of SiH_4, H_2, B_2H_6 and MMS as source gases at substrate temperature (T_{sub}) of 200 ºC under deposition pressure (Pr) of 70 Pa. The n-μc-Si:H layers were deposited from a mixture of SiH_4, H_2, and PH_3 as source gas at substrate temperature (T_{sub}) of 200 ºC under deposition pressure (Pr) of 200 Pa. The intrinsic layers were also deposited from a mixture of SiH_4 and H_2 gases at substrate temperature (T_{sub}) of 200 ºC under deposition pressure (Pr) of 50 Pa by using 60 MHz VHF-PECVD technique. By using the same deposition technique, for bottom cells, the p-μc-SiO:H layers were deposited from a mixture of SiH_4, H_2, B_2H_6 and CO_2 gases at substrate temperature (T_{sub}) of 200 ºC under deposition pressure (Pr) of 200 Pa. The i-μc-Si:H layers were deposited from a mixture of SiH_4, H_2 gases at substrate temperature (T_{sub}) of 200 ºC under deposition pressure (Pr) of 399 Pa. The n-μc-Si:H layers were deposited from a mixture of SiH_4, H_2, and PH_3 gases at substrate temperature (T_{sub}) of 200 ºC under deposition pressure (Pr) of 200 Pa. In this study, n-SiO_x:H ILs were deposited using RF-PECVD technique from a mixture of SiH_4, H_2, and PH_3 gases under different conditions while deposition conditions of top and bottom cells were kept constant. The deposition conditions of top and bottom cells are summarized in Table 5-1 and Table 5-2.

Table 5-1 Deposition condition of a-Si:H top cell

	SiH_4 (sccm)	H_2 (sccm)	B_2H_6/PH_3 (sccm)	MMS (sccm)	Pressure (Pa)	Power (W)	Tsub (ºC)	Electrode gap (cm)
p-layer	10	130	8.0	5.4	70	2	200	3
buffer	10	130	-	5.4	70	2	200	3
i-layer	8.4	10	-	-	50	1	200	2
n-layer	3.3	200	2.0	-	200	15	200	1.5

Table 5-2 Deposition condition of μc-Si:H bottom cell

	SiH_4 (sccm)	H_2 (sccm)	B_2H_6/PH_3 (sccm)	CO_2 (sccm)	Pressure (Pa)	Power (W)	Tsub (ºC)	Electrode gap (cm)
p-layer	3.3	240	0.3	0.55	200	10	200	1.5
i-layer	4.0	40	-	-	399	59	200	1.0
n-layer	3.3	200	3.0	-	200	10	200	1.5

5.3.2 Effect of intermediate layer

Firstly, effect of SiO_x IL on the performance of a-Si:H/μc-Si:H double-junction solar cells was investigated as shown in figure 5-4. A double-junction solar cell with 50 nm thick intermediate layer inserted at interface of sub-cells was fabricated. For comparison, a double-junction solar cell without any intermediate layers was also prepared. In this experimental study, SiO_x ILs were all deposited using RF-PECVD technique. The substrate temperature, plasma power, and electrode gap were set to be 200 ºC, 10 W, and 1.5 cm respectively. A mixture of SiH_4, H_2, PH_3 and CO_2 gases was introduced into the chamber of 200 Pa pressure. SiH_4, H_2, PH_3, and CO_2 flow rate gases were 3.3, 300, 10, and 9.5 sccm respectively. Here, the refractive index and in-plane dark conductivity of the SiO_x intermediate layer employed in this solar cell were ~2.1 and $2x10^{-6}$ S/cm, respectively. Here, it should be note that the condition of top and bottom cells fabricated in this experiment is not the same as that mentioned above in Table 5-1 and 5-2.

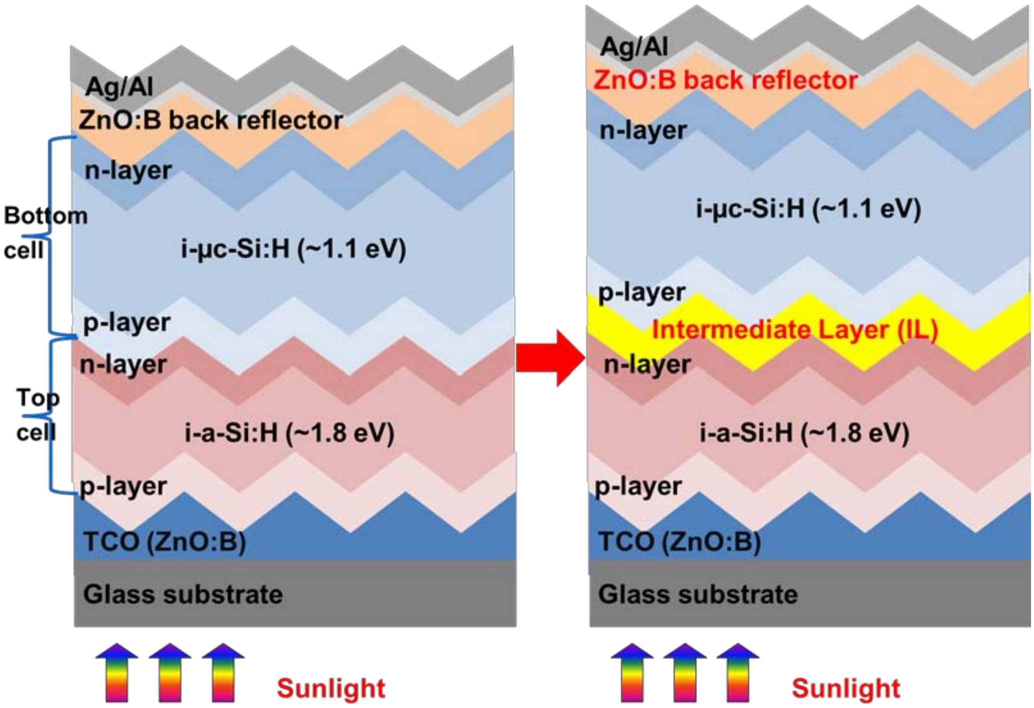

Figure 5-4 Schematic of the a-Si:H/μc-Si:H double-junction solar cells with IL compared to the conventional one without IL

Figure 5-5 shows the initial photo *J-V* characteristics for the fabricated a-Si:H/μc-Si:H solar cell with and without SiO_x IL. As can be seen from figure 5-5, by introducing this SiO_x IL, the open-circuit voltage (V_{oc}) improved from 1.32 to 1.35 V, the short-current density (J_{sc}) increased 9.47 to 10.72 mA/cm^2, and the fill factor (FF) was also enhanced from 0.68 to 0.70. These results indicate that SiO_x intermediate layer plays an important role to improve the tunnel junction of the double-junction solar cells and current-matching of component cells.

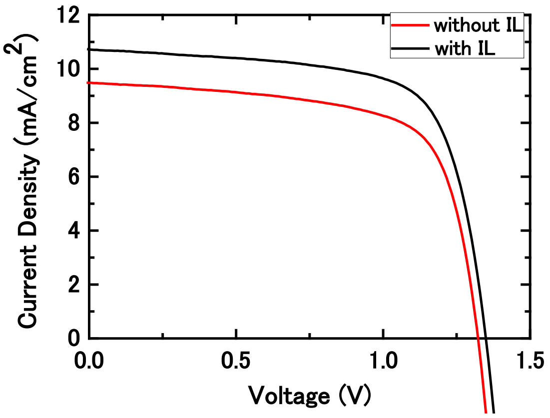

	Voc (V)	*Jsc* (mA/cm^2)	*FF*	*Eff*
Without IL	1.32	9.48	0.68	8.6
With IL	1.35	10.72	0.70	10.1

Figure 5-5 Initial photo *J-V* characteristics for the fabricated a-Si:H/μc-Si:H solar cell with and without SiO_x intermediate layer

Figure 5-6 displays spectral response of a-Si:H/μc-Si:H solar cells with and without SiO_x IL. From figure 5-6, it can be seen that the current density of the top cell increased from 9.48 to10.72 mA/cm^2 by inserting this SiO_x IL. However, it was also found that the current density of the bottom cell with SiO_x IL decreased from 11.66 to11.24 mA/cm^2. A drop in current density of the bottom cell is probably because of decrease in light at a long wavelength region transmitted into the bottom cells when the SiO_x intermediate layer was employed. In this case, the top cells with and without intermediate layer limited the current density of the device. Thus, further optimization of intermediate layer is urgently needed to increase reflection at a short wavelength region and improve solar cell efficiency.

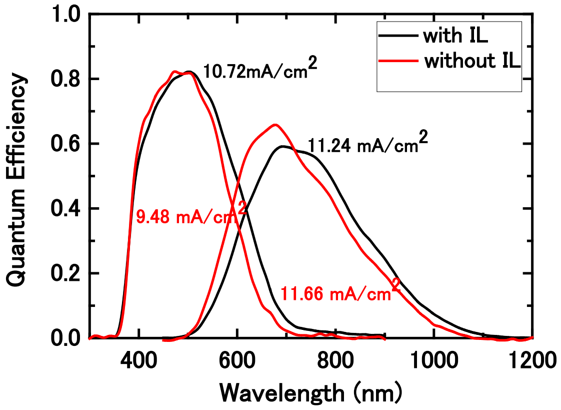

Figure 5-6 Spectral response of a-Si:H/μc-Si:H solar cell with and without SiO_x intermediate layer

5.3.3 Effect of CO_2 addition in intermediate layer

According to the result in the previous section, further optimization of intermediate layer with better optical properties, i.e., low reflective index, is necessary to improve the current density of top cells. As previously described in Chapter 4, Oxygen content is a key factor affecting refractive index of SiO_x films leading to improved internal reflection. In this experiment, effect of CO_2 flow rate for SiO_x IL deposition process on the performance of a-Si:H/μc-Si:H solar cells was therefore investigated. Here, ~50-nm-thick phosphorus-doped SiO_x intermediate layers with various CO_2 flow rate were deposited at top/bottom cell interface by RF-PECVD technique under the deposition pressure of 200 Pa. A mixture of SiH_4, H_2, PH_3, and CO_2 gases was used as a source gas. The CO_2 flow rate was varied from 8 to 12.5 sccm, while SiH_4, H_2, and PH_3 were maintained constant at 3.30, 300, and 10 sccm, respectively. The substrate temperature, the plasma power, and electrode gap were respectively fixed at 200 ºC, 10 W and 2.0 cm. The deposition conditions of the top and bottom cells were kept the same for all fabricated solar cells. In this case, the refractive index of SiO_x IL with CO_2 flow rate of 8.5, 9.5, 11, and 12.5 sccm was respectively 2.18, 2.15, 2.08 and 1.95, while the conductivity was $9.9x10^{-6}$, $2.9x10^{-6}$, $7.3x10^{-7}$ and $7.0x10^{-8}$ S/cm, respectively. Here, it should be noticed that the condition of top and bottom cells fabricated in this experimental series is the same as that mentioned above in Table 5-1 and 5-2.

Figure 5-7 demonstrates the photovoltaic parameters of the fabricated a-Si:H/µc-Si:H solar cells as a function of CO_2 flow rate for SiO_x IL deposition. From this figure, we can see that open-circuit voltage (V_{oc}) and fill factor (FF) slightly dropped when CO_2 flow rate was changed from 8.5 to 9.5 sccm and then it tended to saturate with increasing CO_2 flow rate from 9.5 sccm. A drop in V_{oc} and FF is mainly from effect of CO_2 flow rate increased which led to decline in electrical property of SiO_x IL, also probably due to deterioration in n-top/IL or IL/p-bottom interfaces. On the other hand, short-circuit current density (J_{sc}) and performance of solar cells increased with an increase of CO_2 flow rate up to 11 sccm and then it dropped when CO_2 flow rate was 12.5 sccm or more. A drop of J_{sc} and efficiency (*Eff*) is possibly that relatively high oxygen content resulted in lower refractive index, which led to increase of the light reflection into the top cells for the long wavelength region, and thus deteriorated current-matching of solar cells. This is also in a good agreement with the spectrum response shown in figure 5-7. Here, it can be notice that the best solar cell performance (*Voc*=1.34, *Jsc*= 10.90 mA/cm^2, *FF*=0.69, *Eff*=9.9%) could be obtained at CO_2 flow rate of 11 sccm.

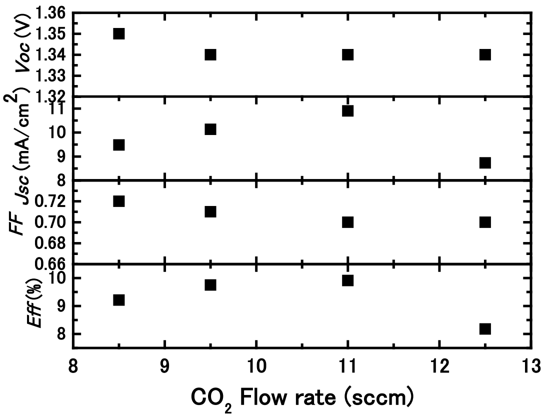

Figure 5-7 Photovoltaic parameters of the fabricated a-Si:H/µc-Si:H solar cells as a function of CO_2 flow rate for SiO_x intermediate layer deposition

Figure 5-8 illustrates spectral response of a-Si:H/µc-Si:H solar cells as a function of CO_2 flow rate for SiO_x IL deposition. It was found that the total current density of solar cells increased up to10.90 mA/cm^2 at CO_2 flow rate of 11 sccm and then it dropped. A decrease in total current density of solar cell for CO_2 flow rate of 12.5 sccm is probably because of more internal reflection in a long wavelength region into the top cell which caused the reduction of current density of the bottom cell. In this experimental regime, the bottom current limits the current of completed devices for all of fabricated solar cells. However, the best current matching between sub-cells achieved from the solar cell with CO_2 flow rate of 11 sccm.

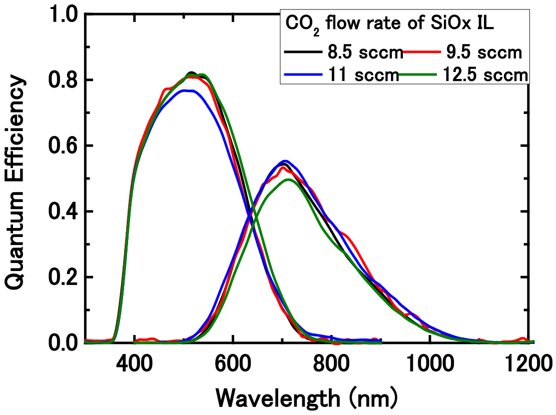

(a)

CO_2 flow rate of SiOx IL (sccm)	*Jsc* total (mA/cm^2) (*I-V*)	*Jsc* top (mA/cm^2) *QE*	*Jsc* bottom (mA/cm^2) *QE*
8.5	9.48	11.43	8.68
9.5	10.62	11.47	9.13
11	10.90	11.06	9.29
12.5	8.73	11.98	7.94

(b)

Figure 5-8 Spectral response of a-Si:H/μc-Si:H solar cells as a function of CO_2 flow rate for SiO_x intermediate layer deposition

5.3.4 Effect of thickness of intermediate layer

To further investigate the current-matching condition of the a-Si:H/μc-Si:H solar cell, the effect of thickness of intermediate layers was examined. The thickness of SiO_x IL was changed from 30 to 60 nm. SiH_4, H_2, PH_3, and CO_2 were kept constant at

3.3, 300, 10, and 11 sccm, respectively. The substrate temperature, the plasma power, deposition pressure and electrode gap were respectively set to be 200 °C, 10 W, 200 Pa and 2.0 cm. The deposition conditions of the top and bottom cells were fixed the same with as mentioned in Table 5-1 and Table 5-2 for all of fabricated solar cells.

Figure 5-9 shows photovoltaic parameters of the fabricated a-Si:H/µc-Si:H solar cells as a function of SiO_x intermediate layer thickness. From figure 5-9, one can see that J_{sc} and V_{oc} increased up to 11.19 mA/cm^2 and 1.35 V respectively, when the IL was changed from 30 to 50 nm and they dropped at as intermediate layer thickness was 60 nm. A decrease in J_{sc} is probably because too thick intermediate layer affects growth of microcrystalline silicon bottom cell leading to decreased current and thus declined current-matching condition. This reason is consistent with the spectral response given in figure 5-10. On the other hand, the *FF* declined as the intermediate layer thickness increased from 30 to 50 nm, and then it improved for the IL thickness of 60 nm. As a result, the high efficiency of around 10.3% was obtained when the IL were 40 and 50 nm. These results revealed that the optimum thickness of IL should be 40-50 nm.

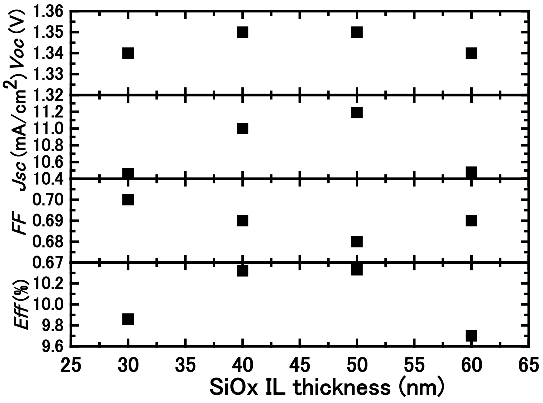

Figure 5-9 Photovoltaic parameters of the fabricated a-Si:H/µc-Si:H solar cells as a function of SiO_x intermediate layer thickness

Figure 5-10 presents the spectral response of a-Si:H/μc-Si:H solar cells as a function of SiO_x IL thickness. From figure 5-10, it was found that J_{sc} of the bottom cells decreased as SiO_x IL thickness increased. As mentioned above, it is seemingly because of a decline in growth of microcrystalline silicon bottom cells. Moreover, the total J_{sc} more than 11 mA/cm^2 achieved when the intermediate layers were 50 and 60 nm. This result suggested that the intermediate layers with higher than 50 nm may improve the internal reflection in a short wavelength region leading to increase of the top current density. However, the current density of all the fabricated solar cells was limited by the bottom current. Therefore, further investigation into properties of layers related to bottom cells, i.e., n-top cell and intermediate layer is urgently needed in order to improve bottom cell current.

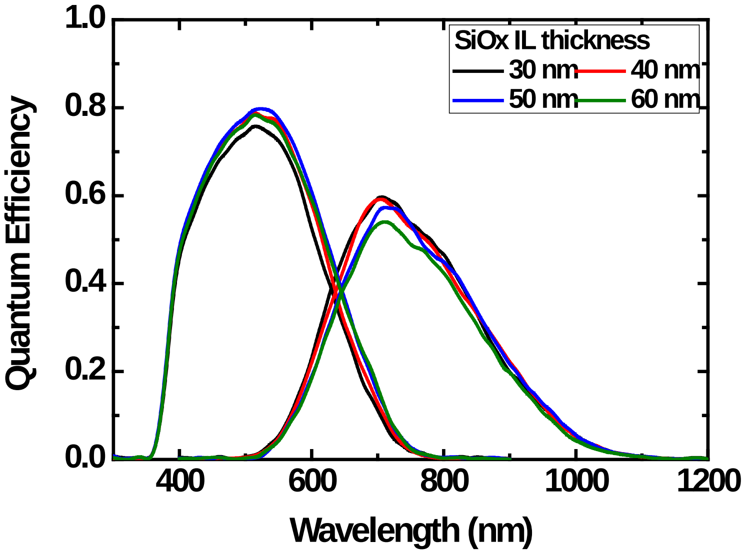

Figure 5-10 Spectral response of a-Si:H/μc-Si:H solar cells as a function of SiOx intermediate layer thickness

5.4 Fabrication of μc-Si:H single junction solar cells with the n-μc-SiO$_x$:H films used as a nBRL

5.4.1 Fabrication details

The μc-Si:H single-junction solar cells with novel structure of p-μc-SiO:H/ i-μc-Si:H/ n-SiO$_x$:H/ Ag/ Al were fabricated on textured ZnO:B coated glass substrates. The fabricated solar cell structure is shown in figure 5-11. The intrinsic layer was prepared using a 60 MHz VHF-PECVD technique while the boron-doped p-layer and the phosphorous-doped n-layer were both deposited using B_2H_6 and PH_3 as source gases, respectively, by 13.56 MHz RF-PECVD technique. Here, the thicknesses of p-layer and i-layer were kept at 35 nm and 1200 nm, respectively. Different n-SiO$_x$:H layers with various R (CO_2/SiH_4) and the appropriate thickness was employed into a μc-Si:H p-i-n solar cell in order to investigate effect of n-SiO$_x$:H layers ,acting as both a n-layer and a ZnO layer at back reflector, on solar cell performance. Ag and Al back electrodes were evaporated using a thermal evaporation technique to divide a prepared sample into cells with area of 0.086 cm^2. In order to evaluate the performance of prepared μc-Si:H single-junction solar cells, photo current density-voltage (*J*-*V*) characteristics of these cells were measured at 25ºC under 1-sun (Air Mass 1.5, 100 mW/cm^2) solar simulator radiation. The quantum efficiency (*QE*) measurement was performed to examine the spectral response of the fabricated solar cells. Furthermore, the μc-Si:H solar cells with standard n-μc-Si:H adopting a ZnO/Ag as a back reflector were also fabricated to compare with newly developed structure.

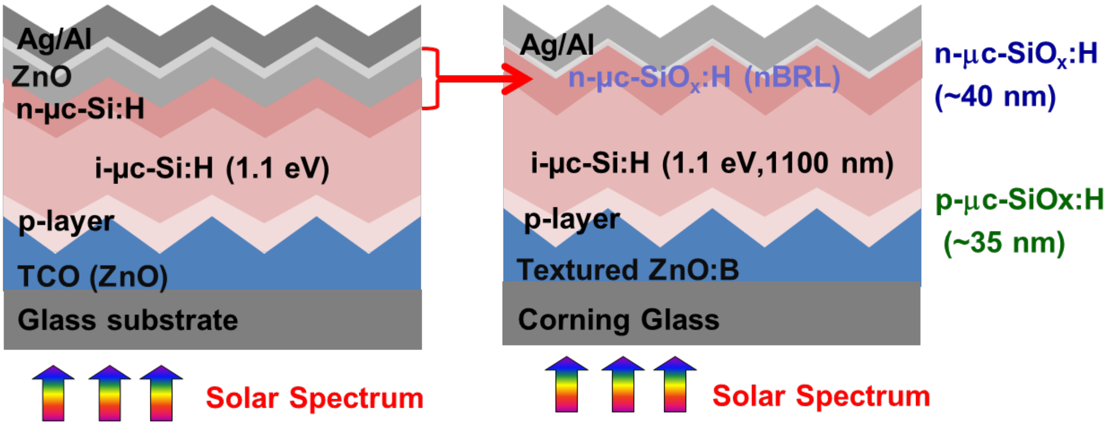

Figure 5-11 Schematic of the novel μc-Si:H solar cell structure compared with the conventional one

5.4.2 Effect of nBRL with various CO_2 flow rate on μc-Si:H solar cell performance

The n-SiO_x:H layers with various R were introduced into a p-i-n μc-Si:H solar cell functioning as both a n-layer and a ZnO layer at back reflector. The performance of fabricated cells was evaluated by photo J-V characteristics and QE measurement. Figure 5-12 describes the photovoltaic parameters of fabricated solar cells measured from solar simulator under standard condition illumination. As can be clearly seen from figure 5-12, the current density (J_{sc}) first significantly increased up to 22.6 mA/cm^2 with increasing R up to 3.3 and then dropped when R was 3.9. An increase in J_{sc} is mainly because of (1) larger refractive index difference between intrinsic layer and n-SiO_x:H layer that results in better reflection of light at i/n interface and longer optical light path inside the absorber layer and/or (2) reduction in the free-carrier absorption loss which is higher in case of ZnO back reflector [15]. In the same way, fill factor slightly improved as R increased and then strongly declined at R of 3.9. The strong deterioration in fill factor when R was 3.9 is due to increased series resistance in the device. The quite same open circuit voltage (V_{oc}) was observed even if R was increased. As a result, the cell efficiency of as high as 8.1 % (V_{oc}=0.51V, J_{sc}= 22.6 mA/cm^2, FF=0.70) was obtained by employing newly developed n-SiO$_x$:H layer with R=3.3.

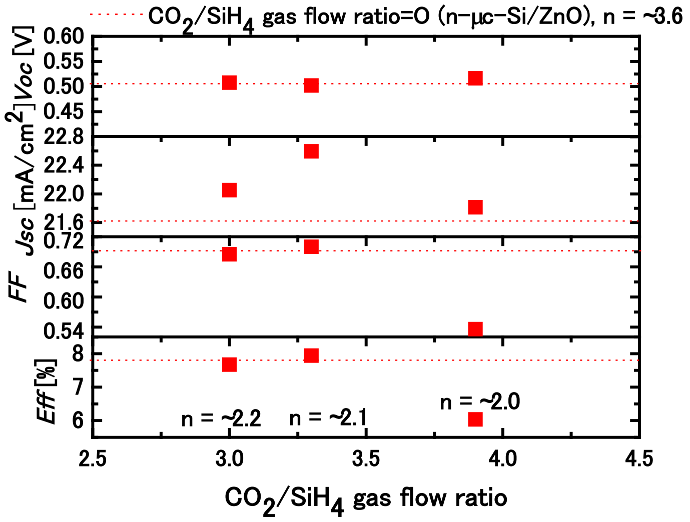

Figure 5-12 Photovoltaic parameters of μc-Si:H single-junction solar cells as a function of n-SiO$_x$:H layers with various CO$_2$/SiH$_4$ gas flow ratio.

Figure 5-13 illustrates quantum efficiency of μc-Si:H single solar cells with two kinds of n-SiO$_x$:H layers compared to one with conventional n-μc-Si:H/ZnO layer. It can clearly be seen that using the n-type SiO$_x$:H layer instead of n-μc-Si:H/ZnO back reflector the spectrum response especially, in the long wavelength region of 600-1000 nm was enhanced. This result leads to relative increase in J_{sc} by 4.8%. The increase in J_{sc} is likely a consequence of improved entire internal light-trapping. On the contrary, the drop of J_{sc} at R=3.9 probably results from increased defect in n-layer which leads to enhanced recombination loss. However, it should be noted that J_{sc} shown here are the values determined from *QE* measurement.

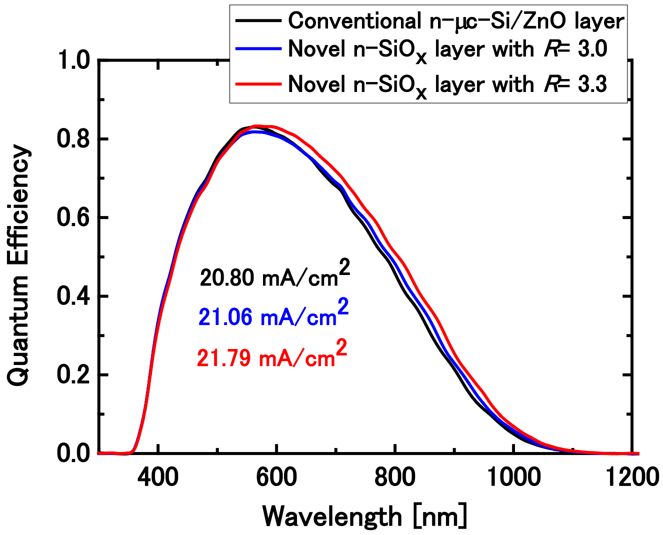

Figure 5-13 Quantum efficiency of μc-Si:H single-junction solar cells with two kinds of n-SiO$_x$:H layers compared to the one with conventional n-μc-Si:H/ZnO layer

5.4.3 Effect of nBRL thickness on μc-Si:H solar cell performance

Additionally, the effect of n-SiO$_x$:H layers with various thicknesses on the performance of optimized μc-Si:H solar cells was also investigated. The photovoltaic parameters of the solar cells, when the thickness of optimized n-SiO$_x$:H layers was varied between 40-70 nm, was shown in figure 5-14 . As can be seen from the result, almost same J_{sc} was obtained as the thickness increased up to 55 nm and slightly deteriorated for thickness of 70 nm. Also, the result from the quantum efficiency, as shown in figure 5-15, revealed that the solar cell with nBRL thickness of 40 nm has the best J_{sc}. Therefore, the better J_{sc} of the μc-Si:H cell with the n-SiO$_x$:H layer thickness of 40 nm could be obtained due to the improved whole quality of the solar cell under the further optimized deposition condition.

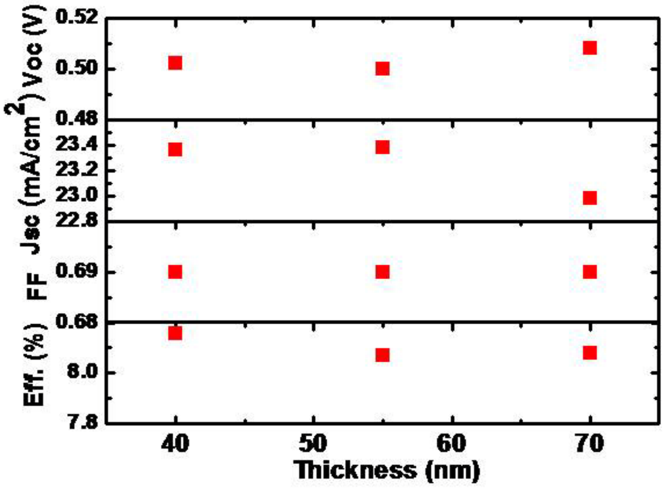

Figure 5-14 Photovoltaic parameters of μc-Si:H solar cells as function of n-SiO_x:H layers with different thickness

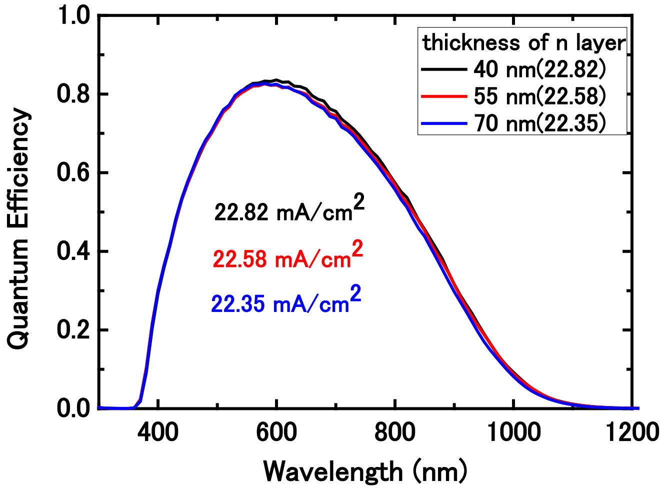

Figure 5-15 Quantum efficiency of μc-Si:H solar cells as function of n-SiO_x:H layers with different thickness

5.5 Fabrication of a-Si:H/μc-Si:H double junction solar cells with the n-μc-SiO$_x$:H films used as a nIL and a nBRL

5.5.1 Fabrication details

The novel a-Si:H/μc-Si:H double-junction solar cells with novel structure of p-a-SiC:H/i-a-Si:H/n-SiO$_x$:H/p-μc-SiO:H/i-μc-Si:H/n-SiO$_x$:H/Ag/Al, shown in figure 5-16, were fabricated on textured ZnO:B coated glasses. The intrinsic layers for both sub-cells (i-a-Si:H and i-μc-Si:H) were deposited by using a 60 MHz VHF-PECVD technique. The i-layer thicknesses of a-Si:H top cell and μc-Si:H bottom cell were kept at 260 nm and 2000 nm, respectively. The boron-doped layers of the top cell (p-a-SiC:H) was deposited using 13.56 MHZ RF-PECVD technique while the deposition of p-bottom cell (p-μc-SiO:H) used 60 MHz VHF-PECVD technique. The n-layers of both top and bottom cell were deposited using RF-PECVD technique. Different n-SiO$_x$:H layers with various *R* were inserted between i-layer of top cell and p-layer of bottom cell, and also, between i-layer of bottom cell and metal back reflector layer. The thickness of both n-SiO$_x$:H layers was approximately 40 nm. The photo *J*-*V* characteristics and the quantum efficiency of this cell were measured under AM 1.5, 100 mW/cm^2 standard condition to evaluate the fabricated cell performance.

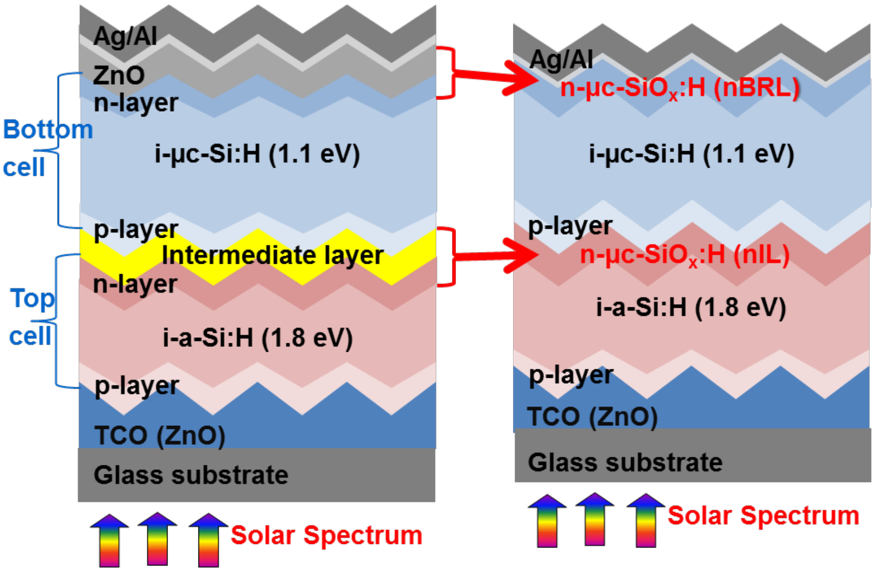

Figure 5-16 Schematic of the novel μc-Si:H solar cell structure compared to the conventional one.

5.5.2 Effect of nIL and nBRL on a-Si:H/μc-Si:H solar cell performance

The a-Si:H/μc-Si:H double-junction solar cell with a novel structure was successfully fabricated. The optimal n-SiO_x:H layer with excellent optical and electrical properties was incorporated into the novel solar cell structure as two dual-functional layers. A a-Si:H/μc-Si:H with conventional structure was also prepared to use for comparison purpose. Figure 5-17 shows *J*-*V* characteristics of the fabricated a-Si:H/μc-Si:H solar cell with newly developed n-SiO_x:H layer compared to the conventional one with n-μc-Si/ZnO layer. From the results, one can see that by employing the novel structure with the proper dual-functional n-SiO_x:H layer the improved J_{sc} and V_{oc} were observed. Especially, the total J_{sc} was enhanced by 1 mA/cm^2. We can consider that the increase of J_{sc} is mostly due to the reduction of parasitic absorption loss in both n-layer of sub-cells and ZnO back reflective layer. Correspondingly, a significant improvement of J_{sc} by ~1 mA/cm^2 in the bottom cell mainly results from reduction in reflection of long wavelength light by n-SiO_x:H layer inserted into the component cells interface and carrier absorption loss in ZnO back reflective layer while in top cell due to lower absorption loss in n-layer.

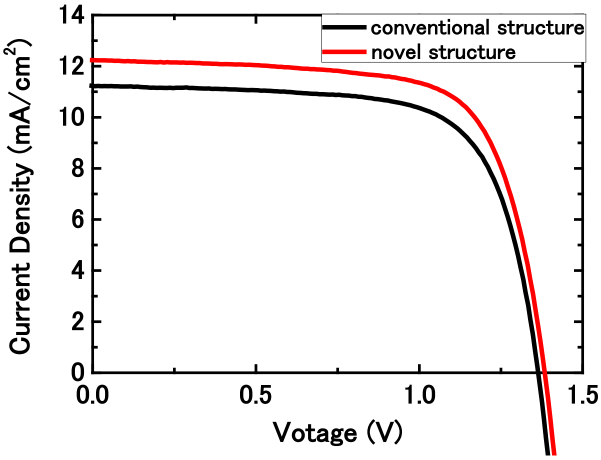

(a)

	V_{oc} (V)	J_{sc} (mA/cm^2)	*FF*	*Eff*
Conventional	1.36	11.23	0.70	10.70
Novel	1.38	12.24	0.70	11.92

(b)

Figure 5-17 *J-V* characteristics of the a-Si:H/µc-Si:H solar cell with novel and conventional structure

Figure 5-18 shows the quantum efficiency curves of the novel a-Si:H/µc-Si:H solar cells compared with the conventional one. From this figure, one can see that the gain in J_{sc} of both top and bottom cells was observed. The J_{sc} of the top cell and the bottom cell was increased by ~0.4 mA/cm^2 and ~1 mA/cm^2, respectively. It is important to be noted that the PV characteristics shown here are the value of the novel tandem solar cell we have already applied the p-µc-SiO_x:H film into a p-bottom layer instead of the conventional p-μc-SiO:H layer.

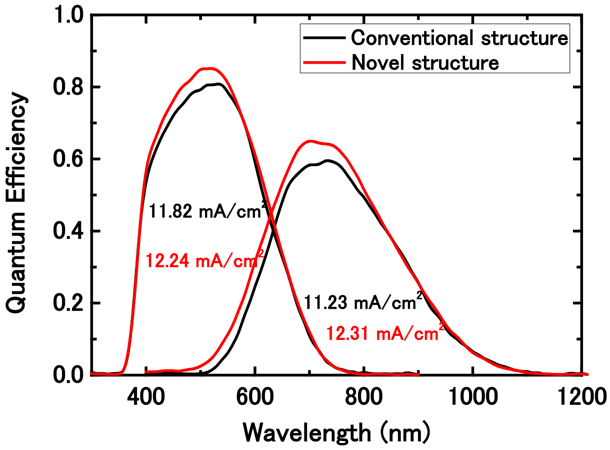

Figure 5-18 Quantum efficiency curves of the a-Si:H/ μc-Si:H solar cell with novel and conventional structure

5.6 Effect of plasma treatment on the performance of a-Si:H/μc-Si:H double junction solar cells

5.6.1 Introduction

We have successfully fabricated the novel hydrogenated amorphous silicon / hydrogenated microcrystalline silicon doube-junction solar cells (a-Si:H/ μc-Si:H) using n-type hydrogenated microcrystalline silicon oxide films (μc-SiO$_x$:H) as a multi-functional layer, for the first time, in order to decrease parasitic absorption losses from doped layers and a ZnO back reflective layer [16]. Also, because it was shown that the open circuit voltage (V_{oc}) can be improved by applying the wider band gap p-type μc-SiO$_x$:H film to the p-i-n μc-Si:H solar cell as a p-layer [17], we replaced the conventional p-μc-Si:H layer with this kind of p-μc-SiO$_x$:H layer for the bottom cell of a-Si:H/μc-Si:H solar cells. However, it was found that by using the p-μc-SiO_x:H films the V_{oc} and *FF* of the fabricated tandem cells were lower due to poorer cell interface property. In this work, to overcome this problem, the CO_2 plasma treatment was introduced before the deposition of a bottom p-μc-SiO_x:H layer. The effects of CO_2 plasma treatment, which perform before p-μc-SiO_x:H deposition, on the n-μc-SiO_x:H / p-μc-SiO_x:H interface of the test samples was investigated. Also, the a-Si:H/μc-Si:H double-junction solar cells with the novel structure of p-a-SiO_x:H/ i-a-Si:H/ n-μc-SiO_x:H / CO_2 plasma / p-μc-SiO_x:H/ i-μc-Si:H / n-μc-SiO_x:H/ Ag/ Al using CO_2 plasma treatment condition, which was optimized so far, were fabricated on the textured ZnO:B coated Soda-lime glasses to compare with the one without CO_2 plasma treatment. The effects of CO_2 plasma treatment, which perform between n-μc-SiO_x:H top-layer and p-μc-SiO_x:H bottom-layer interface, on solar cell performance was investigated. Moreover, advantages of the CO_2 plasma treatment were also discussed.

5.6.2 Optimization of CO_2 plasma condition

The test samples with the structure of glass/n-μc-SiO_x:H/CO_2 plasma treatment/ p-μc-SiO_x:H as shown in figure 5-19 were deposited in order to investigate the effect of CO_2 gas plasma treatment on the properties of p-μc-SiO_x:H films. The p- and n-layers were deposited using plasma enhanced chemical vapor deposition with an excitation frequency of 13.56 MHz at substrate temperature of 200 ºC. The gases used for their depositions were SiH_4, H_2, CO_2, as well as B_2H_6 and PH_3 as dopants, respectively. Their film thicknesses of each sample deposited on Corning Glass were measured by spectroscopic ellipsometry and estimated as 25 nm and 40 nm, respectively. The lateral conductivity of test samples was measured by coplanar electrodes. Also, the crystalline volume fraction (X_c) of test samples was determined from the Raman spectrum measurement. The Raman spectrum measurement was performed using a Semiconductor laser with a wavelength of 532 nm in order to characterize the structural properties of the films. The topography and local conductivity of the sample structure as shown in figure 5-19(b) were then measured by conductive atomic force microscopy (C-AFM) using Shimadzu WET-SPM Environment Controlled Scanning Probe Microscope. All AFM measurement results as shown here were performed in contact mode using the Cr/Pr coated cantilevers. The sample without CO_2 plasma treatment was also fabricated to compare the one using CO_2 plasma treatment. The duration of CO_2 plasma treatment was changed by keeping other condition parameters constant in order to find the optimized plasma treatment time.

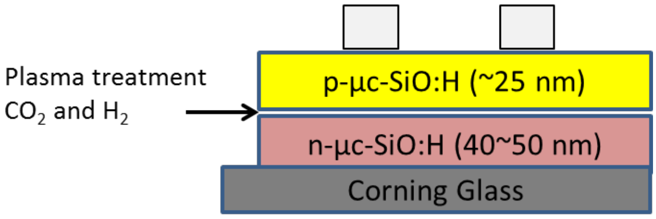

(a)

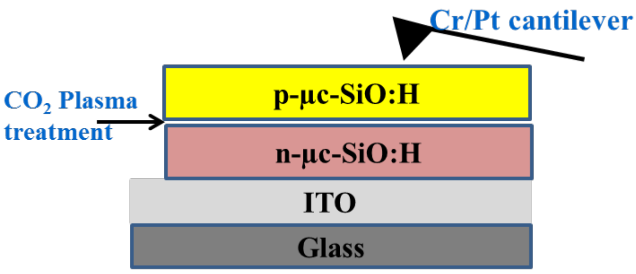

(b)

Figure 5-19 cross-sectional views of test sample structures

The lateral conductivity and crystalline volume fraction (*Xc*) of 25 nm thick B_2H_6-doped p-μc-SiO_x:H layer ,deposited on an n-μc-SiO_x:H layer of 40 nm, as a function of CO_2 plasma treatment time are shown in figure 5-20. The other parameters of CO_2 plasma treatment were kept constant at power of 10 W, pressure of 10 Pa and CO_2 flow rate of 10 sccm. From the results, it was found that the conductivities of p-layer firstly increased up to around 8 x 10^{-3} S/cm and then decreased down to around 2 x 10^{-4}, which tended to saturate even through the prolonged treatment was applied. On the other hand, the crystalline volume fraction of films improved when the CO_2 plasma treatment was performed between 10~40 sec. It seems that the CO_2 plasma treatment can be expected to promote the crystallization of p-μc-SiO_x:H as found in p-μc-Si:H case as well [18-19]. Also, the improved properties of n-μc-SiO_x:H/ p-μc-SiO_x:H interface can be expected. Apart from that, the CO_2 plasma treatment of 20 sec optimized so far was chosen to use for solar cell application.

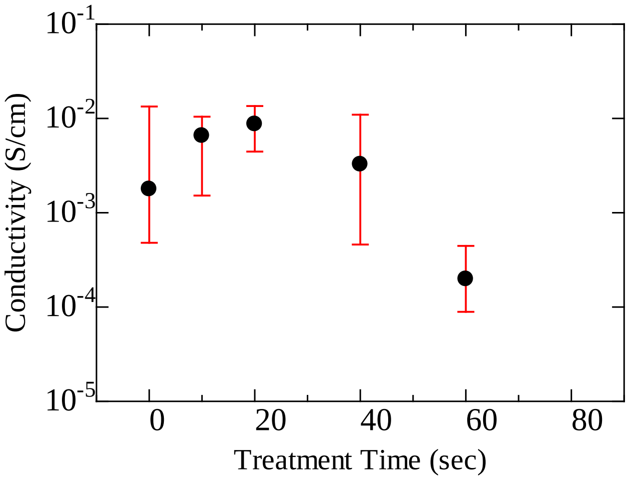

(a)

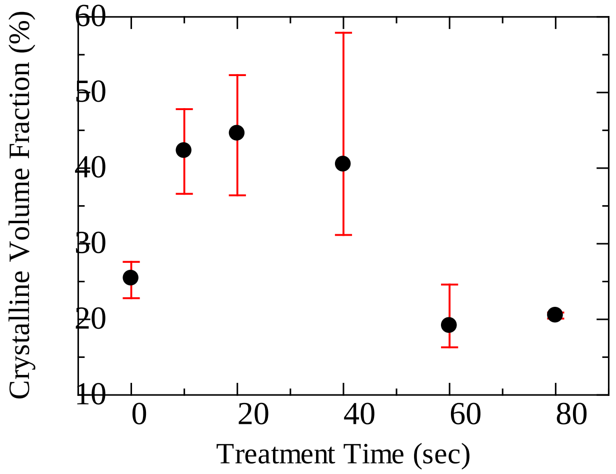

(b)

Figure 5-20 (a) the lateral conductivity and (b) crystalline volume fraction of test samples with various CO_2 treatment time

The topography picture and local current image of the test sample with CO_2 plasma treatment (b) compared to the one without plasma treatment (a) were shown in the figure 5-21. From this , it was shown that the topography picture of the sample with and without CO_2 plasma treatment are in the quite same condition while the current mapping of the sample with CO_2 plasma treatment shows higher current over the probed area of the sample. This is one of evidences which indicate that the electrical property of the sample after CO_2 plasma treatment is improved.

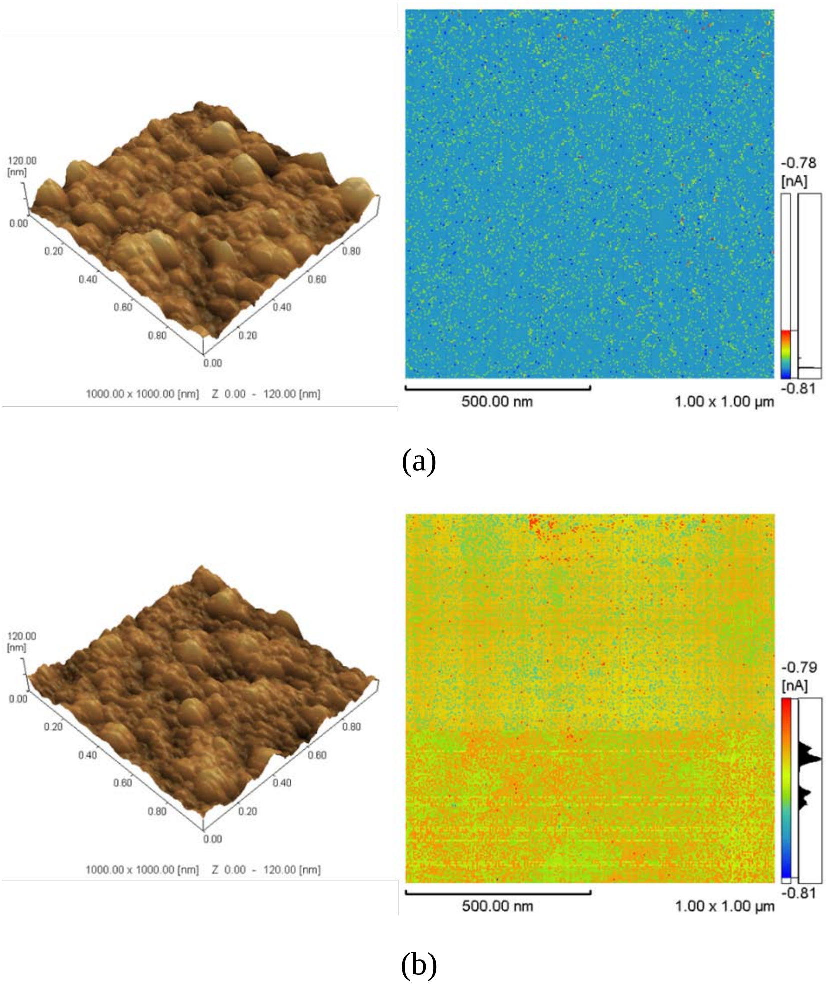

Figure 5-21 (a) Topography picture and local current image of the test sample without CO_2 plasma treatment. (b) Topography picture and local current image of the test sample with CO_2 plasma treatment

5.6.3 Effect of CO_2 condition on µc-Si:H single junction solar cells

The p-i-n-type µc-Si:H single-junction solar cells were fabricated on soda-lime glass/ZnO:B substrates. Here, the structure of the fabricated solar cells here was soda-lime glass/ textured-ZnO:B/ CO_2 plasma /p-µc-SiO_x:H/ i-µc-Si:H/ n-SiO_x:H/ Ag/ Al. The intrinsic layer was prepared using a 60 MHz very high frequency plasma enhanced chemical vapor deposition (VHF-PECVD) technique while the microcrystalline boron-doped p-layer and phosphorous-doped n-layer were both fabricated by 13.56 MHz RF-PECVD technique. The thickness of i-layer was 1.2 µm. The CO_2 plasma with treatment time of 20 sec was applied before p-i-n film deposition. The µc-Si:H solar cell without plasma treatment was also fabricated to compare with the one using CO_2 plasma treatment. The photo *J-V* characteristics of fabricated cells were measured under standard condition (AM 1.5, 100 mW/cm^2). The spectrum response of these cells was analyzed using external quantum efficiency (*QE*) measurement.

Figure 5-22 shows the *J-V* characteristic and quantum efficiency of µc-Si:H cells with and without CO_2 plasma treatment before p-layer deposition. By introducing CO_2 plasma treatment time of 20 sec in the µc-Si:H solar cells before p-i-n layer deposition, it was found that the fill factor (*FF*) and current density (J_{sc}) were improved. This is probably because p-µc-SiO_x:H layer became more crystalline resulting in lower absorption in the p-layer and better interface property with ZnO. This result is similar to what Elias et. al has been achieved with O_2 treatment performed before p-a-SiC:H deposition [20].The initial efficiency of 7.2% could be obtained with introduction of this CO_2 plasma. However, the uderlying of this fabricated µc-Si:H solar cells was ZnO:B TCO that different from a tandem solar cell, whose underlying layer is a n-µc-SiO_x:H film.

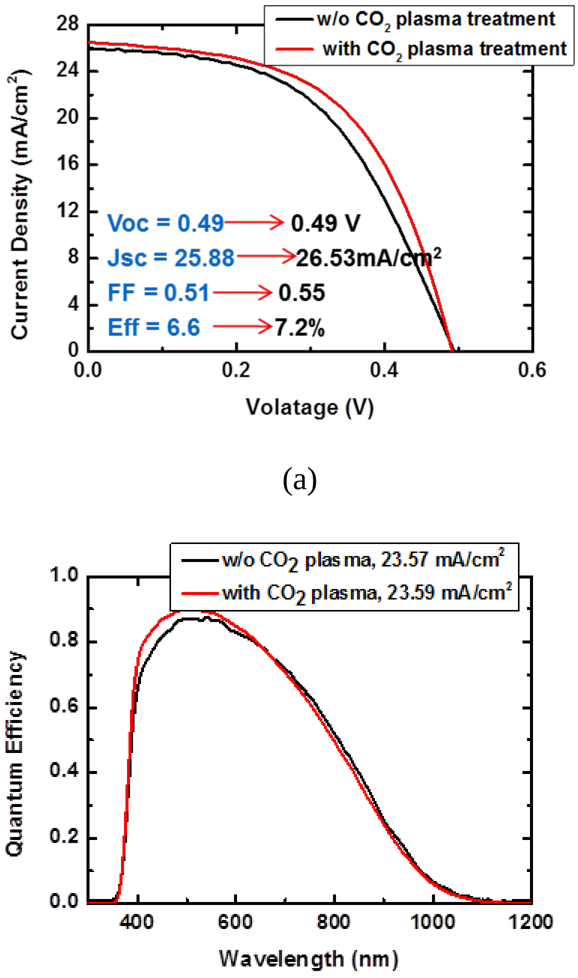

(a)

(b)

Figure 5-22 *J-V* characteristic and quantum efficiency of µc-Si:H cells with and w/o CO_2 plasma treatment

5.6.4 Effect of CO_2 condition on a-Si:H/µc-Si:H double junction solar cells

We also applied this CO_2 plasma in the novel a-Si:H/µc-Si:H double-junction solar cells. The a-Si:H/µc-Si:H double-junction solar cells with the novel structure of p-a-SiO_x:H/ i-a-Si:H/ n-µc-SiO_x:H / p-µc-SiO_x:H/ i-µc-Si:H / n-µc-SiO_x:H/ Ag/ Al were also fabricated on the textured soda-lime glasses coated with ZnO:B. The optimization of CO_2 plasma treatment with treatment time of 20 second was introduced after the deposition of top n-μc-SiO_x:H layer. The thicknesses of i-top layer and i-bottom layer were kept at ~260 and ~2000 nm, respectively. The cells were characterized by the illuminated *J-V* characteristics and the quantum efficiency of the cells was also measured under standard condition to evaluate the cell performance.

The *J-V* characteristic of a-Si:H/μc-Si:H cells with the CO_2 plasma treatment was measured to compared to the one without CO_2 plasma as shown in figure 5-23. From the result, it was found that with this CO_2 plasma treatment optimized so far, the *FF* was improved. At the same time, the quiet degradation of solar cell performance was observed. The increase in *FF* is probably due to the better cell interface property between top and bottom cell. However, the total J_{sc} of the solar cell significantly decrease, especially, the current density of the bottom cell. Here, one can consider that CO_2 plasma treatment, which we have optimized so far, can improve the interface between n-SiO_x:H top-layer/ p-μc-SiO_x:H bottom-layer but deteriorate the properties of the μc-Si:H bottom cell.

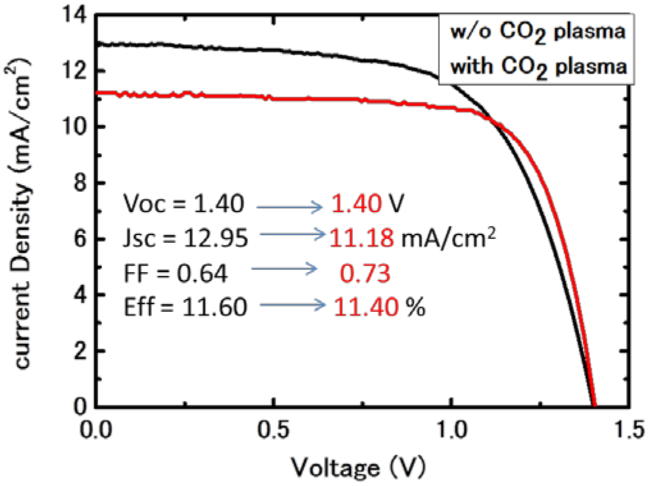

(a)

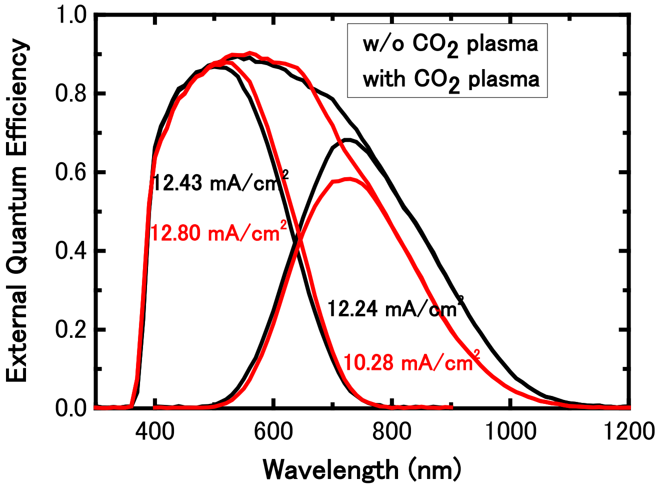

(b)

Figure 5-23 *J*-*V* characteristic and quantum efficiency of a-Si:H/μc-Si:H solar cells with and w/o CO_2 plasma treatment

5.7 Summary

In this chapter, the optimization of n-SiO_x:H films for use as intermediate layer (IL) inserted between top and bottom cells was firstly performed and their effects on a-Si:H/μc-Si:H double-junction solar cell performance were studied by adjusting their thickness and optical and electrical properties. The results revealed that the IL that we have optimized was effective to be applied into the tandem solar cells, here a-Si:H/μc-Si:H double-junction solar cells. Also, We for the first time proposed a-Si:H/ μc-Si:H double-junction solar cells with novel structure of p-a-SiC:H/ i-a-Si:H/ n-SiO_x:H/ p-μc-SiO_x:H/ i-μc-Si:H/ n-SiO_x:H/ Ag/ Al as a candidate to lower the optical losses and thus increase the solar cell performance, especially current density (J_{sc}). By using the optimum n-SiO_x:H layer instead of n-μc-Si:H/ZnO back reflector into a μc-Si:H single-junction solar cell as a nBRL, the spectral response, particularly, in the long wavelength region could be improved and then J_{sc} value was relatively increased up to 4.4%. Similarly, for the a-Si:H/µc-Si:H solar cell with novel structure using the proper dual-functional n-SiO_x:H layers as a nIL and a nBRL, the relative improvement in J_{sc} value by 9% was obtained and therefore the initial efficiency as high as 11.9% (V_{oc}=1.38 V, J_{sc}=12.24 mA/cm^2, FF=0.70) was achieved. These results approved that the first layer of newly developed n-SiO_x:H layers (nIL) can work as a n-layer of the top cell and at the same time it can also be functioned as an IL. On the other hand, the second n-SiO_x:H layer (nBRL) can work as a n-layer of the bottom cell and a ZnO back reflective layer. As a result, the reduction in optical losses could be obtained. Furthermore, these novel solar cell structures are beneficial for mass production since they were simplified.

In addition, we have also employed plasma treatment technique prior to the deposition of p-µc-SiO_x:H layer of bottom cells in order to improve interface between n-SiO_x:H top-layer/ p-µc-SiO_x:H bottom-layer. The CO_2 plasma condition was characterized and optimized. After, the optimized CO_2 plasma condition, we have done so far, was applied into a-Si:H/µc-Si:H solar cell. From the results, we can see that the optimized CO_2 plasma condition could improve FF. On the other hand, the current density deteriorated and smaller solar cell efficiency was observed. These results reveal that the CO_2 plasma technique can be one of promising methods for improvement of solar cell performance. However, CO_2 plasma condition, we have used here, has to be further studied in order to avoid the reduction of current density, especially, bottom cells.

References

[1] J. Meier, S. Dubail, R. Fluckiger, D. Fischer. H. Keppner, and A. Shah: *Proc. 1st World Conference on Photovoltaic Energy Convension*, (1994) 409.

[2] B. Yan, G. Yue. J. Yang, and S. Guha: *Proc. 33rd IEEE PVSC* (2008)001.

[3] J. Yang, B. Yan, G. Yue, and S. Guha: *Proc. 31st IEEE PVSC* (2005) 1359.

[4] K. Yamamoto, A. Nakajima, M. Yoshimi, T. Sawada, S. Fukuda, T. Suezaki, M. Ichikawa, Y. Koi, M. Goto, T. Meguro, T. Matsuda, M. Kondo, T. Sasaki, and Y. Tawada: *Tech. Digest of 15th Int'l PVSEC* (2005) 529.

[5] D.L Staebler and C.R. Wronski: *Appl. Phys. Let.* **31** (1979) 292.

[6] D. Fischer, S. Dubail, J.A. Anna Selvan, N. Pellaton Vaucher, R. PIatz, Ch. Hof, U. Kroll, J. Meier, P. Torres, H. Keppner, N. Wyrsch, M. Goetz, A. Shah, and K. D. Ufert,: *Proc. 25th IEEE International Photovoltaic Science & Engineering Conference*, (1996) 1053.

[7] D. Domine, J. Bailat, J. Steinhauser, A. Shah, C. Ballif: *Proc.4th world Cof. on Photovoltaic Energy Conversion* (2006) 1465.

[8] S.Y. Myong, K. Sriprapha, S. Miyajima, A. Yamada, and M. Konagai: *Appl. Phys. Lett.* **90** (2007) 263509.

[9] K. Yamamoto, M. Yoshimi, Y. Tawada, S. Fukuda, T. sawada, T. Meguro, H. Takata, T. Suezaki, Y. Koi, and K. hayashi: *Sol. Energy Mater.Sol. cells* **74** (2002) 449.

[10] P. Delli Veneri, L. V. Mercaldo and I. Usatii: *Appl. Phys. Lett.* **97** (2010) 023512.

[11] A. Lambertz, T. Grundler and F. Finger: *24th EU-PVSEC* (2009) 2402.

[12] X. Zhang, Q. Yue, X. Zheng, X. Geng, S. Xiong and Y. Zhao: *25th EUPVSEC & 5th WIP* (2010) 3232.

[13] A. Sarker, C. Banerjee and A K Barua: *J. Phys. D:Appl. Phys.* **35** (2002) 1205.

[14] H. Watanabe, K. Haga, and T. Lohner: *J. Non–Cryst. Solids* **164-166** (1993) 1085.

[15] M. Despeisse et al.: *Appl. Phys. Lett.* **96** (2010) 073507.

[16] B. Janthong, A. Hongsingthong, T. Krajangsang, L. Zhang, P. Sichanugrist and M. Konagai: *Journal of Non-Crystalline Solids*, **358** (2012) 2478.

[17] T. Krajangsang, I.A. Yunaz, S. Miyajima and M. Konagai: P*roceedings of the 35th Photovoltaic Specialists Conference*, (2010) 1532.

[18] P. Pernet. M. Goetz, H. Keppner, A. Shah: *Proc. MRS Symp., Boston,* (1996) 889.

[19] P. Pernet, M. Hengsberger, C. Hof, M. Goetz, A. Shah: *proceeding of 16th EC Photovoltaic Solar Energy Conference,* (2000) 498.

[20] E. Elias, L. Angeles, K. E. Knapp and Tarzana: United States Patent, *Patent Number 4,873,118*, Oct. 10, 1989.

Chapter 6

Optimization of Front Anti-reflection Layers inserted between Glass/TCO (FAL) and TCO/p-layer (FALp), and their applications to silicon-based single-junction solar cells

6.1 Introduction

In thin-film silicon-based solar cells, light-trapping management is highly important for improving short circuit current density (J_{sc}) and, in turn, increasing solar cell performance[1-5]. Light-trapping approaches to increasing the efficiency of incident light absorption in the intrinsic absorber layer of solar cells, e.g., using a front contact with textured transparent conductive oxide (TCO)[6-10], a back reflector with highly reflective textured TCO/metal layer[11-15] and a highly reflective intermediate reflector[16-19], have been reported by several research groups. In the case of a glass superstrate structure, optical reflection losses occur owing to a refractive index (n) mismatch between interfaces in solar cells. As previously reported [20, 21], a TiO_2 (n~2.5) layer was inserted at TCO (n~2.0)/Si (n~3.5) interfaces in p-i-n solar cells in order to suppress optical reflection loss. However, loss still occurred owing to optical reflection at the glass (n~1.5)/TCO (n~2.0) interfaces. Recently, an a-SiN_x:H layer and an MgO layer inserted between glass and TCO has been applied to hydrogenated amorphous silicon (a-Si:H) solar cells to reduce the optical reflection between these two refractive layers[22-23]. Also, an n-type SiO_x-based material has widely been studied for photovoltaic applications [24-27]. It has successfully been prepared and applied to a p-i-n solar cell instead of ZnO/Ag back contact [15] including used as an intermediate layer in tandem solar cells [16]. In our previous work as described in chapter 5, a silicon- oxide-based material whose refractive index can be adjusted by varying oxygen content was successfully prepared and applied to a-Si:H/µc-Si:H solar cells [28]. As a result, this material has the potential to be used as a new refractive-index matching layer.

In this chapter, according to theoretical calculations, the optimizations of SiO_x films and their applications to silicon-based thin film solar cells has been studied. Firstly, a-SiO_x films was characterized and introduced into silicon-based solar cells as an additional refractive-index matching layer inserted between glass and the front ZnO:B TCO layer (front anti-reflection layer: FAL) in order to decrease reflection loss. The effect of the optimized FAL on µc-Si:H solar cell performance was investigated and discussed compared to the conventional solar cells without FAL. Next, the characterization of n-type µc-SiO_x films was carried out in order to find the optimal one used as an additional refractive-index matching layer inserted between front ZnO:B TCO layer/p-layer (FALp). The silicon-based thin film solar cells including a-Si:H and µc-Si:H solar cells with the optimized FALp were fabricated and compared with the conventional solar cells without FALp. The investigation of effect of FALp on solar cell performance was carried out and presented.

6.2 Optimization of a-SiO_x:H films used as a Front Anti-reflection Layer inserted between glass/TCO (FAL)

6.2.1 Experimental Details

As described in the optical calculation part of this thesis, the preferred properties of a front anti-reflection layer (FAL) with refractive index of ~1.73 and thickness of 80-100 nm, which was obtained from theoretical calculations, are required. Therefore, in this experiment as shown in figure 6-1(a), a-SiO$_x$ films were deposited on Corning 7059 glass sheets using SiH_4, H_2, and CO_2 as the source gases by the 13.56 MHz radio frequency plasma-enhanced chemical vapor deposition (RF-PECVD) technique in order to investigate refractive index (n) and optical band gap (E_{04}). For the film deposition condition used in this study, CO_2 flow rate was adjusted in order to explore the optimal FAL with considerable optical properties, i.e., a refractive index of ~1.75 and wider optical band gap. Here, the thickness of the deposited films was maintained at approximately 60 nm. The refractive index and the optical band gap (E_{04}) measured by spectroscopic ellipsometry were used to characterize the optical properties of these films. In order to further investigate the properties of FAL and confirm the calculation results, the test samples with the structure as shown in figure 6-1(b) were prepared on both etched glass and flat glass for comparison with the conventional one without FAL. The ZnO:B film was deposited on the flat glass and etched glass samples. The ZnO:B film deposition condition we used was reported in chapter 7[29]. The ZnO:B layer thickness used in these test samples was kept at 1.5 μm, whereas the optimum thickness of the FAL for application to solar cells was also determined. The optical properties of the prepared samples, i.e., transmittance, reflectance, as well as haze were measured using a UV-VIS-NIR spectrophotometer. Also, the surface morphology and rms roughness of these samples were analyzed by atomic force microscope (AFM). Hall measurement was performed to investigate the electrical properties of these samples.

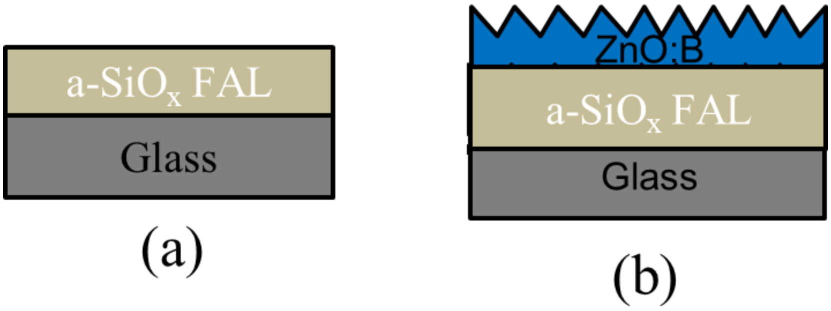

Figure 6-1 (a) a-SiO$_x$:H films deposited on Corning 7059 glass (b) test samples with glass/a-SiO$_x$:H/ZnO:B configuration

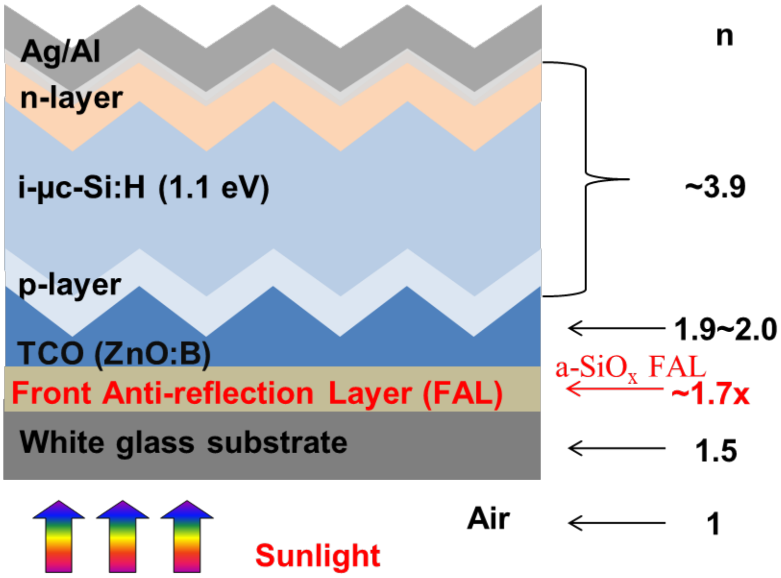

Figure 6-2 Structure of a solar cell for experimental study (Refractive indices shown here are the values at 600 nm.)

6.2.2 Effect of FAL on the optical properties of ZnO:B TCO films

The a-SiO$_x$ FAL film with n of ~1.75 and E_{04} of ~2.9 could be obtained by optimizing CO_2 flow rate. The optimized thickness of the SiO$_x$ FAL we have investigated was ~60 nm. The optical properties of SiO$_x$ films were investigated by varying CO_2 gas flow rate as shown in figure 6.3. Next, the test samples were firstly deposited on flat glass in order to confirm the calculation results. The transmittance and reflectance spectra of the sample as a function of thickness were measured and shown in figure 6-4. In addition, the sample with FAL was deposited on flat glass compared to the one without FAL as shown below in figure 6-5. In order to improve the scattering effect of substrates, the samples with and without FAL were also prepared on the textured glass as shown in figure 6-6.

The optical properties of SiO_x films, i.e. refractive index (n) and optical band gap (E_{04}), as well as Raman spectrum of SiO_x films were described in figure 6-3. As we can see from the results, the SiO_x film with n of ~1.75, which has a quite close to the calculated value we have preferred, could be obtained for the CO_2 flow rate at 12 sccm and the optical band gap E_{04} of ~3.3 could also be given. At the same time, the Raman spectra of all SiO_x films show the amorphous peak. It reveals that all SiO_x films are amorphous-based material without crystalline phase incorporated inside the films.

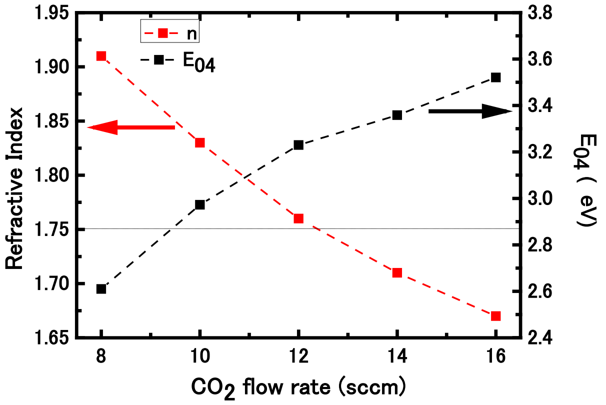

(a)

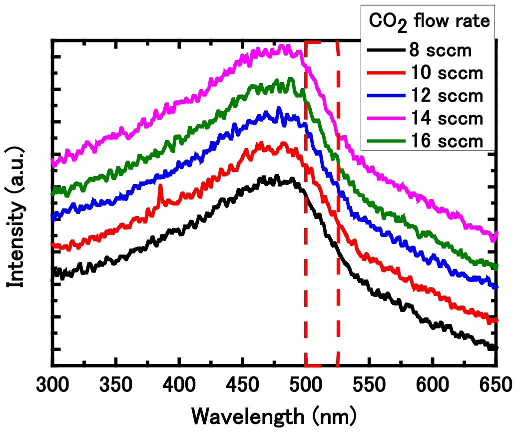

(b)

Figure 6-3 (a) Optical properties and (b) Raman spectrum of SiO_x films with different CO_2 flow rate

Figure 6-4 presents the transmittance and reflectance spectra of the samples with glass/a-SiO_x:H/ZnO:B configuration as a function of thickness of FAL. As shown in figure 6-4 (a), it was found that the transmittance of the samples increased when the samples became thicker, particularly, the wavelength region over 600 nm. On the other hand, the transmittance in the wavelength region under 600 nm decreased with increasing the thickness; which has the same tendency as the results from the reflectance spectra. Figure 6-4(b) shows the reflectance spectra of the samples with glass/a-SiO_x:H/ZnO:B configuration as a function of thickness of FAL. From the result, it was seen that the reflectance spectrum in the long wavelength region of 600-1400 nm decreased with increasing the thickness. However, the sample with the thickness of more than 80 nm showed the decreased reflectance in the wavelength region of less than 600 nm. These results reveal that the optimized thickness of FAL applied in solar cells should be between 60 to 80 nm.

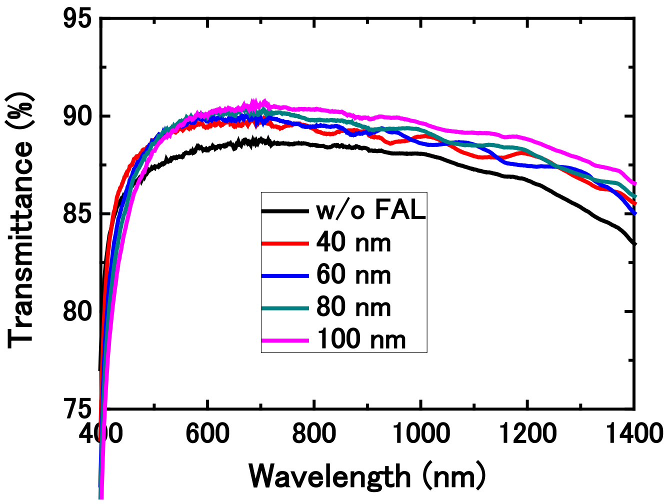

(a)

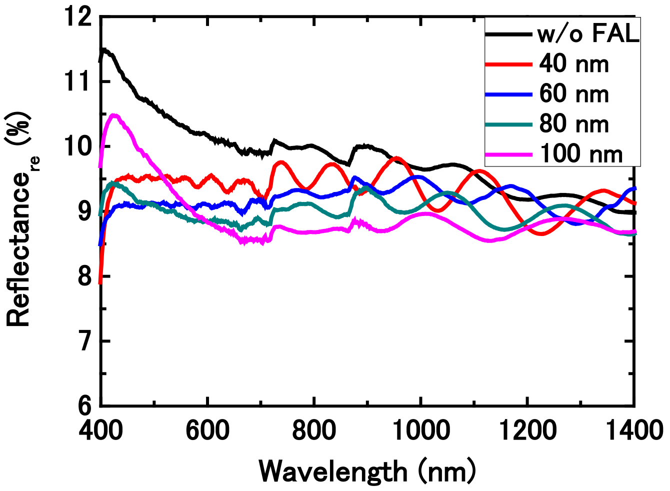

(b)

Figure 6-4 (a) transmittance and (b) reflectance spectra of the samples with glass/ a-SiO_x:H/ ZnO:B configuration as a function of thickness of FAL

Figure 6-5 explains transmittance spectra and haze value of the flat glass substrates with FAL compared to the substrate without FAL. As can be seen from figure

6-5, in case of flat glass substrates, the transmittance and the haze value of the sample with FAL was higher than the one without FAL over the wavelength region, especially longer than 500 nm. It is clear that the optical properties of the substrates could be improved using this optimized FAL.

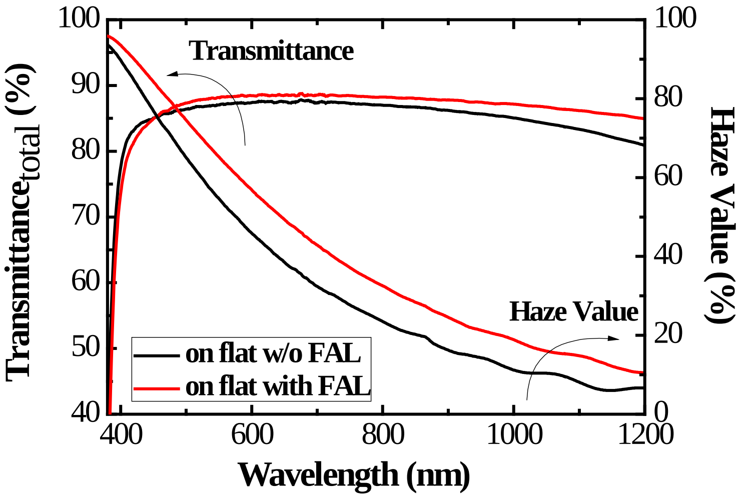

Figure 6-5 Transmittance spectra and haze value of the flat glass substrates with and without FAL.

In order to further enhance light management of substrates, textured substrates were applied in this work. Figure 6-6 shows the transmittance spectra and spectral haze values of samples on the textured substrate. From this figure it can be observed that the substrate with FAL shows a higher transmittance spectrum than that without FAL, especially in the long-wavelength region (> 500 nm). In the case of the substrate with FAL, a higher spectral haze value can also be observed. This result may lead to an improved light-scattering and suppression of optical reflection loss when such a FAL is incorporated into silicon-based solar cells.

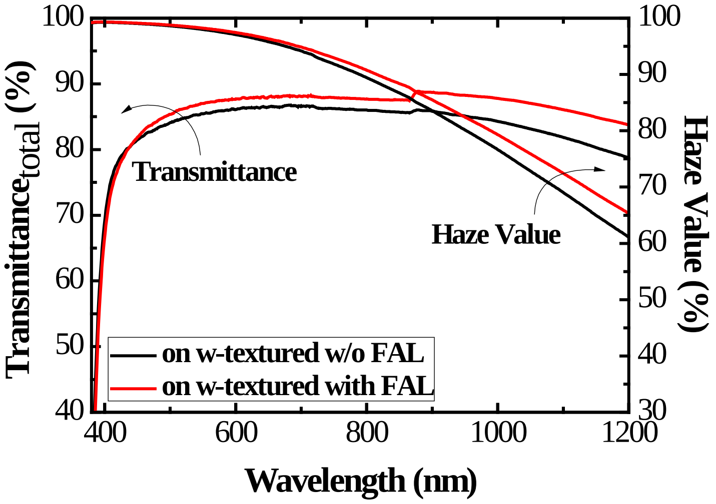

Figure 6-6 Transmittance spectra and haze value of the textured glass substrates with and without FAL.

6.2.3 Effect of FAL on the electrical properties of ZnO:B TCO films

Moreover, to confirm the influence of the FAL before application to solar cells, we also investigated the effect of this optimized FAL on the electrical properties of the substrates coated with ZnO:B film. Table 6-1 shows the electrical properties of the ZnO:B-coated substrates with FAL compared to the substrates without FAL. The numbers represented in the table are the average values calculated from three measurements. As can be seen from this table, it is interesting to note that the electrical properties of both substrates did not change significantly. These results indicate that insertion of the FAL into glass/ZnO TCO interface may not affect the electrical properties of ZnO:B films.

Table 6-1 Electrical properties of ZnO-coated glass substrates with and without the FAL

	Without FAL	with FAL
Carrier concentration (cm^{-3})	$9.63\pm1.23\times10^{19}$	$1.04\pm0.10\times10^{20}$
Mobility ($cm^2/(V\cdot s)$)	20.14 ± 1.24	21.26 ± 1.97
Resistivity ($\Omega\cdot cm$)	$3.12\pm0.06\times10^{-3}$	$2.85\pm0.04\times10^{-3}$
Sheet resistance (Ω/sq)	15.6 ± 0.15	13.9 ± 0.21

In addition, AFM measurement was also conducted in order to observe the surface morphology and roughness of ZnO:B films deposited on etched glass with and without the FAL. It is shown in the surface morphology image in figure 6-7 that no clear difference in surface morphology of both substrates was observed. On the other hand, a few changes in surface rms roughness from ~202 nm to ~211 nm can be seen from the ZnO film with the FAL. These results reveal that the surface morphology of ZnO films may not be influenced by FAL inserted between glass and TCO.

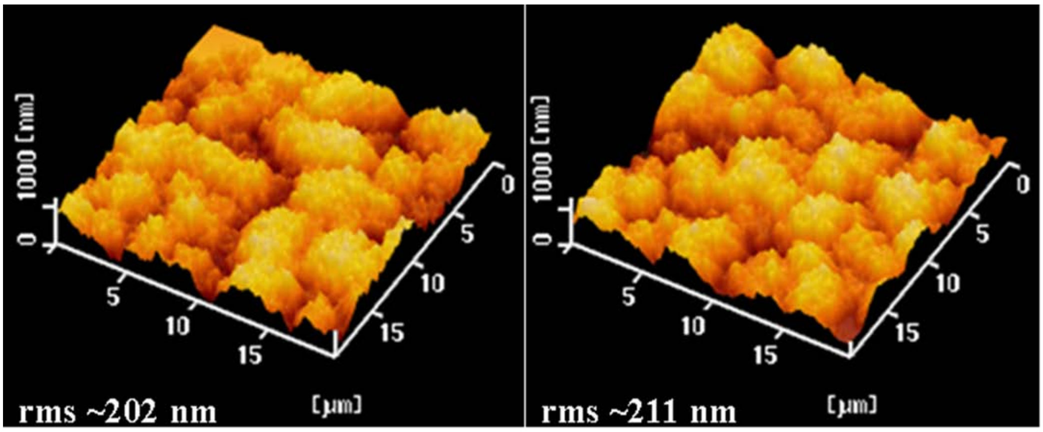

Figure 6-7 AFM images of ZnO-coated glass substrates with and without the FAL

6.3 Application of FAL to silicon-based single-junction solar cells

6.3.1 Fabrication Details

P-i-n-type µc-Si:H single-junction solar cells with an area of 0.086 cm^2 were fabricated using the optimized FAL as an additional refractive-index matching layer inserted between glass and front ZnO:B transparent conductive oxide (TCO). The structure of these solar cells was as follows: MgF$_2$-coated glass substrate/a-SiO$_x$ FAL/textured ZnO:B/ p-µc-SiO$_x$:H/ i-µc-Si:H/ n-SiO$_x$:H/ Ag /Al. The thickness of the instinct layer deposited by the VHF-PECVD technique was approximately 1.2 µm. The thicknesses of the doped p- and n- layers deposited by the RF-PECVD technique were ~35 and ~60 nm, respectively. The thickness of the optimized FAL was ~60 nm. The photo-*J-V* characteristics of the fabricated cells were measured under standard conditions (25 ºC, 1-sun, Air Mass 1.5, 100 mW/cm^2) to evaluate solar cell performance. The spectral response of these cells was analyzed using external quantum efficiency (*EQE*) measurement. Furthermore, µc-Si:H cells without FAL were also fabricated and compared with a cell with FAL.

6.3.2 Effect of FAL on µc-Si:H single-junction solar cell performance

The µc-Si:H solar cells with the optimized FAL inserted between glass and ZnO:B TCO were fabricated to confirm the effect of the FAL on solar cell performance. In figure 6-8, the photo-*J-V* characteristics of µc-Si:H solar cells with and without the optimized FAL is illustrated. As can be seen from this figure, it is shown that by applying this FAL, J_{sc} was increased by 1.6 mA/cm^2. This suggests that the optical reflection loss could be decreased. Moreover, quite the same V_{oc} and FF for both cells were observed. It means that the incorporation of this FAL does not deteriorate the properties of the ZnO:B layer.

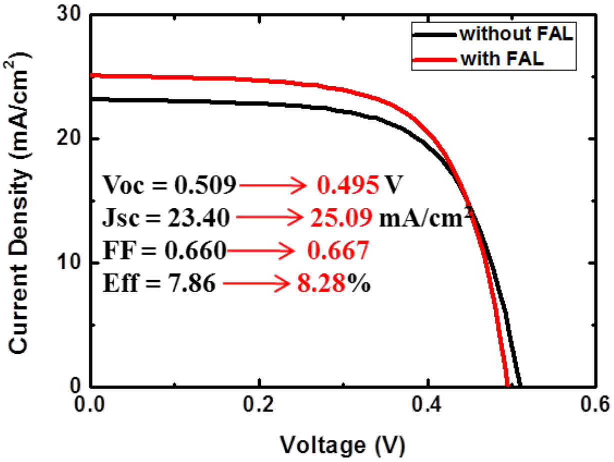

Figure 6-8 Photo-*J*-*V* characteristics of μc-Si:H solar cells with and without FAL.

Figure 6-9 shows the *EQE* and total cell absorption [30] (1-R_{cell}) of the μc-Si:H solar cells with and without FAL. In figure 6-9, it is demonstrated that the optimized FAL can reduce the optical reflection of solar cell and noticeably enhances its spectral response particularly in the wavelength region of 550-950 nm. Also, the total cell absorption reveals that the FAL could reduce the reflection loss at the glass/ ZnO:B interface. Compared to the standard cell without FAL, a relative increase in J_{sc} by 5% could be achieved. The relative improvement of J_{sc} by 5%, which is different from the absolute value obtained from the optical transmittance of ZnO-coated glass substrates (~3%), may result from the difference in refractive index profiling. In the case of transmittance, the profiling of refractive index is 1 (air)/ 1.5 (glass) / 1.75 (FAL) / 1.9 (ZnO) / 1(air), while that for the cell is 1 (air)/ 1.5 (glass) / 1.75 (FAL) / 1.9 (ZnO) / 3.5 (p-SiO).

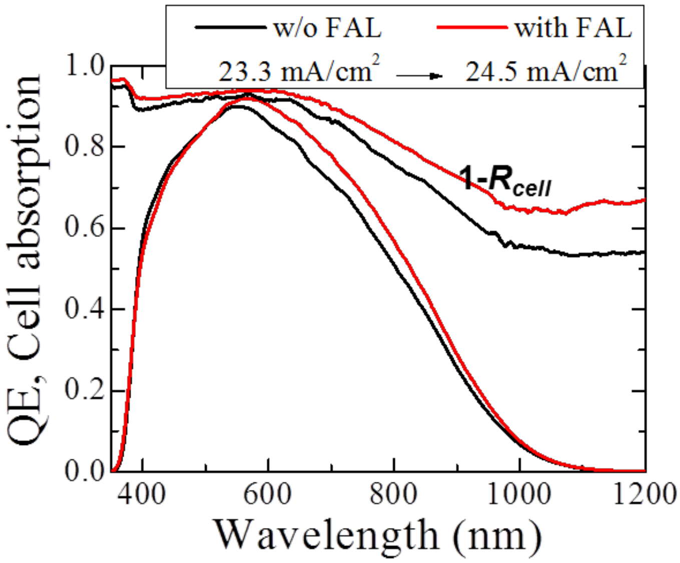

Figure 6-9 *EQE* and total absorption of μc-Si:H solar cells with and without FAL.

6.4 Optimization of n-μc-SiO$_x$:H films used as a FALp

Here in this work, we have studied how to apply n-μc-SiO$_x$ films into the p-i-n type a-Si:H and μc-Si:H solar cells as a new refractive-index matching layer inserted at ZnO/p-layer interface (FALp). If this layer can be used instead of TiO$_2$/ZnO layers, this can be applied into a-Si/μc -Si tandem p-i-n solar cell in the future and can enhance the tandem solar cell performance. Furthermore, this n-μc-SiO$_x$:H can be fabricated by PECVD technique right before the p-layer deposition which is convenient compared to sputtered-TiO$_2$/ZnO layers, which has been reported [31].

Here, optical calculation of a front anti-reflection layer inserted into transparent conductive oxide (TCO) ZnO/silicon p-layer interface (FALp) with various refractive indices and thicknesses was firstly performed using the simulator called OPTICAL in order to estimate the optimal thickness and refractive index (n) of FALp. Secondly, the optimization of n-μc-SiO$_x$:H films for use as a FALp was experimentally performed in order to find out the considerable properties of FALp. Finally, the preparations of a-Si:H and µc-Si:H solar cells with the optimized n-µc-SiO$_x$:H FALp were performed compared to the solar cells without FALp. The effect of FALp on each solar cell performance was analyzed and discussed.

6.4.1 Optical calculation of FALp

We have calculated the transmittance and reflectance spectra of a front anti-reflection layer inserted into transparent conductive oxide (TCO) ZnO/silicon p-layer interface (FALp) with various refractive indices and thicknesses by using the simulator called OPTICAL [32]. The model structure used in this calculation was glass/ZnO/FALp/p-Si as shown in figure 6-10. The effects of the wavelength-dependent refractive index and the thickness of each FALp on optical performance at ZnO/silicon p-layer interface were analyzed. Here, the ZnO layer thickness was kept at 1.5 µm. The refractive indices of all FALp used in this analysis were obtained from the experimentally deposited SiO$_x$ films.

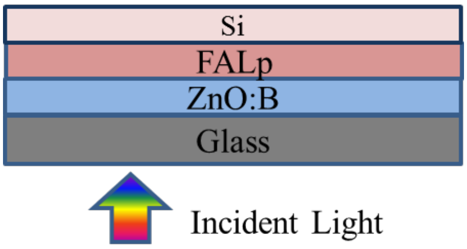

Figure 6-10 Schematic structure used for optical calculation

The transmittance and reflectance spectra of FALp with variation of refractive indices were computed compared to the one without FALp. Figure 6-11 shows the transmittance and reflectance spectra of FALp when refractive index was varied from

2.1 to 3.0 comparing with the one without FALp while the thickness of FALp was fixed at 60 nm. From the result, the transmittance became higher in the long wavelength region (>600 nm) but lower in short wavelength region (<600 nm) when the refractive index increased. By considering the trade-off between the improvement of transmittance in long wavelength and reduction in short wavelength, it was found that the FALp with n of range 2.49 to 2.74 has a superior transmittance spectrum, especially in long wavelength region (>600 nm), as well as better reflectance spectrum over whole wavelength, which can be expected to suppress optical reflection loss at ZnO/p-silicon interface. This value is quite close to the value calculated from the equation $n = (n_{TCO} \times n_{Si\text{-}layer})^{1/2}$.

The transmittance and reflectance spectra of FALp as a function of thickness were computed. Figure 6-12 gives the transmittance and reflectance spectra of FALp when thickness was increased from 20 to 100 nm while the refractive index of FALp was kept 2.61. From figure 6-12 we can observe that the value of maximum transmittance for each FALp thickness increased as the thickness increased and it was also found that the maximum transmittance shifted to the long wavelength region with increasing thickness. However, for reflectance spectra, one can see that the FALp thickness at ~60 nm has superior reflectance, especially the wavelength region (> 600 nm), compared to the others.

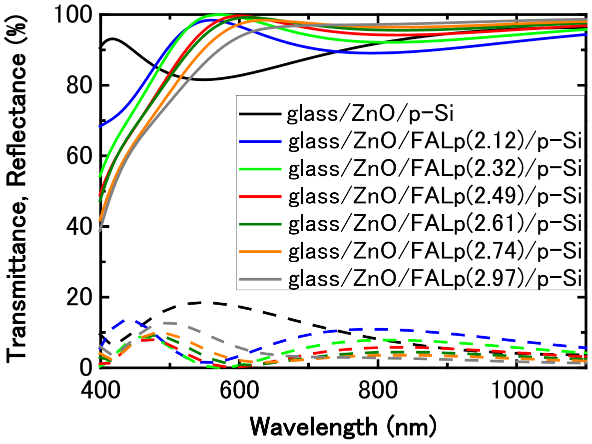

Figure 6-11 Transmittance and reflectance spectra of glass/ZnO/FALp/p-Si with various refractive indices.

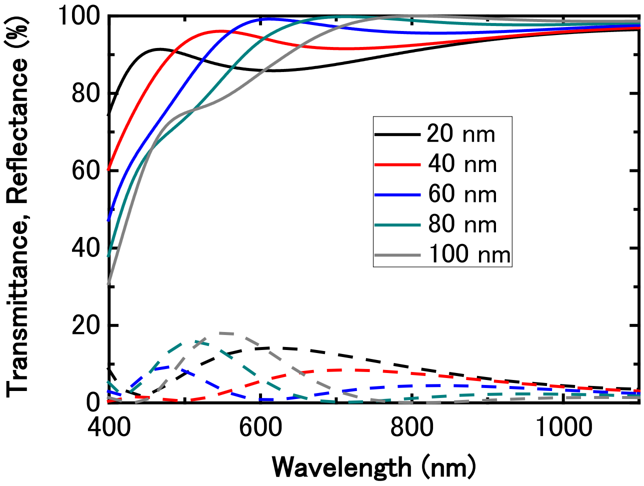

Figure 6-12 Transmittance and reflectance spectra of glass/ZnO/FALp(2.61)/p-Si with different thickness

6.4.2 Experimental details

N-type SiO_x films were deposited on Corning 7059 glass substrates at 200 ºC substrate temperature using SiH_4, H_2, PH_3 and CO_2 as source gases by 13.56 MHz RF-PECVD technique. In this study, for the film deposition, the CO_2 flow rate was adjusted in order to explore the optimal FALp film with considerable optical and electrical properties as shown in table 6-2. Here, the thickness of deposited films was maintained at around 50-60 nm. The refractive index and the optical band gap (E_{04}) measured from spectroscopic ellipsometry were used to characterize the optical properties of these films. In order to investigate the electrical properties of FALp film, the in-plan dark conductivity was measured by coplanar electrodes. The structural property of deposited films was also investigated by Raman scattering spectroscopy. It should be noted that refractive indices mentioned in this paper are the values at the wavelength of 600 nm.

Table 6-2 shows the deposition condition of SiOx:H films with various CO_2 flow rate

Substrate Temperature (°C)	**200**
Deposition Pressure (Pa)	200
Plasma Power Density (W/cm^2)	0.065 (10 W)
Electrode gap (cm)	1.5
SiH_4 flow rate (sccm)	3.30
H_2 flow rate (sccm)	200
CO_2 flow rate (sccm)	**0-8**
PH_3 flow rate (sccm)	3.0

6.4.3 Effect of CO_2 flow rate for SiO_x FALp

The SiO_x FALp film with refractive index (n) of ~2.68 and optical band gap (E_{04}) of ~2.31 eV could be obtained by optimizing CO_2 flow rate. The influence of CO_2 flow rate on the properties of SiO_x FALp films was firstly investigated. Figure 6-13 depicts the in-plan dark conductivity and Raman spectrum measurements of deposited films. From this result, it was found that the conductivity declined from ~20 to ~10^{-11} S/cm when CO_2 flow rate was increased corresponding to the Raman spectrum changed from microcrystalline phase to amorphous phase. As reported in papers, the drop of conductivity with increasing CO_2 flow rate is mainly due to an increase of Si-O bonding in the film which only presents in the amorphous phase [33]. Also, from the result shown in figure 6-14, the Raman spectra reveal that no crystalline peak at 520 cm^{-1} was observed when the CO_2 flow rate was increased more than 4 sccm.

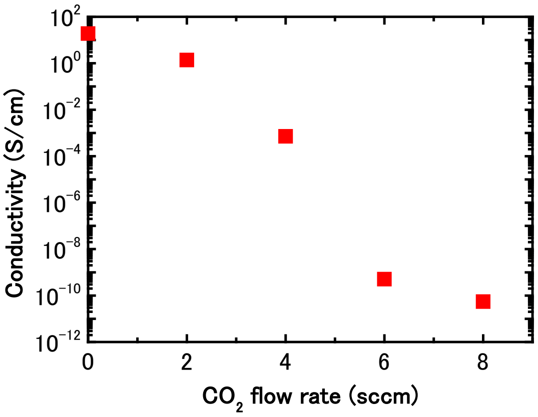

Figure 6-13 In-plan conductivity of n-SiO_x:H films as a function of CO_2 flow rate

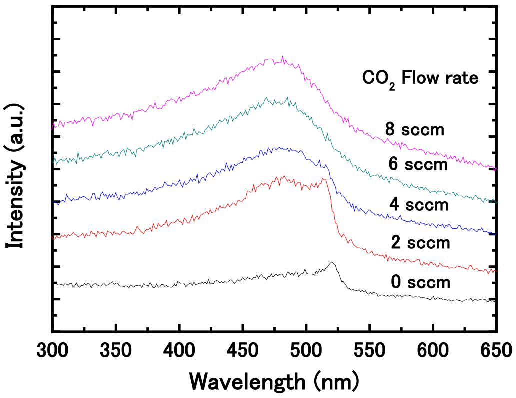

Figure 6-14 Raman spectrum of n-SiO_x:H films as a function of CO_2 flow rate

In addition, from figure 6-15 the variation in refractive index (n) and optical band gap (E_{04}) of deposited SiO_x FALp films with different CO_2 flow rate is shown. It was seen that the refractive index decreased with increasing CO_2 flow rate while the E_{04} increased as the CO_2 flow rate increased. The reduction of refractive index is probably due to an increase of oxygen concentration in the films, which corresponds to lower optical band gap [15]. Here, the preferred SiO_x FALp film having the significant optical and sufficiently conductive properties was obtained.

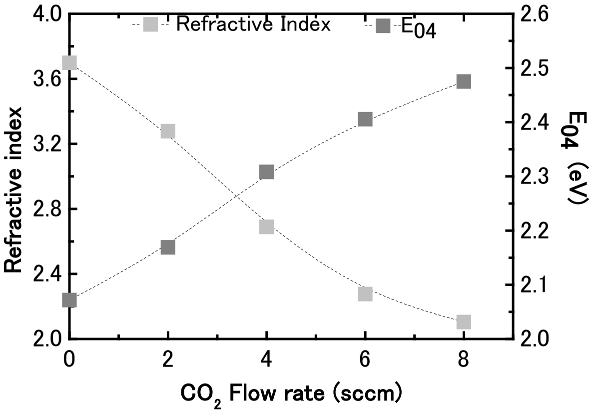

Figure 6-15 (a) Refractive index and (b) optical band gap (E_{04}) of n-SiO_x films as a function of CO_2 flow rate

6.5 Application to silicon-based thin film solar cells

6.5.1 Fabrication details

P-i-n-type a-Si:H and μc-Si:H single-junction solar cells were fabricated using the optimized FALp inserted at front TCO/silicon layer interface as an additional refractive-index matching layer. The structure of these a-Si:H solar cells fabricated by plasma enhanced chemical vapor deposition (PECVD) technique was RIE-etched glass/

textured-ZnO:B/ FALp/ p-a-SiOx:H /i-a-Si:H/ n-SiOx:H/ Ag/ Al as shown in figure 6-16. The thicknesses of intrinsic layer deposited using VHF-PECVD technique and the FALp deposited using RF-PECVD technique were 300 nm and ~60 nm respectively. Also, the µc-Si:H solar cells were fabricated by using these optimized FALp with structure of glass/ textured-ZnO:B/ FALp/ p-µc-SiOx:H/ i-µc-Si:H/ n-SiOx:H/ Ag/ Al. The intrinsic layer was prepared using a 60 MHz very high frequency (VHF) PECVD technique while the boron-doped p-layer and the phosphorous-doped n-layer of both top and bottom cells were all fabricated by 13.56 MHz RF-PECVD technique. The thicknesses of i-layer and the FALp were 1.2 µm and ~60 nm, respectively. The photo *J-V* characteristics of both of the fabricated solar cells were measured at 25ºC under 1sun (AM1.5, 100 mW/cm^2) solar simulator radiation. The spectral response of these cells was analyzed using external quantum efficiency (*QE*) measurement.

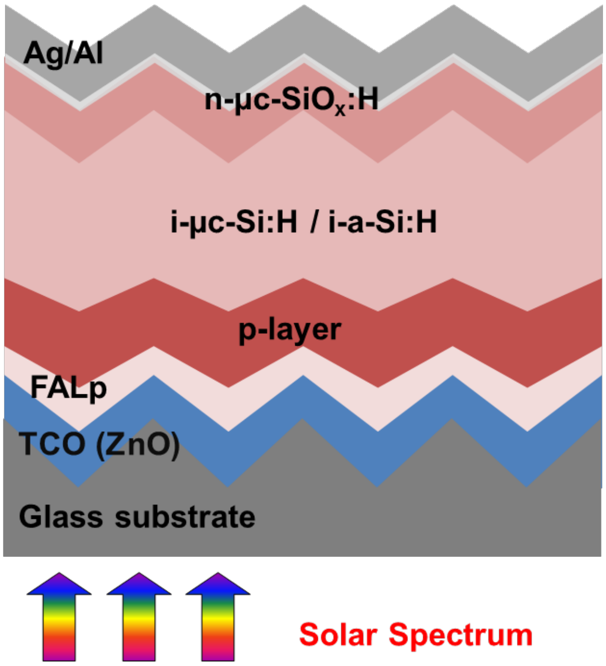

Figure 6-16 Structure of a-Si:H and µc-Si:H solar cells with FALp

5.5.2 Effect of FALp on a-Si:H single junction solar cells

The SiO_x FALp film optimized so far was applied to a-Si:H single-junction solar cells to compare with the one without FALp. As can be seen from figure 6-17, by employing this SiO_x FALp film into a-Si:H solar cells it was found that a few changes in Photo-*I*-*V* parameters was observed, especially, the improved V_{oc}. This is probably due to greater electrical properties of interface between TCO/p-layer. However, *QE* at the short wavelength region of 350-550 nm are slightly decreased. One of the reasons, we can consider, is because of parasitic absorption of the FALp layer. The further optimization of FALp is still required for an application to a-Si:H solar cells.

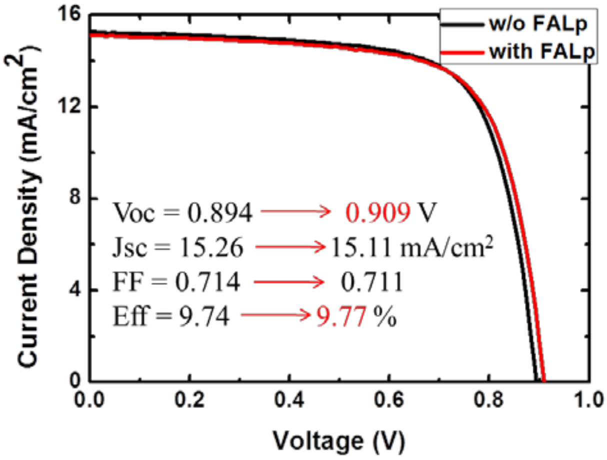

(a)

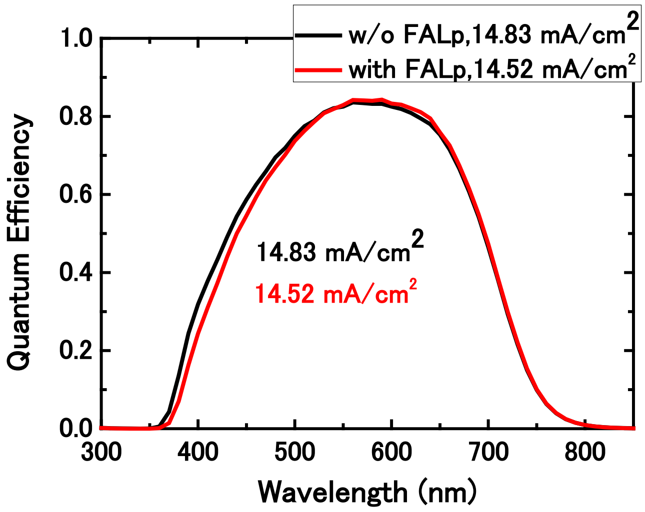

(b)

Figure 6-17 (a) *I-V* characteristics and (b) Quantum efficiency of a-Si:H solar cells with and without FALp

6.5.3 Effect of FALp on μc-Si:H single junction solar cells

In this section the effect of FALp on μc-Si:H solar cell performance was discussed. For applying the optimized FALp into μc-Si:H solar cells, it was found that the short circuit current (J_{sc}) of the solar cell was improved from 23.93 to 24.35 mA/cm^2. Moreover the quite same open circuit voltage (V_{oc}) and fill factor (*FF*) were observed. From *QE* measurement shown in figure 6-18, it was demonstrated that the spectral response in the range of 500-900 nm was improved. However, the spectral response at the short wavelength region (<500 nm) was reduced. This is probably because that the thickness of SiO_x FALp films has not been optimized yet. The further optimization of the film for application to μc-Si:H solar cell is required in order to improve current density of complete cells.

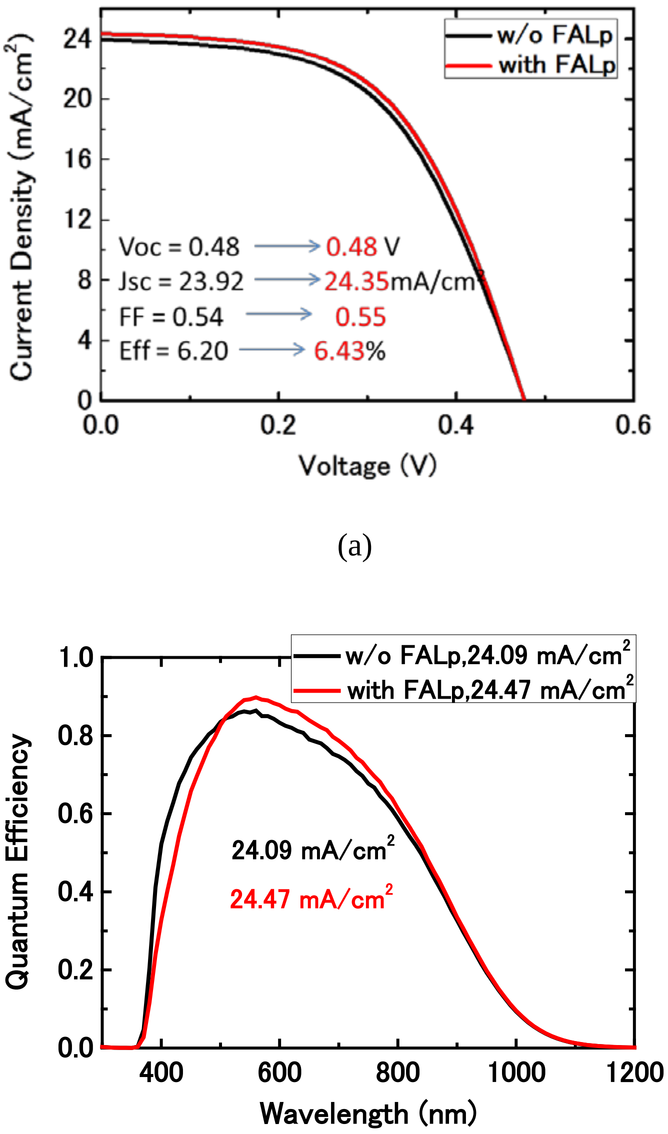

(a)

(b)

Figure 6-18(a) *I-V* characteristics and (b) Quantum Efficiency of μc-Si:H solar cells with and without FALp

6.6 Summary

In this chapter, characterization of a-SiO_x films has been defined by studying optical properties of films used for a FAL. The optical properties of a-SiO_x films were investigated by transmittance, reflectance, and haze value measurement. Also, electrical properties of ZnO:B films coated on glass/a-SiO_x substrate were investigated in order to confirm effect of FAL on properties of ZnO:B films compared to the sample without a-SiO_x FAL. Then, µc-Si:H solar cells with the optimized a-SiO_x FAL were fabricated to compared the ones without FAL. The effect of applying the optimized a-SiO_x FAL on the solar cell performance was also discussed here. From the results, the optical reflection loss of the glass/ZnO interface can be reduced by applying the optimal SiO_x FAL to the solar cells. By inserting optimized SiO_x FAL with n of ~1.75 into the glass/ZnO interface of the µc-Si:H solar cell, J_{sc} could relatively be increased by about 5%, especially in the 550-950 nm region. Furthermore, this optimized FAL did not deteriorate the properties of the ZnO layer as well because no significant changes in V_{oc} and FF were observed. As a result, the cell with an efficiency as high as 8.28% ($V_{oc} = 0.495$ V, $J_{sc} = 25.09$ mA/cm^2, $FF = 0.667$) could be realized. A higher current density of bottom cells in multi-junction solar cells can also be obtained by incorporation of the optimized FAL

Moreover, optimization of n-µc-SiO_x:H films for use as a FALp was also performed to find the films with excellent properties, optical and electrical, for application to silicon-based thin film solar cells, i.e., a-Si:H and µc-Si:H solar cells. The n-µc-SiO_x:H film with E_{04} of ~2.68, n of ~2.31 and sufficient conductivity was obtained and the effect of this optimized film on the performance of a-Si:H and µc-Si:H solar cells was also discussed. From the results, the optical reflection loss of the ZnO/p-silicon interface can be decreased by applying the optimal SiO_x FALp at that interface. By inserting SiO_x FALp optimized so far with n of ~2.68 and and E_{04} of ~2.31 eV into the ZnO/p-silicon interface of both a-Si:H and µc-Si:H solar cell, QE at the short and long wavelength regions are slightly decreased and increased respectively. For μc-Si:H solar cell, *Jsc* (obtained from *QE* measurment) improved by ~0.4 mA/cm^2, especially in the 500-900 nm region. Furthermore, with FALp no significant change in V_{oc} and *FF* of fabricated solar cells was observed. However, the spectral response at short wavelength region (<500 nm) for both a-Si:H and μc-Si:H solar cells was reduced. This is probably because that the thickness and refractive index of SiO_x FALp films has not been optimized yet. The further optimization of the film is still required. Multi-junction solar cells with higher efficiency are also expected to achieve by the incorporation of further optimized FALp. This trend is similar to the one using TiO_2. The results show that this novel n-μc-SiOx:H film will be beneficial for use as a front anti-reflection layer instead of TiO_2/ZnO.

References

[1] J. Krc, K. Brecl, F. Smole, and M. Topic: *Sol. Energy Mater. Sol. Cells* **90** (2006) 3339.

[2] J. Muller, B. Rech, J. Springer, and M. Vanecek: *Sol. Energy* **77** (2004) 917.

[3] M. Kambe, M. Fukawa, N. Taneda, Y. Yoshikawa, K. Sato, K. Ohki, S. Hiza, A. Yamada, and M. Konagai: *Proc. 3rd World Conf. Photovoltaic Energy Conversion* (2003) 1812.

[4] S. Fay, S. Dubail, U. Kroll, J. Meier, Y. Ziegler, and A. Shah: *Proc. 16th European Photovoltaic Solar Energy Conf.* (2000) 361.

[5] A. Shah, M. Vanecek, J. Meier, F. Meillaud, J. Guillet, D. Fischer, C. Droz, X. Niquille, S. Fay, E. Vallat-Sauvain, V. Terrazzoni-Daudrix, and J. Bailat: *J.non-Cryst. Solids* **338-340** (2004) 639.

[6] W. W. Wenas, A. Yamada, M. Konagai, and K. Takahashi: *Jpn. J. Appl. Phys.* **30** (1991) L441.

[7] A. Yamada, W. W. Wenas, M. Yoshino, M. Konagai, and K. Takahashi: *Jpn. J. Appl. Phys.* **30** (1991) L1152.

[8] W. W. Wenas, A. Yamada, M. Yoshino, M. Konagai, and K. Takahashi: *J. Appl. Phys.* **70** (1991) 7119.

[9] M. Berginski, J. Hupkes, M. Schulte, G. Schope, H. stiebig, B. Rech, and M. Wuttig: *J. Appl. Phys.* **101** (2007) 074903.

[10] J. C. Lee, V. Dutta, J. Yoo, J. Yi, J. Song, and K. H. Yoon: *Superlattices Microstruct.* **42** (2007) 369.

[11] K. Tabuchi, W.W. Wenas, A. Yamada, M. Konagai, and K. Takahashi: *Jpn. J. Appl. Phys.* **32** (1993) L3764.

[12] W. W. Wenas, A. De, A. Yamada, M. Konagai, and K. Takahashi: *Sol. Energy Mater. Sol. Cells* **34** (1994) 313.

[13] X. D. Zhang, Y. Zhao, Y. T. Gao, F. Zhu, C. C. Wei, X. L. Chen, J. Sun, G. F. Hou, X. H. Geng, and S. Z. Xiong: *J. non-Cryst. Solids* **352** (2006) 1863.

[14] X. Zhang, Q. Yue, X. zheng, X. Geng, S. xiong, and Ying Zhao: *Proc. 5th World Conf. Photovoltaic Energy Conversion (*2010) 3232.

[15] P. D. Veneri, L.V. Mercaldo, and I. Usatii: *Appl. Phys. Lett.* **97** (2010) 023512.

[16] P. Buehlmann, J. Bailat, D. Domine, A. Billet, F. Meilaud, A. Feltrin, and C. Ballif: *Appl. Phys. Lett.* **91** (2007) 143505.

[17] D. Domine, P. Buehlmann, J. Bailat, A. billet, A. Feltrin, and C. Ballif: *Phys. Status Solidi: Rapid Res. Lett.* **4** (2008) 163.

[18] C. Das, A. Lambertz, J. Huepkes, W. Reetz, and F. Finger: *Appl. Phys. Lett.* **92** (2008) 053509.

[19] T. Grundler, A. Lambertz, and F. Finger: *Phys. Status Solidi* **C 7** (2010) 1085.

[20] T. Fujibayashi, T. Matsui, and M. Kondo: *Appl. Phys. Lett.* **88** (2005) 183508.

[21] C. Das, A. M. Berginski, J. Huepkes, A. Gordijn, J. Kirchhoff, W. Reetz, A.Lambertz, F. Finger, and W. Beyer: *Proc. 22nd European Photovoltaic Solar Energy Conf.* (2007) 2112.

[22] C. H. Hsu, Y. P. Lin, and C. C.Tsai: *Proc. 26th European Photovoltaic Solar Energy Conf.* (2011) 2528.

[23] D.W. Kang, J.S. Woo, S. Lee, H.M. Lee, and M.K. Han: *Proc.26th European Photovoltaic Solar Energy Conf.*(2011) 2625.

[24] P. Sichanugrist, T. Yoshida, Y. Ichikawa, and H. sakai: *J. non-Cryst. Solids* **164-166** (1993) 1081.

[25] A. Sarker, C. Banerjee, and A K Barua: *J. Phys.* A **35** (2002) 1205.

[26] V. Smirnov, W. Bottler, A. Lambertz, H. Wang, R. Carius, and F. Finger: *Phys. Status Solidi* **3-4** (2010) 1053.

[27] L. Xiao, O. Astakhov, R. Carius, A. Lambertz, T. Grundler, and F. Finger: *Phys. Status Solidi* **3-4** (2010) 941.

[28] B. Janthong, T. Krajangsang, A. Hongsingthong, L. Zhang, P. Sichanugrist, and M. Konagai: *Proc. 37th IEEE Photovoltaic Specialists Conf.* (2011).

[29] A. Hongsingthong, T. Krajangsang, I. A. Yunaz, S. Miyajima, M. konagai: *Appl. Phys. Express* **3** (2010) 051102.

[30] M. Berginski, J. Hüpkes, A. Gordijn, W. Reetz, T. Wätjen, B. Rech, and M. Wuttig: *Sol. Energy Mater. Sol. Cells* **92** (2008) 1037.

[31] D.W. Kang, S.W. Ahn, H.M. Lee, and M.K. Han: *Jpn. J. Appl. Phys.* **51** (2012) 10NB10.

[32] E. Centurioni: *Appl. Opt.* **44** (2005)7532.

[33] H. Watanabe, K. Haga, and T. Lohner, *J. Non–Cryst. Solids* **164-166** (1993) 1085.

Chapter 7

Novel a-Si:H/µc-Si:H Double Junction Solar Cells Fabricated on Newly Developed Double-textured ZnO:B White Glass Substrates

7.1 Introduction

Cost reduction and efficiency improvement are still major issues in current photovoltaic technology development. Multi-junction silicon-based thin film solar cells such as an a-Si:H/ µc-Si:H solar cell were successfully developed by IMT, University of Neuchâtel [1] and can still be considered as promising candidates to reduce cost and obtain high conversion efficiency for future photovoltaic applications. In order to enhance short-circuit current density (J_{sc}) as well as conversion efficiency of devices, light-trapping management, e.g., a textured front transparent conductive oxide (TCO) [2-6], a textured highly reflective back reflector [6-8] and/or a highly reflective intermediate layer [9-12], are needed. An a-Si:H/ µc-Si:H tandem cell with initial efficiency of approximately 15.0 % was announced as the world record efficiency by the R&D group of Kaneka Corporation [12]. Now, one way to further enhance the light trapping effect is to use a double-textured (so-called "W-textured") ZnO:B glass substrate. This W-textured ZnO:B-coated glass substrate has two scale sizes of texture. One is the nano-size texture which comes from textured ZnO:B deposited by the metal organic chemical vapor deposition (MOCVD) method [2-3], and the other one is micro-size texture which comes from RIE-etched glass. In our previous study [13], we had used a 7059-type Corning glass and etched it by the Reactive Ion Etching (RIE) technique, in order to obtain a suitably textured surface. Thereby, the resulting W-textured ZnO:B film has a larger feature size of ~2 µm; it was deposited on an etched Corning glass substrate for the first time. Furthermore, we had also applied this W-textured technique onto a new EAGLE-XG-type Corning glass substrate [14] and the same trend was found. Recently, a record initial efficiency as high as 14.4 % of a-Si:H/ µc-Si:H solar cells fabricated on textured substrates coated by the low-pressure chemical vapor deposition (LPCVD)[1] method were reported by IMT, University of Neuchâtel group as well [5]. However, full details of their W-textured ZnO:B substrates have not been reported so far, but we found that its haze properties are similar to those of the substrates we have developed on 7059 glass samples [13].

On the other hand, from cost-effective point of view and in order to achieve different morphologies of W-textured glass substrates, we have also considered soda-lime glass (SLG) as alternative glass substrates [15-16]; thereby, one can obtain W-textured ZnO:B films with larger feature sizes (~4 µm) than in the case of Corning 7059 and EAGLE-XG glass samples. We also found that the W-textured ZnO:B film coated on SLG has high haze values in the long wavelength region. As the result, an initial efficiency of 12.4 % has been obtained on SLG [17]. However, to further improve the efficiency and, especially, the current density we have still tried to find new substrates with improved optical properties, retaining thereby the W-textured configuration.

In this chapter, we have applied a new white glass substrate which has higher transmittance than the conventional SLG to silicon-based thin-film solar cells. A white glass is a low-iron glass and has relatively less internal light absorption due to lower

---

[1] LPCVD, which is the term that IMT, University of Neuchâtel group uses, is similar to MOCVD, which is the term that the authors use.

iron content in the glass. According to a previous report it has already been used as a front cover glass for PV modules, because it leads to reduced optical reflection losses [18]. Here, we have investigated the relationship between the refractive index of each side of the white glass and the resulting RMS roughness of the ZnO:B films coated on these RIE-etched glass samples. ZnO:B films have been deposited on these glass samples to achieve W-textured TCO substrates by the MOCVD method. Moreover, to confirm the effect of these newly developed substrates on solar cell performance, a-Si:H/μc-Si:H tandem solar cells [19] were fabricated on the W-textured ZnO:B-coated white glass substrates and compared with the tandems fabricated on the SLG. The optimization of ZnO:B films coated on white glass substrates and their applications to a-Si:H/μc-Si:H tandem solar cells was discussed.

7.2 Fundamental aspects of ZnO:B film and its deposition technique

In this section, the basic properties of ZnO thin film and its deposition technique will be briefly explained. The ZnO is in the group of IIB-VIA binary semiconductors, a class of materials valuable for chief technological applications. Wurtzite-type crystal is made of interpenetrating hexagonal close-packed sub-lattices of the anion (oxygen) and cation (zinc) displaced along the [0001] direction as shown in figure 7-1.

ZnO is a hexagonal unit cell, and fits in to the C_{6v}^{4} space group (P6_3*mc*, Z= 2), with two formula units per primitive cell, with all atoms occupying C_{3v} sites. Zinc atom in the wurtzite lattice is bounded by sp^3 covalent bonding to four oxygen atoms, which are located in the vertices of a slightly distorted tetrahedron. The Zn and O-atoms distance is 1.9915 Å along to the *c*-axis [20]. The distance separating them in the remaining directions is 1.9760 Å. The Zn-O bond in bulk ZnO shows mixed covalent-ionic character, and has been proven to be less ionic than the bonds of other common *s*-metal oxides. The wurtzite lattice is characterized by three parameters, e.g. the basal plane lattice constant *a*, the uniaxial lattice constant *c*, and the internal coordinate *u*, which establishes the relative position of the anion and cation sub-lattices along the *c* axis. The basic properties of measured ZnO are summarized in table 7-1 [21].

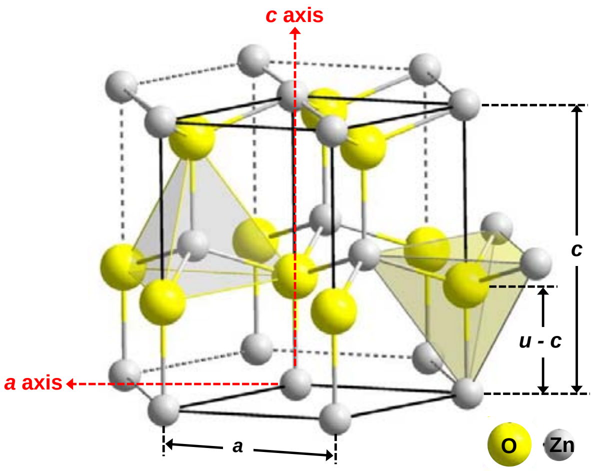

Figure 7-1 Wurtzite crystal structure of ZnO with hexagonal structure has a point group 6 mm symmetry [21].

Table 7-1 Basic properties of ZnO at 300 K.

Property	Values
Lattice parameters	
a_0	0.32495 nm
c_0	0.52069 nm
a_0/c_0	1.602
u	0.345
Density	5.606 g/cm^3
Stable phase	Wurtzite
Melting point	1975 °C
Static dielectric constant	8.656
Thermal conductivity	0.6, 1 – 1.2 W/Km
Linear expansion coefficient (1/℃)	a_0: 6.5×10^{-6} c_0: 3.5×10^{-6}

Figure 7-2 illustrates the energy band structure for wurtzite ZnO obtained from a first principle's calculation by Vogel *et al.* [22]. The electronic band structure is given as the energy-momentum (E-k) relationship. The maximum of the valence band and the minimum of the conduction band for ZnO occur at the same point in k space and therefore the band gap is direct. ZnO has a wide band gap which has been measured to be 3.37 eV at 300 K [23]. The direct and wide band gap of ZnO together is particularly important for possible application in the manufacturing of optoelectronic devices. A recent typical calculation of the band structure of ZnO is also shown in table 7-2.

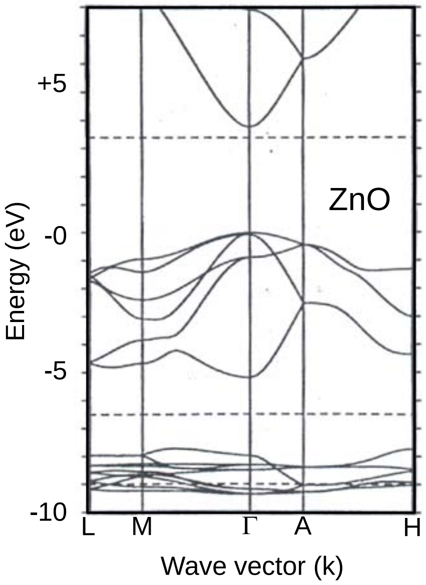

Figure 7-2 The band structure of ZnO (after Vogel *et al.*, 1995).

Table 7-2 Parameters related to the electronic band structure of ZnO at 300 K.

Property	Values
Energy gap	3.37 eV
Exciton binding energy	60 meV
Electron effective mass	0.24
Electron Hall mobility (bulk ZnO)	200 cm2/V·s
Hole effective mass	0.59
Hole Hall mobility	5 – 50 cm^{2}/ V·s
Intrinsic carrier concentration	< 10^{16} cm^{-3} max n-type doping > 10^{20} cm^{-3} electrons max p-type doping < 10^{17} cm^{-3} holes

Generally, undpoed ZnO film is an intrinsic semiconductor with energy gap of around 3.2 eV at 300 K. In fact, undpoed ZnO has up to date been shown to be n-type conducting ZnO. For that reason the n-type conductivity is excess Zn which act as a donor, which results in a non stoichiometric compound and a struc disorder. They can be explained by the intrinsic defect levels in bulk ZnO. The common native defects in ZnO have been identified to be the oxygen vacancy V_O, zinc vacancy V_{Zn}, oxygen interstitial O_i, zinc interstitial Zn_i and oxygen antisite Zn_O [24]. The impurity donors in ZnO have been attributed to H and the group III elements Al, Ga and B. The acceptor impurities in ZnO on the other hand have been identified as the group I elements. The dominant donors in ZnO responsible for the observed n-type conductivity have for quite some time been attributed to the native defects, V_O and Zn_i [25-26]. This assumption was the result of the abundance of n-type ZnO. The assumption was later challenged when Kohan *et al.* in 2000 showed V_O and Zn_i were deep donors and also had high formation energies [27], thereby excluding them as possible dominant donors in ZnO. In 2001, Zhang *et al.* showed that both V_O and Zn_i should indeed have donor transitions, but revealed that V_O is not a shallow donor but a deep donor and therefore could not be the dominant donor in ZnO [24]. However that both V_O and Zn_i have high formation energies. This suggests therefore that they could not be the dominant donors in ZnO since they both cannot account for the high free carrier concentrations. Vanheusden *et al.* have been reported that the V_O is very deep, suggested that the free carrier concentration measured in ZnO samples was too high and suggested Zn_i as the shallow donor in ZnO [28]. In these days, many group researchers accepted the possibility of native defects not being the origin of the n-type conductivity in ZnO and therefore diverted their attention to n-type impurity dopants as candidates in explaining the n-type conductivity in ZnO [24,29]. The foremost one of these dopants that has perhaps been given a lot of attention by various researchers is boron (B). This is the case because boron is very abundant and can be easily incorporated in ZnO during the crystal growth process. Additionally, many potential acceptors in ZnO have been investigated in search for reproducible p-type ZnO. These acceptors include both the native defects and extrinsic p-type dopants. The theoretical studies revealed that these defects are shallow [24], but the report also shows that these defects have high formation energies which means that they can be easily compensated by the intrinsic donors such as V_O and Zn_i which have relatively lower formation energies. It is currently believed therefore, that ZnO can not be doped p-type via native defects. This study is part of the ongoing research in the ZnO field because much of the ZnO-based technology is dependent on the control of doping in the material.

All ZnO samples studied in this research were deposited on glass substrates by MOCVD technique using oxygen sources such as H_2O as oxidants for diethylzinc ($Zn(C_2H_5)_2$, DEZ). Ar was selected as carrier gas and gas flows for DEZ, H_2O and D_2O were ranging between 0 to 200 sccm. 1%-hydrogen-diluted B_2H_6 was employed as dopant gas and the B_2H_6 flow rate was ranging between 0 to 10 sccm. The heater temperature was ranging between 25 to 300 ^oC. Figure 7-3 shows the schematic image of the MOCVD system used for the ZnO film deposition. As seen in figure 7-3, the essential equipment consists as follows; source gas (Ar, B_2H_2, metal-organics), gas lines, controlling system (regulators, mass flow controllers, valves etc.), reactor chamber, heater, evacuation system and exhaust gas treatment system. The metal-organics are in bubbles, which are soaked in the temperature-controlled baths. The reactor chamber is carried out by the bubbling of carrier gas such as Ar gas, N_2 and H_2. Generally, the reactor design can be classified into two groups (vertical and horizontal types). In our laboratory, MOCVD system is also normally classified into two groups by its operating low pressure. The general advantages and disadvantages of MOCVD compared to sputtering are shown in table 7-3. The most important attribute in the deposition of II-VI compound by using this MOCVD technique is the arrangement for mixing the gases to restrain the pre-reaction between the constituent gas streams. The reactor chamber design has concentrated on introducing the gases to the reactor separately, normally by admitting the groups VI compound at the reactor chamber and the metal alkyl through a delivery gas tube much closer to the heater stage.

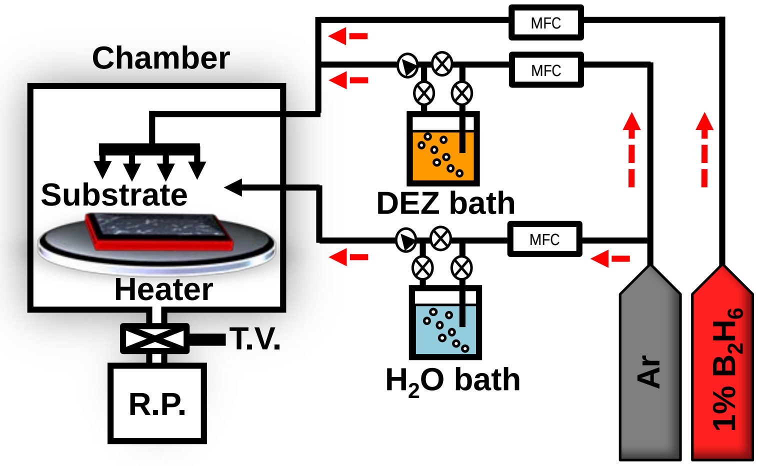

Figure 7-3 Schematic image of the MOCVD system used for the ZnO-film deposition

Table 7-3 Comparison the deposition of ZnO films by MOCVD and sputtering techiques.

Property	MOCVD	Sputtering
Usual deposition process	non equilibrium	equilibrium
Orientation	c-axis parallel, perpendicular and inclined	c-axis perpendicular
Surface texture growth	intensified growth	growth plus etching
Fiber texture growth	mixed orientations	fiber texture growth
Growth rate	high	low
Surface morphology	variety of morphologies depending on the orientation	columnar and granular
Mechanical property and resistance against environment conditions	moderate	very good
Ability for post treatment of the grown films	poor	good
Growth of surface textured ZnO on device	good	post-treatment the device is possible

7.3 Optimization of surface texture of double-textured ZnO:B films

coated on white glass substrate

7.3.1 Experimental details

Firstly, we have investigated the relationship between refractive index (*n*) on each side of white glass samples before Reactive Ion Etching (RIE) process and root-mean-square (RMS) surface roughness of ZnO:B films coated by MOCVD technique on either side of the glass after etching. White glass samples with different refractive indices of each side were etched by the RIE technique using mixture of carbon tetrafluoride (CF_4) and oxygen (O_2) as an etchant gas, before ZnO:B film deposition, in order to find the relationship between the refractive index of the glass and the RMS surface roughness of the ZnO:B films. The ZnO:B films were then deposited on the RIE-etched glass samples, by the MOCVD technique using water (H_2O) as an oxidant for diethylzinc (DEZ) and 1%-hydrogen-diluted diborane (B_2H_6) as a dopant gas. The thickness of the ZnO:B films was kept constant at around 2 µm. The conditions for ZnO:B film deposition are given in the previous report [13,35]. Secondly, the morphology of RIE-etched white glass samples and ZnO:B films deposited on those white glass substrates was investigated with varying the etching time. The time required for white- glass-sample etching was varied from 0 (without etching) to 150 min. The etching pressure and the RF (radio frequency) power density were kept constant at 18 Pa and 1.5 W/cm^2 (200 W), respectively.

The refractive index and other optical properties such as haze value of the white glass sample and ZnO:B-coated white glass substrates were measured by Spectroscopic Ellipsometry (SE) and by Spectrophotometer, respectively. The optical properties such as transmittance and reflectance of the substrates were measured by a

Shimadzu dual beam UV/VIS/NIR Solid-spec 3700 spectrophotometer equipped with an integrating sphere. A monochromatic beam produced by a grating over the wide wavelength range is directed on the glass side of the substrates, through the entrance port of the integrating sphere. Next, the surface morphology and RMS surface roughness of the etched white glass samples and those ZnO:B films coated on the white glass samples were evaluated by a scanning electron microscope (SEM) and by an atomic force microscope (AFM), respectively.

Figure 7-4 shows the refractive index of each side of the white glass and the SEM surface morphology of ZnO:B coated on them. From these SEM images, it was found that the surface morphology of ZnO:B coated on the white glass side with lower *n* is more suitable for the fabrication of solar cells than the other one because double-textured (W-textured) ZnO:B morphology with high surface roughness was observed in the first case. This can also be confirmed by looking at the spectral haze value as shown in figure 7-5. The ZnO:B coated on the glass side with lower *n* has a higher haze value than the one with higher *n*. The difference between the refractive index of both sides of the white glass is probably due to the manufacturing method of the glass, (float glass manufacturing method); in this manufacturing method, Tin (Sn)[2] from the floating bath diffuses and forms tin oxide (SnO_x) on the glass surface. It seems that this SnO_x layer increases the refractive index and reduces ability of RIE etching.

---

[2] Tin is suitable for the float glass process because it has a high specific gravity, is cohesive and is immiscible into the molten glass. The glass flows onto the tin surface forming a floating ribbon with perfectly smooth surfaces on both sides and an even thickness.

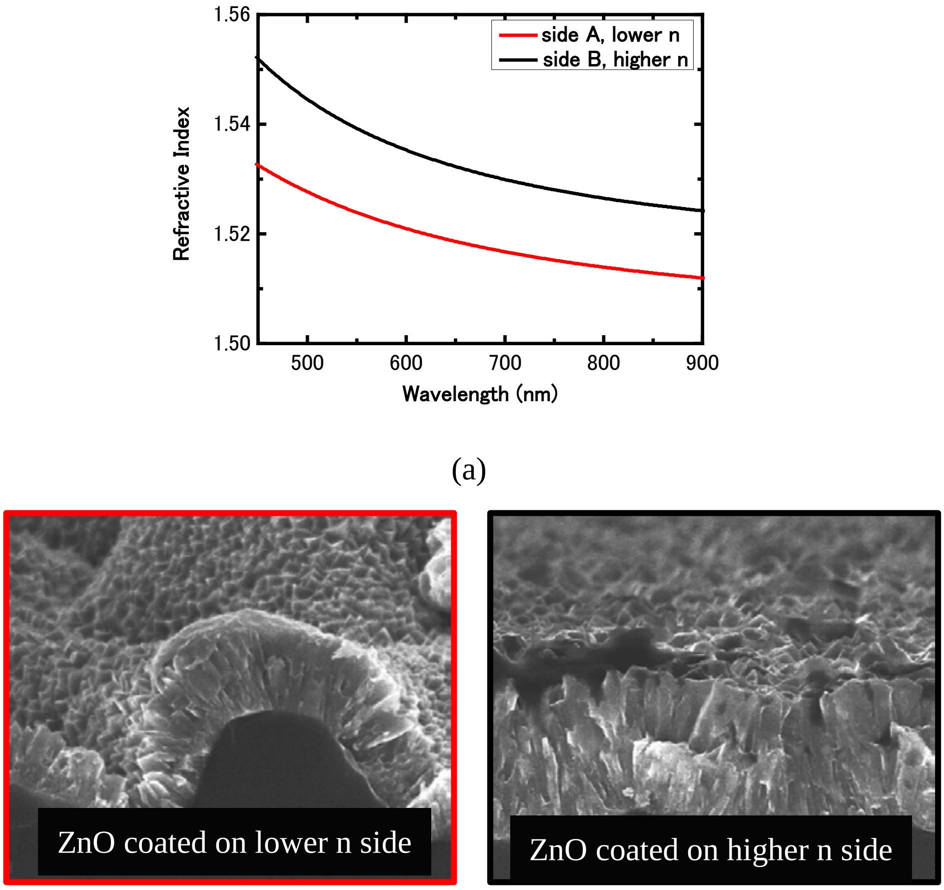

(a)

(b)

Figure 7-4 (a) Refractive index (*n*) of each side of the white glass and (b) SEM images of their ZnO:B-coated on each side; side-a is the side with lower *n*, side-b is the side with higher *n*

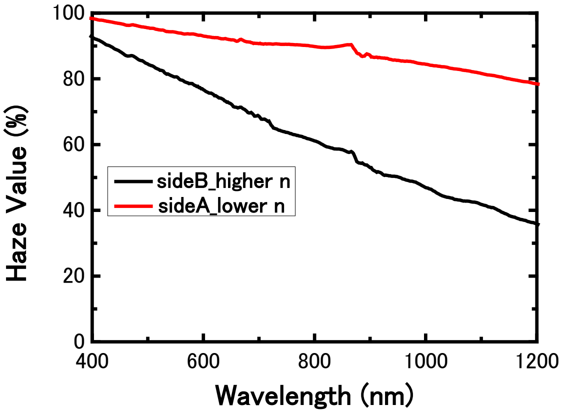

Figure 7-5 Spectral haze value of ZnO:B film coated on each side of the white glass

7.3.2 Evaluation of surface morphology of etched white glass samples and ZnO:B films coated on those white glass substrates with different etching time

The white glass sample was etched by RIE using a mixture of CF_4 and O_2 as the etchant gas. The surface morphology and RMS roughness of the RIE-etched white glass samples was observed by varying the etching time from 0 (without etching) to 150 min as shown in figure 7-6 and 7-7. Figure 7.6 presents the surface images of the etched glass samples before ZnO:B deposition with varied glass-etching time. with increasing the etching time from 0 to 60 min, the surface of the etched glass changed from a flat surface to a lot of larger craters with lateral size of ~2μm, depth size of 2~4 μm. some of the distinct larger texture surface with lateral feature size and depth size of more than 6 μm can be observed when the etching time was increased up to 120 min. However, with increasing the etching time up to 150 min the glass surface was occupied by smaller feature size than the one with shorter etching time. Figure 7.7 shows the AFM images and RMS roughness of the etched glass samples before ZnO:B film deposition with various glass-etching time. From the figure, one can note that the feature of the etched glass with larger lateral size and deeper depth size can be found when the etching time increased. At the same time, the RMS roughness of etched glass increased from ~33 nm to ~206 nm as the etching time increased up to 120 and decreased down to ~ 161 nm with etching time up of longer than 120 min: here, it was 150 min. This indicated the same tendency with feature size measured by SEM micrograph investigation. Thus, we can conclude that there is a relationship between feature size and RMS roughness; the difference in RMS roughness probably caused by largely enhanced lateral feature size and depth size of the etched white glasses.

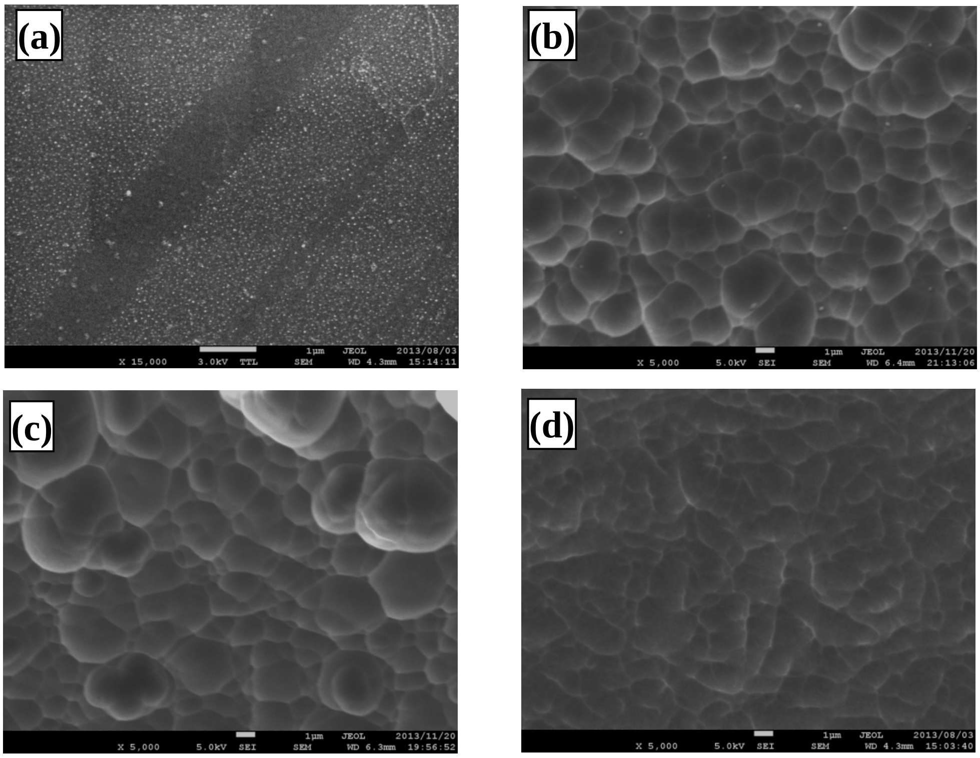

Figure 7-6 SEM micrographs of glass substrates prior to ZnO:B films deposition with various etching time. (a) 0 min (without etching), (b) 60 min, (c) 120 min, (d) 150 min

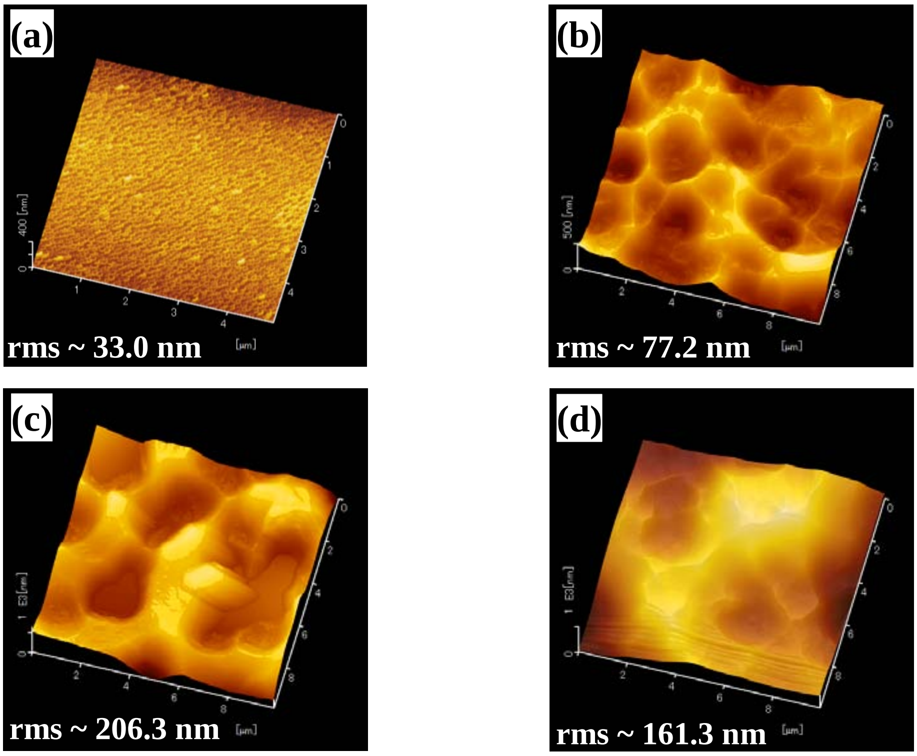

Figure 7-7 AFM images of glass substrates prior to ZnO:B film deposition with various etching time: (a) 0 min (without etching) (b) 60 min, (c) 120 min, (d) 150 min; The RMS roughness of each glass is also shown

Here, the surface morphology of ZnO:B film deposited on the etched white glass with different etching time was investigated and discussed. The ZnO:B films were prepared on the etched white glass samples with the different etching time, i.e. 0 (without etching), 60, 120 and 150 min. The SEM images and AFM morphology were measured and depicted in the figure 7-8 and 7-9, respectively. In the figure 7-8, one can see that the ZnO:B film on the non-etching glass showed typical pyramidal texture like the conventional one coated on the flat corning glass. On the other hand, other ZnO:B films deposited on the etched-glasses with different etching time of 60, 120 and 150 min showed the mountain-chain-like double texture with various larger feature sizes, especially, ZnO:B films with larger feature size on the glass samples etched for 120 and

160 min. However, the lateral feature size of the ZnO:B film for the etching-time 150 min was smaller than the one with etching-time 120 min and also the depth of valley at grain boundary became deeper, which more defect will easily occur when it is applied to solar cells, especially in microcrystalline solar cells [30]. In addition, the figure 7-9 presents AFM images of ZnO:B films as a function of glass-etching time. As we can see in the figure, the RMS roughness of ZnO:B films remarkably increased from ~72 to ~213 nm when the etching-time increased from 0 to 120 min and became ~120 nm for the etching-time of 150 min. Consequently, the highest RMS roughness and larger feature size were obtained for the etching-time of 120 min. For this optimized glass substrate with higher RMS roughness and larger feature size, the further-improved light-scattering can be expected when it is applied to solar cells [16]. In conclusion, as mentioned in our previous work, it is evident that the micro-size surface morphology of ZnO:B films strongly results from the morphology of the etched-glass samples; the larger texture glass sample it is the higher RMS roughness of ZnO:B films coated on it has [31]. These results clearly revealed that the surface morphology of ZnO:B films could be modified by controlling the glass sample surface.

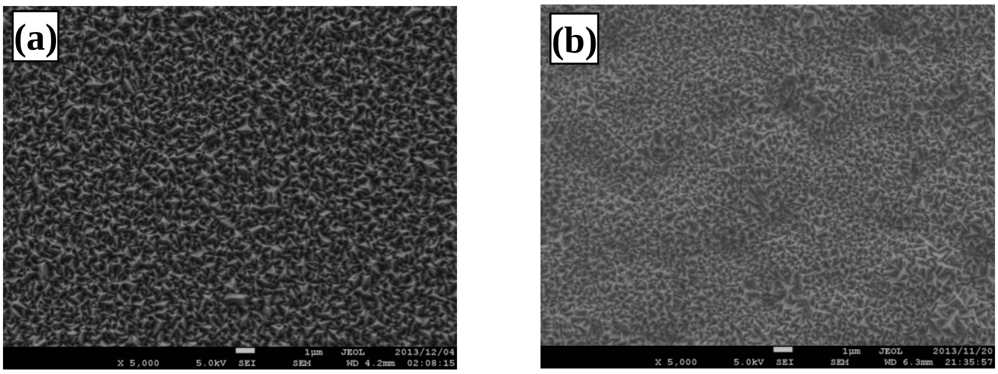

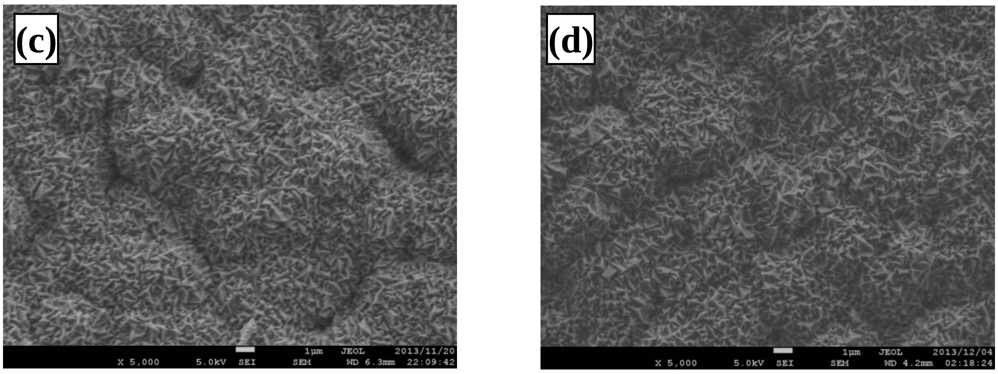

Figure 7-8 SEM micrographs of ZnO:B films as a function of glass-etching time: (a) 0 (without etching), (b) 60, (c) 120, (d) 150 min

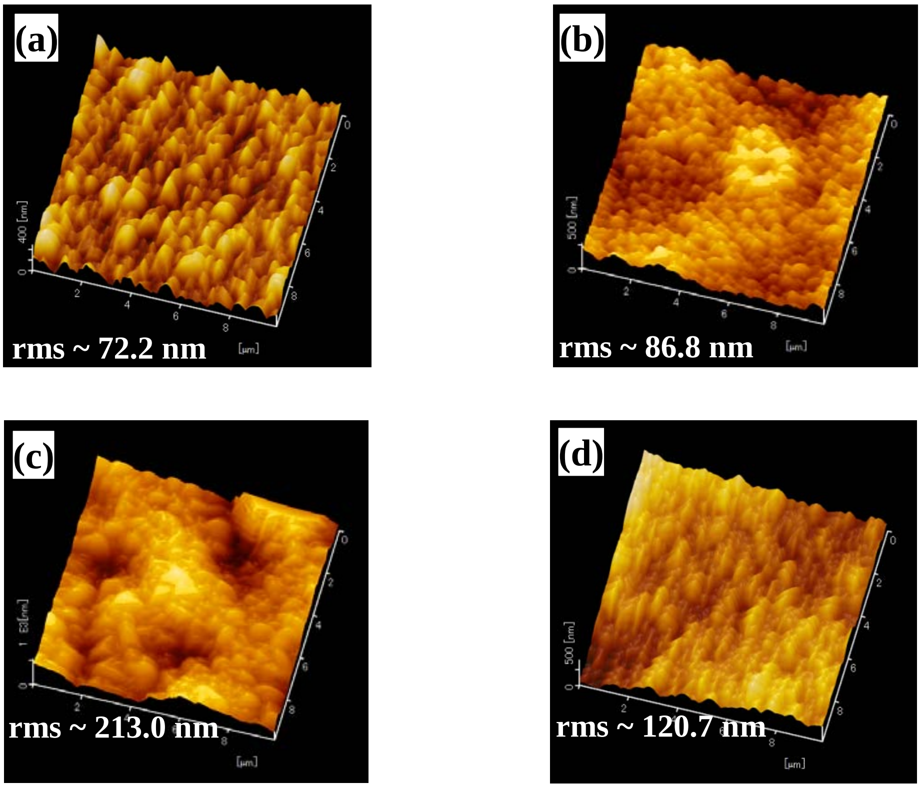

Figure 7-9 AFM images of ZnO:B films as a function of glass-etching time: (a) 0 (without etching), (b) 60, (c) 120, (d) 150 min; The RMS roughness of each film is also shown

7.3.3 Optical properties of double-textured ZnO:B films coated on white glass substrates with different etching time

Next, the transmittance and haze value of the ZnO:B films coated on etched-glass sample were measured and presented in the figure 7-10. From the result, the transmittance of more than 80% can be found over wavelength region for all ZnO:B-coated glass substrates. However, the transmittance of all substrates gradually decreased in the long wavelength region, especially longer than 1000 nm, due to the influence of free carrier absorption in films [32]. At the same time, the haze value showed the similar tendency with RMS roughness of the substrates. The haze value improved up to higher than 90% at the wavelength 0f 800 nm as the etching-time increased from 0 to 120 min and slightly decreased for the etching time of 150 min. these results indicated that the high RMS roughness led to high haze value and the light-scattering effect can be improved by optimizing the glass sample treatment before ZnO:B deposition.

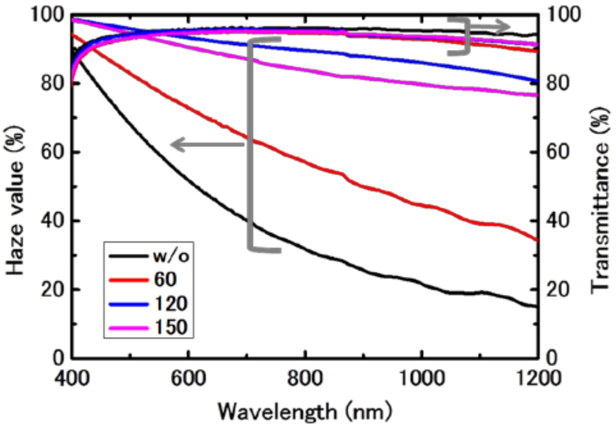

Figure 7-10 Transmittance and Haze value of ZnO:B films deposited on etched-glass sample with various etching-time

Furthermore, angular distribution function (ADF) of each ZnO:B film under various etching-time was measured at the wavelength of 600 and 1000 nm as shown in the figure 7-11. ADF, which is an intensity ratio between direct-transmitted light and each scattered-angle`s light, indicate how much potential a TCO substrate has for application to solar cells as a front contact. Namely, the higher ADF at each scattered-angle shows greater potential for use as a TCO substrate. As we can see from the figure 7-11, the both of ADF at the wavelength of 600 and 1000 nm was enhanced with increasing the etching-time up to 120 min and slightly decrease in ADF was found for the etching-time of 150 nm. The highest ADF could be obtained from the substrate etched by RIE for 120 min. As reported in a paper, the higher ADF shows the improved current density in a-Si:H solar cell [33]. As a result, the higher current density of solar cells can be expected by applying the ZnO:B substrate etched by RIE for 120 min.

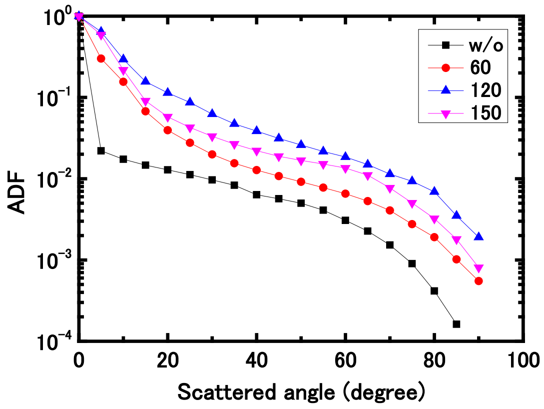

(a)

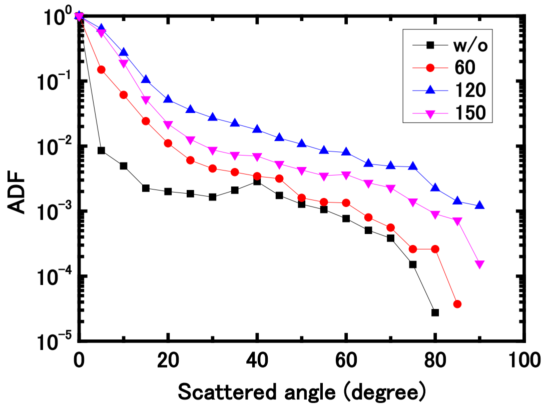

(b)

Figure 7-11 Angular distribution function (ADF) of ZnO:B films, deposited on etched-glass sample with different etching-time, measured at (a) 600 nm and (b)1000 nm

7.4 Fabricated of novel a-Si:H/μc-Si:H double junction solar cells on the white glass substrates compared to the conventional one fabricated on flat corning glass

In this part, novel a-Si:H/ μc-Si:H double-junction solar cells with the layer sequence: white glass/ W-textured ZnO:B/ p-a-SiO_x:H/ i-a-Si:H/ n-μc-SiO_x:H/ p-μc-Si:H/ i-μc-Si:H/ n-μc-SiO_x:H/ Ag/ Al were fabricated on the optimized white glass substrate by a conventional plasma enhanced chemical vapor deposition (PECVD) system using silane (SiH_4), hydrogen (H_2), diborane (B_2H_6), phosphine (PH_3) and carbon dioxide (CO_2) as source gases, at substrate temperatures of about 220 ^{o}C. Also, the novel double-junction solar cells with the structure were fabricated on the etched soda-lime glass in order to compare the ones fabricated on the white glass substrates. For the a-Si:H/ μc-Si:H double-junction solar cell fabrication, i-layer thickness of a-Si:H and µc-Si:H were around ~300 nm and ~2 µm, respectively. The current-voltage characteristics of the fabricated solar cells were measured under 1-sun (AM1.5, 100 mW/cm^2) illumination. The external quantum efficiency (*EQE*) measurement was performed to estimate the spectral response of these solar cells.

The comparison of SEM surface morphology for ZnO:B films deposited on etched white glass with those deposited on etched soda-lime glass was presented in figure 7-12. As we can see the results, one can observe significant differences in the surface morphology: in case of ZnO:B film deposited on etched soda-lime glass one has cauliflower-like double texture (W-texture), whereas in case of ZnO:B deposited on etched white glass one has mountain-chain-like double texture. Moreover, as shown in figure 7-13 the mountain-chain-like W-texture of ZnO:B deposited on etched-white glass led to higher haze value over the whole wavelength region than the conventional pyramidal texture of flat corning glass. Again, higher transmittance over all the wavelength region can also be observed for mountain-chain-like W-texture ZnO:B. From a fundamental point of view, for the front TCO substrate of thin-film silicon solar cells, we need to have the right shape of texture with larger feature sizes and larger angles at the tip of texture: the latter property will minimize cell shunting occurring at the tip according to the report presented by AIST group, Japan [30]. At the same time we also need to have a high haze value in order to enhance the right-trapping effect. The mountain-chain-like shape of texture found in the case of the white glass substrate is a suitable shape, which can serve all requirements and can lead to higher solar cell performance, since this mountain-chain-like shape has fewer valleys, which cause the cracks in the film [34]. Hence, improved performance for solar cells fabricated on this kind of white glass substrate is expected.

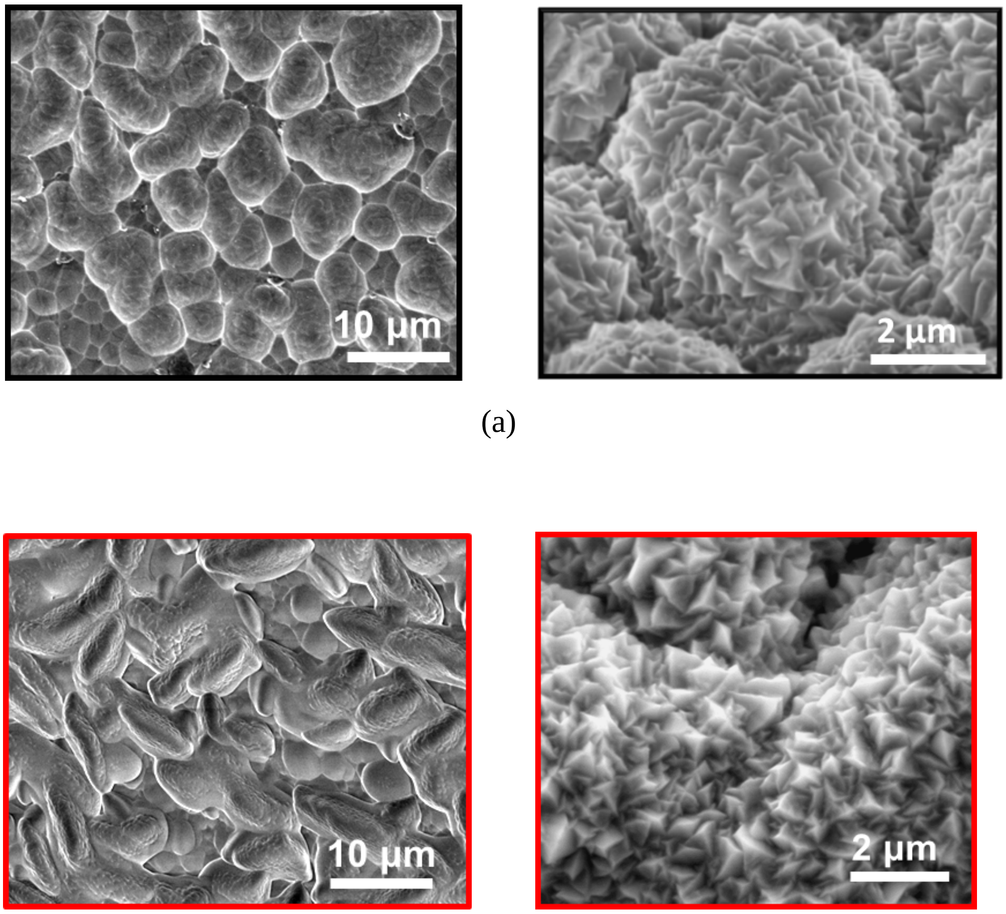

(a)

(b)

Figure 7-12 SEM micrographs of two glass samples and their ZnO:B films coated on (a) flat corning glass and (b) etched-white glass

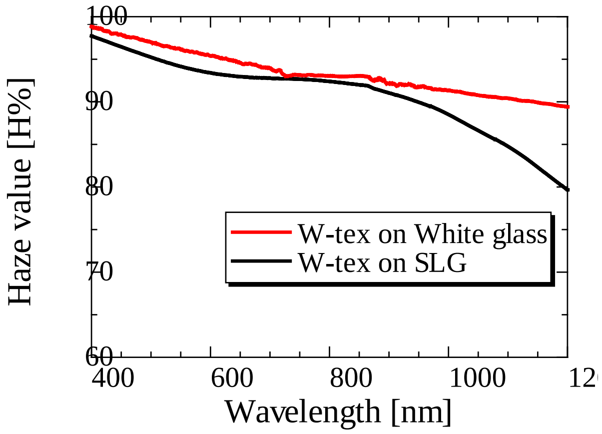

Figure 7-13 Haze value of ZnO:B films deposited on etched-glass sample

Novel a-Si:H/μc-Si:H double-junction solar cells were fabricated on double-textured ZnO:B-coated white glass substrates compared with the one fabricated on etched soda-lime glass . Figure 7-14 presents the current-voltage (*I-V*) characteristics and external quantum efficiency (*EQE*) of the tandem solar cell fabricated on the W-textured ZnO:B-coated white glass substrate in comparison with the one fabricated on W-textured ZnO:B-coated etched-soda-lime glass substrate. As we can see from these results the white glass substrate leads to an increase in J_{sc} from 12.2 mA/cm^2 to 13.4 mA/cm^2, corresponding to the improved spectral response, especially in the long wavelength region (>500 nm). As a result, the a-Si:H/ μc-Si:H solar cell fabricated on this newly developed white glass substrate has a high initial efficiency of 13.3% which is higher than the one obtained for soda-lime glass, demonstrating, thereby, that this newly developed W-textured substrate is a promising material for the fabrication of high-efficiency thin-film silicon solar cells.

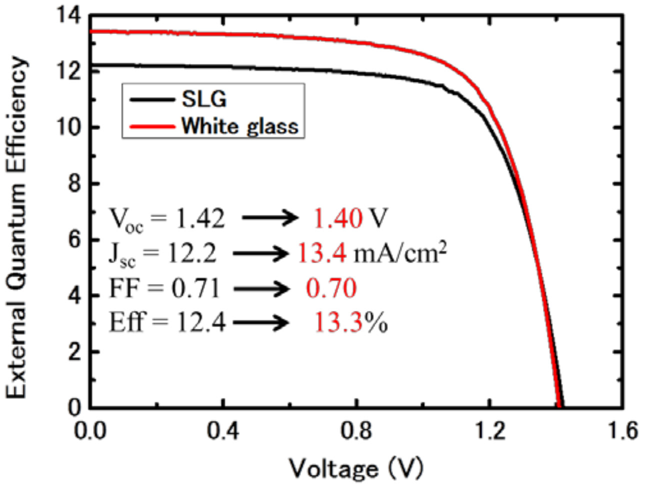

(a)

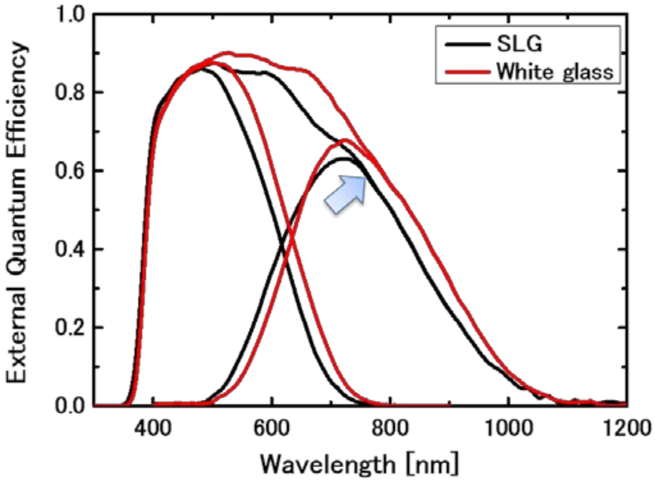

(b)

Figure 7-14 (a) *I-V* characteristics and (b) Quantum efficiency of the tandem solar cells fabricated on flat corning glass and etched white glass substrates

7.5 Summary

In this chapter, we have successfully fabricated W-textured ZnO:B films, with a very high haze value and greater angular distribution function (ADF), coated on white glass. At the beginning the effect of glass-etching time on the morphology and optical properties of the substrates was investigated to find the optimal properties for use as a front TCO contact in solar cells. It was found that the surface morphology of ZnO:B films deposited, by MOCVD, on white glass samples is mountain-chain-like double texture, while the one of ZnO:B films deposited on soda-lime glass samples shows cauliflower-like double texture. Moreover, the mountain-chain-like double texture of the white glass results in a haze value, which is higher over the whole wavelength region than the conventional cauliflower-like double texture obtained for soda-lime glass (SLG). ZnO:B-coated substrates with a larger feature size of 10 μm were obtained with longer RIE etching times. By applying these white glass substrates to a-Si:H/μc-Si:H tandem solar cells, the short-circuit current density J_{sc} could be increased from 12.2 mA/cm^2 to 13.4 mA/cm^2, corresponding to an improved spectral response, especially in the long wavelength region (>500 nm). Consequently, the initial efficiency of the solar cells could be increased up to 13.2 %. Therefore, the ZnO:B films obtained here, by deposition on etched white glass, should be considered as a basis for promising substrates, for use as front transparent contact layers in silicon-based thin film solar cells.

References

[1] J. Meier, S. Dubail, S. Golay, U. Kroll, S. Fay, E. Vallat-Sauvain, L. Feitknecht, J. Dubail and A. Shah: *Sol. Energy Mater. Sol. Cells* **74** (2002) 457.

[2] S. Fay, U. Kroll, C. Bucher, E. Vallat-Sauvian and A. Shah: *Sol. Energy Mater. Sol. Cells* **86** (2005) 385.

[3] J. Wang, S. Venkataraj, Corsin Battaglia, P. Vayalakkara and Armin G. Aberle: *Jpn. J. Appl. Phys.* **51** (2012) 10NB08.

[4] M. Berginski, J. Hupkes, M. Schulte, G. Schope, H. stiebig, B. Rech, and M. Wuttig et al.: *J. Appl. Phys.* **101** (2007) 074903.

[5] U.kroll et al.: *Proceeding of 26th European Photovoltaic Solar Energy Conference, Hamburg, Germany, Sep 5-9* (2011) 2340.

[6] W. W. Wenas, A. De, A. Yamada, M. Konagai, and K. Takahashi: *Sol. Energy Mater. Sol. Cells* **34** (1994) 313.

[7] X. D. Zhang, Y. Zhao, Y. T. Gao, F. Zhu, C. C. Wei, X. L. Chen, J. Sun, G. F. Hou, X. H. Geng, and S. Z. Xiong: *J. non-Cryst. Solids* **352** (2006) 1863.

[8] P. D. Veneri, L.V. Mercaldo, and I. Usatii: *Appl. Phys. Lett.* **97** (2010) 023512.

[9] P. Buehlmann, J. Bailat, D. Domine, A. Billet, F. Meilaud, A. Feltrin, and C. Ballif: *Appl. Phys. Lett.* **91** (2007) 143505.

[10] D. Domine, P. Buehlmann, J. Bailat, A. billet, A. Feltrin, and C. Ballif: *Phys. Stat. Sol. (RRL)2,* **4** (2008) 163.

[11] T. Grundler, A. Lambertz, and F. Finger: *Phys. Status Solidi C7,* **3-4** (2010) 1085.

[12] Susumu Fukuda et al.: *Proceeding of 21st European Photovoltaic Solar Energy Conference, Dresden, Germany, Sep 4-8* (2011)1535.

[13] A. Hongsingthong, T. Krajangsang, I.A. Yunaz, S. Miyajima, and M. Konagai: *Appl.*

Phys. Express **3** (2010) 051102.

[14] H. Wada, R. Ishikawa, K. Nishikubo, P. Sichanugrist, and M. Konagai: *Proceeding of 27th European Photovoltaic Solar Energy Conference, Frankfurt, Germany, Sep 24-28* (2012) 2120.

[15] A. Hongsingthong,T. Krajangsang, B. Janthong, P. Sichanugrist and M. Konagai: Proceeding of 37th IEEE Photovoltaic Specialists Conference ,Washington USA, June 19-24 , 2011, p. 00791.

[16] A.Hongsingthong, T. Krajangsang, H. Fujioka, P. Sichanugrist and M. Konagai: *Proceeding of 26th European Photovoltaic Solar Energy Conference, Hamburg Germany, Sep 5-9* (2011) 2633.

[17] Y. Moriya, T. Krajangsang, P. Sichanugrist and M. Konagai: *Proceeding of 38th IEEE Photovoltaic Specialists Conference, Texas USA, June 3-8* (2012) 003020.

[18] U. Blieske, T. Doege, P. Gayout, M. Neander, D. Neumann and A. Prat: *Proceeding of 3rd World Conference on Photovoltaic Energy Conversion, Osaka, Japan, May 11-18* (2003) 188.

[19] B. Janthong, A.Hongsingthong, T. Krajangsang, L. Zhang, P. Sichanugrist and M. Konagai: *J. Non-Cryst. Solids* **358** (2012) 2478.

[20] H. Schulz and K. H. Thiemann: *Solid State Commun.* **32** (1979) 783.

[21] S. J. Pearton, D. P. Norton, K. Ip, Y.W. Heo and T. Steiner: *Progress in Material Science* **50** (2005) 293.

[22] D. Vogel, P. Kruger and J. Pollmann: *Phys. Rev. B* **52** (1995) 14316.

[23] B. Theys, V. Sallet, F. Jomard and A. Lusson: *J. Appl. Phys.* **91** (2002) 3922.

[24] S. B. Zhang, S.-H., Wei and A. Zunger: *Phys. Rev. B* **63** (2001) 075205.

[25] F. A. Kroger: *The Chemistry of Imperfect Crystals*, North Holland, Amsterdam,

1974.

[26] D. C. Look, J. W. Hemsky and J.R. Sizelove: *Phys. Rev. Lett.* **82** (1999) 2552.

[27] A. F. Kohan, G. Ceder, D. Morgan and C. G. Van de Walle: *Phys. Rev. B* **61** (2000) 15019.

[28] K. Vanheusden, C. H. Seager, W. L. Warren, D. R. Tallant and J. A. Voigt: *Appl. Phys. Lett.* **68** (1996) 483.

[29] C. G. Van de Walle: *Phys. Rev. Lett.* **85** (2000) 1012.

[30] H. Sai, K. Saito, N. Hozuki and M. Kondo: *Appl. Phys. Lett.* **102** (2013) 053509.

[31] H. Wada, A. Hongsingthong, L. Zhang, P. sichanugrist and M. Konagai: *Tech. Dig. 21st PVSEC* (2011).

[32] W. W. Wenas, A. Yamada, K. Takahashi, M. Yoshino and M. Konagai: *J. Appl. Phys*. **70** (1991) 7119.

[33] G. Jost, T. Merdzhanove, T. Zimmermann, J. Kirchhoff, J. Hüpkes: *Proc. of 27th EU-PVSEC* (2013) 2543.

[34] M. Python, O. Madani, D. Domine, F. Meillaud, E. Vallat-Sauvain. And C. Ballif: *Sol. Energy Mater. Sol. Cells* **93** (2009) 1714.

[35] A. Hongsingthong: “*Development of Techniques to Control the Surface Morphology of ZnO Thin Films and Their Applications to Front TCO in Si-based thin Film Solar Cells*”, Doctoral Thesis, Tokyo Institute of Technology (2012).

Chapter 8

General Conclusions and Future Prospects

8.1 General conclusions

This thesis presents the results of research on light-trapping approaches applied to silicon-based thin film solar cells including a-Si:H/μc-Si:H tandem solar cells. We have theoretically and experimentally studied the effects of light-trapping approaches, i.e. the employment of optical layers: n-top layer with function of intermediate layer (nIL), n-bottom layer with function of ZnO back reflective layer (nBRL), front anti-reflection layers inserted between glass/TCO (FAL) and between TCO/p-layer (FALp) as well as double-textured white glass substrate, on solar cell performance. The Numerical analysis of these optical layers: nIL, nBRL and additional refractive-index-mismatch layers (FAL and FALp) was systemically performed using both of simulators called “OPTICAL” and “ASA”. Different silicon oxide (SiO_x) films have been optimized and applied into silicon based thin film solar cells as optical layers corresponding to those of individual application purposes. Firstly, phosphorous-doped μc-SiO_x:H films were optimized and employed into μc-Si:H single-junction solar cells as a nBRL, and then applied to a-Si:H/μc-Si:H double-junction solar cells with novel structure as a nIL and a nBRL. Also, both of a-Si:H and μc-Si:H single-junction solar cells using optimized phosphorous-doped μc-SiO_x:H films as a FALp were fabricated and analyzed. Next, a-Si:H films were optimized and the μc-Si:H single-junction solar cells with the optimized a-Si:H films used as FAL were fabricated and evaluated. Moreover, the a-Si:H/μc-Si:H tandem cell with novel structure, fabricated on newly developed double-textured white glass substrate, was for the first time proposed using optimized nIL and nBRL and the higher efficiency of 13.3% (V_{oc}=1.14 V, J_{sc}=13.40 mA/cm^2, FF=0.70) was achieved.. The main results of this study are described as follows in details.

In chapter 3, optical analysis and theoretical simulation was performed using OPTICAL and ASA simulators, respectively. The optical calculation of IL, nBRL, and FAL using OPTICAL simulator was firstly done to investigate their effect on the optical properties, such as reflectance or transmittance spectra, of the test sample structure simulated from the experimentally fabricated solar cells. We have also studied the effect of refractive index and thickness combinations of single and triple intermediate layers, inserted between sub-cells, on the light-reflectance in the tandem solar cells. From the simulation results, it is clear that the wavelength region of reflection could be freely modified by adjusting the thickness and/or the refractive index of intermediate layers. Compared to the single, the reflectance of SiO_x triple intermediate layers at short wavelength region could be increased, whereas at the long wavelength region could be suppressed. Thus, a multi-stacked intermediate layer, especially triple intermediate layer, would be beneficial for use in a-Si:H /μc-Si:H tandem cell. Furthermore, the optical calculation results indicated that, for a single IL, the lower refractive index IL is the higher reflectance over wavelength region the test structure have. For nBRL, the effect of nBRL with variation of refractive index and thickness on the reflectance spectra of test structure was found out. From the result one can understand that the SiO_x film with refractive index of ~1.9 can be expected to replace at the back reflector instead of n-μc-Si/ZnO layer because the same reflectance could be observed. In addition, the thickness of nBRL should be optimized between 60-80 nm. Then, the optical study of FAL with varied refractive index on transmittance of test model was carried out. As can be found from the results, the optimal FAL obtained from this calculation was the one with refractive index of ~1.74 and the thickness should be 60-80 nm. The finding FAL shows the higher transmittance of test structure when it was inserted into glass/ZnO interface and the thickness of FAL of thicker than 80 nm shows the drop in transmittance spectra particularly, in the short wavelength (< 650 nm). Moreover, the effect of these optical layers (nIL, nBRL and FAL) on the current density of silicon-based thin film solar cells including a-Si:H /μc-Si:H double-junction solar cells was investigated to confirm the results, that is reflectance and transmittance spectra of sample test structure, calculated from OPTICAL simulator. By inserting FAL with different refractive index into μc-Si:H solar cells, it was seen that the current density of the solar cells improved as the refractive index decreased down to ~1.74 but the refractive index less than that showed the reduction in current density, i.e. lower spectral response in the long wavelength region. In the same way, the current density of μc-Si:H solar cells increased when the refractive index of nBRL was decreased down to ~1.74 ; due to greater light-reflection between n-layer/metal electrode. Additionally, nBRL with varied refractive index was also applied into a-Si:H/μc-Si:H solar cells to observe the effect on solar cell performance. By inserting nBRL into the solar cells, the J_{sc} of the bottom solar cells slightly enhanced when the refractive index of the nBRL of the bottom cell became smaller. From this simulation results, it was found that the nBRL with lower refractive index can be used in order to improve the current density of the bottom cell in a double-junction solar cell with a current-limited bottom.

In chapter 4, the preparation and characterization of n-type SiOx films were described. It was found that it is possible to fabricate the n-type SiOx films using 13.56 MHz RF-PECVD technique from a mixture SiH_4, H_2, PH_3 and CO_2 as a source gas. The optical, electrical, and structural properties of the fabricated SiOx films were investigated. The optical band gap and the refractive index of the films could mainly be controlled by variation of CO_2 and H_2 flow rates. The conductivity of the films increased with increasing the PH_3 flow rate, in contrast, it declined with an increase in CO_2 flow rate. Besides, it can also be seen that the films deposited on the high temperature substrate had better conductivity, however, those of refractive index also increased. By optimizing the source gas flow rates and other deposition conditions, a few SiO_x films with refractive index lower than 2.0 and reasonably good in-plane conductivity (~10^{-6} S/cm) have been obtained and are expected to be used in silicon-based thin film solar cells as optical layers, IL, nIL, nBRL, FAL and FALp. Afterwards, each of these optimum films will be applied to thin film silicon solar cells including a-Si:H/µc-Si:H double-junction solar cells as optical layers corresponding to function needs.

In chapter 5, the optimization of n-SiO_x films for use as intermediate layer (IL) inserted between top and bottom cells was firstly performed and their effects on a-Si:H/µc-Si:H performance were studied by adjusting their thickness and optical properties. The results revealed that the IL that we have optimized was effective to be applied into the tandem solar cells. Also, We for the first time proposed a-Si:H/ µc-Si:H double-junction solar cells with novel structure of p-a-SiC:H/ i-a-Si:H/ n-SiO_x:H/ p-µc-SiO:H/ i-µc-Si:H/ n-SiO_x:H/ Ag/ Al as a candidate to lower the optical losses and thus increase the solar cell performance, especially current density (J_{sc}). By using the optimum n-SiO$_x$:H layer instead of n-µc-Si:H/ZnO back reflector into a µc-Si:H single-junction solar cell as a nBRL, the spectrum response, particularly, at the long wavelength could be improved and then Jsc value was relatively increased up to 4.4%. Similarly, for the a-Si:H/µc-Si:H solar cell with novel structure using the proper dual-functional n-SiO$_x$:H layers as a nIL and a nBRL, the relative improvement in J_{sc} value by 9% was obtained and therefore the initial efficiency as high as 11.9% (V_{oc}=1.38 V, J_{sc}=12.24 mA/cm^2, FF=0.70) was achieved. These results approved that the first layer of newly developed n-SiO$_x$:H layers (nIL) can work as an n-layer of the top cell and at the same time it can also be functioned as an IL. On the other hand, the second n-SiO$_x$:H layer (nBRL) can work as an n-layer of the bottom cell and a ZnO back reflective layer. As a result, the reduction in optical losses could be obtained. Furthermore, these novel solar cell structures are beneficial for mass production since they were simplified.

In chapter 6, characterization of a-SiO$_x$ films has been defined by studying optical properties of films used for a FAL. The optical properties of a-SiO$_x$ films were investigated by transmittance, reflectance, and haze value measurement. Also, electrical properties of ZnO:B films coated on glass/a-SiO$_x$ substrate were investigated in order to confirm effect of FAL on properties of ZnO:B films compared to the sample without a-SiO$_x$ FAL. Then, µc-Si:H solar cells with the optimized a-SiO$_x$ FAL were fabricated to compared the ones without FAL. The effect of applying the optimized a-SiO$_x$ FAL on the solar cell performance was also discussed here. From the results, the optical reflection loss of the glass/ZnO interface can be reduced by applying the optimal SiO$_x$

FAL to the solar cells. By inserting optimized SiO_x FAL with n of ~1.75 into the glass/ZnO interface of the µc-Si:H solar cell, J_{sc} could relatively be increased by about 5%, especially in the 550-950 nm region. Furthermore, this optimized FAL did not deteriorate the properties of the ZnO layer as well because no significant changes in V_{oc} and *FF* were observed. As a result, the cell with an efficiency as high as 8.28% (V_{oc} = 0.495 V, J_{sc} = 25.09 mA/cm^2, *FF* = 0.667) could be realized. A higher current density of bottom cells in multi-junction solar cells can also be obtained by incorporation of the optimized FAL

Moreover, optimization of n-µc-SiO_x:H films was also performed to find the films with excellent properties for application to silicon-based thin film solar cells, i.e., a-Si:H and µc-Si:H solar cells. The n-µc-SiO_x:H film with E_{04} of ~2.68, n of ~2.31 and sufficient conductivity was obtained and the effect of this optimized film on the performance of a-Si:H and µc-Si:H solar cells was also discussed. From the results, the optical reflection loss of the ZnO/p-silicon interface can be decreased by applying the optimal SiO_x FALp at that interface. By inserting SiO_x FALp optimized so far with n of ~2.68 and and E_{04} of ~2.31 eV into the ZnO/p-silicon interface of both a-Si:H and µc-Si:H solar cell, *QE* at the short and long wavelength regions are slightly decreased and increased respectively. For µc-Si:H solar cell, J_{sc} (obtained from *QE* measurment) improved by ~0.4 mA/cm^2, especially in the 500-900 nm region. Furthermore, with FALp no significant change in V_{oc} and *FF* of fabricated solar cells was observed. However, the spectral response at short wavelength region (<500 nm) for both a-Si:H and µc-Si:H solar cells was reduced. This is probably because that the thickness and refractive index of SiO_x FALp films has not been optimized yet. The further optimization of the film is required. Multi-junction solar cells with higher efficiency are also expected to achieve by the incorporation of further optimized FALp. This trend is similar to the one using TiO_2. The results show that this novel n-μc-SiOx:H film will be beneficial for use as a front anti-reflection layer instead of TiO_2/ZnO.

In addition, we have employed plasma treatment technique prior to the deposition of p-μc-SiO_x:H layer of bottom cells in order to improve interface between n-SiO_x:H top-layer/ p-μc-SiO_x:H bottom-layer. The CO_2 plasma condition was characterized and optimized. After, the optimized CO_2 plasma condition, we have done so far, was applied into a-Si:H/μc-Si:H solar cell. From the results, we can see that the optimized CO_2 plasma condition could improve *FF*. On the other hand, the current density deteriorated and smaller solar cell efficiency was observed. These results reveal that the CO_2 plasma technique can be one of promising methods for improvement of solar cell performance. However, CO_2 plasma condition, we have used here, has to be further studied in order to avoid the reduction of current density, especially, bottom cells.

In chapter 7, In this chapter, we have successfully fabricated W-textured ZnO:B films, with a very high haze value and greater angular distribution function (ADF), coated on white glass. At the beginning the effect of glass-etching time on the morphology and optical properties of the substrates was investigated to find the optimal properties for use as a front TCO contact in solar cells. It was found that the surface morphology of ZnO:B films deposited, by MOCVD, on white glass samples is mountain-chain-like double texture, while the one of ZnO:B films deposited on soda-lime glass samples shows cauliflower-like double texture. Moreover, the mountain-chain-like double texture of the white glass results in a haze value, which is higher over the whole wavelength region than the conventional cauliflower-like double texture obtained for soda-lime glass (SLG). ZnO:B-coated substrates with a larger feature size of 10 μm were obtained with longer RIE etching times. By applying these white glass substrates to a-Si:H/μc-Si:H tandem solar cells, the short-circuit current density J_{sc} could be increased from 12.2 mA/cm^2 to 13.4 mA/cm^2, corresponding to an improved spectral response, especially in the long wavelength region (>500 nm). Consequently, the initial efficiency of the solar cells could be increased up to 13.2 %. Therefore, the ZnO:B films obtained here, by deposition on etched white glass, should be considered as a basis for promising substrates, for use as front transparent contact layers in silicon-based thin film solar cells.

8.2 Future Prospects

As mentioned above, the main achievement of this work was the fabrication of the novel a-Si:H/μc-Si:H double-junction solar cell with conversion efficiency as high as 13.2% (V_{oc}=1.41V, J_{sc}=13.40 mA/cm^2, FF=0.70) by implementing the techniques as follows (i) employing the optimized optical layers, i.e. intermediate layer (IL), intermediate layer with function of n-top layer (nIL), n-bottom layer with function of back reflective layer (nBRL), as well as anti-reflection layers inserted glass/TCO interface (FAL) and TCO/P-Si layer (FALp) as additional refractive-index matching layers, (ii) new development of double-textured ZnO:B coated on etched white glass substrates. By applying these techniques into silicon-based thin film solar cell, I-V parameters, especially J_{sc}, were improved and thus higher conversion efficiency was also achieved. However, in this study, there still are some challenges of developing techniques and room for improvement of solar cell performance. In case of IL and nIL, the higher J_{sc} can be obtained and current-matching can be improved by further optimizing optical (more lower n) and electrical (more higher conductivity) of μc-Si:H films use as nIL for n-top, n-middle and n-bottom layers in triple-junction solar cells. In case of FALp, the spectral response in short wavelength region should be improved and then J_{sc} increased by further trading off electrical and optical properties. Also, in order to obtain greater V_{oc} and *FF,* plasma treatment, for example, here CO_2 plasma, have to be employed between n/p interfaces in each sub-cell to improve contact property. Also, as reported in many papers, application of multi-junction solar cell, e.g., a-Si:H/ a-SiGe:H/ μc-Si:H triple junction solar cells, is also necessarily performed in order achieve superior solar cell performance. As shown in figure 8-1, the integration of the techniques mentioned above is described. By using these techniques, the highest conversion efficiency of ~21%, which was the value calculated from theoretical analysis in our group, can be expected. Moreover, in order to reach that goal, further theoretical analysis considering light-scattering effect, refractive index and other optical properties of the TCO substrate, p-i-n layer for each component cell, as well as back electrode should be performed to more understanding of a complete device and obtain more reliable results.

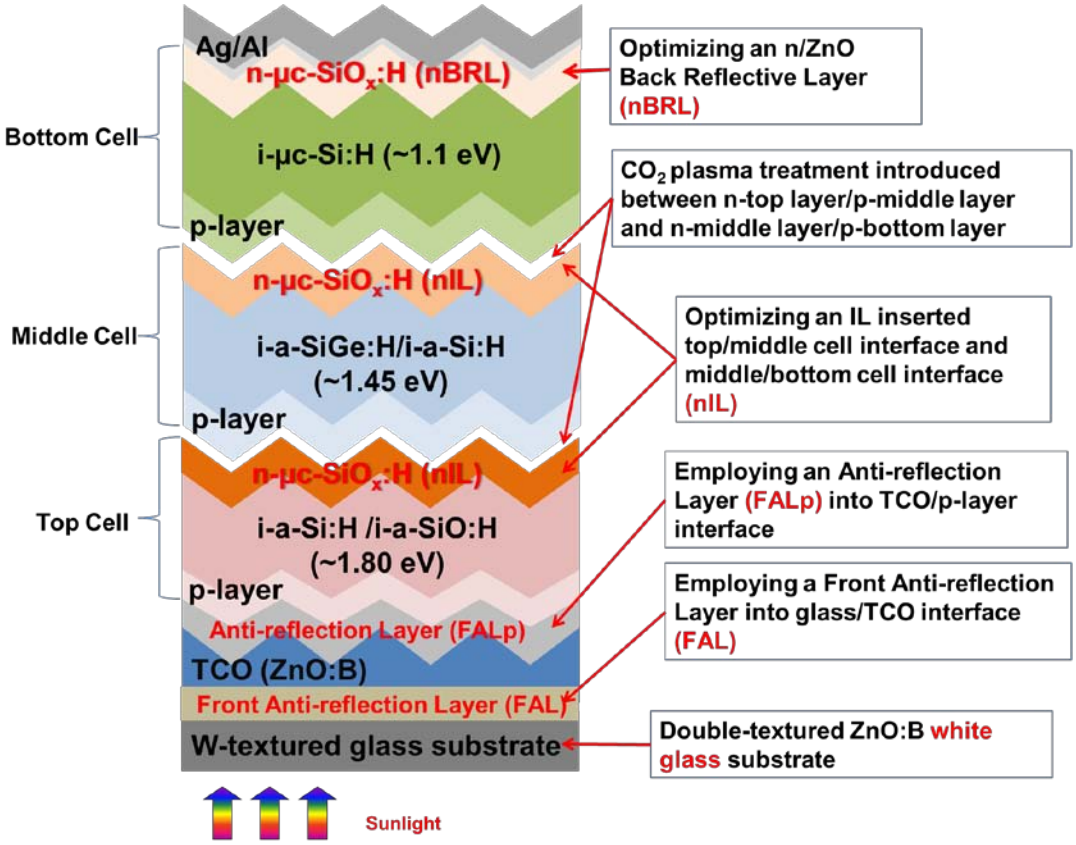

Figure 8-1 Expected applications of light-trapping approaches and additional techniques to multi-junction solar cells such as a triple junction solar cell.

Acknowledgements

While working on this thesis, the author has the benefit of consultations with and communications from many members at Konagai/Miyajima Lab and Yamada Lab. The author wishes to take this opportunity to thank them all for their valuable suggestions and support. Firstly, the author is sincerely indebted to Professor Makoto Konagai for his patience, guidance, and warm inspiration through the author`s graduation study.

The author`s acknowledgements are also to Professor Akira Yamada and Associate Professor Shinsuke Miyajima, for their valuable advices, comments, and suggestions through this study.

The author would like to give special thanks to Professor Mitsumasa Iwamoto, Professor Shigeki Nakagawa, Dr.Yukimi Ichikawa (JST Future-PV), for their valuable comments and encouragements.

The author would also like to express my appreciation to Dr. Porponth Sichanugrist, Dr. Ihsanul Afdi Yunaz, Assistant Prof. Yasuyoshi Korokawa, Assistant Prof. Yuzuru Ueda and Dr.Tatsuro Watahiki, for their warm and constructive advises, critical comments and kindly support throughout this study.

The author would like to express my gratitude to Professor Christopher Wronski (Pennsylvania State University), Professor Jürgen H. Werner (University of Stuttgart), Professor Ruud E.I. Schropp (Utrecht University) and Prof. Arvind Shah (PV-Lab, IMT Neuchâtel) for their contribution and advices to my study.

The author would also like to thank Mr.Hidetaka Tokioka and Shinsaku Yamaguchi (from Mitsubishi Electric Corporation) for their critical comments and

valuable discussions in research collaboration in 2010.

The author also wishes to thank all members of the Konagai Lab and Yamada Lab, especially EIKO System members those who made a lot of effect to start up the new system and discuss the valuable experimental data, especially Drs. Shunsuke Kasashima, Liping Zhang, Aswin Hongsingthong, Taweewat Krajangsang, Sorapong Inthisang, Do Yun Kim, Messrs. Hidetoshi Wada, Hideaki Fujioka, Yuki Moriya, Ms. Shinae Kim and all other EIKO team members, as well as the author`s classmates, Messrs. Daisuke Hamashita, Shigeru Yamada and Satoshi Onishi, who participated in the interesting discussions and made suggestions for improving the research work through this study and enjoying my daily life during staying in Japan.

And also, special thanks are also extended to the secretaries for their kind assistance for daily and campus life: Ms. Kimiko Furukawa, Ms. Manami Kawauchi, Ms. Yuko Yoshida, Ms. Yuki Kojima and Ms.Rie Mikado.

Last but not least, the author is greatest debt to the author`s beloved family for their love, patience, care and worm encouragement to overcome the challenges and problems throughout doing this research. Without their support and help, the author could not have succeeded in this thesis.

March 2013

Bancha Janthong

List of publications

Journal Papers

1. Bancha Janthong, Aswin Hongsingthong, Taweewat Krajangsang, Liping Zhang, Porponth Sichanugrist and Makoto Konagai
   "Novel a-Si:H/μc-Si:H tandem cell with lower optical loss"
   Journal of Non-Crystalline Solids 358 (2012) 2478-2481.

2. Bancha Janthong, Aswin Hongsingthong, Yuki Moriya, Porponth Sichanugrist, Christophe R. Wronski and Makoto Konagai
   "Optical Improvement of ZnO-Coated Glass with New Refractive-Index Matching Layer Inserted at Glass/ZnO Interface"
   Japanese Journal of Applied Physics 51 (2012) 10NB14.

3. Bancha Janthong, Yuki Moriya, Aswin Hongsingthong, Porponth Sichanugrist and Makoto Konagai
   "Management of light-trapping effect for a-Si:H/μc-Si:H tandem solar cells using novel substrates, based on MOCVD ZnO and etched white glass"
   Solar Energy Materials and Solar Cells 119 (2013) 209-213

International Conferences

1. Bancha Janthong, Ihsanul Afdi Yunaz, Hidetada Tokioka, Shinsuke Miyajima and Makoto Konagai
   "Optical Design of Multi-Stacked Intermediate Layer with Wavelength-Selective Reflectance for a-Si:H/μc-Si:H Tandem Solar Cells"
   35th IEEE Photovoltaic Specialists Conference, Hawaiian Convention Center in Waikiki, Hawaii, USA, June 20-25, 2010 (poster presentation)

2. Bancha Janthong, Taweewat Krajangsang, Aswin Hongsingthong, Liping Zhang, Porponth Sichanugrist and Makoto Konagai
   "Improvement of Internal Light-Trapping for Silicon Based Solar Cells with a Newly

Developed Structure”
37th IEEE Photovoltaic Specialists Conference, Washington State Convention Center, Seattle, Washington, USA, June 19-24, 2011 (poster presentation)

3. Aswin Hongsingthong, Taweewat Krajangsang, Bancha Janthong, Porponth Sichanugrist and Makoto Konagai
“Effect of High-Haze Zinc Oxide Films Fabricated on Soda-Lime Glass Substrate for Thin-Film Silicon Solar Cells”
37th IEEE Photovoltaic Specialists Conference, Washington State Convention Center, Seattle, Washington, USA, June 19-24, 2011 (oral presentation)

4. Shunsuke Kasashima, Ryohei Uzawa, Bancha Janthong, Sorapong Inthisang, Taweewat Krajangsang, Porponth Sichanugrist and Makoto Konagai
“Performance of Multi-Junction Silicon-Based Thin Film Solar Cells Under Concentrated Sunlight”
37th IEEE Photovoltaic Specialists Conference, Washington State Convention Center, Seattle, Washington, USA, June 19-24, 2011 (poster presentation)

5. Bancha Janthong, Aswin Hongsingthong, Taweewat Krajangsang, Liping Zhang, Porponth Sichanugrist and Makoto Konagai
“Novel a-Si:H/μc-Si:H Tandem Cell with Lower Optical Loss”
24th International Conference on Amorphous and Nanocrystalline Semiconductors, Nara, Japan, August 21-26, 2011 (oral presentation)

6. Sorapong Inthisang, Taweewat Krajangsang, Bancha Janthong, Porponth Sichanugrist and Makoto Konagai
“Fabrication of Novel Structure a-$Si_{1-x}O_x$:H/a-Si:H/μc-Si:H Triple-Junction Solar Cells ”
26th European Photovoltaic Solar Energy Conference and Exhibition, CCH Congress Center and International Fair, Hamburg, Germany, September 5-9, 2011 (oral presentation)

7. Bancha Janthong, Aswin Hongsingthong, Yuki Moriya, Porponth Sichanugrist, Christophe R. Wronski and Makoto Konagai
   "Optical Improvement of ZnO-Coated Glass with New Refractive-Index Matching Layer Inserted at Glass/ZnO Interface"
   21st International Photovoltaic Science and Engineering Conference, Hilton Fukuoka Sea Hawk, Fukuoka, Japan, November 28-December 2, 2011 (poster presentation)

8. Hideaki Fujioka, Bancha Janthong, Porponth Sichanugrist, and Makoto Konagai
   "Preparation of P-type microcrystalline silicon oxide film at low temperature and its application to solar cells"
   21st International Photovoltaic Science and Engineering Conference, Hilton Fukuoka Sea Hawk, Fukuoka, Japan, November 28-December 2, 2011 (poster presentation)

9. Bancha Janthong, Takehiro Aino, Porponth Sichanugrist, and Makoto Konagai
   "Light-trapping Improvement of P-i-n silicon-based solar cells with New Refractive-Index Matching Layer Inserted at ZnO/p Interface"
   26th European Photovoltaic Solar Energy Conference and Exhibition, Frankfurt, Germany, September 24-28, 2012 (poster presentation)

10. Bancha Janthong, Yuki Moriya, Aswin Hongshingthong, Porponth Sichanugrist, and Makoto Konagai, "Management of light-trapping effect for novel a-Si:H/μc-Si:H tandem solar cells using Zno/etched white glass substrates"
    22st International Photovoltaic Science and Engineering Conference, Hangzhou, China, November 5- 9, 2012 (oral presentation)

11. Shunsuke Kasashima, Yuki Moriya, Bancha Janthong, Sinae Kim, Porponth Sichanugrist, and Makoto Konagai,
    "Development of a-Si:H/μc-Si:H/μc-Si:H triple-junction solar cells"
    22st International Photovoltaic Science and Engineering Conference, Hangzhou, China, November 5- 9, 2012 (oral presentation)

12. Hidetoshi Wada, Bancha Janthong, Porponth Sichanugrist, and Makoto Konagai, "Improved light trapping effect for thin film silicon solar cells fabricated on W-textured white glass substrates"
25th International Conference on Amorphous and Nanocrystalline Semiconductors, Toronto, Ontario Canada, August 18-23, 2013 (oral presentation)

13. Bancha Janthong, Yuki Moriya, Porponth Sichanugrist, and Makoto Konagai "Improvement of a multi-functional n-μc-SiO and p-μc-SiO interface for novel a-Si:H/μc-Si:H solar cells by introducing CO_2 plasma treatment"
28th European Photovoltaic Solar Energy Conference and Exhibition, Paris, France, September 30- October 04, 2013 (oral presentation)

International Forums, Workshops

1. Bancha Janthong, Ihsanul Afdi Yunaz, Hidetada Tokioka, Shinsuke Miyajima, and Makoto Konagai
"Optical Study of Multi-Stacked Intermediate Layers for a-Si:H/μc-Si:H Tandem Solar Cells"
Korea-Japan Top University League Workshop on Photovoltaics 2010, Wooribyul Seminar Room, Korea Advanced Institute Science and Technology, Daejeon, Korea, August 1-2, 2010 (oral presentation)

2. Bancha janthong, Aswin Hongsingthong, Porponth Sichanugrist and Makoto Konagai
"Enhancement of Short-Circuit Current for Microcrystalline Silicon Solar Cells Using a Dual-functional n-SiOx Layer"
4th International Forum on Multidisciplinary Education and Research for Energy Science, Hawaii, USA, December 17-21, 2011 (oral presentation)

3. Bancha Janthong, Yuki Moriya, Porponth Sichanugrist and Makoto Konagai
   "Reduction of optical losses for silicon-based thin film solar cells using a dual-functional n-SiO_x:H layer "
   Korea-Japan Top University League Workshop on Photovoltaics 2012,
   Korea University, Seoul, Korea, August 1-4, 2012 (oral presentation)

4. Bancha janthong, Yuki Moriya, Porponth Sichanugrist and Makoto Konagai
   "Reduced optical reflection loss of microcrystalline silicon solar cells with new refractive-index matching layer inserted at glass/ZnO interface"
   1st ACEEES International Educational Forum on Environment and Energy Science,
   Hawaii`s Big Island, USA, December 14-18, 2012 (oral presentation)

Domestic Conferences, Symposiums, Forums, Workshops

1. (invited) Aswin Hongsingthong,Taweewat Krajangsang, Bancha Janthong, Liping Zhang, Ihsanul Afdi Yunaz, Akira Yamada and Makoto Konagai
   "Fabrication of W-Texture ZnO Thin Films with a High Haze Value by MOCVD Technique"
   2nd Thin Film Solar Cells Seminar, Plaza Industrial Ota, Tokyo, Japan, November 15-16, 2010 (oral presentation)

2. 藤丘　英明, Bancha Janthong, Porponth Sichanugrist, 小長井　誠
   "低屈折率 n 型微結晶 $Si_{1-x}O_x$:H 薄膜によるヘテロ接合型微結晶 Si 太陽電池の構造簡略化"
   2011 年秋季　第72回応用物理学会学術講演会、山形大学、山形市、2011年8月29日～2011年9月2日

Achievements

1. Best Poster Award

   Bancha Janthong, Taweewat Krajangsang, Aswin Hongsingthong, Liping Zhang, Porponth Sichanugrist and Makoto Konagai

   "Improvement of Internal Light-Trapping for Silicon Based Solar Cells with a Newly Developed Structure"

   37th IEEE Photovoltaic Specialists Conference, Washington State Convention Center, Seattle, Washington, USA, June 19-24, 2011 (poster presentation)

2. Best Collaboration Award

   Bancha janthong, Richard Baliban, Kurniawan Tedi

   4th International Forum on Multidisciplinary Education and Research for Energy Science, Hawaii, USA, December 17-21, 2011

3. Best Collaboration Award

   Bancha janthong, Sangho Lee, jason T. Clement

   1st ACEEES International Educational Forum on Environment and Energy Science, Hawaii`s Big Island, USA, December 14-18, 2012